Linear Stability of Convection in an Inclined Porous Channel Filled with Nanofluid, Casson Fluid, and Dusty Fluid

A THESIS SUBMITTED TO
NATIONAL INSTITUTE OF TECHNOLOGY WARANGAL (T.S.)
FOR THE AWARD OF THE DEGREE OF

DOCTOR OF PHILOSOPHY
IN
MATHEMATICS

BY

NIDHI HUMNEKAR
(Roll No : 719096)

Under the supervision of
Prof. D. SRINIVASACHARYA

DEPARTMENT OF MATHEMATICS
NATIONAL INSTITUTE OF TECHNOLOGY
WARANGAL - 506 004, (T.S.) INDIA
FEBRUARY - 2024

C E R T I F I C A T E

This is to certify that the thesis entitled " **Linear Stability of Convection in an Inclined Porous Channel Filled with Nanofluid, Casson Fluid, and Dusty Fluid** " submitted to National Institute of Technology Warangal, for the award of the degree of ***Doctor of Philosophy***, is the bonafide research work done by **NIDHI HUMNEKAR** under my supervision. The contents of this thesis have not been submitted elsewhere for the award of any degree.

Prof. D. Srinivasacharya
Professor
Department of Mathematics
National Institute of Technology Warangal
Telangana State, INDIA

.

DECLARATION

This is to certify that the work presented in the thesis entitled **Linear Stability of Convection in an Inclined Porous Channel Filled with Nanofluid, Casson Fluid, and Dusty Fluid**, is a bonafide work done by me under the supervision of **Prof. D. SRINIVASACHARYA** and has not been submitted elsewhere for the award of any degree.

I declare that this written submission represents my ideas in my own words and where others' ideas or words have been included, I have adequately cited and referenced the original sources. I also declare that I have adhered to all principles of academic honesty and integrity and have not misrepresented or fabricated or falsified any idea / data / fact /source in my submission. I understand that any violation of the above will be a cause for disciplinary action by the Institute and can also evoke penal action from the sources which have thus not been properly cited or from whom proper permission has not been taken when needed.

Nidhi Humnekar

Roll No. 719096

Date:____________

Dedicated to

My Father

Late Shri. Narayan Humnekar

ACKNOWLEDGEMENTS

It is a rare privilege and boon that I could associate myself with Prof. D. Srinivasacharya, Professor of Mathematics, National Institute of Technology Warangal, India, for pursuing my research work. I sincerely extend my gratitude to him for his invaluable guidance and constant encouragement throughout the preparation of this thesis and his involvement and meticulous supervision while my work was in progress. With his inimitable qualities as a good teacher, he chiseled my path towards perfection. Ever since I met him, he has been a perpetual source of motivation, inspiration, encouragement and enlightenment. He is responsible for making the period of my research work as an educative and enjoyable learning experience. The thesis would not have seen the light of the day without his unrelenting support and cooperation. I deem it a privilege to have worked under his amiable guidance. My vocabulary is inadequate to express my gratitude.

I am grateful to Prof. Y. N. Reddy (Retd.), Prof. K.N.S. Kasi Viswanadham, Prof. J. V. Ramana Murthy, and Prof. Debashis Dutta, Department of Mathematics, National Institute of Technology Warangal for their help and support throughout my research period.

I thank the members of the Doctoral Scrutiny Committee, Dr. Ch. Ramreddy, Department of Mathematics, National Institute of Technology Warangal, and Prof. Rashmi Ranjan Rout, Department of Computer Science, National Institute of Technology Warangal for their valuable suggestions, moral support and encouragement while my work was in progress.

I place on record my gratitude to Dr. A. Benerji Babu (Head) and all other faculty members of the Department of Mathematics, National Institute of Technology Warangal for their constant encouragement. Also, I thank the office staff.

I express my cordial thanks to Prof. Bidyadhar Subudhi, Director, National Institute of Technology, Warangal for awarding me Institute Fellowship (MHRD, GoI) to carry out my research work. I thank him for his kind support and encouragement at every stage of this endeavor.

I owe my special thanks to Dr. I.G. Sudha, Dr. G. Shiva Kumar, Dr. Dipak Barman, Dr. Omprakash Meena, Dr. K. Naresh, Dr. Abhinav Srivastava, Dr. V. Pujita, Dr. K. Sita Ramana, Dr. Raghvendra Pratap Singh, Dr. B. Rajender, Dr. R. Shravan Kuman, Dr. Bikash Modak, and Dr. Harlal Saran, for their support. I thank Ms. Smriti Tiwari, Ms. Khushbu Singh, Mr. Pankaj Barman, Mr. Sarthak Sharma and all other research colleagues in the Department of Mathematics, National Institute of Technology Warangal and my friends, who helped me during my Ph.D for being cooperative and also for making my stay in the NITW campus fruitful and enjoyable every moment.

My deepest gratitude to my Parents, Late Sri. Narayan Humnekar and Smt. Kalpana Humnekar, brother, Mr. Nitin Humnekar, sisters, Ms. Nilima Humnekar and Ms. Neha Humnekar, and other family members for their continuous support and constant encouragement over the years. All of their love and affection have been motivating force behind what I am today.

Finally, last but not the least, I would like to thank Raunak Chaudhary for his continuous support and encouragement throughout my Ph.D. journey.

. Nidhi Humnekar

ABSTRACT

In recent years, the study of convective transport through porous media has emerged as an intriguing and significant subject, owing to its relevance in various industrial and engineering applications. Additionally, the exploration of convective instability in fluid-saturated porous layers, heated from below, has long captivated the attention of researchers across different physical conditions. This field finds extensive utility in geophysics, food processing, oil reservoir modeling, thermal insulation construction, and nuclear reactors. Understanding the mechanism of instability in incompressible nanofluid, Casson fluid, and dusty fluid flows through porous media is of utmost importance due to its practical implications in engineering. Nanofluids, which are created by uniformly dispersing and suspending metallic particles on a nanometer scale in conventional heat transfer fluids like water, oil, or ethylene glycol, are particularly relevant and Casson fluid refers to a type of non-Newtonian fluid that exhibits a non-linear relationship between shear stress and shear rate. The primary objective of this thesis is to conduct a linear stability analysis of incompressible nanofluid, Casson fluid and dusty fluid flows in an inclined channel filled with a porous medium.

This thesis is organized into four parts and fourteen chapters. Part- I is composed of a single chapter, Chapter 1. This chapter serves as an introduction and covers several concepts, including nanofluid, Casson fluid, dusty Casson fluid, and porous medium. Additionally, it includes a review of relevant literature related to these topics.

Part-II contains six chapters, namely Chapters 2, 3, 4, 5, 6 and 7. Chapter - 2 investigates convective stability of nanofluid flow in inclined porous channel, considering Brownian motion, thermophoresis, and Brinkman's equation. In Chapter - 3, deals the impact of local thermal non-equilibrium (LTNE) on nanofluid flow stability in an inclined channel filled with a porous medium. Chapter - 4 considers the effects of double diffusion and a magnetic field on the stability of nanofluid flow in an inclined porous channel. Chapter 5 investigates the effect of variable viscosity on the stability of nanofluid flow in an inclined porous channel. Chapter- 6 investigates numerically the local thermal non-equilibrium state of the fluid, particle, and solid-matrix phases for the stability of nanofluid flow in an inclined channel with variable viscosity filled with a porous medium. In Chapter- 7, the effects of double diffusion and variable viscosity on the stability of a nanofluid-saturated Darcy-Brinkman porous medium in an inclined channel are investigated.

Part III comprises three chapters, namely Chapters 8, 9, and 10. Chapter 8 delves into the examination of the stability of Casson fluid flow in an inclined channel with a highly permeable porous medium. The analysis takes into account the presence of a heat source or

sink. In Chapter 9, the investigation shifts towards exploring the stability of Casson fluid flow in an inclined porous channel, considering the effects of chemical reaction and radiation. Chapter 10 is dedicated to investigating the impact of variable viscosity on the stability of Casson fluid flow in an inclined porous channel.

Part-IV contains three chapters, namely Chapters 11, 12, and 13. In Chapter 11, the focus shifts to the investigation of the impact on the stability of two-phase dusty Casson fluid flow in an inclined porous channel. In Chapter 12, the emphasis is placed on studying the impact of variable viscosity on the stability of two-phase dusty Casson fluid flow in an inclined porous channel. Chapter 13 discusses the impact of heat source/sink and radiation on the stability of two-phase dusty Casson fluid flow in an inclined porous channel. In each of the preceding chapters, the non-linear governing equations and their associated boundary conditions are initially cast into dimensionless form through a suitable set of non-dimensional transformations and then converted into a system of linear ordinary differential equations by linear stability analysis and the normal mode technique. Chebyshev's spectral collocation method is used to solve the resultant system of ordinary differential equations. The impact of relevant parameters on the onset of convection is depicted in graphs and tables. In addition, for some problems, the pattern of streamlines, isotherms, and isonanoconcentrations is plotted at a critical level over a single period.

Part V is comprised of a solitary chapter, namely Chapter 14, which serves the purpose of summarizing the research findings, presenting overall conclusions, and future work scope.

NOMENCLATURE

a	overall wave number
B	strength of the magnetic field
$\mathbf{B}_0$	uniform magnetic field
c	wave speed
c_{p}	specific heat at constant pressure
C_s	specific heat of particle at constant pressure
C	concentration
C_1, C_2	constant concentrations
D	Mass diffusion coefficient
Da	Darcy number
D_{B}	Brownian diffusion coefficient
D_{CT}	Soret type diffusivity
D_{f}	Dufour parameter
D_ρ	Mass concentration parameter
D_{S}	solutal diffusivity
D_{T}	thermophoretic diffusion coefficient
D_{TC}	Dufour type diffusivity
$\mathbf{g}$	gravitational acceleration
h	interphase heat transfer coefficient
Ha	Hartmann number
$\mathbf{j}$	current
k	variable viscosity
K	permeability
k_m	Thermal conductivity of the porous medium
L	layer thickness
Le	Lewis number
Ln	thermo-solutal Lewis number
N_{A}	modified diffusivity ratio
N_{B}	modified particle density increment
N_{HP}	Nield number for the fluid/particle interface
N_{HS}	Nield number for the fluid/solid-matrix interface
p	pressure
Pr	Prandtl number
Q	heat source/sink parameter
q_r	Radiative heat flux
R^*	Reaction rate of solute
Re	Reynolds number
Ra	Rayleigh number
R_d	Radiation parameter
Rm	basic density Rayleigh number

R_c	Chemical reaction parameter
Rn	concentration Rayleigh number
Rs	solutal Rayleigh number
Sr	Soret parameter
Sc	Schmidt number
t	time
T	temperature
T_1, T_2	constant temperatures
U_{b}, U_{pb}	basic velocities
$\mathrm{v}a$	Vadasz number
$\vec{V}$	velocity of fluid
(x, y, z)	Cartesian coordinates

Greek symbols

α	streamwise wave number
α_d	momentum dust particle
α_T	thermal dust particle
α_{f}	thermal diffusivity for fluid phase
α_{nf}	thermal diffusivity for nanofluid
α_{m}	thermal diffusivity of the porous medium
β	spanwise wave number
β_{C}	solutal expansion coefficient
β_{T}	thermal expansion coefficient
γ	Casson parameter
γ_{m}	heat capacity ratio
$\gamma_{\mathrm{P}}, \gamma_{\mathrm{S}}$	modified thermal capacity ratios
γ_1	specific heat ratio
δ	small disturbance parameter
ϵ	porosity
ε_{m}	thermal diffusivity ratio
$\varepsilon_{\mathrm{P}}, \varepsilon_{\mathrm{S}}$	modified thermal diffusivity ratios
η	growth rate
θ	inclination angle
λ	gravity variation parameter
Λ	viscosity ratio
μ	dynamic viscosity
$\tilde{\mu}$	effective dynamic viscosity
μ_b	dynamic plastic viscosity
μ_l	viscosity at refrence temperature T_l
ν	kinematic viscosity
ρ	density
ρ_{f}	density for the fluid
ρ_{p}	particle density
$(\rho c)_{\mathrm{f}}$	heat capacity of the fluid
$(\rho c)_{\mathrm{p}}$	heat capacity of the particle material
$(\rho c)_{\mathrm{s}}$	heat capacity of the solid-matrix material

σ	thermal capacity ratio
τ_m	velocity relaxation time of the particles
τ_T	thermal relaxation time of the particles
ϕ	volume fraction
ϕ_1, ϕ_2	constant volume fractions
ψ	stream function

Superscripts

$*$	dimensionless variable
$'$	perturbation variable
tr	transpose of a matrix

Subscripts

$0, b$	basic solution
c	critical
f	fluid phase
p	particle phase
s	solid phase

Contents

[1]Published in "***Journal of Porous Media***" 26(8), pp:21-33, DOI:10.1615/JPorMedia.2023045044

[2]Published in "***Computational Thermal Sciences: An International Journal***" 15(6), pp: 41-59, DOI: 10.1615/ComputThermalScien.2023046825'

[3]Communicated in "***Propulsion and Power Research***"

[4]Published in "***Numerical Heat Transfer; Part A: Applications***" pp:1-14, DOI: https://doi.org/10.1080/10407782.2023.2252176

[5]Published in "***Proceedings of the Institution of Mechanical Engineers, Part E: Journal of Process Mechanical Engineering***" pp:1-15, DOI: 10.1177/09544089241234406

[6]Published in "***Applied Mathematics and Mechanics (English Edition)*** 45(3), pp:563-580, DOI: https://doi.org/10.1007/s10483-024-3096-6"

[7]Communicated in "***Fluid Dynamics***"

[8]Communicated in "***Computational Mathematics and Mathematical Physics***"
[9]Communicated in "***Reviews in Mathematical Physics***"

[10]Communicated in "***The ANZIAM Journal***"
[11]Communicated in "***ZAMM - Journal of Applied Mathematics and Mechanics*** "
[12]Communicated in "***Transport in Porous Media***"

Part I

INTRODUCTION

Chapter 1

Preliminaries and Review

1.1 Introduction

Convective transport in porous media has gained significant attention in recent years due to its wide range of applications across mechanical, chemical, and civil engineering disciplines. These applications encompass a broad spectrum of fields, including the movement of moisture in fibrous insulation, the dispersion of chemical pollutants in saturated soil, the extraction of geothermal energy, food processing and storage, geophysical systems, underground waste disposal (both nuclear and non-nuclear), electrochemistry, thermal insulation in buildings, metallurgy, the design of pebble-bed nuclear reactors, and cooling systems for electronic devices. Different models, such as Darcy [1], Brinkman-extended Darcy [2], Forchheimer-extended Darcy [3], and the generalized flow models, were proposed in the literature to explain the mathematical and physical aspects associated with convective transport in porous media.

The recent emergence of nanofluids, which are engineered suspensions of nanoparticles in liquids, has captured the attention of numerous researchers. These nanofluids have generated significant interest due to their potential to enhance heat transfer rates in engineering systems while mitigating issues such as erosion, sedimentation, and clogging that plagued previous mixtures containing larger particles. Nanofluids have a wide range of applications in various technical fields, including the automotive industry, medicine, power plant cooling systems, and computer systems. One of the most crucial and compelling areas of study in heat and mass transfer theory involves the convection resulting from heated or cooled objects with different geometries and physical conditions in a porous medium saturated with nanofluids. This particular scenario holds immense theoretical and practical importance.

The concept of stability plays a significant role in the mathematical investigation of physical systems, influencing their development. As real-world examples show, stability considerations frequently play a role in the practical application of various technical systems. Engineering constructions like bridges, plates, and shell structures subjected to pressure loading or unloading by flowing fluids, as well as high-speed vehicles, truck-trailer combinations, railway trains, and hydrodynamic challenges, all require stability as a crucial factor. The term "hydrodynamic stability" refers to the response of laminar flow to a small disturbance. If a flow returns to its previous laminar state after a certain period of time and remains in that state, it is deemed stable. However, it is considered unstable if it transitions to a different state. Researchers have employed linearized stability analysis to solve hydrodynamic and hydromagnetic stability problems in various geometries using different fluid models in recent decades.

1.2 Nanofluids

Nanofluids are advanced engineered fluids that consist of a base fluid, such as water or oil, infused with tiny suspended particles called nanoparticles. These nanoparticles, typically ranging in size from 1 to 100 nanometers, are dispersed within the base fluid to create nanoscale composite materials. The addition of nanoparticles to the base fluid results in unique and improved properties compared to traditional fluids. Nanofluids exhibit enhanced thermal conductivity, meaning they can transfer heat more efficiently than regular fluids. This property makes nanofluids extremely attractive for thermal management and heat transfer applications [4]. The applications of nanofluids span across various fields and industries, e.g., nanofluids offer improved cooling capabilities for electronic devices such as computer chips and LEDs, which generate significant heat during operation [5]. They can absorb solar radiation more effectively, thereby increasing the heat transfer and energy conversion rates in solar collectors and thermal energy storage systems [6, 7]. They have the potential to enhance the efficiency of cooling systems in automotive engines and aircraft. And nanofluids are being explored in medical diagnostics and treatments. They have the potential to enhance imaging techniques, such as magnetic resonance imaging (MRI), and improve targeted drug delivery systems [8, 9].

The Boungiorno and Tiwari-Das models are two popular approaches used to study the convective flows of nanofluids. These models provide mathematical formulations to analyze the behavior of nanofluids. Tiwari and Das [10] developed a model to analyze the behaviour of nanofluids by taking the volumetric fraction of nanoparticles into consideration. Buongiorno [11] considered seven slip mechanisms, namely, inertia, Brownian diffusion, thermophoresis, diffusiophoresis, magnus effect, fluid drainage, and gravity that can produce a relative velocity between nanoparticles and the base fluid. In the absence of turbulent effects, he concluded that only Brownian diffusion and thermophoresis are important slip mechanisms in nanofluids. Based on this observation, Buongiorno proposed a mathematical model for the nanofluid based on these effects. Brownian motion refers to the random movement of nanoparticles due to thermal fluctuations, while thermophoresis describes the motion of particles induced by temperature gradients. The Buongiorno model considers the combined effect of these phenomena to estimate the convective heat transfer coefficient and temperature distribution in nanofluid flow.

The fundamental equations for the Buongiorno model consist of the continuity equation, momentum equation, energy equation, and nanoparticle concentration equation given by:

$$\nabla \cdot \vec{V} = 0, \tag{1.1}$$

$$\rho_{\mathrm{f}} \left(\frac{\partial \vec{V}}{\partial t} + \vec{V} \cdot \nabla \vec{V} \right) = \rho_{\mathrm{f}} \mathbf{g} - \nabla p + \mu \, \nabla^2 \vec{V}, \tag{1.2}$$

$$\left(\frac{\partial T}{\partial t} + \vec{V} \cdot \nabla T \right) = \alpha_{\mathrm{nf}} \nabla^2 T + \sigma \left[D_{\mathrm{B}} \, \nabla \phi \cdot \nabla T + \frac{D_{\mathrm{T}}}{T_{\mathrm{m}}} \, \nabla T \cdot \nabla T \right], \tag{1.3}$$

$$\left(\frac{\partial \phi}{\partial t} + \vec{V} \cdot \nabla \phi \right) = D_{\mathrm{B}} \, \nabla^2 \phi + \frac{D_{\mathrm{T}}}{T_{\mathrm{m}}} \, \nabla^2 T. \tag{1.4}$$

where $\vec{V}$ is the velocity vector, T is the temperature, ϕ is the nanoparticle volume fraction, D_{B} is the Brownian diffusion coefficient, D_{T} is the thermophoretic diffusion coefficient, T_{m} is the reference temperature, μ is the viscosity of the fluid, $\mathbf{g}$ is the gravitational acceleration, α_{nf} is the thermal diffusivity for nanofluid, and $\sigma = (\rho c)_{\mathrm{p}}/(\rho c)_{\mathrm{f}}$ is the ratio between heat capacity of nanofluid and nanoparticles.

1.3 Casson Fluids

Casson fluid is a non-Newtonian fluid that describes the behavior of certain viscoelastic materials, such as suspensions and pastes. Unlike Newtonian fluids, which exhibit a linear relationship between shear stress and shear rate, Casson fluids display a non-linear behavior characterized by yield stress and a non-zero viscosity at zero shear rates. It was first introduced by Casson [12] as a mathematical model to describe the behavior of certain types of semi-solid materials, such as mud, chocolate, and paint. The unique properties of Casson fluids make them important in various industrial and biomedical applications. For example, they are commonly used in the production of paints, cosmetics, and food products, where their shear thinning behavior helps to improve the flow and consistency of the materials [13]. In medicine, Casson fluids are used to model the behavior of blood and other biological fluids, and to study the flow of fluids through blood vessels and other tissues [14].

The Casson model proposes that the fluid consists of a network of internal structures or particles embedded in a continuous medium [15]. These structures interact and rearrange under applied stress, giving rise to the unique rheological properties exhibited by Casson fluids. The model introduces two fundamental parameters: yield stress and Casson viscosity. The yield stress represents the minimum stress required to initiate flow, while the Casson viscosity accounts for the resistance to flow once yielding has occurred [16].

The dynamical equations for a Casson fluid with an isotropic rheology are as follows:

$$\tau_{ij} = \begin{cases} 2\left(\mu_b + \frac{p_y}{\sqrt{2\pi_c}}\right)e_{ij}, & \pi < \pi_c \\ 2\left(\mu_b + \frac{p_y}{\sqrt{2\pi}}\right)e_{ij}, & \pi > \pi_c \end{cases}$$

p_y is known as yield stress of the fluid, mathematically expressed as:

$$p_y = \frac{\mu_b\sqrt{2\pi}}{\gamma} \tag{1.5}$$

μ_b is known as plastic dynamic viscosity of the non-Newtonian fluid, π is the product of the component of deformation rate with itself (i.e. $\pi = e_{ij}e_{ij}$), where e_{ij} is the $(i, j)^{th}$ component of the deformation rate and π_c is the critical value based on the non-Newtonian model. In a case of Casson fluid (Non Newtonian) flow, where $\pi > \pi_c$, it is possible to say that

$$\mu = \mu_b + \frac{p_y}{\sqrt{2\pi}} \tag{1.6}$$

Substituting (1.5) into (1.6), the kinematics viscosity of Casson fluid is now depending on plastic dynamic viscosity μ_b, density ρ and Casson parameter γ

$$\zeta = \frac{\mu_b}{\rho}\Big(1 + \frac{1}{\gamma}\Big) \tag{1.7}$$

The Casson model's fundamental equations consist of the continuity equation, momentum equation, and energy equation given by:

$$\nabla \cdot \vec{V} = 0, \tag{1.8}$$

$$\rho\left(\frac{\partial \vec{V}}{\partial t} + \vec{V} \cdot \nabla \vec{V}\right) = \rho \mathbf{g} - \nabla p + \Big(1 + \frac{1}{\gamma}\Big)\mu\, \nabla^2 \vec{V}, \tag{1.9}$$

$$\left(\frac{\partial T}{\partial t} + \vec{V} \cdot \nabla T\right) = \alpha_{\mathrm{f}} \nabla^2 T \tag{1.10}$$

where p is the pressure of Casson fluid phase, α_{f} is the thermal diffusivity for Casson fluid, γ is Casson parameter.
Based on mathematical study, the range of Casson fluid parameter (γ) suitable for this model is 0 to ∞. When $\gamma \to 0$, the yield stress is negligible compared to its plastic viscosity, essentially behaving like a Newtonian fluid, where as at $\gamma \to \infty$, it acts as non-Newtonian fluid.

1.4 Two-phase Dusty Casson Fluids

The fluid flows along with dust particles have an extensive range of mechanical applications like transport processes, cement and steel manufacturing industries, flying ash from thermal plants, and chilling consequences of AC's. Two-phase flow occurs when two distinct aggregation states of the same material or two distinct substances exist concurrently. All combinations are feasible, including gaseous and liquid, gaseous and solid, and liquid and solid. Dusty fluid flow can yield a number of forms, including flows that transform from pure liquid to vapor due to outside heat-separated flows and distributed two-phase flows in which one of the phases exists as particles, bubbles, or droplets in a continuous phase (i.e., liquid or gas). Furthermore, bubbles, rain, and sea waves are examples of two-phase flows. Two-phase flows in microgravity are used in a wide variety of critical applications, including fluid handling and storage, as well as thermal and power systems on spacecraft (e.g., condensers, evaporators, and piping systems). The two-phase dusty fluid has numerous practical applications in various industries, such as boiling and condensation, chemical processing, the oil and gas industry, refrigeration and air conditioning, and biomedical applications [17]

The two-phase flows involving solid particles scattered in a Casson fluid have significant applications in industries. In a two-phase dusty Casson fluid flow, the Casson fluid acts as the continuous phase, providing the medium through which the solid particles move. The dispersed solid particles can range in size, concentration, and properties depending on the specific application. The interaction between the particles and the Casson fluid introduces additional complexities to the flow, such as particle-particle and particle-fluid interactions, particle settling, and the formation of particle clusters or agglomerates. Two-phase dusty Casson fluid flow refers to the behavior and dynamics of a mixture consisting of Casson fluid and dispersed solid particles. This system involves the simultaneous flow of the Casson fluid and the suspended particles, which can have significant impacts on the overall flow behavior and characteristics.

The two-phase dusty Casson fluid flow is governed by the following equations:
For the fluid phase:

$$\nabla \cdot \vec{V} = 0 \tag{1.11}$$

$$\rho\left(\frac{\partial \vec{V}}{\partial t} + \vec{V} \cdot \nabla \vec{V}\right) = \rho \mathbf{g} - \nabla p + \left(1 + \frac{1}{\gamma}\right)\mu \, \nabla^2 \vec{V} + \frac{\rho_p}{\tau_m}(\vec{V}_p - \vec{V}), \tag{1.12}$$

$$\rho C_p\left(\frac{\partial T}{\partial t} + \vec{V} \cdot \nabla T\right) = k_f \nabla^2 T + \frac{\rho_p C_s}{\tau_T}(T_p - T) \tag{1.13}$$

For the particle phase:

$$\nabla \cdot \vec{V_p} = 0 \tag{1.14}$$

$$\frac{\rho_p}{\epsilon}\left(\frac{\partial \vec{V_p}}{\partial t} + \frac{1}{\epsilon}(\vec{V_p} \cdot \nabla)\vec{V_p}\right) = -\nabla p_p - \frac{\rho_p}{\tau_m}(\vec{V_p} - \vec{V}) \tag{1.15}$$

$$\rho_p C_s\left(\frac{\partial T_p}{\partial t} + \vec{V_p} \cdot \nabla T_p\right) = -\frac{\rho_p C_s}{\tau_T}(T_p - T) \tag{1.16}$$

where T is the temperature Temperature of fluid phase, T_p is the temperature of particle phase, p is the pressure of fluid phase, p_p is the pressure of particle phase, ρ is the density of fluid phase, ρ_p is the density of particle phase, C_p is the specific heat of fluid at constant pressure, C_s is the specific heat of particle at constant pressure, τ_m is the velocity relaxation time of the particles, τ_T is the thermal relaxation time of the particles,

1.5 Porous Medium

Porous media refers to materials or substances that contain interconnected voids or pores, which allow for the flow and storage of fluids within them. Examples of porous media include soil, rock formations, filters, and sponges. The study of porous media is essential in various fields, including geology, hydrology, petroleum engineering, environmental science, and chemical engineering [18].

Porous media exhibit unique physical and flow properties due to the complex structure of interconnected pores. The arrangement, size, and connectivity of the pores significantly influence the behavior of fluid flow, heat transfer, and mass transport within the medium. To understand and characterize porous media, several models have been proposed to describe the mathematical and physical aspects of porous media. Among these, the Darcy model and a series of its modifications attracted much acceptance.

Darcy Model

Darcy [1] introduced the fundamental equation that governs fluid motion in a vertical porous column. This equation represents a delicate equilibrium between viscous force, gravitational force, and pressure gradient. Mathematically, it can be expressed as follows:

$$\vec{V} = -\frac{K}{\mu}\left(\nabla p - \rho\,\mathbf{g}\right), \tag{1.17}$$

where $\vec{V}$ is the space averaged velocity (or Darcian velocity), K is the (intrinsic) permeability of the medium.

The aforementioned law appears to be in excellent agreement with experimental results for one-dimensional flows and systems with low porosity. This model is only pertinent to seepage flows, i.e., flows with a low Reynolds number ($O(Re) < 1$), because it does not account for inertial effects.

Darcy-Forchheimer Model

Forchheimer [3] conducted experimental investigations and proposed an adjustment to the momentum equation to incorporate the influence of inertial effects. He suggested including a term proportional to the square of the velocity. The modified form of Darcy's equation, taking into account Forchheimer's modification, is as follows:

$$\left[1+\frac{\rho\, c_{\mathrm{F}}\sqrt{K}}{\mu}|\vec{V}|\right]\vec{V} = -\frac{K}{\mu}\left[\nabla p - \rho\mathbf{g}\right], \tag{1.18}$$

where c_{F} is the dimensionless form drag coefficient and it varies with the nature of the porous medium. The coefficients introduced by Darcy and Forchheimer incorporate the characteristics of both the fluid properties and the microstructure of the porous medium. Several experimental studies have confirmed the model's validity.

Darcy-Brinkman Model

Brinkman [2] proposed a modification to Darcy's equation by introducing the Laplace term. This adjustment was based on the assumption that when flow occurs through a porous medium with high permeability, it should reduce to viscous flow in the limit. Brinkman recognized the significance of accounting for the viscous force exerted by a flowing fluid on a densely packed arrangement of spherical particles within the porous material. To balance the pressure gradient, he added the term $\tilde{\mu}\nabla^2\vec{V}$ to the equation. Here, $\tilde{\mu}$ represents the effective viscosity, which can be calculated as $\tilde{\mu} = \mu(1-2.5(1-\epsilon))$, where μ is the viscosity of the fluid and ϵ is the porosity of the medium. The applicability of the Brinkman model is primarily limited to porous media with high porosity, as supported by experimental observations. The governing equation of the Brinkman model is given as:

$$-\left[\nabla p - \rho\mathbf{g}\right] = \frac{\mu}{K}\vec{V} - \tilde{\mu}\nabla^2\vec{V}. \tag{1.19}$$

1.6 Basic Terminology

Oberbeck-Boussinesq Approximation

The Oberbeck-Boussinesq approximation is a simplification used in fluid dynamics to model certain types of flows, particularly those involving small density variations. It is commonly employed in situations where the effects of buoyancy, such as natural convection, dominate the flow behavior. This approximation allows for the decoupling of density variations from other flow properties, simplifying the governing equations and enabling easier analysis and computation [19].

The density difference $\rho - \rho_\infty$ in the buoyancy portion of the momentum equation for nanofluids can be conveniently and simply defined as

$$\rho = \phi\rho_{\mathrm{p}} + (1-\phi)\rho_{\mathrm{f1}}[1 - \beta_{\mathrm{T}}(T - T_1)], \tag{1.20}$$

where ρ_{p} is the nanoparticle density, ϕ is the nanoparticle volume fraction, T_1 is the reference temperature and ρ_{f1} is the fluid density at reference temperature at some point in the medium, β_{T} is the coefficient of thermal expansion. If the density ρ varies linearly with T over the range of values of the physical quantities encountered in the transport process, β_{T} in Eq. (1.20) are given by

$$\beta_{\mathrm{T}} = -\frac{1}{\rho}\left(\frac{\partial \rho}{\partial T}\right)_{\mathrm{p,C}}.$$

Local Thermal Non-Equilibrium (LTNE)

Local thermal equilibrium (LTE) is achieved when the temperature and heat flux rate at the interface between the solid and fluid phases are balanced, implying no heat transfer between them. This assumption applies when one phase dominates or the porous medium has a small characteristic length scale. However, this assumption is not valid when there are significant temperature differences between the solid and fluid phases or when dealing with high-speed flows. In such cases, the solid and fluid phases have notably different temperatures, leading to a state called local thermal non-equilibrium (LTNE). In LTNE, the fluid temperature rapidly varies with the location of a nanoscale particle, making the system more complex. To accurately represent LTNE, separate temperature equations are required for the solid particle and fluid phases. Nield and Bejan [20] provided the simplest form of the heat transport equation as follows

$$(1-\epsilon)(\rho c)_{\mathrm{s}}\frac{\partial T_{\mathrm{s}}}{\partial t} = (1-\epsilon)\nabla \cdot k_{\mathrm{s}}\nabla T_{\mathrm{s}} + h(T_{\mathrm{f}} - T_{\mathrm{s}}), \tag{1.21}$$

$$\epsilon(\rho c_{\mathrm{p}})_{\mathrm{f}}\left[\frac{\partial T_{\mathrm{f}}}{\partial t} + \vec{V}\cdot\nabla T_{\mathrm{f}}\right] = \epsilon\nabla \cdot k_{\mathrm{f}}\nabla T_{\mathrm{f}} + h(T_{\mathrm{s}} - T_{\mathrm{f}}), \tag{1.22}$$

where h is the inter-phase heat transfer coefficient, ∇T is the temperature gradient and ϵ is the porosity of the porous medium. The subscripts s and f refer to the solid and fluid phases respectively. The specific heat of the solid is denoted by c, c_{p} is the specific heat at constant pressure of the fluid and k is the thermal conductivity.

Hydrodynamic Stability

A physical system is said to be stable when it returns to its original state after being perturbed in some way. To analyze a system's stability, it is subjected to arbitrary small perturbations, and the system's response to these perturbations is evaluated. To be of the permanent type, an equilibrium state or steady flow must not only satisfy the governing equations but also be stable against arbitrary small perturbations.

Hydrodynamic stability concerns the stability and instability of fluid motions. Hydrodynamic stability theory determines the reaction of a steady motion of a fluid (base flow) to small disturbances. The stability of fluid flow is determined by the growth rate of disturbances. If the disturbances grow over time, the flow is considered unstable. Conversely, the flow is considered stable if all the possible disturbances that it can be subjected to decay over time. The origins of this theory can be traced back to the nineteenth century, to Helmholtz, Kelvin, Rayleigh, and Reynolds.

Method of Normal Mode

Normal mode analysis is a technique employed in linear stability analysis to assess the stability of a system around a steady-state solution. It involves linearizing the system's differential equations around the equilibrium point, assuming perturbations in the form of exponential growth or decay, and substituting this assumed solution into the linearized equations to derive an eigenvalue problem.

1.7 Literature Review

The study of the onset of linear stability of convection in a channel is very important in the fields of geothermal system engineering, aquifer hydrology, and pollutant transport in the water-soil system. Horton and Rogers [21] and Lapwood [22] are the first to investigate the onset of convection in a porous medium. Since then, many researchers have examined the instability mechanism of viscous fluid flows in a horizontal and vertical porous layer under a variety of physical conditions.

The study of double-diffusive convection in porous media is an active research topic due to its various applications in the domains of chemical engineering, nuclear industries, food processing, oceanography, geophysics, cancer treatment, biotechnology, and biological fluid movement [23]. Several researchers have investigated the linear stability of convection using double diffusion in a porous medium saturated with Newtonian and non-Newtonian fluids. Mahantesh [24] explored the impact of double diffusion and chemical reaction on the stability of a porous layer saturated with a binary fluid mixture. Deepika [25] discussed the role of Soret and double diffusion in the start of convection in a horizontal fluid filled porous layer. Beaume *et al.* [26] analyzed the three-dimensional doubly diffusive convection in a binary fluid. Attia *et al.* [27] studied the role of cross diffusion on thermo-solutal convection in a horizontal layer with uniform heat and mass fluxes. Shivakumara *et al.* [28] considered the consequences of the applied magnetic field on the stability of convection in the horizontal fluid layer with double diffusion. Shankar *et al.* [29] studied the stability of buoyant flow in a vertical layer of a Darcy porous medium with double diffusion. Noon and Haddad [30] analyzed the influences of variable gravity, rotation, and chemical reaction on the linear and nonlinear stability of a thermosolutal convection in a Darcy porous medium. Dhiman *et al.* [31] analyzed mathematically the thermohaline convection in a viscoelastic fluid saturated porous layer.

The variable viscosity of fluids has a significant impact on fluid flow behavior and is an important consideration in various scientific and engineering applications. In industries such as polymer processing, food processing, and chemical processing, the viscosity of the fluid changes with the change in temperature, pressure, and composition. In environmental science, the variable viscosity of fluids plays a crucial role in understanding the transport and mixing of pollutants in the atmosphere and oceans. The viscosity of air changes with altitude and temperature, while the viscosity of seawater varies with depth and salinity [32]. In biological systems, the viscosity of body fluids such as blood, saliva, and mucus changes with the physiological condition of the body. The variable viscosity of these fluids affects the flow behavior, transport of nutrients and drugs, and various other biological processes [33]. In geophysical fluid dynamics, the variable viscosity of fluids plays an important role in understanding the dynamics of the Earth's atmosphere and oceans. The viscosity of air and seawater changes with temperature, pressure, and composition, affecting the flow behavior and circulation patterns [34]. In heat transfer applications, the variable viscosity of fluids plays a significant role in determining the convective heat transfer rate. The viscosity of the fluid affects the fluid flow behavior and the boundary layer development, which in turn influences the heat transfer process [35]. Many researchers investigated linear stability analysis with changing viscosity. Goyal *et al.* [36] investigated the effect of viscosity fluctuations on the density-induced instability of two miscible fluids in a Hele-Shaw cell in vertical orientation. Yadav *et al.* [37] investigated the effect of viscosity variation, double-diffusive convection, and thermal conductivity on the onset of a nanofluid-saturated porous layer that was heated and salted from below. Umavathi *et al.* [38] analyzed the linear and non-linear stability of convection in a double diffussive Maxwell nanofluid saturated porous medium. In a Rayleigh-Bénard situation with rotation, recently Aanam *et al.* [39] theoretically investigated the dynamics of a ferrofluid with temperature and viscosity that are dependent on the magnetic field.

A renewed interest in studying convective heat and mass transport in porous media has also arisen as a result of the influence of magnetic fields on the flow structure and effectiveness of various systems utilizing electrically conducting fluids. Several researchers have studied linear stability analysis in the presence of a transverse magnetic field. Zhang and Zikanov [40] analyzed the consequence of magnetic field on the linear convective stability of a liquid metal flow in a duct with bottom heating. Hudoba and Molokov [41] explored the influence of heat source and magnetic field on the linear stability of buoyant convective flow in a channel. Singh *et al.* [42] studied the importance of the transverse magnetic field on the linear convective stability in a differently heated channel. Camobreco *et al.* [43] analyzed the linear stability of periodic pulsatile flows in a duct with a transverse magnetic field.

Nanofluids are formed by dispersing nanometer-sized, small solid or metallic particles in normal heat transfer fluids [4]. These fluids will have higher thermal conductivity than conventional heat transfer fluids. Nanofluids are utilized in oil recovery, solar water heating, hybrid-powered engines, interfacial tension reduction, profile modification, indoor ventilation with radiators, and microelectronics. The method of employing both nanofluid and porous medium has received significant attention, which has prompted much research in this area. In-depth analysis is provided by Kasaeian *et al.* [44] on the utilization of porous media and nanofluids together to enhance heat transfer in thermal systems characterized by different geometrical configurations, flow patterns, and boundary conditions. Linear stability analysis in a nanofluid saturated porous medium has been the subject of investigation by various researchers. Rana and Chand [45] developed a linear stability analysis model to investigate thermal convection in a rotating nanofluid-filled porous layer governed by the Darcy-Brinkman model. Umavathi and Prathap [46] analyzed the stability, both linear and nonlinear, of a porous layer saturated with viscoelastic nanofluid. Khalid *et al.* [47] investigated the impact of an internal heat source, feedback control, and double diffusion on the initiation of convection in a rotating layer of nanofluid. Akbarzadeh and Mahian [48] analyzed the beginning of natural convection in a nanofluid filled porous layer sandwiched between two solid walls. Yadav [49] examined the consequences of rotation and changing gravitational field on the beginning of convection in an inhomogeneous nanofluid porous layer. Srinivasacharya and Barman [50] researched convective instability in the vertical porous layer comprising nanofluid. Ketchate *et al.* [51] explored the stability of the flow of hybrid nanofluid between two stationary parallel plates containing porous medium. Ketchate *et al.* [52] investigated the stability of Al_2O_3/water nanofluid mixed convection in a porous medium-packed channel subjected to heating from the bottom and cooling from above. Kaur and Sharma [53] analyzed the linear and nonlinear stability of thermal convection in porous media saturated with Oldroyd-B nanofluids.

In all the above studies on convective transport in nanofluid saturated porous medium, it is assumed that fluid and solid-matrix phases are in local thermal equilibrium (LTE). This presumption of the fluid and porous medium being in an LTE condition may not hold true if there is a significant temperature variation between the phases or if there is a quick heat transfer for high-speed flow. The effects of local thermal non-equilibrium (LTNE) must be taken into account since the temperatures of the fluid and solid-matrix phases are no longer uniform. The behavior of nanofluid flow under local thermal non-equilibrium conditions can help engineers and researchers to design more efficient heat transfer systems. The impact of LTNE on thermal convective instability was first studied by Banu and Rees [54], even though the study of flow in porous media was started in the late 1990s. Since then, numerous studies on the effects of LTNE on convection in porous medium have been published with various physical and geometrical effects. Ingham and Pop [55], Straughan [56] and Nield and Bejan [18] presented the literature on the LTNE model for fluid phase and solid-matrix in the temperature equation. The investigation of the LTNE state for nanofluids has become a significant area of research due to their fascinating applications in microwave heating, fast heat transfer, refrigeration, and the drying of food. Mahajan and Sharma [57] investigated the consequence of LTNE on the start of convection in a magnetic nanofluid layer. Rana *et al.* [58] explained the simultaneous impacts of a heat source, magnetic field, and local thermal non-equilibrium (LTNE) on thermal instability led to the onset of convection in an electrically conducting Al_2O_3-Cu/water hybrid nanoliquid flowing over parallel plates with rough boundaries. Siddabasappa and Siddheshwar [59] studied the global and linear stability analyses of Darcy-Brinkman-Bénard convection in a liquid-saturated porous medium with a non-uniform gravity field using the LTNE model. Srinivasacharya and Barman [60] examined the consequence of the LTNE state on the stability of nanofluid flow in a vertical channel packed with a porous medium. Enagi *et al.* [61] investigated the impact of LTNE, internal heat, and maximum density on the stability of a rotating porous layer under varying temperatures for both the solid and fluid phases.

Casson fluid is a type of non-Newtonian fluid that exhibits yield stress and shear thinning behavior. Linear stability analysis can provide valuable insights into the behavior of Casson fluid flow, including the onset of turbulence and the influence exerted by a number of different parameters on the stability of the flow. Numerous investigations have been published in the literature on the stability of the flows in a porous channel filled with Casson fluids. Yahaya *et al.* [62] analyzed the stability of the magnetohydrodynamic flow of a Casson fluid across a contracting sheet with heterogeneous-homogeneous reactions. The stability of the flow and heat transport across a stretched sheet in a Casson fluid was examined by Hamid *et al.* [63]. Lund *et al.* [64] looked at the thermal radiation's effect and viscous dissipation effect on the stagnation point flow of MHD Casson fluid over a contracting or expanding surface. Parvin *et al.* [65] examined numerically the effects of the rate of extending and compressing sheet on the mixed convection flow Casson fluid. Yashkun *et al.* [66] analyzed the stability of stagnation-point flow of Casson fluid over a heated permeable stretching or contracting sheet. Mahanta *et al.* [67] investigated the effects of slip velocity on the stability of stagnation point flow of MHD Casson fluid flow across a stretching surface. Dey *et al.* [68] focused on the stability analysis of MHD Casson fluid flow with heat and chemical reaction over an elongating permeable sheet. In a rigid parallel channel with a homogeneous magnetic field, Kundenatti and Misbah [69] investigated the temporal stability of linear two-dimensional perturbations of the plane Poiseuille flow of Casson fluid.

Two-phase dusty fluid flow is a type of flow in which two different types of substances are present and interact with each other. Specifically, it involves the flow of a fluid that contains solid particles or dust, which are suspended within it. This type of flow is commonly found in many industrial and natural systems, such as pneumatic transport systems, fluidized bed reactors, and volcanic eruptions. takes into account both the viscous and the yield stress properties of the fluid. Saffman [70] investigated the stability of dusty gas in laminar flow and used a simple example to demonstrate some characteristics of dusty fluid. The effects of thermal Marangoni convection in magneto-Casson liquid flow through a suspension of dust particles were studied by Mahanthesh and Gireesha [71]. Ali *et al.* [72] studied the two-phase flow of dust and viscoelastic fluids between two rigid parallel plates. Ali *et al.* [73] reported the effect of MHD two-phase fluctuations of viscoelastic dusty particle flow in a horizontal parallel plate. Reza-E-Rabbi *et al.* [74] investigated computationally the multiphase fluid flow behavior over a stretching sheet in the presence of nanoparticles. The experimental properties of heat transmission and multi-phase flow in a long gravity-assisted heat pipe were discussed by Chen *et al.* [75]. Ali *et al.* [76] studied the effects of heat transfer and magnetic field on the magnetohydrodynamic two-phase free convective flow of dusty Casson fluid between parallel plates.

The existence of a heat source or sink can significantly affect the flow of the Casson fluid, leading to changes in the temperature, velocity, and shear stress distribution within the fluid [77]. Mythili and Sivraj [78] examined the implications of a non-uniform heat source on unsteady chemically reacted Casson fluid flow over a flat plate and vertical cone with viscosity and thermal conductivity variations. Makinde and Rundora [79] explored the time dependent convective flow of a chemically reactive Casson fluid in a vertical channel with permeable walls containing the porous medium. Zia *et al.* [80] considered the consequences of cross diffusion, radiation, and exponential heat sources on the three-dimensional mixed convective flow of a Casson fluid over a heated surface. Goud *et al.* [81] examined the implication of heat source on the motion of a Casson fluid through a fluctuating vertically permeable plate. Awais *et al.* [82] analyzed the implications of a magnetic field on the flow of Casson fluid in a porous medium caused by a shrinking surface subjected to heat absorption or germination.

The radiation effects in fluids are crucial for the design and optimization of various industrial and biomedical applications. In nuclear waste disposal, the ability to predict changes in the rheological properties of drilling mud due to radiation exposure can help to prevent well collapse and improve waste containment [83]. In medical imaging and radiation therapy, the radiation effects on blood flow behavior can aid in the development of more effective treatment strategies [84]. The primary mechanism of radiation-induced changes in Casson fluids is the generation of free radicals, which can cause chain scission and cross linking of the fluid molecules. This process can result in changes in the fluid's viscosity, yield stress, and other rheological properties. Bakar *et al.* [85] analyzed the stability of a mixed convection flow through a vertical cylinder permeated by a nanofluid and subjected to thermal radiation. Linear stability analysis of thermally-radiated micropolar fluids in an MHD flow with convective boundary conditions was investigated by Lund *et al.* [86]. Lund *et al.* [64] explored the stability of MHD stagnation point flow of Casson fluid over a contracting or expanding surface due to the influence of thermal radiation and viscous dissipation. Wakif *et al.* [87] examined the effects of surface roughness and thermal radiation on the thermo-magneto-hydrodynamic stability of nanofluids composed of alumina and copper oxide.

Chemical reactions have a significant impact on the rheological properties of Casson fluids, yield stress, and flow behavior. Chemical reactions also affect the thermal and mechanical stability of Casson fluids. The presence of reactive species in the fluid can lead to degradation or decomposition, which can alter the fluid's properties [88]. Additionally, chemical reactions generate heat or consume heat, affecting the temperature of the Casson fluid and its viscosity [78]. Steinberg and Brand [89] introduced chemical reactivity in porous mediums to analyze the convective instabilities of binary mixtures. Srivastava [90] investigated the electro-thermal convective stability of a binary fluid in a horizontal channel with a chemical reaction. Dey *et al.* [68] focused on stability analysis of MHD Casson fluid flow over a long permeable sheet with chemical reactivity. The effect of magnetic cross-field, thermal radiation, and a second order chemical reaction on the unsteady three dimensional flow of electrically conducting Cu–Al_2O_3/water hybrid nanofluid flow past a bidirectionally stretchable melting surface was investigated by Suganya *et al.* [91].

Convection along inclined surfaces has been receiving attention because of many industrial applications in areas such as electroplating, chemical processing of heavy metals, ash or scrubber waste treatment, etc. Barletta and Rees [92] analyzed the thermo-convective instability in an inclined porous layer from a local thermal non-equilibrium perspective. Barletta and Celli [93] discussed the instability of mixed convection in an inclined porous channel. Matta and Hill [94] investigated the thermosolutal instability of double-diffusive convection in an inclined porous layer using a concentration-based internal heat source. Celli and Barletta [95] studied the onset of buoyancy-driven convection in an inclined porous layer with an isobaric boundary. Wen and Chini [96] examined the flow structure and dynamics of moderate-Rayleigh-number thermal convection in a two-dimensional inclined porous layer. Matta and Gajjela [97] used linear stability analysis to explore the Hadley flow in an inclined porous body. Roy *et al.* [98] considered the onset of thermohaline convective instability in an inclined porous layer with permeable boundaries.

1.8 Aim and Scope

It is not always physically realistic to consider the flow past a vertical or horizontal surface. The inclinations are always possible, and hence, there is a need to frame a generalized mathematical model involving the inclination of the surface to carry out the investigation. With such a generalized model, it gets easier to switch to either of the two cases, a horizontal surface or a vertical surface.

The aim of the present thesis is to study the linear stability analysis of nanofluid, Casson fluid, and dusty Casson fluid flow in an inclined channel. Characteristics such as local thermal non-equilibrium, magnetic effect, Soret and Dufour effects, variable viscosity effect, heat source/sink effect, radiation, and chemical reaction effects are considered. In all these problems, the inclined channel is assumed to be filled with porous medium.

1.9 Outline of the Thesis

This thesis consists of FIVE parts and FOURTEEN chapters.

Part - I consists of a single chapter, Chapter 1. It deals with the introduction and presents the motivation for the investigations carried out in the thesis. A survey of pertinent literature is presented, explaining the significance of the problems considered. The basic equations governing the nanofluid based on the Buongiorno model, Casson fluid, and two-phase dusty Casson fluid have been given in this chapter.

Part - II deals with the linear stability of convection in an inclined porous channel filled with nanofluid. This part consists of six chapters (Chapters 2, 3, 4, 5, 6, and 7). In each of these chapters, the Brinkman extended Darcy model is accounted for in the momentum equation of the governing flow through the porous layer. The governing equations and their associated boundary conditions are initially cast into dimensionless form. Small perturbations are imposed on the basic velocity, temperature, and pressure. The generalized eigenvalue problem for the perturbed state is obtained from a normal mode analysis. This eigenvalue problem is solved using the Chenyshev spectral collocation method.

In Chapter - 2, the convective stability of nanofluid flow in an inclined porous channel is numerically investigated. The nanofluid model accounts for the effects of Brownian motion and thermophoresis. In addition, the flow in the porous region governs Brinkman's equation. The influence of inclination angle, porosity, Prandtl number vs. Darcy number, the critical Rayleigh number, and associated wavenumber are graphically displayed. Moreover, disturbances of streamlines, isotherms, and isonanoconcentrations for different values of inclination angle, Darcy number, and Lewis number are expressed.

Chapter - 3, which analyzes the stability of the flow of nanofluid saturated porous medium in an inclined channel, is examined numerically when the fluid, particle, and solid-matrix phases are not in local thermal equilibrium (LTE). The impact of the LTNE parameters, namely, inter-phase heat transfer parameters, modified thermal capacity ratios, and modified thermal diffusivity ratios between the fluid and particle phases and fluid and solid phases, on the breakdown of convection has been disclosed. Further, patterns of the streamlines, isotherms (fluid), isotherms (particle), isotherms (solid matrix), and isonanoconcentrations have been presented for Nield numbers (inter-phase heat transfer parameters) and inclination angle at the critical level.

In Chapter - 4, the effect of the transverse magnetic effect on the instability mechanism of double-diffusive convection in an inclined channel filled with nanofluid is considered. The instability boundaries have been investigated for various values of the magnetic effect, inclination angle, Darcy number, thermo-solutal Lewis number, Dufour parameter, and Soret parameter. Also, patterns of the streamlines, isotherms, isonanoconcentrations, and isosolutes are shown graphically for various values of inclination angle under critical situations.

Chapter - 5, investigates the effect of variable viscosity on stability analysis in an inclined porous channel saturated with nanofluid. The instability boundaries have been investigated for various values of Darcy number, variable viscosity parameter, inclination angle, porosity, and Prandtl number. Further, the patterns of streamlines, isotherms, and isonanoconcentrations have been examined for the governing parameters related to nanofluid at the critical level.

In Chapter - 6, the influence of local thermal non-equilibrium and changing viscosity on the stability of nanofluid flow in an inclined porous channel is considered. The instability boundaries have been discussed graphically for different values of Darcy number, variable viscosity parameter, inclination angle, interphase heat transfer parameters, and modified thermal capacity ratios.

Chapter - 7, investigates the influence of variable viscosity and double diffusive nanofluid convective flow stability in an inclined porous channel. The influences of the inclination angle, Darcy number, thermosolutal Lewis number, Dufour number, and Soret number on the critical Rayleigh number and critical wavenumber are depicted graphically.

Part - III deals with the stability of convective flows in an inclined channel filled with a Casson fluid. This part consists of three chapters (Chapters 8, 9, and 10). In all these chapters, the eigenvalue problem for the perturbed state is obtained from a normal mode analysis and solved using the Chebyshev spectral collocation technique.

Chapter - 8 analyzes the stability of Casson fluid flow in an inclined channel containing a highly permeable porous medium in the presence of a heat source or sink. The onset of convection has been discussed graphically for different values of Darcy number, inclination angle, Casson parameter, heat source/sink parameter, Prandtl number, and porosity. Further, the patterns of streamlines and isotherms have been examined for different values of inclination angle at the critical level.

In Chapter - 9, the effects of radiation and chemical reaction in an inclined channel filled with Casson fluid are considered. The critical Rayleigh number and critical wavenumber are computed and graphically presented for various values of inclination angle, Darcy number, radiation parameter, chemical reaction parameter, Prandtl number, and porosity parameter. The influence of these parameters on the flow instability is analyzed. Additionally, the distribution of streamlines and isotherms has been studied for various inclination angle values at the critical level.

In Chapter - 10, the stability of the flow of Casson fluid-saturated porous medium in an inclined channel is examined numerically with variable viscosity. The influence of the governing parameters inclination angle, Casson parameter, variable viscosity parameter, Prandtl number, and porosity parameter on flow instability is studied. Further, the patterns of streamlines and isotherms have been examined for different values of inclination angle at the critical level.

Part - IV deals with the stability of convective flows in an inclined channel filled with a dusty fluid. This part consists of three chapters (Chapters 11, 12, and 13). In all these chapters, the eigenvalue problem for the perturbed state is obtained from a normal mode analysis and solved using the Chebyshev spectral collocation technique.

Chapter - 11 presents the impact on the stability of two-phase dusty Casson fluid flow in an inclined porous channel. The stability region has been discussed for the occurrence of physical parameters such as the inclination angle, mass concentration parameter, momentum dust parameter, Prandtl number, and porosity parameter for the dusty Casson phase and dusty phase.

Chapter - 12 deals with the impact of variable viscosity on the stability of two-phase dusty Casson fluid flow in an inclined porous channel. The influence of the governing parameters (inclination of the channel, variable viscosity parameter, mass concentration parameter, momentum dust parameter, Prandtl number, and porosity parameter) on the flow instability is studied for the dusty Casson phase and dusty phase.

In Chapter - 13, the onset of heat source/sink and radiation on the stability of the two-phase dusty flow of Casson fluid in a porous channel with an inclination is investigated numerically. The effects of the inclination of the channel, heat source/sink parameter, mass concentration parameter, radiation parameter, momentum dust parameter, Prandtl number, and porosity parameter are analyzed and presented graphically.

Part - V consists of a single chapter, Chapter - 14, which includes the principal conclusions of the thesis and the directions in which further investigations may be carried out.

In all the above chapters, it is assumed the porous medium is homogeneous and hydrodynamically as well as thermally isotropic.

A list of references is given at the end of the thesis. The references are arranged in serial order. In some of the chapters, details that were already presented in the earlier chapters are avoided. A review of the existing literature is presented in the introduction. In each of the chapters, only a brief introduction to the concerned problem is given. Also, the physical meaning of the various parameters is repeated in each chapter for easy readability.

A considerable part of the work in the thesis is published or accepted for publication in reputed journals. The remaining part is communicated for possible publication. The details are presented below.

List of papers published

1. **Humnekar N.**, and Srinivasacharya D. (2024). "Influence of variable viscosity and double diffusion on the convective stability of a nanofluid flow in an inclined porous channel", ***Applied Mathematics and Mechanics (English Edition)***, 45(3), pp:563-580, DOI: https://doi.org/10.1007/s10483-024-3096-6. (I.F.-4.4, Springer, **SCI**)

2. **Humnekar Nidhi**, and Srinivasacharya Darbhasayanam (2024). "Influence of variable viscosity and local thermal non-equilibrium on nanofluid flow stability in an inclined porous channel", ***Proceedings of the Institution of Mechanical Engineers, Part E: Journal of Process Mechanical Engineering***, pp:1-15 DOI: 10.1177/09544089241234406. (I.F.-2.4, Sage, **SCI**)

3. **Humnekar N.**, and Srinivasacharya (2023). "The stability of the nanofluid flow in an inclined porous channel with variable viscosity". ***Numerical Heat Transfer, Part A: Applications***, pp:1-14, DOI: https://doi.org/10.1080/10407782.2023.2252176. (I.F.-2, Taylor & Francis, **SCI**)

4. Srinivasacharya D., and **Humnekar N.** (2023). "Influence of local thermal non-equilibrium on the stability of nanofluid flow in an inclined channel filled with porous medium". ***Computational Thermal Sciences: An International Journal***, 15(6), pp: 41-59, DOI: 10.1615/ComputThermalScien.2023046825. (I.F.-1.5, Begell House, **SCI**)

5. Srinivasacharya D., and **Humnekar N.** (2023). "Linear Convective Stability in an Inclined Channel Filled with a Nanofluid Saturated Porous Medium. ***Journal of Porous Media***, 26(8), pp:21-33, DOI:10.1615/JPorMedia.2023045044. (I.F.-2.3, Begell House, **SCI**)

List of papers communicated

6. "The stability of double diffusive convection in an inclined porous channel filled with nanofluid and subjected to a magnetic field", ***Propulsion and Power Research.***
7. 'The heat source/sink effect on the stability of the Casson fluid flow in an inclined porous channel", ***Fluid Dynamics***.
8. "The impact of chemical reaction and radiation on the stability of the Casson fluid flow in an inclined porous channel", ***Computational Mathematics and Mathematical Physics***.
9. "The variable viscosity effect on the stability of the Casson fluid flow in an inclined Porous channel",***Reviews in Mathematical Physics***
10. "The stability of two-phase dusty Casson fluid flow in an inclined porous channel", ***The ANZIAM Journal***.
11. "The effect of variable viscosity on the flow stability of two-phase dusty Casson fluid in a porous inclined channel", ***ZAMM - Journal of Applied Mathematics and Mechanics*** .
12. "The effects of heat source/sink and radiation on the flow stability of two-phase dusty Casson fluid in a porous inclined channel", ***Transport in Porous Media***.

Part II

STABILITY OF NANOFLUID FLOW IN AN INCLINED POROUS CHANNEL

Chapter 2

Linear Convective Stability in an Inclined Channel Filled with a Nanofluid Saturated Porous Medium [1]

2.1 Introduction

The study of the linear stability of convection in an inclined porous channel is important in geothermal systems, aquifer hydrology, and water-soil pollution transmission. The instability processes of viscous fluid flow in horizontal and vertical porous layers have been widely studied, but a comprehensive mathematical model that accounts for layer inclination is needed. Several investigators, for example, Rana *et al.* [99, 100, 101], Barletta and Rees [92], Barletta and Celli [93], Matta and Hill [94], Matta and Gajjela [97], Celli and Barletta [95], Wen and Chini [96], and Roy *et al.* [98] have analyzed the stability of convection in inclined porous layer filled with Newtonian and different non-Newtonian fluids in the presence of various physical effects such as rotation, local thermal non-equilibrium, mixed convection, electrohydrodynamics, double diffusion, thermohaline convection etc. These studies used the Brinkman model and Oberbeck-Boussinesq approximation to investigate the initiation of convection in inclined porous channels with permeable boundaries, revealing their complex dynamics.

Nanofluids, introduced by Choi [4], are heat transfer fluids that contain nanometer-sized solid/metallic particles. Brownian diffusion and thermophoresis are key nanoparticle/base-

[1]Published in "***Journal of Porous Media***" 26(8), pp:21-33, DOI:10.1615/JPorMedia.2023045044

fluid slip processes [11]. Due to nanoparticle Brownian motion and thermophoresis, nanofluids have lower critical Rayleigh numbers than regular fluids [102]. Rayleigh-Benard convection beginning in a rotating nanofluid layer was studied by Khalid [47] using an internal heat source, double diffusion, and feedback control. Turkyilmazoglu [103] used linear stability theory to study nanofluid hydrodynamic stability, while Singh and Khandelwal [104] examined the mixed convection flow of several nanofluids in a vertical conduit with varied heating.

This chapter examines the linear stability of the flow in an inclined channel filled with a porous medium saturated with nanofluid. The current work uses the Brinkman model [2] for flow in porous media and the Buongiorno model [11] for the nanofluid. By using normal modes, a linear stability analysis is carried out. The resulting eigenvalue problem for small disturbances is solved using the Chebyshev spectral collocation methods. A graphical analysis is performed on the derived numerical solution for various values of the governing parameters.

2.2 Mathematical Formulation

Consider the flow of a nanofluid in an inclined channel filled with a porous medium. The flow configuration and coordinate system are depicted in Fig. 2.1. Assume that the angle of inclination with the horizontal line is θ. The width of the channel is $2L$, and the channel plates are located at $y = -L$ and $y = L$, respectively. It is assumed that the porous medium is isotropic and homogenous. The temperatures of the channel walls $y = -L$ and $y = L$ are T_1 and $T_2 (T_1 > T_2)$, and nanoparticle volume fractions are ϕ_2 and ϕ_1, respectively. Using the above assumptions, the Oberbeck-Boussinesq approximation and Darcy-Brinkman model, the governing equations for the flow are given by:

$$\nabla \cdot \vec{V} = 0 \tag{2.1}$$

$$\frac{\rho_f}{\epsilon}\left(\frac{\partial \vec{V}}{\partial t} + \frac{1}{\epsilon}(\vec{V}\cdot\nabla)\vec{V}\right) = -\nabla p - \frac{\mu}{K}\vec{V} + \tilde{\mu}\nabla^2\vec{V} - \{\phi\rho_p + (1-\phi)\rho_f(1-\beta_T(T-T_1))\} \mathbf{g}(\sin(\theta)\hat{e_x} + \cos(\theta)\hat{e_y}) \tag{2.2}$$

$$\frac{\partial T}{\partial t} + \frac{(\rho C)_f}{(\rho C)_m}\vec{V}\cdot\nabla T = \frac{k_m}{(\rho C)_m}\nabla^2 T + \epsilon\frac{(\rho C)_p}{(\rho C)_m}\left(\frac{D_T}{T_1}\nabla T\cdot\nabla T + D_B\nabla T\cdot\nabla\phi\right) \tag{2.3}$$

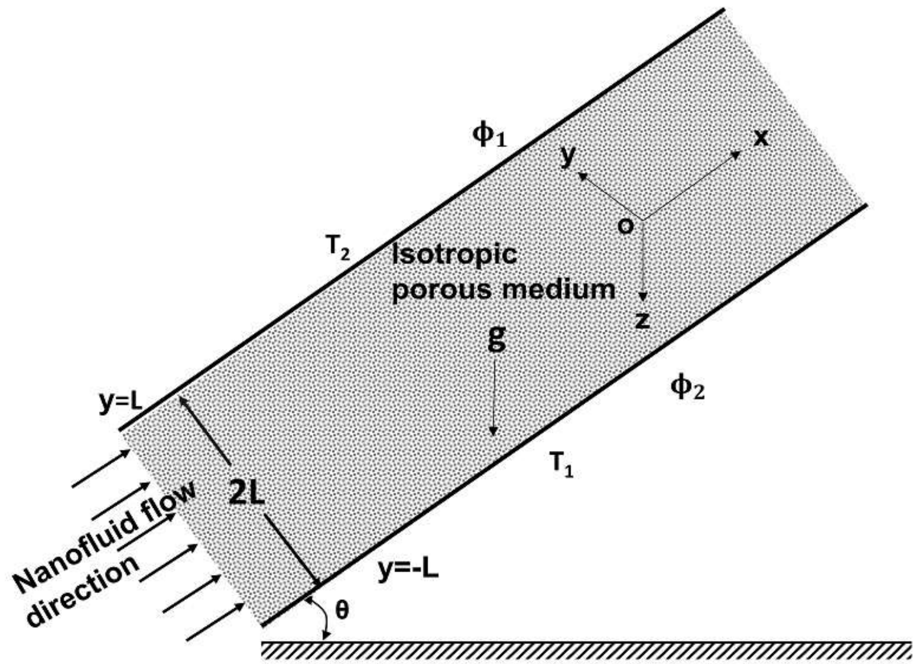

Figure 2.1: "Schematic representation of the problem"

$$\frac{\partial \phi}{\partial t} + \frac{1}{\epsilon}\vec{V} \cdot \nabla \phi = D_B \nabla^2 \phi + \frac{D_T}{T_1} \nabla^2 T \tag{2.4}$$

where the Darcy velocity vector is denoted by $\vec{V}$, the temperature is denoted by T, the volume fraction of nanoparticles is denoted by ϕ, the pressure is denoted by p, and the densities of the base fluid and the nanoparticles are denoted by ρ_f and ρ_p, respectively. The porous medium's viscosity is μ, its effective viscosity is $\tilde{\mu}$, its porosity is ϵ, and its permeability is K. The unit vectors in x and y-directions are denoted by $\hat{e_{\mathrm{x}}}$ and $\hat{e_{\mathrm{y}}}$, respectively, and gravity is denoted by $\mathbf{g}$. The heat capacity of a fluid, a porous medium, and nanoparticle is given by $(\rho C)_f$, $(\rho C)_m$, and $(\rho C)_p$, respectively. k_m is the porous medium's thermal conductivity, D_B is the nanoparticles Brownian diffusion coefficient, and D_T is the thermophoretic diffusion coefficient.

The associated conditions on the boundaries are:

$$\begin{aligned} &\text{At} \quad y = -L: \quad \vec{V} = 0, \quad T = T_1, \quad \phi = \phi_2 \\ \text{and} \quad &\text{at} \quad y = L: \quad \vec{V} = 0, \quad T = T_2, \quad \phi = \phi_1 \end{aligned} \tag{2.5}$$

The non-dimensional variables are:

$$(x^*, y^*, z^*) = \frac{(x, y, z)}{L},\ \vec{V}^* = \frac{\vec{V}L}{\alpha_m},\ p^* = \frac{kp}{\mu\alpha_m},\ t^* = \frac{\alpha_f t}{L^2},$$
$$,T^* = \frac{T - T_1}{T_2 - T_1},\ \phi^* = \frac{\phi - \phi_1}{\phi_2 - \phi_1} \tag{2.6}$$

where $\alpha_m = \frac{k_m}{(\rho C)_f}$, represents thermal diffusivity of porous medium.

on substituting Eq. (2.6) in Eqs. (2.1) -(2.5) and removing asterisk, the non-dimensional form of the Eqs. (2.1) -(2.5) are:

$$\nabla \cdot \vec{V} = 0 \tag{2.7}$$

$$\frac{1}{\mathrm{v}a}\left(\frac{\partial \vec{V}}{\partial t} + \frac{1}{\epsilon}(\vec{V} \cdot \nabla)\vec{V}\right) = -\nabla p + \Lambda Da(\nabla^2 \vec{V}) - \vec{V} + \{RaT - Rn\phi - Rm\}$$
$$(\sin(\theta)\hat{e_{\mathrm{x}}} + \cos(\theta)\hat{e_{\mathrm{y}}}) \tag{2.8}$$

$$\frac{\partial T}{\partial t} + \vec{V} \cdot \nabla T = \nabla^2 T + \frac{1}{Le}\Big(N_B \nabla\phi \cdot \nabla T + N_A N_B \nabla T \cdot \nabla T\Big) \tag{2.9}$$

$$\frac{\partial \phi}{\partial t} + \frac{1}{\epsilon}\vec{V} \cdot \nabla\phi = \frac{1}{Le}\nabla^2\phi + \frac{N_A}{Le}\nabla^2 T \tag{2.10}$$

The corresponding boundary conditions become:

$$\text{At} \quad y = -1: \quad \vec{V} = 0, \quad T = 0, \quad \phi = 1$$
$$\text{and} \qquad \text{at} \quad y = 1: \quad \vec{V} = 0, \quad T = 1, \quad \phi = 0 \tag{2.11}$$

where:
$Pr = \frac{\mu}{\rho_f \alpha_m}$ is Prandtl number, $\mathrm{v}a = \frac{\epsilon pr}{Da}$ is Vadasz number, $Da = \frac{K}{l}$ is Darcy number, $Ra = \frac{\rho_f \mathrm{g}\beta_T KL(T_2 - T_1)}{\mu\alpha_m}$ is Rayleigh number, $Rn = \frac{(\rho_p - \rho_f)(\phi_2 - \phi_1)\mathrm{g}KL}{\mu\alpha_m}$ is concentration Rayleigh number, $Rm = \frac{\rho_p\phi_1 + \rho_f(1-\phi_1)\mathrm{g}KL}{\mu\alpha_m}$ is the basic density Rayleigh number, $\Lambda = \frac{\tilde{\mu}}{\mu}$ the effective viscosity-to-fluid viscosity ratio, $N_A = \frac{D_T(T_2 - T_1)}{D_B T_1(\phi_2 - \phi_1)}$ is the modified diffusivity ratio, $N_B = \frac{\epsilon(\rho C)_p(\phi_2 - \phi_1)}{(\rho C)_f}$ is the modified particle density, and $Le = \frac{\alpha_m}{D_B}$ is the Lewis number.

2.3 Basic solution

Here, the flow is supposed to be continuous, unidirectional (in x-direction), and completely developed. With these assumptions, Eqs. (2.7)-(2.10) reduce to:

$$\Lambda\, Da\, \frac{d^2U_b}{dy^2} - U_b = \frac{\partial p_0}{\partial x} - (RaT_0 - Rn\phi_0 - Rm)\sin(\theta) \tag{2.12}$$

$$\frac{\partial p_0}{\partial y} = (RaT_0 - Rn\phi_0 - Rm)\cos(\theta) \tag{2.13}$$

$$\frac{\partial p_0}{dz} = 0 \tag{2.14}$$

$$\frac{d^2T_0}{dy^2} + \frac{N_B}{Le}\frac{d\phi_0}{dy}.\frac{dT_0}{dy} + \frac{N_A N_B}{Le}\left(\frac{dT_0}{dy}\right)^2 = 0 \tag{2.15}$$

$$\frac{d^2\Phi_0}{dy^2} + N_A\frac{d^2T_0}{dy^2} = 0 \tag{2.16}$$

The following are the associated boundary conditions:

$$\begin{aligned} &\text{At} \quad y = -1: \quad U_b = 0, \quad T_0 = 0, \quad \phi_0 = 1 \\ \text{and} \quad &\text{at} \quad y = 1: \quad U_b = 0, \quad T_0 = 1, \quad \phi_0 = 0 \end{aligned} \tag{2.17}$$

where $U_b(y)$, $T_0(y)$, $\phi_0(y)$, and $p_0(x, y, z)$ are basic velocity in x- direction, basic temperature, basic volume fraction and basic pressure, respectively.

The following approximations to T_0 and ϕ_0 are derived from Eqs. (2.15) and (2.16):

$$T_0 = \frac{1+y}{2} \qquad \text{and} \qquad \phi_0 = \frac{1-y}{2} \tag{2.18}$$

On substituting Eq. (2.18) into Eqs. (2.12) - (2.14) we get:

$$\Lambda\, Da\, \frac{d^2U_b}{dy^2} - U_b = \frac{\partial p_0}{\partial x} - \left(\frac{Ra+Rn}{2}\right) y\sin(\theta) - \left(\frac{Ra-Rn}{2} - Rm\right)\sin(\theta) \tag{2.19}$$

$$\frac{\partial p_0}{\partial y} = \left(\frac{Ra+Rn}{2}\right) y\cos(\theta) + \left(\frac{Ra-Rn}{2} - Rm\right)\cos(\theta) \tag{2.20}$$

$$\frac{\partial p_0}{dz} = 0 \tag{2.21}$$

From Eqs. (2.20) and (2.21), we obtain

$$p_0(x,y) = \left(\frac{Ra + Rn}{4}\right) y^2 \cos(\theta) + \left(\frac{Ra - Rn}{2} - Rm\right) y \cos(\theta) + p_0(x) \tag{2.22}$$

By substituting Eq. (2.22) in Eq. (2.19), we get:

$$\Lambda\, Da \frac{d^2 U_b}{dy^2} - U_b = \frac{d}{dx}\left[p_0(x) + \left(\frac{Ra - Rn}{2} - Rm\right) x \sin(\theta)\right] - \left(\frac{Ra + Rn}{2}\right) y \sin(\theta) \tag{2.23}$$

Eq. (2.23) must be same in $\mathbb{R} \times [-1, 1]$ [105], hence there are real values σ (a pressure gradient on the x) and p_1 such that:

$$p_0(x) = \left[\sigma - \left(\frac{Ra - Rn}{2} - Rm\right) \sin(\theta)\right] x + p_1 \tag{2.24}$$

Hence, Eq. (2.23) reduce to

$$\Lambda\, Da \frac{d^2 U_b}{dy^2} - U_b = \sigma - \left(\frac{Ra + Rn}{2}\right) y \sin(\theta) \tag{2.25}$$

The boundary conditions (2.17) are then used to solve Eq. (2.25), along with the global mass conservation ($\int_{-1}^{1} U_b\, dy = 2$) [106]. Hence, the basic velocity is calculated as follows:

$$U_b = \sigma \left[\frac{cosh(y/\sqrt{\Lambda Da})}{cosh(1/\sqrt{\Lambda Da})} - 1\right] + \left(\frac{Ra + Rn}{2}\right) \left[y - \frac{sinh(y/\sqrt{\Lambda Da})}{sinh(1/\sqrt{\Lambda Da})}\right] sin(\theta) \tag{2.26}$$

where:

$$\sigma = \frac{cosh(1/\sqrt{\Lambda Da})}{\sqrt{\Lambda Da}\, sinh(1/\sqrt{\Lambda Da}) - cosh(1/\sqrt{\Lambda Da})}$$

2.4 Linear Stability Analysis

Three-dimensional perturbations will be examined in the stability analysis, introducing minor perturbations to the basic flow as follows:

$$\begin{aligned}\vec{V}(u,v,w) &= U_b(y) + \vec{U}'(x,y,z,t)\\ T &= T_0(y) + T'(x,y,z,t)\\ \phi &= \phi_0(y) + \phi'(x,y,z,t)\\ p &= p_0(x) + p'(x,y,z,t)\end{aligned} \tag{2.27}$$

where $\vec{U}'$, T', ϕ' and p' are very small perturbations in the velocity, temperature, nanoparticle volume fraction and pressure. Introducing the Eq. (2.27) into Eqs. (2.7) - (2.10) and the ignoring the nonlinear terms, we obtain:

$$\nabla \cdot \vec{U}' = 0 \tag{2.28}$$

$$\begin{aligned}\frac{1}{\mathrm{v}a}\left(\frac{\partial \vec{U}'}{\partial t} + \frac{1}{\epsilon}((\vec{U}' \cdot \nabla)U_b + (U_b \cdot \nabla)\vec{U}')\right) = -\nabla p' + \Lambda Da(\nabla^2 \vec{U}') - \vec{U}' + \{RaT' - \\ Rn\phi'\}(\sin(\theta)\hat{e_{\mathrm{x}}} + \cos(\theta)\hat{e_{\mathrm{y}}})\end{aligned} \tag{2.29}$$

$$\frac{\partial T'}{\partial t} + \left(U_b\frac{\partial T'}{\partial x} + \vec{\mathrm{U}}'\frac{dT_0}{dy}\right) = \nabla^2 T' + \frac{N_B}{Le}\left(\frac{d\phi_0}{dy}\frac{\partial T'}{\partial y} + \frac{dT_0}{dy}\frac{\partial \phi'}{\partial y}\right) + \frac{2N_A N_B}{Le}\frac{dT_0}{dy}\frac{\partial T'}{\partial y} \tag{2.30}$$

$$\frac{\partial \phi'}{\partial t} + \frac{1}{\epsilon}\left(\vec{\mathrm{U}}'\frac{d\phi_0}{dy} + U_b\frac{\partial \phi'}{\partial x}\right) = \frac{1}{Le}\nabla^2\phi' + \frac{N_A}{Le}\nabla^2 T' \tag{2.31}$$

Implementing normal mode analysis, the perturbations are given by:

$$(\vec{U}', T', p', \phi') = (\hat{\mathbf{u}}(y), \hat{T}(y), \hat{p}(y), \hat{\phi}(y))e^{i(\alpha x + \beta z - \alpha c t)} \tag{2.32}$$

The real numbers α and β describe the wave numbers in streamwise and spanwise orientations, respectively. $c = c_r + ic_i$ is the wave speed. If $c_i = 0$, $c_i < 0$ and $c_i > 0$ the disturbances are neutrally stable, stable and unstable, respectively.

On utilizing the Eq. (2.32) in Eqs. (2.28)-(2.31) yields:

$$
\begin{aligned}
\Lambda Da\left[\frac{d^4\hat{v}}{dy^4}-2\frac{d^2\hat{v}}{dy^2}(\alpha^2+\beta^2)+(\alpha^2+\beta^2)^2\hat{v}\right]-\frac{i\alpha}{\text{va}}\left(\frac{U_b}{\epsilon}-c\right)\left[\frac{d^2\hat{v}}{dy^2}-(\alpha^2+\beta^2)\hat{v}\right]+\frac{i\alpha}{\epsilon\text{va}} \\
\frac{d^2U_b}{dy^2}\hat{v}-\left[\frac{d^2\hat{v}}{dy^2}-(\alpha^2+\beta^2)\hat{v}\right]-Ra\left[\frac{d\hat{T}}{dy}i\alpha\sin(\theta)+(\alpha^2+\beta^2)\cos(\theta)\hat{T}\right] \\
+Rn\left[\frac{d\hat{\phi}}{dy}i\alpha\sin(\theta)+(\alpha^2+\beta^2)\cos(\theta)\hat{\phi}\right]=0
\end{aligned}
\tag{2.33}
$$

$$
\begin{aligned}
\frac{1}{\text{va}}(-i\alpha c)\hat{\eta}+\frac{1}{\epsilon\text{va}}\left[\beta\hat{v}\frac{dU_b}{dy}+U_b\hat{\eta}i\alpha\right]-\Lambda Da\left[\frac{d^2\hat{\eta}}{dy^2}-(\alpha^2+\beta^2)\hat{\eta}\right]+\hat{\eta}-\beta Ra\hat{T}\sin(\theta) \\
+\beta Rn\hat{\phi}\sin(\theta)=0
\end{aligned}
\tag{2.34}
$$

$$
\hat{v}\frac{dT_0}{dy}+i\alpha(U_b-c)\hat{T}-\left[\frac{d^2\hat{T}}{dy^2}-(\alpha^2+\beta^2)\hat{T}\right]-\frac{N_B}{Le}\left[\frac{d\phi_0}{dy}+2N_A\frac{dT_0}{dy}\right]\frac{d\hat{T}}{dy}-\frac{N_B}{Le}\frac{dT_0}{dy}\frac{d\hat{\phi}}{dy}=0
\tag{2.35}
$$

$$
\frac{1}{\epsilon}\frac{d\phi_0}{dy}\hat{v}+i\alpha\left(\frac{1}{\epsilon}U_b-c\right)\hat{\phi}-\frac{1}{Le}\left[\frac{d^2\hat{\phi}}{dy^2}-(\alpha^2+\beta^2)\hat{\phi}\right]-\frac{N_A}{Le}\left[\frac{d^2\hat{T}}{dy^2}-(\alpha^2+\beta^2)\hat{T}\right]=0
\tag{2.36}
$$

where u,v,and w are the velocity components and $\eta=\beta u=\alpha v$.

The following are the associated conditions on the boundary

$$
\hat{v}=\frac{d\hat{v}}{dy}=\hat{\eta}=\hat{T}=\hat{\phi}=0 \qquad \text{at} \qquad y=\pm 1
\tag{2.37}
$$

2.5 Numerical solution

A generalized eigenvalue problem with c as the complex eigenvalue is transformed by the set of governing equations (2.33) to (2.36). "Chebyshev spectral collocation" was used to find a solution to the problem in MATLAB [107]. Then the range $[-1,1]$ was discretized utilizing the following $(N+1)$ Gauss-Lobatto collocation points.

$$
y_i=\cos\left(\frac{\pi i}{N}\right), \quad i=0,1,2,...,N.
\tag{2.38}
$$

At the collocation points, the unidentified functions "$\hat{v}$, $\hat{\eta}$, $\hat{T}$, and $\hat{\phi}$" are approximated as follows:

$$\begin{aligned}
\hat{v}(y) &\approx \sum_{j=0}^{N} \hat{v}(y_j)P_j(y_i), \quad \hat{\eta}(y) \approx \sum_{j=0}^{N} \hat{\eta}(y_j)P_j(y_i), \\
\hat{T}(y) &\approx \sum_{j=0}^{N} \hat{T}(y_j)P_j(y_i), \quad \hat{\phi}(y) \approx \sum_{j=0}^{N} \hat{\phi}(y_j)P_j(y_i),
\end{aligned} \tag{2.39}$$

where $i = 0, 1, ..., N$, and P_j is j^{th} Chebyshev polynomial is defined as $P_j(y) = \cos(j \cos^{-1} y)$.

The $\mathbf{m}^{th}$ order of differentiation of unidentified functions at collocation points is denoted as:

$$\begin{aligned}
\frac{d^{\mathbf{m}}\hat{v}}{dy^{\mathbf{m}}} &= \sum_{j=0}^{N} \mathbf{D}^{\mathbf{m}}_{\mathbf{ji}}\hat{v}(\xi_j), \quad \frac{d^{\mathbf{m}}\hat{\eta}}{dy^{\mathbf{m}}} = \sum_{j=0}^{N} \mathbf{D}^{\mathbf{m}}_{\mathbf{ji}}\hat{\eta}(\xi_j), \\
\frac{d^{\mathbf{m}}\hat{T}}{dy^{\mathbf{m}}} &= \sum_{j=0}^{N} \mathbf{D}^{\mathbf{m}}_{\mathbf{ji}}\hat{T}(\xi_j), \quad \frac{d^{\mathbf{m}}\hat{\phi}}{dy^{\mathbf{m}}} = \sum_{j=0}^{N} \mathbf{D}^{\mathbf{m}}_{\mathbf{ji}}\hat{\phi}(\xi_j),
\end{aligned} \tag{2.40}$$

here, the components of the Chebyshev spectral differentiation matrix $\mathbf{D}$ are defined as follows:

$$\mathbf{D}_{ij} = \begin{cases} \frac{2N^2+1}{6}, & i = j = 0, \\ \frac{c_i}{c_j}\frac{(-1)^{i+j}}{y_i - y_j}, & i \neq j;\ i, j = 0, 1, 2, ..., N, \\ -\frac{y_j}{2(1-y_j^2)}, & i = j;\ i, j = 1, 2, 3, ..., N-1, \\ -\frac{2N^2+1}{6}, & i = j = N, \end{cases} \tag{2.41}$$

where

$$c_i = \begin{cases} 2, & i = 0 \ or \ N, \\ 1, & \text{Or else.} \end{cases}$$

Substituting Eqs. (2.39)-(2.40) into Eqs. (2.33) to (2.36), we obtain the following $(4N+4) \times (4N+4)$ generalized eigenvalue problem:

$$\mathbf{A}Y = c\mathbf{B}Y \tag{2.42}$$

with

$$\mathbf{A} = \begin{bmatrix} A_{11} & \mathbf{0} & A_{13} & A_{14} \\ A_{21} & A_{22} & A_{23} & A_{24} \\ A_{31} & \mathbf{0} & A_{33} & A_{34} \\ A_{41} & \mathbf{0} & A_{43} & A_{44} \end{bmatrix}, \quad \mathbf{B} = \begin{bmatrix} B_{11} & \mathbf{0} & \mathbf{0} & \mathbf{0} \\ \mathbf{0} & B_{22} & \mathbf{0} & \mathbf{0} \\ \mathbf{0} & \mathbf{0} & B_{33} & \mathbf{0} \\ \mathbf{0} & \mathbf{0} & \mathbf{0} & B_{44} \end{bmatrix} \quad \text{and} \quad Y = \begin{bmatrix} \mathbb{V} \\ \mathbb{E} \\ \mathbb{T} \\ \mathbb{P} \end{bmatrix}.$$

Here c is the complex eigenvalue, Y indicates $(4N+4)\times 1$ complex eigenfunction, and $\mathbf{A}$ and $\mathbf{B}$ represent $(4N+4)\times(4N+4)$ complex matrices.
where

$$\begin{aligned}
\mathbb{V} &= \left[v(y_0), v(y_1), ..., v(y_{N-1}), v(y_N)\right]^T,\\
\mathbb{E} &= \left[\eta(y_0), \eta(y_1), ..., \eta(y_{N-1}), \eta(y_N)\right]^T,\\
\mathbb{T} &= \left[T(y_0), T(y_1), ..., T(y_{N-1}), T(y_N)\right]^T,\\
\mathbb{P} &= \left[\phi(y_0), \phi(y_1), ..., \phi(y_{N-1}), \phi(y_N)\right]^T,
\end{aligned}$$

$$\begin{aligned}
A_{11} &= \Lambda Da\Big[\mathbf{D}_4 + 2\mathbf{D}_2(\alpha^2+\beta^2) + (\alpha^2+\beta^2)^2\mathbf{I}\Big] - \frac{i\alpha}{\mathrm{va}}\frac{U_b}{\epsilon}\Big[\mathbf{D}_2 - (\alpha^2+\beta^2)\mathbf{I}\Big]\\
&+ \frac{i\alpha}{\epsilon\mathrm{va}}\frac{d^2U_b}{dy^2}\mathbf{I} - \Big[\mathbf{D}_2 - (\alpha^2+\beta^2)\mathbf{I}\Big],\\
A_{13} &= -i\alpha Ra\sin(\theta)\mathbf{D} - (\alpha^2+\beta^2)Ra\cos(\theta)\mathbf{I},\\
A_{14} &= i\alpha Rn\sin(\theta)\mathbf{D} + (\alpha^2+\beta^2)Rn\cos(\theta)\mathbf{I},
\end{aligned}$$

$$\begin{aligned}
A_{21} &= \frac{\beta}{\epsilon\mathrm{va}}\frac{dU_b}{dy}\mathbf{I}, A_{22} = \frac{1}{\mathrm{va}\epsilon}U_b i\alpha\mathbf{I} - \Lambda Da\Big[\mathbf{D}_2 - (\alpha^2+\beta^2)\mathbf{I}\Big] + \mathbf{I},\\
A_{23} &= -\beta Rasin(\theta)\mathbf{I}, \quad A_{24} = \beta Rnsin(\theta)\mathbf{I},
\end{aligned}$$

$$\begin{aligned}
A_{31} &= \frac{dT_0}{dy}\mathbf{I}, \quad A_{33} = i\alpha U_b\mathbf{I} - \left[\mathbf{D}_2 - (\alpha^2+\beta^2)\mathbf{I}\right] - \frac{N_B}{Le}\left[\frac{d\phi_0}{dy} + 2N_A\frac{dT_0}{dy}\right]\mathbf{D},\\
A_{34} &= -\frac{N_B}{Le}\frac{dT_0}{dy}\mathbf{D},
\end{aligned}$$

$$\begin{aligned}
A_{41} &= \frac{1}{\epsilon}\frac{d\phi_0}{dy}\mathbf{I}, \quad A_{43} = -\frac{N_A}{Le}\Big[\mathbf{D}_2 - (\alpha^2+\beta^2)\mathbf{I}\Big],\\
A_{44} &= i\alpha\frac{U_b}{\epsilon}\mathbf{I} - \frac{1}{Le}\left[\mathbf{D}_2 - (\alpha^2+\beta^2)\mathbf{I}\right]
\end{aligned}$$

$$B_{11} = -\frac{i\alpha}{\mathrm{va}}\left[\mathbf{D}_2 - (\alpha^2+\beta^2)\mathbf{I}\right], B_{22} = \frac{i\alpha}{\mathrm{va}}\mathbf{I}, B_{33} = i\alpha\mathbf{I}, B_{44} = i\alpha\mathbf{I}.$$

Here $\mathbf{D}_1$ and $\mathbf{D}_2$ are acquired from the conventional first and second Chebyshev derivative matrices. $\mathbf{D}$ and $\mathbf{D}^2 = \mathbf{D} \times \mathbf{D}$ subsequent to applying boundary conditions $\hat{v}(\pm 1) = 0$. $\mathbf{D}_4$ is fourth derivative matrix that enforces the constrained boundary condition $\hat{v}(\pm 1) = \hat{v}_y(\pm 1) = 0$ and is provided by:

$$\mathbf{D}_4 = \left[diag(1 - y^2)\mathbf{D}^4 - 8diag(y)\mathbf{D}^3 - 12\mathbf{D}^2\right] diag(1/(1 - y^2)),$$

$U_{\rm B} = {\rm diag}[U_{\rm B}(y_i)]$, $\Theta_{\rm B} = {\rm diag}[\Theta_{\rm B}(y_i)]$, $\Phi_{\rm B} = {\rm diag}[\Phi_{\rm B}(y_i)]$, $\mathbf{0}$ and $\mathbf{I}$ are $(N+1)\times(N+1)$ zeros and identity matrices, respectively. Moreover, diag [ ] represents an $(N+1)\times(N+1)$ matrix is constructed such that all entries, except those on the main diagonal, are equal to zero.

To examine the validity of the method, the eigenvalue problem code is executed with a different grid point count (N), and the resulting least consistent eigenvalues are given in Table 2.1 for a set of other parameters chosen at random. For $N \geq 50$, the least consistent eigenvalue meets a convergence threshold of 10^{-7}. The results remain the same when $N \geq 50$. A similar trend may be noticed for different parameter values. As a consequence, $N = 50$ is used in the numerical calculation. The results of $\theta = \pi/2$ were obtained, which is consistent with the results of Srinivasacharya and Barman [50], as shown in Table 2.1.

2.6 Results and discussion

The linear stability of a flow in an inclined parallel channel with a porous medium saturated with nanofluid is investigated. The influence of the governing parameters θ, ϵ, and Pr on the critical Rayleigh number (Ra_c) and critical wavenumber (α_c) is depicted in Figs. 2.2-2.4. On the horizontal axis, the logarithm of the Darcy number is used to show all of the instability boundaries.

The variation of the critical Rayleigh number Ra_c and the critical wavenumber α_c for different values of the inclination angle θ is shown in Fig. 2.2. As the channel varies from horizontal to vertical, it is noticed that Ra_c decreases. However, as the Darcy number (Da) rises, Ra_c rises as well, indicating that permeability has a stabilizing effect, but θ destabilizes the flow as we move θ from horizontal to vertical. Also, the flow is constant until $Da = 1$, and then there is a rapid spike in Ra_c as Da increases. The fluctuation of Ra_c is slow and smooth for small values of the Darcy number ($Da < 1$). When ($Da > 1$), there is a quick increase in Ra_c. The flow resistance in the porous medium becomes obvious at low Darcy numbers. This flow resistance decreases as permeability increases, and flow in the porous medium improves, indicating that viscous forces play a role in the momentum equation. In the case of critical wavelength, for an increase in Da, α_c grows as well, but after $Da = 1$, it becomes constant. As the value of θ increases, there is an increase in α_c. For further discussion, we will take the inclination angle $\theta = \pi/3$.

Fig. 2.3 shows the boundary of the instability region is a function of the porosity parameter (ϵ) and the permeability parameter (Da). It is seen from Fig. 2.3 that increasing the porosity parameter tends to increase the critical Rayleigh number (Ra_c). This is because porosity is a ratio of void volume over total volume. In a porous medium, this is a measurement of the empty spaces. When the porosity rises, the volume of voids rises as well. Hence, porosity stabilizes the flow. Also, it is noted that there is a little variation in α_c when the value of the porosity parameter increases, but there is an increase in α_c as the value of Da grows.

The influence of the Prandtl number (Pr) on the boundaries of instability is seen in Fig. 2.4. The critical Rayleigh number rises as momentum diffusivity increases in terms of Pr. As a result, the Prandtl number has a stabilizing effect on the system. There is substantial flow resistance with small Darcy numbers in the porous medium. This flow resistance decreases as the permeability increases and the porous medium's flow increases, indicating the importance of the momentum equation for viscous forces. Moreover, when permeability increases, the wavenumber also increases. Also, when Pr rises, the wavenumber rises slowly.

Temperature and volume fraction behavior, as well as the dynamics of the flow field, are presented through the streamlines, isotherms, and isonanoconcentration at the critical stage in Figs. 2.5 -2.13 with fixed values of other parameters Pr=7, ϵ=0.6, Λ=1, Rn=15, $N_A = 8$, and $N_B = 0.2$ with varying inclination angle (θ), Darcy number (Da) and Lewis number (Le). It is to be noted that negative contours indicate clockwise rotation for streamline disturbances, while positive contours indicate anticlockwise rotation. In isotherms and isonanoconcentrations, solid lines represent positive contours, and dashed lines represent negative contours. The flow is primarily regulated by two asymmetric cells, one of which (primary cell) rotates clockwise and the other (secondary cell) rotates counterclockwise. streamlines, isotherms, and isonanoconcentration patterns exhibit symmetry for horizontal inclination, i.e., for $\theta = 0$, as seen in Fig. 2.5. However, the symmetry is no longer visible when the value of θ is changed from horizontal to vertical. It is also obvious that as the inclination angle is increased, the cell size grows as well. And for $\theta = \pi/2$, the primary cell pushes downward to the secondary cell. This is because temperature is transferred mostly by diffusion, indicating the presence of disruptions in the flow configuration. Isonanoconcentartion lines are in symmetry, and the center of the channel is for horizontal inclination.

It moves to the left side of the channel for vertical inclination. It changed to the right side of the channel for other inclinations, as shown in Figs. 2.5-2.7.

Figs. 2.8-2.10 show the effect of the Darcy number (Da) on the pattern of streamlines, isotherms, and isonanoconcentrations for $\theta = \pi/3$ over time. The flow is governed by bi-cellular patterns, namely primary and secondary cell patterns. According to our observations, positive streamline contours correspond to clockwise rotation, whereas negative streamline contours correspond to anti-clockwise rotation. But for Da=1, negative streamline contours correspond to clockwise rotation, whereas positive streamline contours correspond to anti-clockwise rotation. With a rise in the Darcy number, the geometry of the inner cells of this bicellular structure changes. The isonanoconcentration lines for flow in an inclined channel demonstrate that over time, a two-cell structure is growing towards the left side of the channel for Da=0.1, towards the right side of the channel for Da=1. On the other hand, Isonanoconcentration lines spread throughout the channel when Da=10.

Figs. 2.11-2.13 show the effect of the Lewis number (Le) on the pattern of streamlines, isotherms, and isonanoconcentrations for $\theta = \pi/3$ over time. Bi-cellular patterns, namely primary and secondary cell patterns, control the flow. Negative streamline contours correspond to clockwise rotation, whereas positive streamline contours correspond to anti-clockwise rotation, according to our findings. The inner cells of this bicellular arrangement change shape as the Lewis number rises.

The primary cell drags the secondary cell downward as Le increases from 100 to 300. In the case of isotherms, the size of the primary cells is increasing further. In the case of isonanoconcentrations, however, when we raise Le, the isonanoconcentration lines shrink and move to the right, as we can see in Fig. 2.13.

Table 2.1: Comparison between least stable eigenvalue of present result and Srinivasacharya and Barman results: Here, "Da = 1, Pr = 7, Ra = 100, Rn = 15, ϵ = 0.6, N_A = 8, N_B = 0.2, Le = 500, θ=$\pi/2$, Λ=1, α= 1, and β = 0."

N	Present study	Srinivasacharya and Barman [50]
30	7.254272433919 -0.116633842907i	7.254272433915 -0.116633842910i
35	7.254500877203 -0.117015950395i	7.254500877193-0.117015950398i
40	7.254526715378 -0.117063301294i	7.254526715361-0.117063301305i
50	7.254526952586 -0.117067639994i	7.254526952722-0.117067639985i
55	7.254526856872 -0.117067504054i	7.254526857357-0.117067503970i
60	7.254526835133 -0.117067533367i	7.254526835407-0.117067533337i

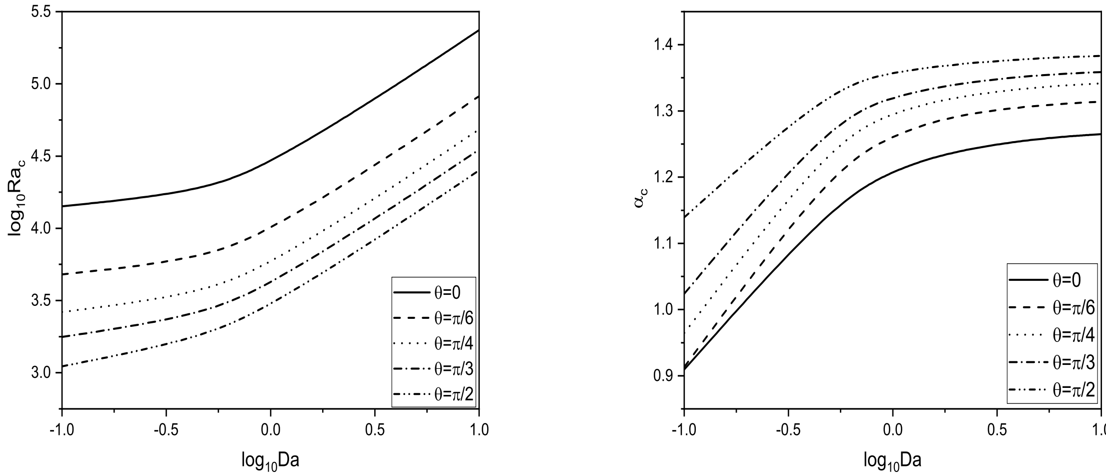

Figure 2.2: "Instability boundaries in ($log_{10}Da$, Ra_c)- plane and ($log_{10}Da$, α_c)-plane for various values of θ with ϵ=0.6, $Rn = 15$, $Le = 500$, $N_A = 8$, Pr=7, Λ=1, and $N_B = 0.2$."

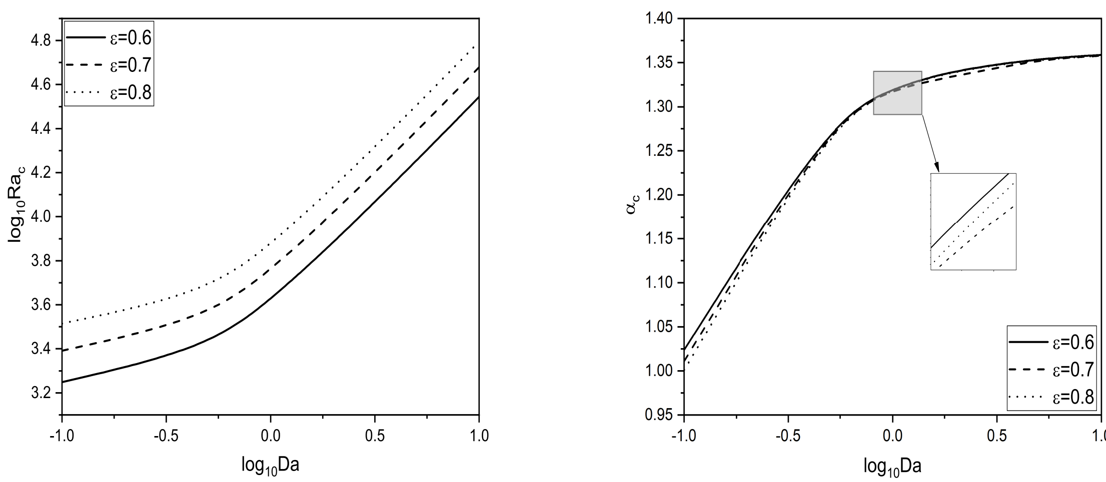

Figure 2.3: "Instability boundaries for ($log_{10}Da$, Ra_c)-plane and ($log_{10}Da$,α_c)-plane for various values of ϵ with θ=$\pi/3$, $Pr = 7$, $Rn = 15$, $Le = 500$, $N_A = 8$, Λ=1, and $N_B = 0.2$."

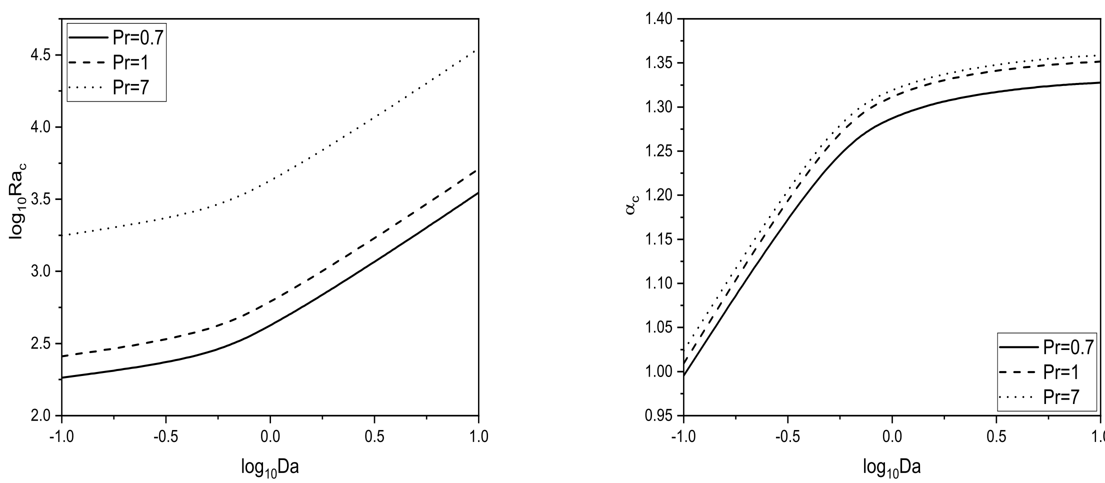

Figure 2.4: "Instability boundaries for ($log_{10}Da$,Ra_c)-plane and ($log_{10}Da$,α_c)-plane for various values of Pr with θ=$\pi/3$, ϵ=0.6, Rn = 15, Le = 500, N_A = 8, Λ=1, and N_B = 0.2."

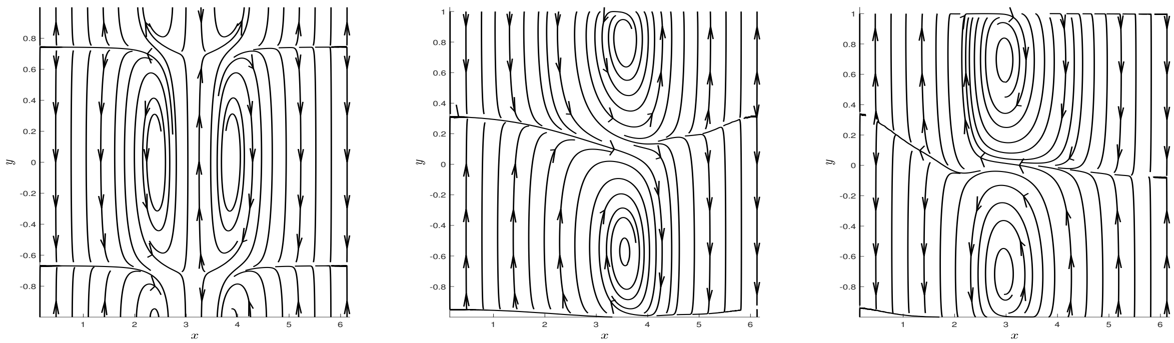

(a) $\theta = 0$ (b) $\theta = \pi/4$ (c) $\theta = \pi/2$

Figure 2.5: "The disturbance of streamlines for different values of θ".

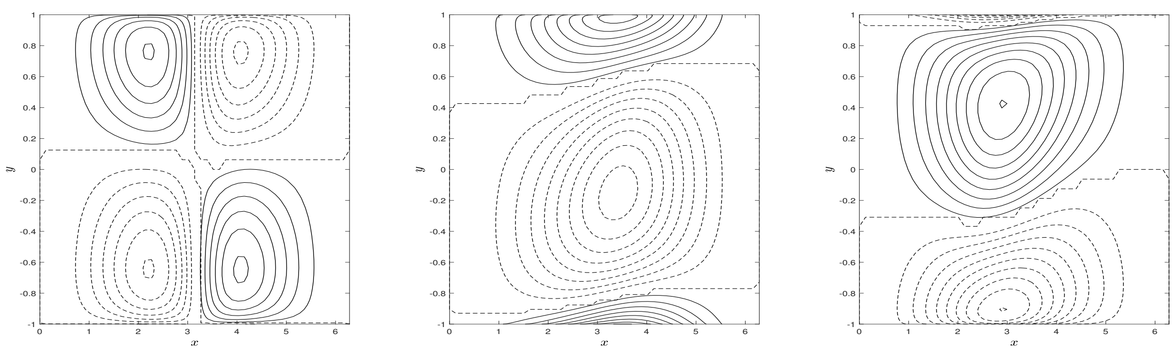

(a) $\theta = 0$ (b) $\theta = \pi/4$ (c) $\theta = \pi/2$

Figure 2.6: "The disturbance of isotherms for different values of θ".

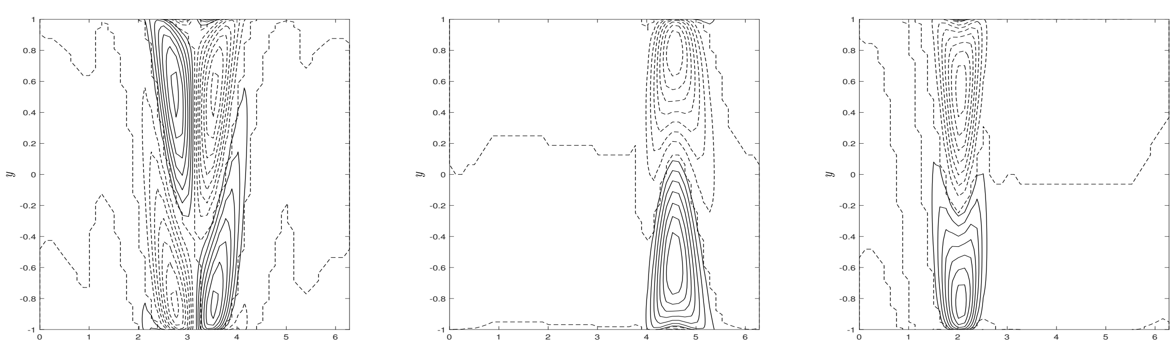

(a) $\theta = 0$ (b) $\theta = \pi/4$ (c) $\theta = \pi/2$

Figure 2.7: "The disturbance of isonanoconcentrations for different values of θ".

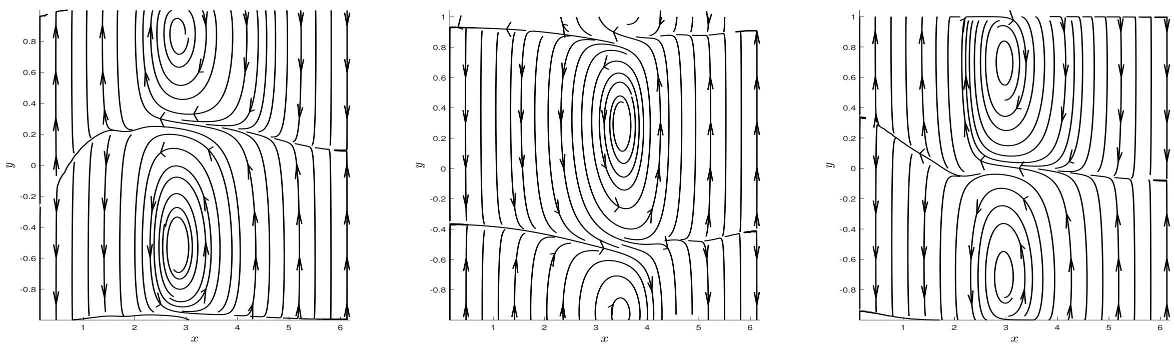

(a) Da=0.1 (b) Da=1 (c) Da=10

Figure 2.8: "The disturbance of streamlines for different values of Da".

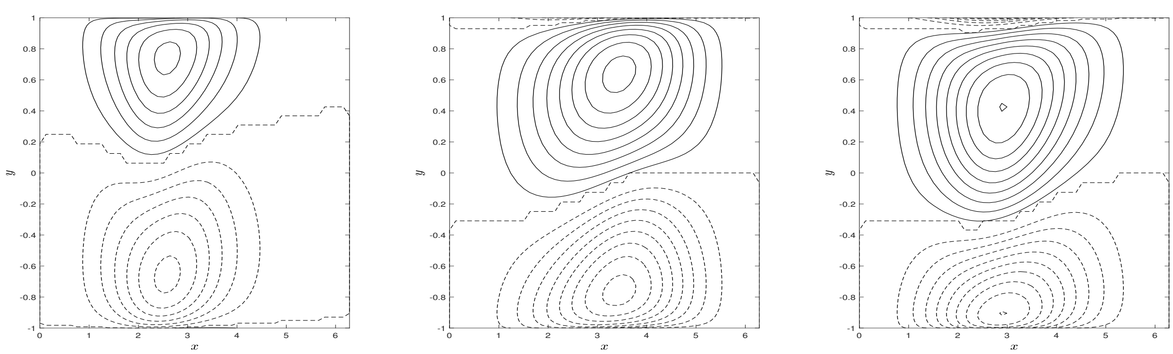

(a) Da=0.1 (b) Da=1 (c) Da=10

Figure 2.9: "The disturbance of isotherms for different values of Da"

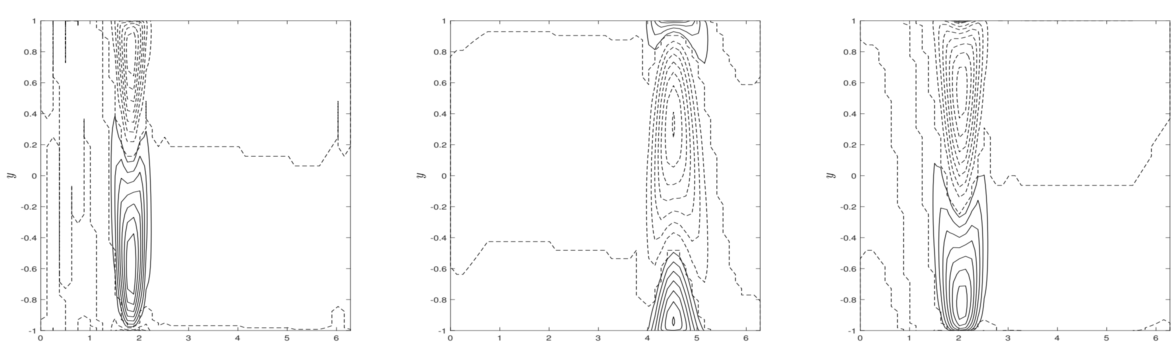

(a) Da=0.1 (b) Da=1 (c) Da=10

Figure 2.10: "The disturbance of isonanoconcentrations for different values of Da"

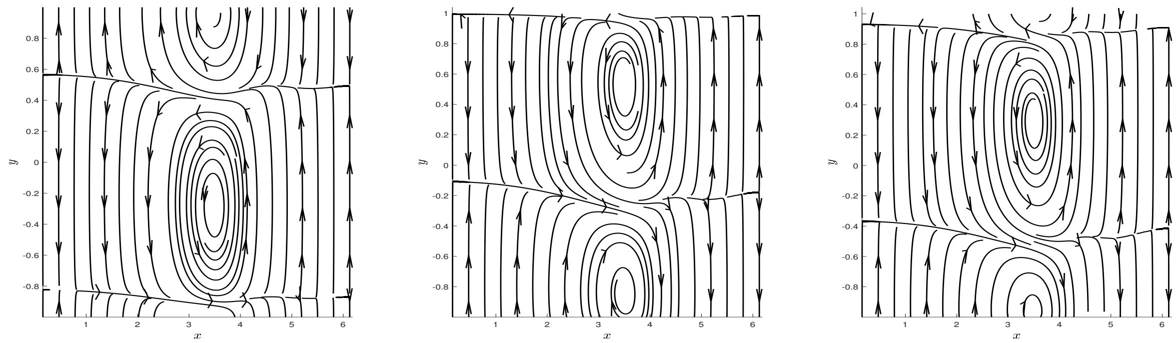

(a) Le=100 (b) Le=300 (c) Le=500

Figure 2.11: “The disturbance of streamlines for different values of Le”.

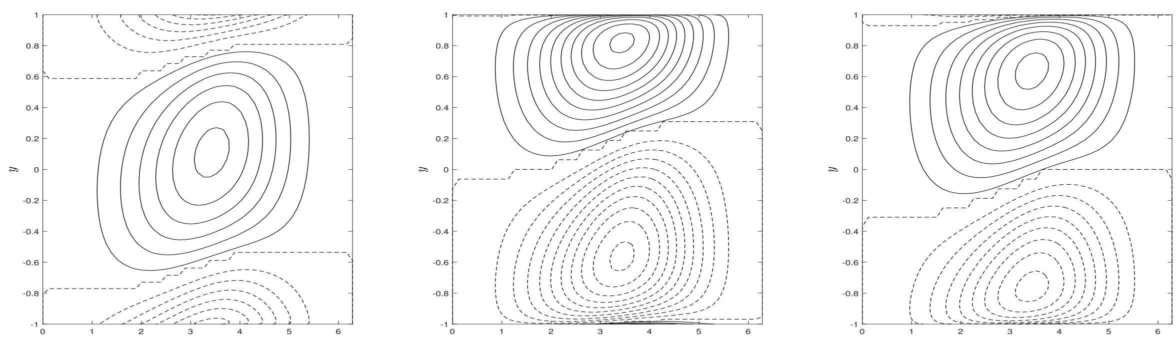

(a) Le=100 (b) Le=300 (c) Le=500

Figure 2.12: “The disturbance of isotherms for different values of Le”

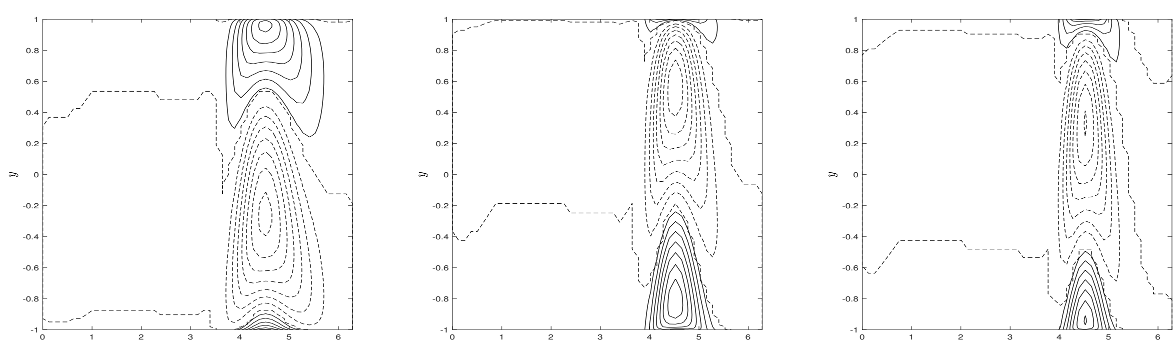

(a) Le=100 (b) Le=300 (c) Le=500

Figure 2.13: “The disturbance of isonanoconcentrations for different values of Le”

2.7 Conclusions

The Brinkman-extended Darcy model is employed to examine the linear stability of convection in an inclined porous channel filled with nanofluid. The critical Rayleigh number (Ra_c) and critical wavenumber (α_c) are computed and graphically presented for various values of θ, Pr, and ϵ versus Da. Moreover, the streamlines, isotherms, and isonanoconcentrations for different values of inclination angle (θ), Darcy number (Da), and Lewis number (Le) for the perturbed state are also presented.

- The inclination of the channel destabilizes the flow.
- For small values of the ($Da < 1$) Darcy number, the variation of Ra_c is slow and smooth. The value of Ra_c increases rapidly when ($Da > 1$).
- The flow in an inclined channel is stabilized by Prandtl number (Pr), and porosity (ϵ). As a result, a rise in these factors delays the onset of convection.
- The least stable flow occurs when the channel is vertical.
- For horizontal inclination, i.e., for $\theta = 0$, streamlines, isotherms, and isonanoconcentration patterns are symmetric. The symmetry is lost when the value of θ is changed from horizontal to vertical.

Chapter 3

Influence of local thermal non-equilibrium on the stability of nanofluid flow in an inclined channel filled with porous medium [1]

3.1 Introduction

This chapter investigates the stability of the flow of nanofluid-saturated porous medium in an inclined channel with a local thermal non-equilibrium (LTNE) effect. Rana *et al.* [58] explained the simultaneous impacts of a heat source, magnetic field, and local thermal non-equilibrium (LTNE) on thermal instability led to the beginning of convection in an electrically conducting Al_2O_3-Cu/water hybrid nanoliquid flowing over parallel plates with rough boundaries. Siddabasappa and Siddheshwar [59] studied the global and linear stability analyses of Darcy-Brinkman-Bénard convection in a liquid-saturated porous medium with a non-uniform gravity field using the LTNE model. Srinivasacharya and Barman [60] examined the consequence of the LTNE state on the stability of nanofluid flow in a vertical channel packed with a porous medium. Enagi *et al.* [61] investigated the impact of LTNE, internal heat, and maximum density on the stability of a rotating porous layer under varying temperatures for both the solid and fluid phases.

[1]Published in "***Computational Thermal Sciences: An International Journal***" 15(6), pp: 41-59, DOI: 10.1615/ComputThermalScien.2023046825'

The literature review reveals that the stability characteristics of a nanofluid in an inclined channel under LTNE conditions between fluid and particle phases and fluid and solid-matrix phases have not been investigated. As a result, the current research examines the impact of LTNE on convection stability in a nanofluid flow for an inclined channel (with inclination θ) filled with a porous medium.

3.2 Mathematical Formulation

Consider an unsteady, incompressible nanofluid flow in an inclined channel of width $2L$ and inclination θ, with impermeable and completely thermally conducting walls as shown in Fig. 2.1. The LTNE state is assumed to exist between the fluid, particle, and solid-matrix phases. The three temperature models are taken into account. As a result, three heat transfer equations, one for each of the three phases, are considered. Except for the density changes in the buoyancy force term, the thermophysical characteristics of the fluid are considered to be constant.

Using the above assumptions, the Oberbeck-Boussinesq approximation and Darcy-Brinkman model [2], the governing equations for the flow are:

$$\nabla \cdot \vec{V} = 0 \tag{3.1}$$

$$\frac{\rho_f}{\epsilon}\left(\frac{\partial \vec{V}}{\partial t} + \frac{1}{\epsilon}(\vec{V}\cdot\nabla)\vec{V}\right) = -\nabla p + \tilde{\mu}\nabla^2\vec{V} - \frac{\mu}{K}\vec{V} - [(1-\phi)\rho_f + \phi\rho_p\ (1-(T_f - T_1)\beta_T)] \mathbf{g}(\sin(\theta)\hat{e_{\mathrm{x}}} + \cos(\theta)\hat{e_{\mathrm{y}}}) \tag{3.2}$$

$$\epsilon(1-\phi_1)(\rho C)_f\left(\frac{\partial T_f}{\partial t} + \frac{1}{\epsilon}\vec{V}\cdot\nabla T_f\right) = \epsilon(1-\phi_1)k_f\nabla^2 T_f + (1-\phi_1)\epsilon(\rho C)_p \left(D_B\nabla\phi\cdot\nabla T_f + \frac{D_T}{T_1}\nabla T_f\cdot\nabla T_f\right) - h_{fp}(T_f - T_p) - h_{fs}(T_f - T_s) \tag{3.3}$$

$$\epsilon\phi_1(\rho C)_p\left(\frac{\partial T_p}{\partial t} + \frac{1}{\epsilon}\vec{V}\cdot\nabla T_p\right) = \epsilon\phi_1 k_p\nabla^2 T_p + h_{fp}(T_f - T_p) \tag{3.4}$$

$$(1-\epsilon)(\rho C)_s\frac{\partial T_s}{\partial t} = (1-\epsilon)k_s\nabla^2 T_s + h_{fs}(T_f - T_s) \tag{3.5}$$

$$\frac{\partial \phi}{\partial t} + \frac{1}{\epsilon}\vec{V} \cdot \nabla \phi = D_B \nabla^2 \phi + \frac{D_T}{T_1} \nabla^2 T \tag{3.6}$$

where The phases fluid, particle, and solid are represented by the subscripts f, p, and s. $(\rho C)_f$, $(\rho C)_p$ and $(\rho C)_s$ are the effective heat capacities, and k_f, k_p and k_s are effective thermal conductivities respectively. h_{fp} and h_{fs} are inter-phase heat transfer coefficients for the fluid-particle, and fluid - solid phases respectively and the remaining quantities are defined in Chapter - 2.

The corresponding boundary conditions are written as

$$\begin{aligned} \text{At} \quad y = -L: \quad & \vec{V} = 0, \quad T_f = T_1, \quad T_p = T_1, \quad T_s = T_1, \quad \phi = \phi_2 \\ \text{at} \quad y = L: \quad & \vec{V} = 0, \quad T_f = T_2, \quad T_p = T_2, \quad T_s = T_2, \quad \phi = \phi_1 \end{aligned} \tag{3.7}$$

The non-dimensional form of the Eqs. (3.1) -(3.6) (on using Eq. (2.6) in Eqs. (3.1) -(3.6) and removing asterisk) are:

$$\nabla \cdot \vec{V} = 0 \tag{3.8}$$

$$\frac{1}{\text{va}}\left(\frac{\partial \vec{V}}{\partial t} + \frac{1}{\text{va}}(\vec{V} \cdot \nabla)\vec{V}\right) = -\nabla p + \Lambda Da(\nabla^2 \vec{V}) - \vec{V} + \{RaT_f - Rn\phi - Rm\}(\sin(\theta)\hat{e_{\text{x}}} + \cos(\theta)\hat{e_{\text{y}}}) \tag{3.9}$$

$$\frac{\partial T_f}{\partial t} + \frac{1}{\epsilon}\left(\vec{V}.\nabla T_f\right) = \nabla^2 T_f + \frac{N_B}{Le}\nabla\phi \cdot \nabla T_f + \frac{N_A N_B}{Le}\nabla T_f \cdot \nabla T_f - N_{HP}(T_f - T_p) - N_{HS}(T_f - T_s) \tag{3.10}$$

$$\frac{\partial T_p}{\partial t} + \frac{1}{\epsilon}\left(\vec{V} \cdot \nabla T_p\right) = \epsilon_p \nabla^2 T_p + \gamma_p N_{HP}(T_f - T_p) \tag{3.11}$$

$$\frac{\partial T_s}{\partial t} = \epsilon_s \nabla^2 T_s + \gamma_s N_{HS}(T_f - T_s) \tag{3.12}$$

$$\frac{\partial \phi}{\partial t} + \frac{1}{\epsilon}\left(\vec{V} \cdot \nabla \phi\right) = \frac{1}{Le}\nabla^2 \phi + \frac{N_A}{Le}\nabla^2 T_f \tag{3.13}$$

The corresponding boundary conditions become:

$$\begin{aligned} \text{At} \quad y = -1: \quad & \vec{V} = 0, \quad T_f = 0, \quad T_p = 0, \quad T_s = 0, \quad \phi = 1 \\ \text{at} \quad y = 1: \quad & \vec{V} = 0, \quad T_f = 1, \quad T_p = 1, \quad T_s = 1, \quad \phi = 0 \end{aligned} \tag{3.14}$$

where $N_{HP} = \frac{h_{fp}L^2}{\epsilon(1-\phi_1)k_f}$ and $N_{HS} = \frac{h_{fs}L^2}{\epsilon(1-\phi_1)k_f}$ are Nield number refers to the interphase heat transfer parameters. $\gamma_p = \frac{(1-\phi_1)(\rho C)_f}{(\rho C)_p \phi_1}$ and $\gamma_s = \frac{\epsilon(1-\phi_1)(\rho C)_f}{(1-\epsilon)(\rho C)_s}$ are modified thermal capacity ratios, $\epsilon_p = \frac{k_p(\rho C)_f}{k_f(\rho C)_p}$ and $\epsilon_s = \frac{k_s(\rho C)_f}{k_f(\rho C)_s}$ are modified thermal diffusivity ratios, respectively.

3.3 Basic state solution

The flow is supposed to be continuous, unidirectional (x-direction), and completely developed in the basic stage. Hence, Eqs. (3.8)-(3.14) can be reduced to a system of ordinary differential equations :

$$(\Lambda Da)\frac{d^2U_b}{dy^2} - U_b = \frac{\partial p_0}{\partial x} - (RaT_{f0} - Rn\phi_0 - Rm)\sin(\theta) \tag{3.15}$$

$$\frac{\partial p_0}{\partial y} = (RaT_{f0} - Rn\phi_0 - Rm)\cos(\theta) \tag{3.16}$$

$$\frac{\partial p_0}{dz} = 0 \tag{3.17}$$

$$\frac{d^2T_{f0}}{dy^2} + \frac{N_B}{Le}\frac{d\phi_0}{dy}.\frac{dT_{f0}}{dy} + \frac{N_AN_B}{Le}\left(\frac{dT_{f0}}{dy}\right)^2 + N_{HP}(T_{p0} - T_{f0}) + N_{HS}(T_{s0} - T_{f0}) = 0 \tag{3.18}$$

$$\epsilon_p\frac{d^2T_{p0}}{dy^2} + \gamma_pN_{HP}(T_{f0} - T_{p0}) = 0 \tag{3.19}$$

$$\epsilon_s\frac{d^2T_{s0}}{dy^2} + \gamma_sN_{HS}(T_{f0} - T_{s0}) = 0 \tag{3.20}$$

$$\frac{d^2\Phi_0}{dy^2} + N_A\frac{d^2T_{f0}}{dy^2} = 0 \tag{3.21}$$

The following are the associated boundary conditions:

$$\begin{aligned} \text{At} \quad y = -1: \quad & U_b = 0, \quad T_{f0} = 0, \quad T_{p0} = 0, \quad T_{s0} = 0, \quad \phi_0 = 1 \\ \text{at} \quad y = 1: \quad & U_b = 0, \quad T_{f0} = 1, \quad T_{p0} = 1, \quad T_{s0} = 1, \quad \phi_0 = 0 \end{aligned} \tag{3.22}$$

Proceeding as in Chapter-2, we get basic solution as:

$$U_b = \sigma\left[\frac{cosh(y/\sqrt{\Lambda Da})}{cosh(1/\sqrt{\Lambda Da})} - 1\right] + \left(\frac{Ra + Rn}{2}\right)\left[y - \frac{\sinh(y/\sqrt{\Lambda Da})}{\sinh(1/\sqrt{\Lambda Da})}\right]\sin(\theta) \tag{3.23}$$

$$T_{f0} = T_{p0} = T_{s0} = \frac{1+y}{2} \quad \text{and} \quad \phi_0 = \frac{1-y}{2} \tag{3.24}$$

where:

$$\sigma = \frac{cosh(1/\sqrt{\Lambda Da})}{\sqrt{\Lambda Da}\,sinh(1/\sqrt{\Lambda Da}) - cosh(1/\sqrt{\Lambda Da})}$$

3.4 Linear stability analysis

As in Chapter - 2, by imposing infinitesimal disturbances (δ) on the basic state solutions, ignoring δ^2 and higher order terms, using the usual normal mode form [50] to express infinitesimal disturbances of corresponding field variables, and removing pressure terms from the resulting equations, the linearized stability equations are obtained as:

$$\Lambda Da\left[\frac{d^4\hat{v}}{dy^4}-2\frac{d^2\hat{v}}{dy^2}(\alpha^2+\beta^2)+(\alpha^2+\beta^2)^2\hat{v}\right]-\frac{i\alpha}{\mathrm{va}}\left(\frac{U_b}{\epsilon}-c\right)\left[\frac{d^2\hat{v}}{dy^2}-(\alpha^2+\beta^2)\hat{v}\right]$$
$$+\frac{i\alpha}{\epsilon\mathrm{va}}\frac{d^2U_b}{dy^2}\hat{v}-\left[\frac{d^2\hat{v}}{dy^2}-(\alpha^2+\beta^2)\hat{v}\right]-Ra\frac{d\hat{T}_f}{dy}i\alpha\sin(\theta)-Ra(\alpha^2+\beta^2)\cos(\theta)\hat{T}_f \tag{3.25}$$
$$+Rn\frac{d\hat{\phi}}{dy}i\alpha\sin(\theta)+Rn(\alpha^2+\beta^2)\cos(\theta)\hat{\phi}=0$$

$$\frac{1}{\mathrm{va}}(-i\alpha c)\hat{\eta}+\frac{1}{\epsilon\mathrm{va}}\left[\beta\hat{v}\frac{dU_b}{dy}+U_b\hat{\eta}i\alpha\right]-\Lambda Da\left[\frac{d^2\hat{\eta}}{dy^2}-(\alpha^2+\beta^2)\hat{\eta}\right]+\hat{\eta}-\beta Ra\hat{T}_f\sin(\theta)$$
$$+\beta Rn\hat{\phi}\sin(\theta)=0 \tag{3.26}$$

$$\frac{1}{\epsilon}\frac{dT_{f0}}{dy}\hat{v}+i\alpha\left(\frac{U_b}{\epsilon}-c\right)\hat{T}_f-\left[\frac{d^2\hat{T}_f}{dy^2}-(\alpha^2+\beta^2)\hat{T}_f\right]-\frac{N_B}{Le}\left[\frac{d\phi_0}{dy}+2N_A\frac{dT_{f0}}{dy}\right]\frac{d\hat{T}_f}{dy}$$
$$-\frac{N_B}{Le}\frac{dT_{f0}}{dy}\frac{d\hat{\phi}}{dy}-N_{HP}(\hat{T}_p-\hat{T}_f)-N_{HS}(\hat{T}_s-\hat{T}_f)=0 \tag{3.27}$$

$$\frac{1}{\epsilon}\frac{dT_{p0}}{dy}\hat{v}+i\alpha\left(\frac{U_b}{\epsilon}-c\right)\hat{T}_p-\epsilon_p\left[\frac{d^2\hat{T}_p}{dy^2}-(\alpha^2+\beta^2)\hat{T}_p\right]-\gamma_pN_{HP}(\hat{T}_f-\hat{T}_p)=0 \tag{3.28}$$

$$i\alpha c\hat{T}_s+\epsilon_s\left[\frac{d^2\hat{T}_s}{dy^2}-(\alpha^2+\beta^2)\hat{T}_s\right]+\gamma_sN_{HS}(\hat{T}_f-\hat{T}_s)=0 \tag{3.29}$$

$$\frac{1}{\epsilon}\frac{d\phi_0}{dy}\hat{v}+i\alpha\left(\frac{U_b}{\epsilon}-c\right)\hat{\phi}-\frac{1}{Le}\left[\frac{d^2\hat{\phi}}{dy^2}-(\alpha^2+\beta^2)\hat{\phi}\right]-\frac{N_A}{Le}\left[\frac{d^2\hat{T}_f}{dy^2}-(\alpha^2+\beta^2)\hat{T}_f\right]=0 \tag{3.30}$$

where $\hat{\eta}=\beta\hat{u}-\alpha\hat{w}$

The following are the associated conditions on the boundary

$$\hat{v}=\frac{d\hat{v}}{dy}=\hat{\eta}=\hat{T}_f=\hat{T}_p=\hat{T}_s=\hat{\phi}=0 \qquad at \qquad y=\pm1 \tag{3.31}$$

3.5 Results and discussion

The set of Eqs. (3.25) - (3.30) expresses a generalized eigenvalue problem with perturbed eigenvalues in terms of wave speed. The solution to this eigenvalue problem is obtained using the Chebyshev spectral collocation method [107].

To examine the validity of the method, the eigenvalue problem code is executed with a different number of grid counts (N), and the resulting least consistent eigenvalues are given in Table 3.1 for a set of other parameters chosen at random. For $N \geq 50$, the least consistent eigenvalue meets a convergence threshold of 10^{-7}, as shown in Table 3.1. The results remain the same when N is enhanced. A similar trend may be noticed for different parameter values. As a consequence, $N = 50$ is used in the numerical calculation. The results of $\theta = \pi/2$ were obtained, which is consistent with the results of Srinivasacharya and Barman [60].

The impact of local thermal non-equilibrium on nanofluid flow stability in an inclined porous channel is investigated in this paper. The flow is controlled by sixteen variables, which are as follows: Da, Λ, Pr, Ra, Rn, ϵ, N_A, N_B and Le (related to the state of LTE), inclination angle (θ), interphase heat transfer parameters N_{HS} and N_{HP}, modified thermal capacity ratios γ_p and γ_s, and modified thermal diffusivity ratios ϵ_p and ϵ_s. Because there are more parameters, the analysis is simplified to focus solely on the effect of LTNE parameters. As a result, for the rest of the discussion, the LTE parameters will be set to $Pr = 7$, $Da = 0.5$, $Rn = 5$, $\Lambda = 1$, $N_A = 8$, $N_B = 0.02$, $\epsilon = 0.6$, and $Le = 100$.

For different LTNE parameters, the change of critical Rayleigh number (Ra_c) and critical wavenumber (α_c) are computed as functions of Nield numbers N_{HP} and N_{HS} and presented in Figs. 3.1 and 3.2. According to Fig. 3.1(a), as N_{HP} increases, the critical Rayleigh number (Ra_c) increases, whereas as N_{HS} increases, Ra_c decreases. Fig. 3.2(a) also depicts a similar trend for variation of Ra_c with inter-phase heat transfer parameters. An enhancement in the values of N_{HP} or N_{HS} enhances the heat release from fluid to solid and fluid to the nanoparticle, respectively. Furthermore, all three phases have almost similar temperatures and act as a single phase, resulting in a local thermal equilibrium state. This is because N_{HP} and N_{HS} become large, and the temperature differences are inversely proportional to inter-phase heat transfer parameters. In the case of critical wavenumber, when N_{HP} rises, α_c increases, and when N_{HS} increases, α_c first drops up to certain values of N_{HS} then rapidly rises in the intermediate values, as shown in Fig. 3.1(b). This could be due to the fluid/particle dominance of heat transfer in the fluid/solid matrix. Furthermore, as shown in Fig. 3.2(b), when N_{HS} rises, α_c falls, and when N_{HP} rises, α_c rises.

The plots for the variation of critical Rayleigh number (Ra_c) and critical wavenumber (α_c) as a function of Nield numbers N_{HP} and N_{HS} for the inclination angle (θ) are displayed in Figs. 3.3 and 3.4. Fig. 3.3(a) shows that Ra_c decreases as θ changes from horizontal to vertical, whereas Ra_c does not change as N_{HP} increases. However, in the case of N_{HS}, Ra_c decreases as N_{HS} and θ both increase, as shown in Fig. 3.4(a). As a result, changing θ from horizontal to vertical destabilizes the flow. This is because when the channel is inclined, the gravitational force acting on the fluid causes a component of the force to act in the direction of the flow. This can lead to the development of instabilities in the nanofluid flow. In the case of critical wavenumber, as θ and N_{HP} increase, so does α_c, as shown in Fig. 3.3(b). Also, as θ moves from horizontal to vertical, α_c rises, and as N_{HS} increases, α_c falls until certain values of N_{HS} and then rises, as shown in Fig. 3.4(b). This could be due to fluid/particle heat transfer dominating fluid/solid matrix heat transfer.

Figs. 3.5 - 3.8 show the behavior of Ra_c and α_c with inter-phase heat transfer parameters N_{HP} and N_{HS} for different values of modified thermal capacity ratios γ_p and γ_s by fixing the other parameter values. As shown in Fig. 3.5(a), Ra_c grows as γ_p increases from 0.01 to 0.1, and Ra_c grows uniformly as N_{HP} increases. simillarly for N_{HS}, as shown in 3.6(a), Ra_c grows as γ_p increases, Ra_c decreases as N_{HS} increases. As a result, γ_p stabilizes the flow for all values of N_{HP} and N_{HS}. Furthermore, as γ_p rises, α_c falls slightly, but as N_{HP} rises, α_c rises, as shown in Fig. 3.5 (b). Also, as N_{HS} rises, α_c rises until a certain value of N_{HS} and then decreases, whereas as N_{HS} rises, α_c first falls for the intermediate values of N_{HS} before rising, as shown in Fig 3.6(b). This could happen as a result of fluid/particle heat transfer dominating fluid/solid matrix heat transfer. As shown in Fig. 3.7(a), Ra_c rises as γ_s rises from 0.01 to 0.03; additionally, Ra_c rises uniformly as N_{HP} rises. In contrast, as shown in Fig. 3.8(a), Ra_c decreases as N_{HS} increases but increases when γ_s decreases. As a result, γ_s stabilizes the flow for all values of N_{HP} and N_{HS}. Furthermore, as γ_s and N_{HP} increase, so does α_c, as shown in Fig. 3.7(b). Also, as γ_s rises, α_c decreases, whereas as N_{HS} rises, α_c first falls in the intermediate values of N_{HS} before rising, as shown in 3.8(b).

Figs. 3.9 - 3.12 show the variation of critical Rayleigh number (Ra_c) and critical wave number (α_c) with inter-phase heat transfer parameters N_{HP} and N_{HS} for different values of the modified thermal diffusivity ratios ϵ_p and ϵ_s by fixing the other parameter values. As displayed in Fig. 3.9(a), Ra_c decreases as ϵ_p rises from 0.1 to 1, and Ra_c increases uniformly as N_{HP} increases. In contrast, for N_{HS}, as shown in Fig. 3.10(a), Ra_c falls as N_{HS} increases, whereas Ra_c decreases as ϵ_p grows. As a result, for all values of N_{HP} and N_{HS} both, ϵ_p destabilizes the flow. As illustrated in Fig. 3.9(b), as ϵ_p increases, α_c decreases, but as N_{HP} increases, α_c increases. Moreover, when N_{HS} rises, α_c first falls in the intermediate values of

N_{HS} before rising, as shown in Fig. 3.10(b), whereas ϵ_p rises, α_c slightly drops. This could happen as a result of fluid/particle heat transfer taking precedence over fluid/solid matrix heat transfer.

As seen in Fig. 3.11(a), Ra_c grows as ϵ_s rises from 0.1 to 0.4; additionally, Ra_c increases gradually as N_{HP} rises. In contrast, for N_{HS}, as displayed in Fig. 3.12(a), Ra_c decreases as N_{HS} raises, but Ra_c increases as ϵ_s rises. As a result, ϵ_s stabilizes the flow for all values of N_{HP} and N_{HS} both. This is because the modified thermal diffusivity ratio can enhance the heat transfer between the fluid and the solid matrix, which can lead to a more stable temperature distribution in the fluid. Additionally, as seen in Fig. 3.11(b), as ϵ_s and N_{HP} increase, α_c rises. Although N_{HS} rises, α_c first falls in the intermediate values of N_{HS} before rising, as seen in Fig. 3.12(b), but with N_{HS}, as ϵ_s rises, α_c increases.

The dynamics of flow field, behavior of temperature, and volume fraction are presented through streamlines, isotherms, and isonanoconcentration at the critical stage in Figs. 3.13 - 3.17 with fixed values of other parameters $\epsilon_p = 0.7, \epsilon_s = 0.2, \gamma_p = 0.04, \gamma_s = 0.01$, $N_{HS} = 50$ and $N_{HP} = 100$ with varying values of inclination angle (θ) from horizontal to vertical. It is to be noted that positive streamline contours correspond to clockwise rotation, whereas negative streamline contours correspond to anti-clockwise rotation. In the case of isotherms and isonanoconcentrations contours, solid lines represent positive contours, while dashed lines represent negative contours. The flow is primarily regulated by two asymmetric cells, one of which (primary cell) rotates clockwise and the other (secondary cell) rotates counterclockwise. For $\theta = \pi/2$, the secondary cell pulls the primary cell downward. This is because temperature is transferred mostly by diffusion, indicating the presence of disruptions in the flow configuration. The patterns of isotherms of fluid, particle, and solid are essentially identical for varying values of θ. The isonanoconcentration lines expand across the channel, but as the channel inclines from horizontal to vertical, they shift to the left portion of the channel.

The effects of the fluid/nanoparticle interphase Nield number (N_{HP}) on the pattern of streamlines, isotherms, and isonanoconcentrations for $N_{HS} = 50$ and $\theta = \pi/3$ are presented in Figs. 3.18 - 3.22. The flow is governed by bi-cellular patterns, namely primary and secondary cell patterns. It is noticed that as the value of N_{HP} is increased, the secondary cell drags the primary cell downward, and the size of the cell also increases. It is interesting to observe that the fluid, particle, and solid matrix phase isotherms do not alter substantially. Further, it is investigated that the isonanoconcentration lines indicate that with time, a two-cell structure expands towards the left portion of the channel for various values of N_{HP}.

The impact of the fluid/solid matrix interphase Nield number (N_{HS}) on the pattern of streamlines, isotherms, and isonanoconcentrations for $N_{HP} = 100$ and $\theta = \pi/3$ over time is shown in Figs. 3.23 - 3.27. Positive streamline contours indicate clockwise rotation, while negative streamline contours indicate anti-clockwise rotation, according to our observations. Further, we observed that isotherms became increasingly dense as the value of N_{HS} increased. When we increase N_{HS} from 1 to 10, the primary cell pulls downwards to the secondary cell, then bounces back to its original place for greater values. We also discovered that for various values of N_{HS}, the isonanoconcentration lines show that a two-cell structure develops towards the left section of the channel with time.

Table 3.1: "Least stable eigenvalue for different number of grid points with $Da = 0.5$, $Pr = 7$, $Rn = 5$, $Ra = 10$, $\epsilon = 0.6$, $N_B = 0.02$, $N_A = 8$, $Le = 100$, N_{HS}=200, N_{HP}=100, γ_p=0.08, γ_s=0.03, $\epsilon_p = 0.7$, $\epsilon_s = 0.2$, Λ=1, α= 1 and $\beta = 0$."

N	**Least stable eigenvalue**
40	3.000398659936 -0.194071517195i
45	3.000399060455 -0.194071530064i
50	3.000399080809 -0.194071416737i
55	3.000398661995 -0.194071518085i
60	3.000398538383 -0.194070880538i

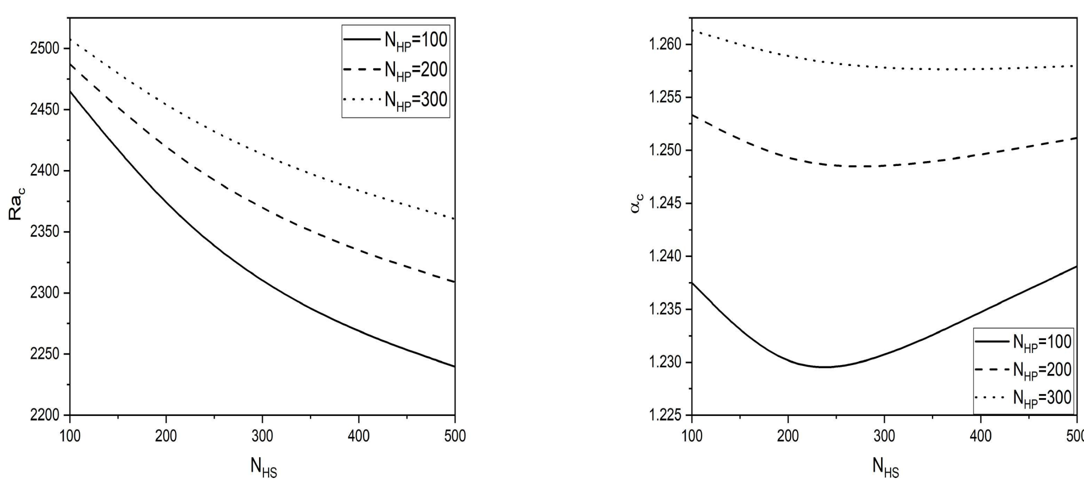

(a) (b)

Figure 3.1: "Variation of (a) critical Rayleigh number and (b) critical wavenumber with N_{HS} for different values of N_{HP} with $\gamma_p = 0.04$, $\gamma_s = 0.01$, $\epsilon_p = 0.7$, $\epsilon_s = 0.2$ and $\theta = \pi/3$."

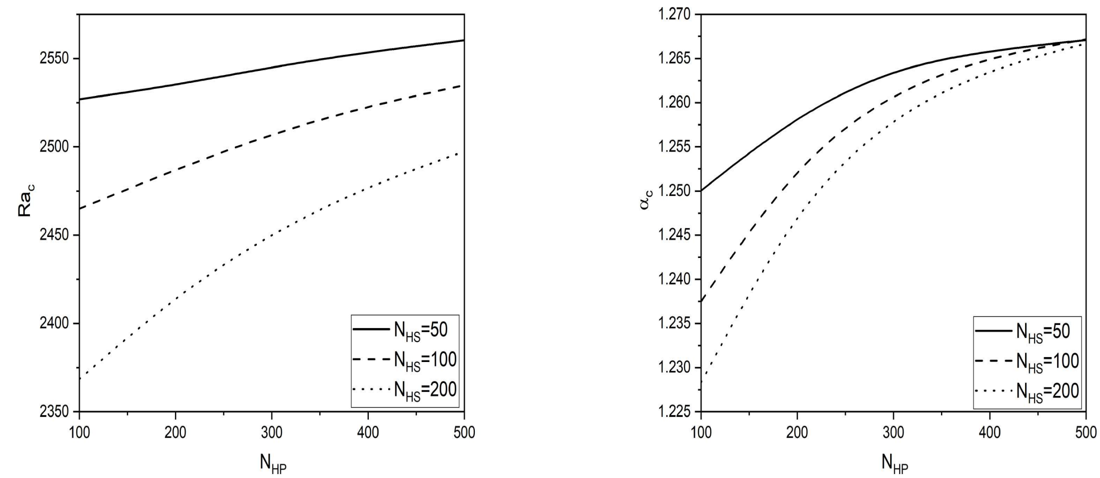

(a) (b)

Figure 3.2: "Variation of (a) critical Rayleigh number and (b) critical wavenumber with N_{HP} for different values of N_{HS} with $\gamma_p = 0.04$, $\gamma_s = 0.01$, $\epsilon_p = 0.7$, $\epsilon_s = 0.2$ and $\theta = \pi/3$."

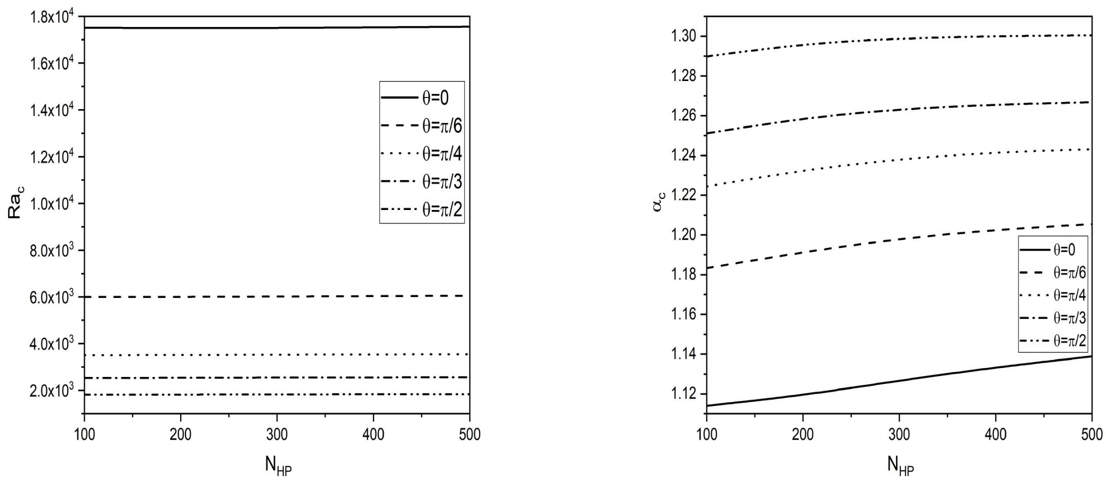

(a) (b)

Figure 3.3: "Variation of (a) critical Rayleigh number and (b) critical wavenumber with N_{HP} for different values of θ with N_{HS}=50, $\gamma_p = 0.04$, $\gamma_s = 0.01$, $\epsilon_p = 0.7$ and $\epsilon_s = 0.2$."

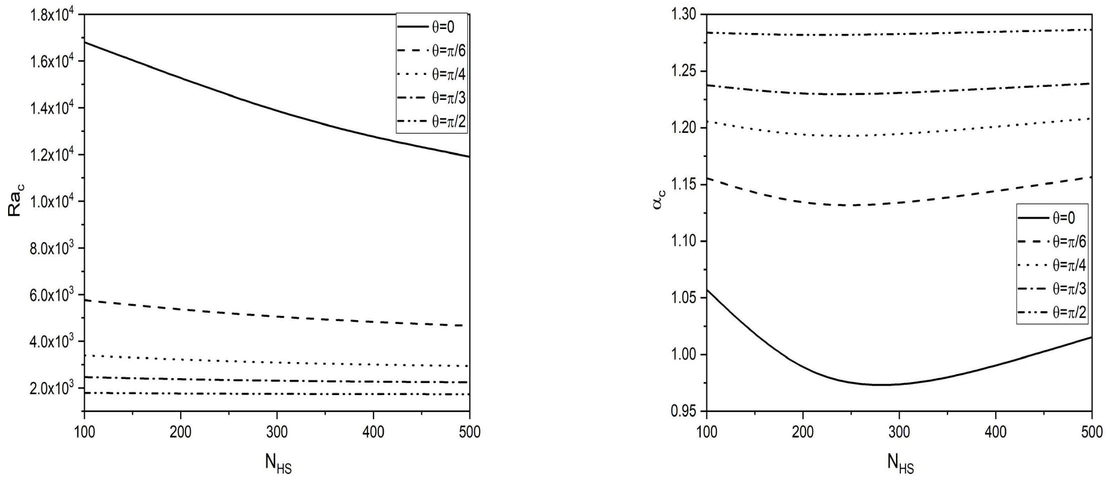

(a) (b)

Figure 3.4: “Variation of (a) critical Rayleigh number and (b) critical wavenumber with N_{HS} for different values of θ with N_{HP}=100, $\gamma_p = 0.04$, $\gamma_s = 0.01$, $\epsilon_p = 0.7$ and $\epsilon_s = 0.2$.”

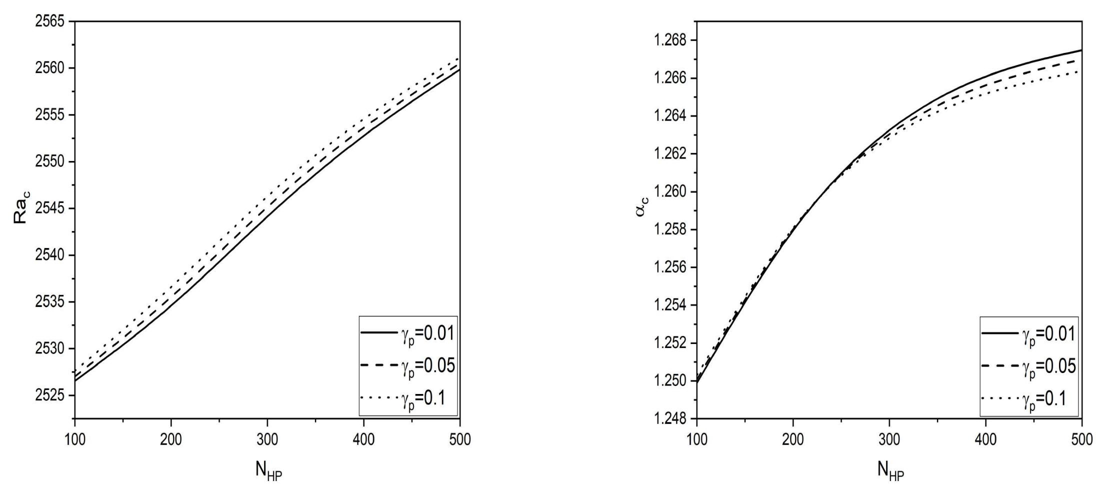

(a) (b)

Figure 3.5: “Variation of (a) critical Rayleigh number and (b) critical wavenumber with N_{HP} for different values of γ_p with $\theta = \pi/3$, N_{HS}=50, $\gamma_s = 0.01$, $\epsilon_p = 0.7$ and $\epsilon_s = 0.2$.”

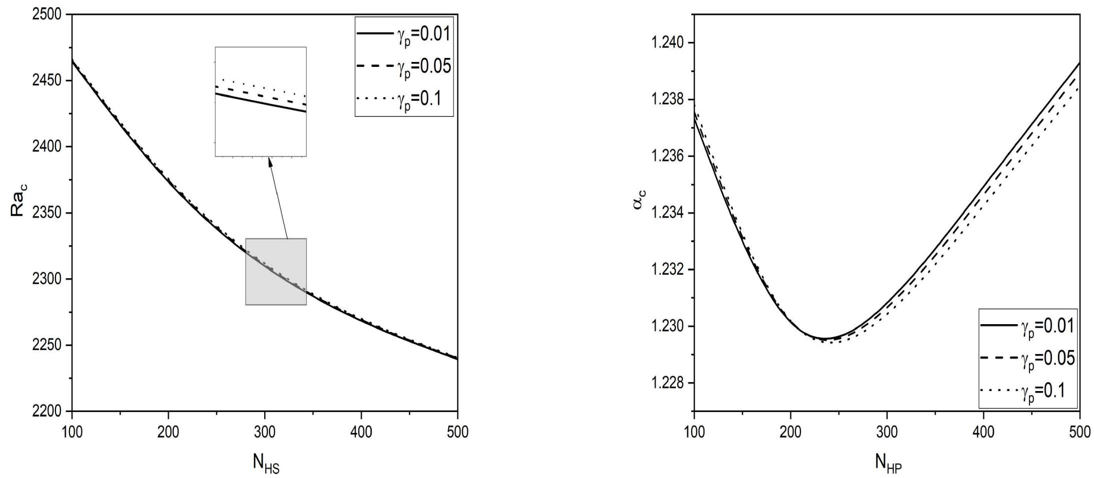

(a) (b)

Figure 3.6: "Variation of (a) critical Rayleigh number and (b) critical wavenumber with N_{HS} for different values of γ_p with $\theta = \pi/3$, N_{HP}=100, $\gamma_s = 0.01$, $\epsilon_p = 0.7$ and $\epsilon_s = 0.2$."

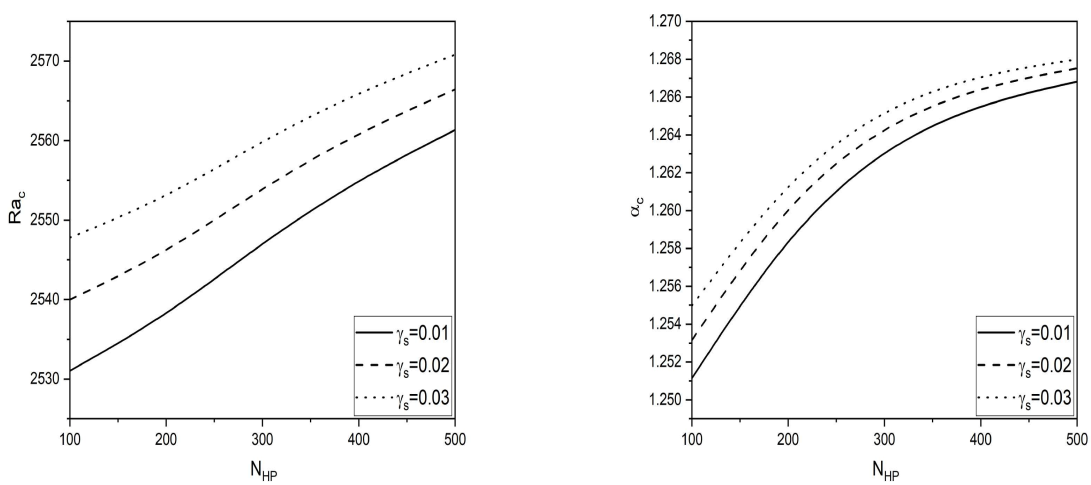

(a) (b)

Figure 3.7: "Variation of (a) critical Rayleigh number and (b) critical wavenumber with N_{HP} for different values of γ_s with $\theta = \pi/3$, N_{HS}=50, $\gamma_p = 0.04$ $\epsilon_p = 0.7$ and $\epsilon_s = 0.2$."

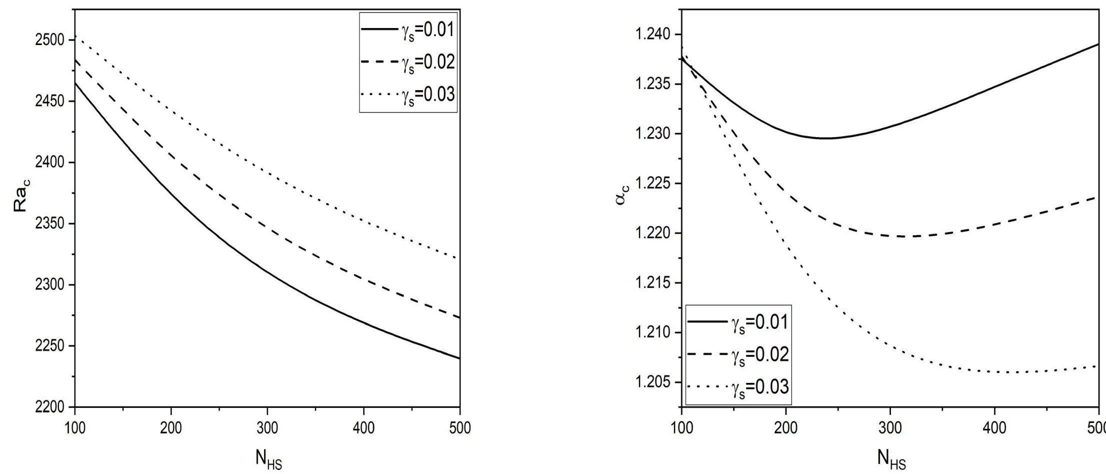

(a) (b)

Figure 3.8: “Variation of (a) critical Rayleigh number and (b) critical wavenumber with N_{HS} for different values of γ_s with $\theta = \pi/3$, N_{HP}=100, $\gamma_p = 0.04$ $\epsilon_p = 0.7$ and $\epsilon_s = 0.2$.”

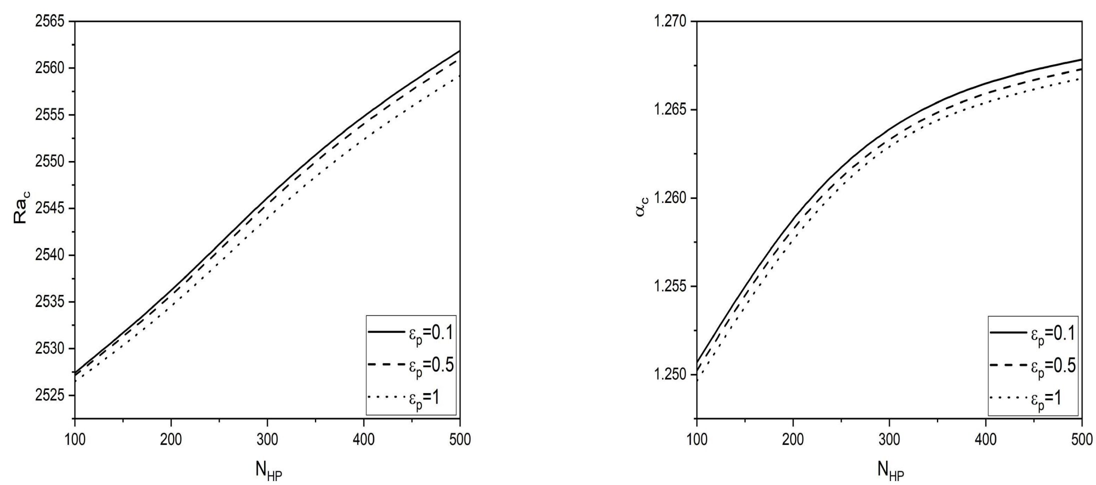

(a) (b)

Figure 3.9: “Variation of (a) critical Rayleigh number and (b) critical wavenumber with N_{HP} for different values of ϵ_p with $\theta = \pi/3$, N_{HS}=50, $\gamma_s = 0.01$, $\gamma_p = 0.04$ and $\epsilon_s = 0.2$.”

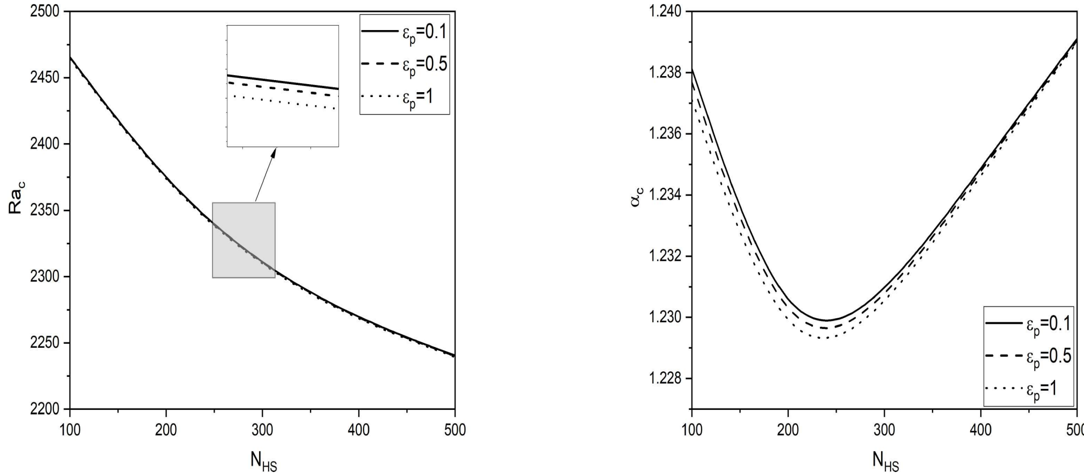

(a) (b)

Figure 3.10: "Variation of (a) critical Rayleigh number and (b) critical wavenumber with N_{HS} for different values of ϵ_p with $\theta = \pi/3$, N_{HP}=100, $\gamma_s = 0.01$, $\gamma_p = 0.04$ and $\epsilon_s = 0.2$."

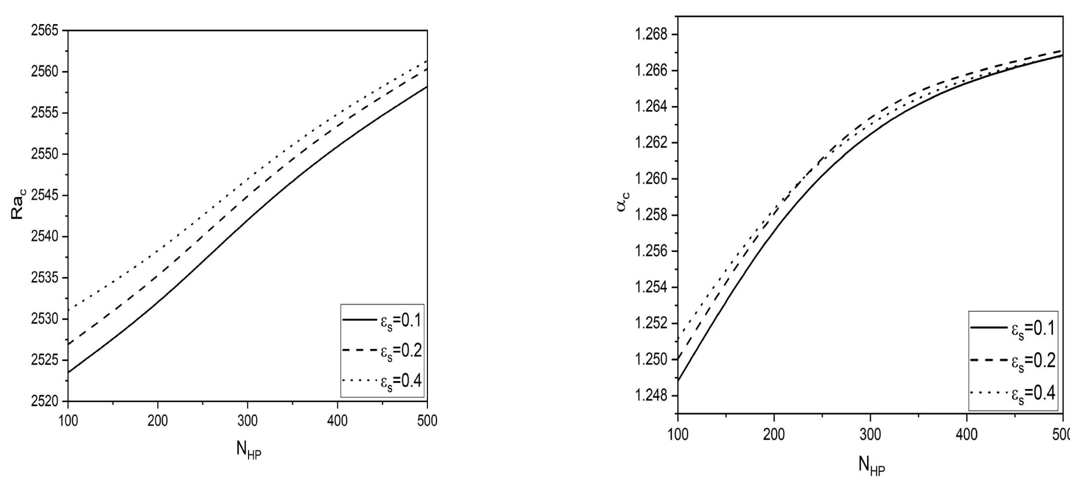

(a) (b)

Figure 3.11: "Variation of (a) critical Rayleigh number and (b) critical wavenumber with N_{HP} for different values of ϵ_s with $\theta = \pi/3$, N_{HS}=50, $\gamma_p = 0.04$ $\gamma_s = 0.01$, and $\epsilon_p = 0.7$."

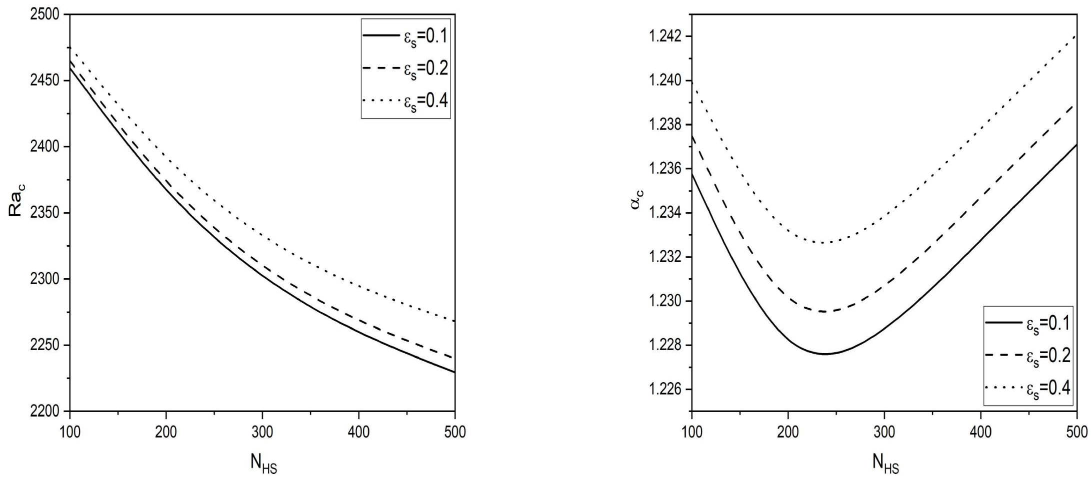

(a) (b)

Figure 3.12: "Variation of (a) critical Rayleigh number and (b) critical wavenumber with N_{HS} for different values of ϵ_s with $\theta = \pi/3$, N_{HP}=100, $\gamma_p = 0.04$ $\gamma_s = 0.01$, and $\epsilon_p = 0.7$."

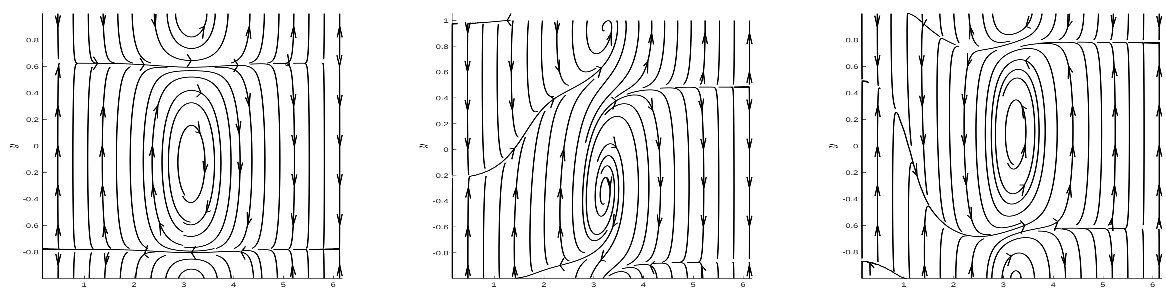

(a) $\theta = 0$ (b) $\theta = \pi/4$ (c) $\theta = \pi/2$

Figure 3.13: "The disturbance of streamlines for different values of θ".

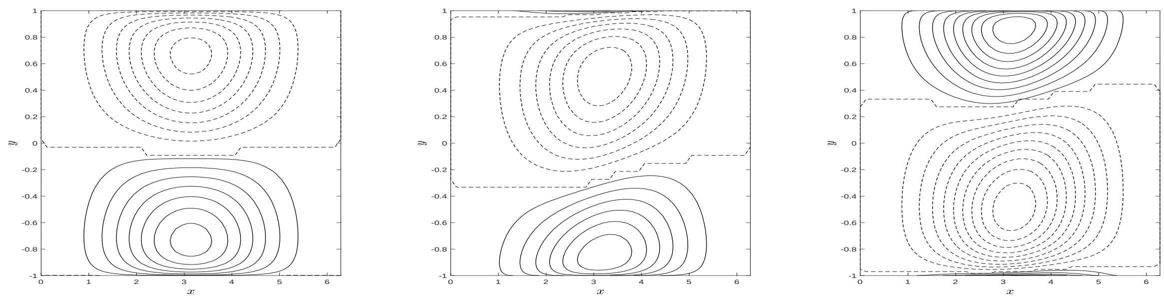

(a) $\theta = 0$ (b) $\theta = \pi/4$ (c) $\theta = \pi/2$

Figure 3.14: "The disturbance of isotherms (fluid) for different values of θ".

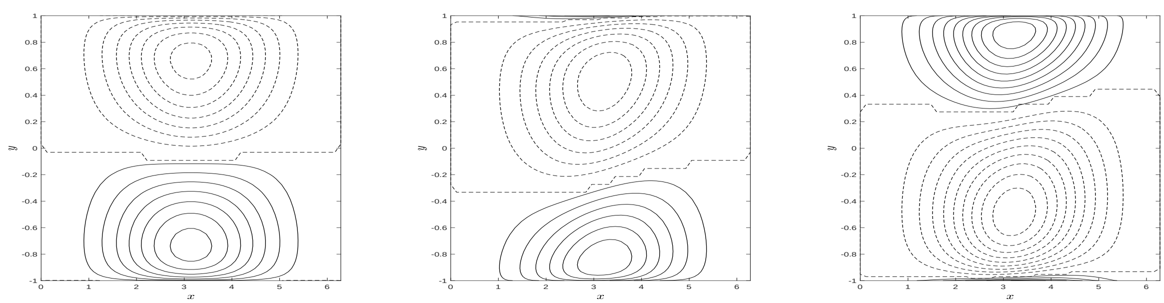

(a) $\theta = 0$ (b) $\theta = \pi/4$ (c) $\theta = \pi/2$

Figure 3.15: "The disturbance of isotherms (particle) for different values of θ".

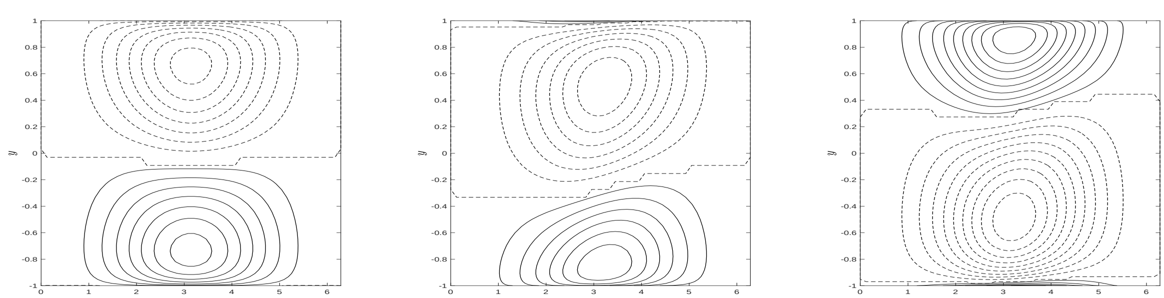

(a) $\theta = 0$ (b) $\theta = \pi/4$ (c) $\theta = \pi/2$

Figure 3.16: "The disturbance of isotherms (solid) for different values of θ".

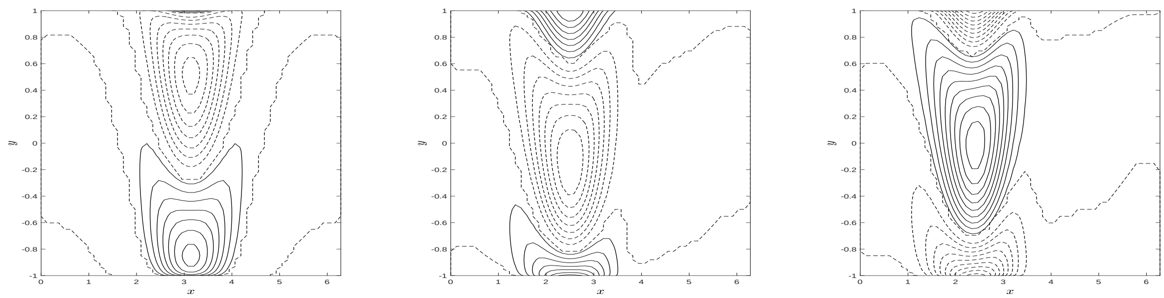

(a) $\theta = 0$ (b) $\theta = \pi/4$ (c) $\theta = \pi/2$

Figure 3.17: "The disturbance of isonanoconcentrations for different values of θ".

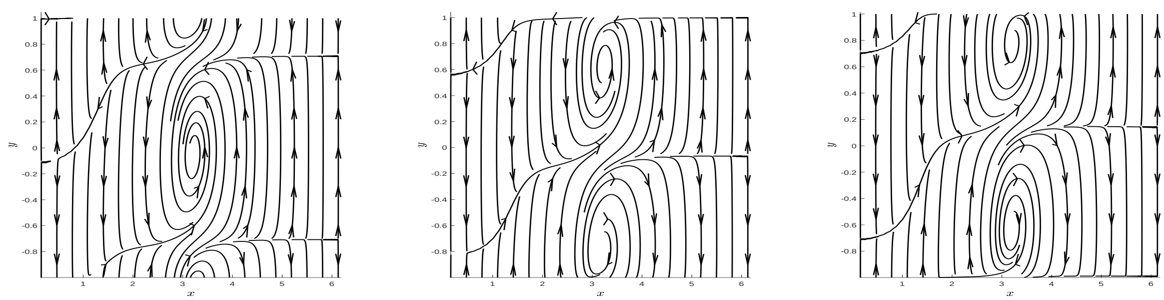

(a) $N_{HP} = 1$ (b) $N_{HP} = 10$ (c) $N_{HP} = 100$

Figure 3.18: "The disturbance of streamlines for different values of N_{HP}".

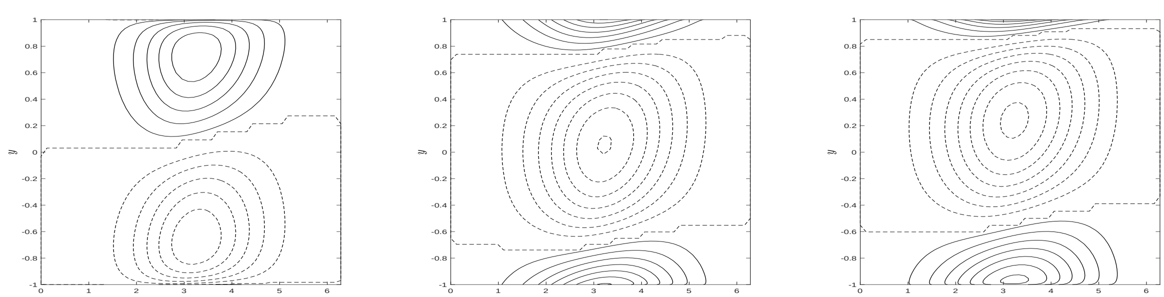

(a) $N_{HP} = 1$ (b) $N_{HP} = 10$ (c) $N_{HP} = 100$

Figure 3.19: "The disturbance of isotherms (fluid) for different values of N_{HP}".

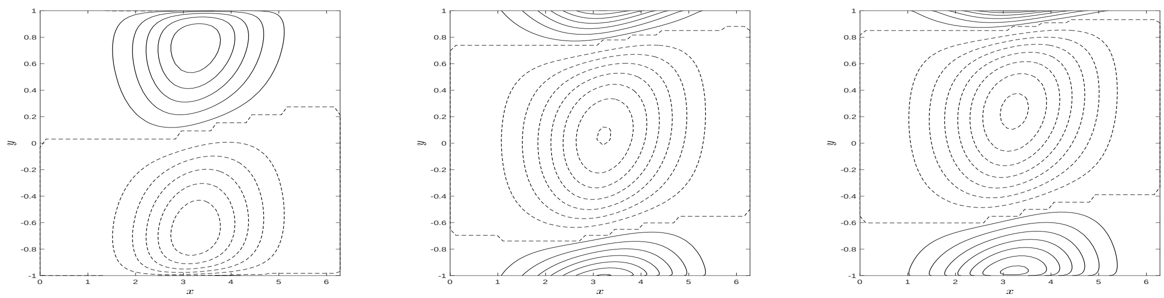

(a) $N_{HP} = 1$ (b) $N_{HP} = 10$ (c) $N_{HP} = 100$

Figure 3.20: “The disturbance of isotherms (particle) for different values of N_{HP}”.

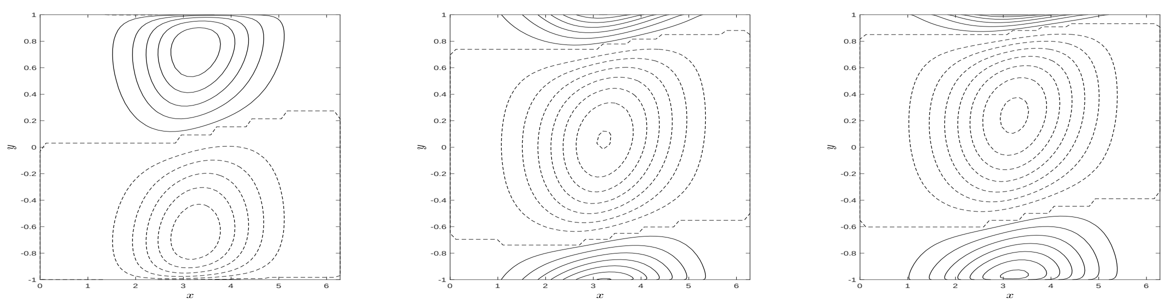

(a) $N_{HP} = 1$ (b) $N_{HP} = 10$ (c) $N_{HP} = 100$

Figure 3.21: “The disturbance of isotherms (solid) for different values of N_{HP}”.

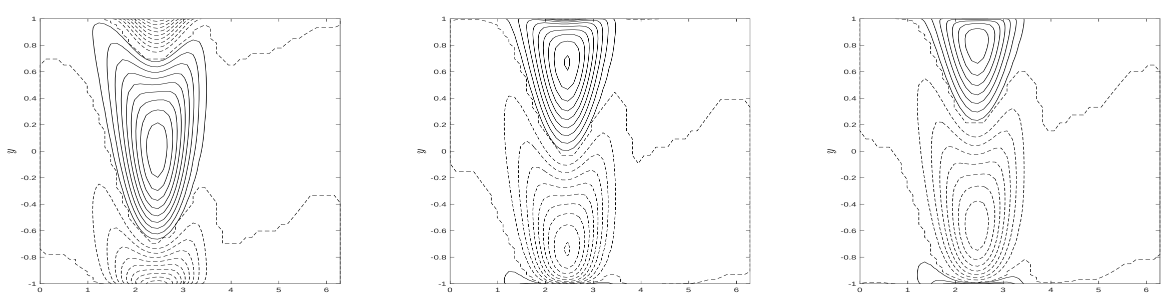

(a) $N_{HP} = 1$ (b) $N_{HP} = 10$ (c) $N_{HP} = 100$

Figure 3.22: “The disturbance of isonanoconcentrations for different values of N_{HP}”.

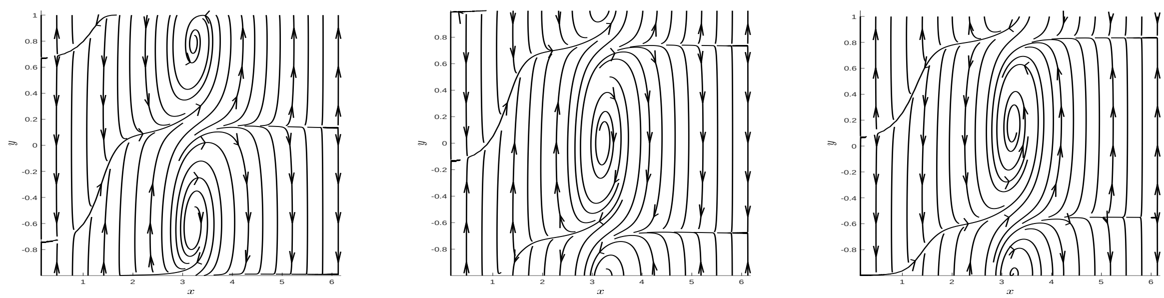

(a) $N_{HS} = 1$ (b) $N_{HS} = 10$ (c) $N_{HS} = 100$

Figure 3.23: "The disturbance of streamlines for different values of N_{HS}".

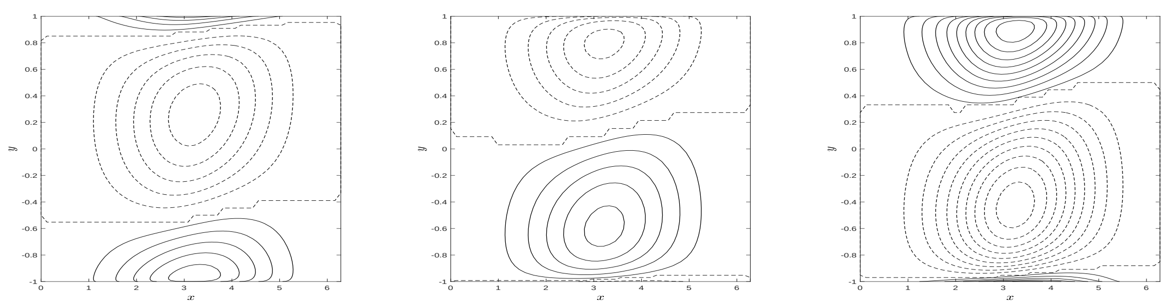

(a) $N_{HS} = 1$ (b) $N_{HS} = 10$ (c) $N_{HS} = 100$

Figure 3.24: "The disturbance of isotherms (fluid) for different values of N_{HS}".

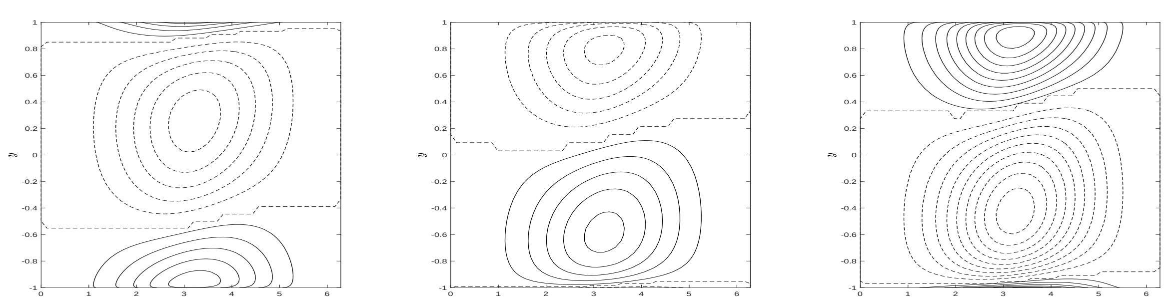

(a) $N_{HS} = 1$ (b) $N_{HS} = 10$ (c) $N_{HS} = 100$

Figure 3.25: "The disturbance of isotherms (particle) for different values of N_{HS}".

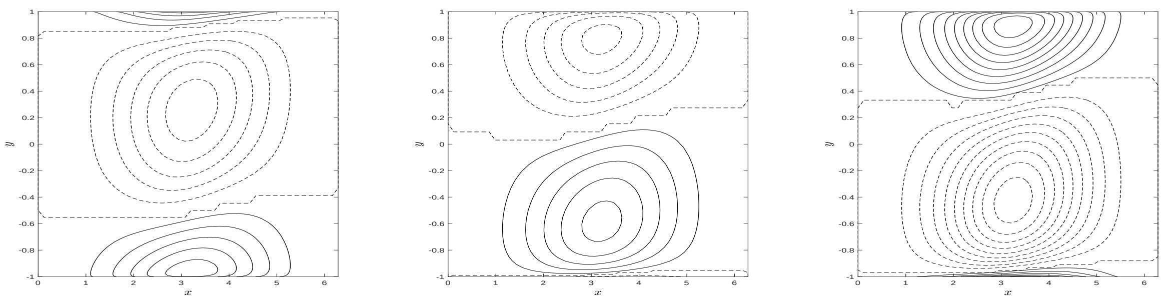

(a) $N_{HS} = 1$ (b) $N_{HS} = 10$ (c) $N_{HS} = 100$

Figure 3.26: "The disturbance of isotherms (solid) for different values of N_{HS}".

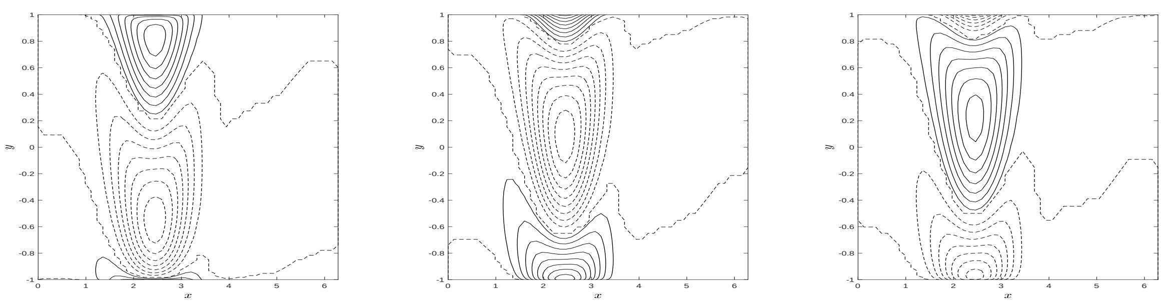

(a) $N_{HS} = 1$ (b) $N_{HS} = 10$ (c) $N_{HS} = 100$

Figure 3.27: "The disturbance of isonanoconcentrations for different values of N_{HS}".

3.6 Conclusions

The effect of local thermal non-equilibrium (LTNE) on the onset of convection in an inclined porous-medium channel filled with a nanofluid flow is studied. The Buongiorno model for the nanofluid and the two-field model for the energy equation, each signifying the fluid and particle phases independently, are used. The influence of LTNE parameters on the critical Rayleigh number and critical wavenumber with inclination $\theta = \pi/3$. Various values of the LTNE parameters are shown graphically. Moreover, the contour plots for streamlines, isotherms, and isonanoconcentration at critical level with variation in fluid/nanoparticle interphase Nield number (N_{HP}) and fluid/solid matrix interphase Nield number (N_{HS}) are drawn and illustrated. The following are the observations:

- When N_{HP} increases, the critical Rayleigh number (Ra_c) increases, and as N_{HS} increases, Ra_c falls. As a result, all values of N_{HP} stabilize the flow, whereas all values of N_{HS} destabilize the flow field.
- When we raise N_{HP}, there is no change in critical Rayleigh number (Ra_c) for all values of inclination angle θ.
- γ_p, γ_s, ϵ_p, and ϵ_s stabilize the flow for all values of N_{HP}.
- For all values of N_{HS}, ϵ_p destabilize the flow, but γ_p, γ_s and ϵ_s stabilize the flow.
- When we raise N_{HS}, critical wavenumber first decreases up to specific values of N_{HS} before quickly increasing in the intermediate levels. This may happen due to the dominance of heat transfer from fluid/solid matrix to fluid/particle.
- For each angle, the patterns of isotherms of fluid, particle, and solid are essentially identical.

Chapter 4

The stability of double diffusive convection in an inclined channel filled with a porous medium saturated with nanofluid and subjected to a magnetic field [1]

4.1 Introduction

Double-diffusive convection research in porous media has extensive applications in numerous disciplines, including biotechnology, nuclear engineering, and chemical engineering. Several researchers have investigated the effects of double diffusion on the stability of porous layers saturated with different Newtonian and non-Newtonina fluids. Shivakumara *et al.* [28] considered the consequences of the applied magnetic field on the stability of convection in horizontal fluid layer double diffusion. Shankar *et al.* [29] studied the stability of buoyant flow in a vertical layer of a Darcy porous medium with double diffusion. Noon and Haddad [30] analyzed the influences of variable gravity, rotation, and reaction on the linear and nonlinear stability in a thermosolutal convection in a Darcy porous medium. Dhiman *et al.* [31] analyzed mathematically the thermohaline convection in a viscoelastic fluid-saturated porous layer.

[1] Communicated in "***Propulsion and Power Research***"

Several researchers have studied linear stability analysis in the presence of a transverse magnetic field. Singh *et al.* [42] studied the importance of a transverse magnetic field on the linear convective stability in a differently heated channel. Camobreco *et al.* [43] analyzed the linear stability of periodic pulsatile flows in a duct with a transverse magnetic field.

The stability properties of a nanofluid in an inclined channel under double-diffusive convection in the presence of a transverse magnetic field have not been reported in the literature. As a result, the current research examines the impact of a transverse magnetic field and double-diffusive convection stability in a nanofluid flow for an inclined channel (with inclination θ) filled with a porous medium.

4.2 Mathematical Formulation

Consider an unsteady, incompressible nanofluid flow in an inclined channel of width $2L$ with impermeable and completely thermally conducting walls. Fig. 2.1 depicts a schematic diagram of the problem. Assume that the angle of inclination with the horizontal line is θ. The width of the channel is $2L$, and the channel plates are located at $y = -L$ and $y = L$, respectively. The temperatures of the channel walls $y = -L$ and $y = L$ are T_1 and $T_2 (T_1 > T_2)$, nanoparticle volume fractions are ϕ_2 and ϕ_1, and solute concentrations are C_1 and C_2 respectively. A uniform magnetic field $\mathbf{B}_0 = \mathrm{B}\hat{e_{\mathrm{y}}}$ is subjected normally to the channel, where B defines the magnetic field strength. The induced magnetic field, in contrast to the magnetic field being applied, can be ignored as the magnetic Reynolds number is quite small.

Using the above assumptions and the Oberbeck-Boussinesq approximation, the equations governing the flow are:

$$\nabla \cdot \vec{V} = 0 \tag{4.1}$$

$$\begin{aligned} \frac{\rho_f}{\epsilon}\left(\frac{\partial \vec{V}}{\partial t} + \frac{1}{\epsilon}(\vec{V}\cdot\nabla)\vec{V}\right) &= -\nabla p + \tilde{\mu}\nabla^2\vec{V} - \frac{\mu}{K}\vec{V} - \{(1-\beta_T(T-T_1) \\ &- \beta_C(C-C_1))\,(1-\phi)\rho_f + \phi\rho_p\}\,\mathbf{g}(\sin(\theta)\hat{e_{\mathrm{x}}} + \cos(\theta)\hat{e_{\mathrm{y}}}) + \mathbf{j}\times\mathbf{B}_0 \end{aligned} \tag{4.2}$$

$$\sigma\frac{\partial T}{\partial t} + \vec{V}\cdot\nabla T = \alpha_m\nabla^2 T + \frac{\epsilon(\rho C)_p}{(\rho C)_f}\Big(\frac{D_T}{T_1}\nabla T\cdot\nabla T + D_B\nabla\phi\cdot\nabla T\Big) + D_{TC}\nabla^2 C \tag{4.3}$$

$$\frac{\partial \phi}{\partial t} + \frac{1}{\epsilon}\vec{V}\cdot\nabla\phi = \frac{D_T}{T_1}\nabla^2 T + D_B\nabla^2\phi \tag{4.4}$$

$$\frac{\partial C}{\partial t} + \frac{1}{\epsilon}\vec{V}\cdot\nabla C = D_S\nabla^2 C + D_{CT}\nabla^2 T \tag{4.5}$$

where, C is the solute concentration, coefficient of thermophoretic diffusion is D_T, The solutal diffusivity for the porous medium is D_S, the Dufour type diffusivity is D_{TC}, and the Soret diffusivity is D_{CT}.

The relationship between magnetic induction field $\mathbf{B}_0$, and the current is $\mathbf{j}$ is defined as:

$$\mathbf{j}\times\mathbf{B}_0 = \gamma(\vec{V}\times \mathrm{B}\hat{e_{\mathrm{y}}})\times \mathrm{B}\hat{e_{\mathrm{y}}}.$$

The following are the conditions on the boundaries of the channel:

$$\begin{aligned} y=-L: \quad & \vec{V}=0, \quad T=T_1, \quad C=C_1, \quad \phi=\phi_2 \\ y=L: \quad & \vec{V}=0, \quad T=T_2, \quad C=C_2, \quad \phi=\phi_1 \end{aligned} \tag{4.6}$$

The non-dimensional form of the Eqs. (4.1) -(4.6) (on using Eq. (2.6) in Eqs. (4.1) -(4.6) and removing asterisk) are:

$$\nabla\cdot\vec{V} = 0 \tag{4.7}$$

$$\begin{aligned} \frac{1}{\mathrm{va}}\left(\frac{1}{\sigma}\frac{\partial\vec{V}}{\partial t} + \frac{1}{\epsilon}(\vec{V}\cdot\nabla)\vec{V}\right) = -\nabla p - \vec{V} + \Lambda Da(\nabla^2\vec{V}) + \left[RaT + \frac{Rs}{Ln} - Rn\phi - Rm\right] \\ (\sin(\theta)\hat{e_{\mathrm{x}}} + \cos(\theta)\hat{e_{\mathrm{y}}}) + DaHa^2(\vec{V}\times\hat{e_{\mathrm{y}}})\times\hat{e_{\mathrm{y}}} \end{aligned} \tag{4.8}$$

$$\frac{\partial T}{\partial t} + \vec{V}\cdot\nabla T = \nabla^2 T + D_f\nabla^2 C + \frac{N_B}{Le}\Big(\nabla\phi\cdot\nabla T + N_A\nabla T\cdot\nabla T\Big) \tag{4.9}$$

$$Le\Big(\frac{1}{\sigma}\frac{\partial\phi}{\partial t} + \frac{1}{\epsilon}\left(\vec{V}\cdot\nabla\phi\right)\Big) = N_A\nabla^2 T + \nabla^2\phi \tag{4.10}$$

$$\frac{1}{\sigma}\frac{\partial C}{\partial t} + \frac{1}{\epsilon}\left(\vec{V}\cdot\nabla C\right) = \frac{1}{Ln}\nabla^2 C + Sr\nabla^2 T \tag{4.11}$$

The associated boundary conditions become:

$$\begin{aligned} y = -1: &\quad \vec{V} = 0, \quad T = 0, \quad C = 0, \quad \phi = 1 \\ y = 1: &\quad \vec{V} = 0, \quad T = 1, \quad C = 1, \quad \phi = 0 \end{aligned} \tag{4.12}$$

here, $Rs = \frac{\rho_f g \beta_C K L (C_2 - C_1)}{\mu D_S}$ represents the solutal Rayleigh number, $D_f = \frac{D_{TC}(C_2 - C_1)}{\alpha_m (T_2 - T_1)}$ represents Dufour parameter, $Sr = \frac{D_{CT}(T_2 - T_1)}{\alpha_m (C_2 - C_1)}$ represents Soret parameter, $Ln = \frac{\alpha_m}{D_S}$ represents the thermo-solutal Lewis number, and $Ha = \mathrm{B}L\sqrt{\frac{\gamma}{\mu}}$ represents the magnetic parameter.

4.3 Basic state solution

During the basic stage, the flow should be continuous, unidirectional (x- direction, and completely developed. Hence, Eqs. (4.7)-(4.11) reduce to:

$$\frac{d^2 U_b}{dy^2} - \left(\frac{1}{\Lambda Da} + \Lambda Ha^2\right) U_b = \frac{1}{\Lambda Da}\frac{dp_0}{dx} - \frac{1}{\Lambda Da}\Big(RaT_0 + \frac{Rs}{Ln}C_0 - Rn\phi_0 - Rm\Big)\sin(\theta) \tag{4.13}$$

$$\frac{dp_0}{dy} = \Big(RaT_0 + \frac{Rs}{Ln}C_0 - Rn\phi_0 - Rm\Big)\cos(\theta) \tag{4.14}$$

$$\frac{dp_0}{dz} = 0 \tag{4.15}$$

$$\frac{d^2 T_0}{dy^2} + \frac{N_B}{Le}\frac{d\phi_0}{dy}.\frac{dT_0}{dy} + \frac{N_A N_B}{Le}\left(\frac{dT_0}{dy}\right)^2 + D_f\frac{d^2 C_0}{dy^2} = 0 \tag{4.16}$$

$$\frac{d^2 \Phi_0}{dy^2} + N_A\frac{d^2 T_0}{dy^2} = 0 \tag{4.17}$$

$$\frac{1}{Ln}\frac{d^2 C_0}{dy^2} + Sr\frac{d^2 T_0}{dy^2} = 0 \tag{4.18}$$

The following are the associated boundary conditions:

$$\begin{aligned} y = -1: &\quad U_b = 0, \quad T_0 = 0, \quad C_0 = 0, \quad \phi_0 = 1 \\ y = 1: &\quad U_b = 0, \quad T_0 = 1, \quad C_0 = 1, \quad \phi_0 = 0 \end{aligned} \tag{4.19}$$

here, $C_0(y)$ is basic concentration, and remaining quantities are defined in Chapter-2. Proceeding as in Chapter-2, we get basic solution as:

$$U_b = \sigma\left[\frac{\cosh(my)}{\cosh(m)} - 1\right] + \frac{1}{2Dam^2}\left(Ra + \frac{Rs}{Ln} + Rn\right)\left[y - \frac{\sinh(my)}{\sinh(m)}\right]\sin(\theta) \tag{4.20}$$

$$T_0 = \frac{1+y}{2}, \quad \phi_0 = \frac{1-y}{2}, \quad \text{and} \quad C_0 = \frac{1+y}{2} \tag{4.21}$$

where:

$$\sigma = \frac{m\,\cosh(m)}{\sinh(m) - m\,\cosh(m)} \quad \text{and} \quad m = \sqrt{\frac{1}{\Lambda Da} + \Lambda Ha^2}$$

4.4 Linear stability analysis

As in Chapter - 2, by imposing infinitesimal disturbances (δ) on the basic state solutions, ignoring δ^2 and higher order terms, using the usual normal mode form [50] to express infinitesimal disturbances of corresponding field variables, and removing pressure terms from the resulting equations, the linearized stability equations are obtained as:

$$\begin{aligned}
\Lambda Da\left[\frac{d^4\hat{v}}{dy^4} - 2\frac{d^2\hat{v}}{dy^2}(\alpha^2+\beta^2) + (\alpha^2+\beta^2)^2\hat{v}\right] - \frac{i\alpha}{\text{va}}\left(\frac{U_b}{\epsilon} - \frac{c}{\sigma}\right)\left[\frac{d^2\hat{v}}{dy^2} - (\alpha^2+\beta^2)\hat{v}\right]\\
+\frac{i\alpha}{\epsilon\text{va}}\frac{d^2U_b}{dy^2}\hat{v} - \left[\frac{d^2\hat{v}}{dy^2} - (\alpha^2+\beta^2)\hat{v}\right] - Ra\frac{d\hat{T}}{dy}i\alpha\sin(\theta) - Ra(\alpha^2+\beta^2)\cos(\theta)\hat{T}\\
-\frac{Rs}{Ln}\frac{d\hat{C}}{dy}i\alpha\sin(\theta) - \frac{Rs}{Ln}(\alpha^2+\beta^2)\cos(\theta)\hat{C} + Rn\frac{d\hat{\phi}}{dy}i\alpha\sin(\theta)\\
+Rn(\alpha^2+\beta^2)\cos(\theta)\hat{\phi} - DaHa^2\frac{d^2\hat{v}}{dy^2} = 0
\end{aligned} \tag{4.22}$$

$$\begin{aligned}
\frac{1}{\sigma\text{va}}(-i\alpha c)\hat{\eta} + \frac{1}{\epsilon\text{va}}\left[\beta\hat{v}\frac{dU_b}{dy} + U_b\hat{\eta}i\alpha\right] - \Lambda Da\left[\frac{d^2\hat{\eta}}{dy^2} - (\alpha^2+\beta^2)\hat{\eta}\right] + \hat{\eta} + DaHa^2\hat{\eta}\\
-\beta Ra\hat{T}\sin(\theta) - \beta\frac{Rs}{Ln}\hat{C}\sin(\theta) + \beta Rn\hat{\phi}\sin(\theta) = 0
\end{aligned} \tag{4.23}$$

$$\begin{aligned}
\frac{dT_0}{dy}\hat{v} + i\alpha\left(U_b - c\right)\hat{T} - \left[\frac{d^2\hat{T}}{dy^2} - (\alpha^2+\beta^2)\hat{T}\right] - \frac{N_B}{Le}\left[\frac{d\phi_0}{dy} + 2N_A\frac{dT_0}{dy}\right]\frac{d\hat{T}}{dy} - \frac{N_B}{Le}\frac{dT_0}{dy}\frac{d\hat{\phi}}{dy}\\
-D_f\left[\frac{d^2\hat{C}}{dy^2} - (\alpha^2+\beta^2)\hat{C}\right] = 0
\end{aligned} \tag{4.24}$$

$$\frac{1}{\epsilon}\frac{d\phi_0}{dy}\hat{v} + i\alpha\left(\frac{1}{\epsilon}U_b - \frac{c}{\sigma}\right)\hat{\phi} - \frac{1}{Le}\left[\frac{d^2\hat{\phi}}{dy^2} - (\alpha^2+\beta^2)\hat{\phi}\right] - \frac{N_A}{Le}\left[\frac{d^2\hat{T}}{dy^2} - (\alpha^2+\beta^2)\hat{T}\right] = 0 \tag{4.25}$$

$$\frac{1}{\epsilon}\frac{dC_0}{dy}\hat{v} + i\alpha\left(\frac{1}{\epsilon}U_b - \frac{c}{\sigma}\right)\hat{C} - \frac{1}{Ln}\left[\frac{d^2\hat{C}}{dy^2} - (\alpha^2+\beta^2)\hat{C}\right] - Sr\left[\frac{d^2\hat{T}}{dy^2} - (\alpha^2+\beta^2)\hat{T}\right] = 0 \quad (4.26)$$

where $\hat{\mathbf{u}}(y) = (\hat{u}, \hat{v}, \hat{w})$, and $\hat{\eta} = \beta\hat{u} - \alpha\hat{w}$

4.5 Results and discussion

The set of Eqs. (4.22) - (4.26) expresses a generalized eigenvalue problem with perturbed eigenvalues in terms of wave speed. The spectral technique [107] is employed to find the solution to this eigenvalue problem. To examine the validity of the method, the eigenvalue problem code is executed in MATLAB with a different grid point count (N), and the resulting least consistent eigenvalues are given in Table 4.1 for a set of other parameters chosen at random. For $N \geq 50$, the least consistent eigenvalue meets a convergence threshold of 10^{-7}. When $N \geq 50$, the results do not change. A similar trend may be noticed for different parameter values. As a consequence, $N = 50$ is used in the numerical calculation. The results of $\theta = \pi/2$ were obtained, which is consistent with the results of Srinivasacharya and Barman [108].

The impact of double diffusion on convective stability in a nanofluid flow with a transverse magnetic field in an inclined porous channel is investigated in this paper. The influence of inclination angle (θ), Darcy number (Da), thermo-solutal Lewis number (Ln), Dufour number (D_f), and Soret number (Sr) on the flow instability is studied in-depth in this paper. The remaining values of parameters are set as $\epsilon = 0.6$, $N_A = 8$, $N_B = 0.2$, Rs=200, Rn=10, Pr=7, Le=1000, $\Lambda = 1$, and $\sigma = 1$.

The plots for the variation of critical Rayleigh number (Ra_c) and critical wavenumber (α_c) as a function of Harmann number (Ha) for the inclination angle (θ) are shown in Fig. 4.1. As θ changes from horizontal to vertical, Ra_c decreases. This demonstrates that θ destabilizes the flow. It is worth noting that rising Ha rises Ra_c. The Lorentz force is commonly produced by applying a magnetic field at right angles to the direction of flow. As a result, the model dissipates a substantial amount of energy to minimize this resistance, which delays convection and acts as a stabilizer. As a consequence, the magnetic field may be employed to effectively manage convection in a nanofluid-saturated medium. When the inclination angle is fixed, it is seen that α_c decreases as Ha increases. However, as θ shifts from horizontal to vertical, the critical wavenumber enhances.

For the permeability parameter (Darcy number Da), the variation of critical Rayleigh number (Ra_c) and critical wavenumber (α_c) as a function of Hartmann number (Ha) is displayed in Fig. 4.2. The critical Rayleigh number rises as the Da increases, indicating that permeability stabilizes the system. At lower Darcy numbers, it is believed that the porous layer has less fluid permeability, causing a pronouncedly high resistance when the fluid passes through the porous medium. As a result, the flow improves in a porous medium, illustrating how viscous forces contribute to the momentum equation. Critical wavenumber rises with increasing permeability, although the growth is slower when Da rises from 1 to 10 than when it rises from 0.1 to 1.

For varying values of thermo-solutal Lewis number (Ln), Fig. 4.3 shows the variation of critical Rayleigh number (Ra_c) and critical wavenumber (α_c) versus the magnetic parameter (Ha). With a rise in the values of Ln, the Ra_c increases slightly. As Ln grows, α_c drops. As a result, Ln stabilizes the flow.

Fig. 4.4 depicts the impact of the Soret number (Sr) on the critical Rayleigh number (Ra_c) and critical wavenumber (α_c). As the value of Sr rises, so does the value of Ra_c. However, the rate of growth is extremely slow. In a nanofluid flow in an inclined channel, the flow field is stabilized by the Soret parameter. This is because the Soret effect raises the solute's density gradient, which causes convective instability at constant temperature. As Sr increases, α_c drops.

The critical Rayleigh number (Ra_c) and critical wavenumber (α_c) patterns against the Ha for different effects of the Dufour parameter (D_f) are shown in Fig. 4.5. The critical Rayleigh number (Ra_c) improves as the Dufour parameter value increases. Moreover, the α_c somewhat lowers as the Dufour value is raised. As a result, it can be concluded that the Dufour parameter (D_f) slightly stabilizes the system.

Figs. 4.6 - 4.9 show streamlines, isotherms, isosolutes, and isonanoconcentrations, for various θ values when $Ha = 2$ and $Da = 10$. Streamlines in a clockwise direction correlate to negative contours, whereas those in an anti-clockwise direction correspond to positive contours. When the channel is horizontal, i.e., $\theta = 0$, Fig. 4.6 shows the development of two vertical cell structures known as Rayleigh-Bernard convection cells. A counter-clockwise vortex forms close to the upper wall, while a clockwise vortex forms near the lower wall. The cells then stretch or elongate in the vertical direction as the inclination angle increases, eventually forming a horizontal cell structure when the inclination angle reaches $\pi/2$, i.e., when the channel becomes vertical. Therefore, streamlines reorient the pattern from a vertical structure to a horizontal structure as the channel inclination changes from horizontal to vertical. Solid lines represent positive contours in the case of isotherms, isosolutes, and isonanoconcentrations contour, whereas dashed lines represent negative contours. A similar pattern is observed in the case of isotherms, isosolutes, and isonanoconcentrations.

Table 4.1: "Convergence of the least stable eigenvalue for $Da = 10$, Ha=2, $Pr = 7$, $Ra = 10$, Rs=200, $Rn = 10$, Ln=40, $\epsilon = 0.6$, $N_A = 8$, $N_B = 0.2$, $Le = 1000$, $Sr = 0.5$, $D_f = 0.04$, $\Lambda = 1$, θ=$\pi/3$, $\sigma = 1$, α= 1 and $\beta = 0$."

N	**Least stable eigenvalue**
40	2.337864911005 -0.034982366316i
45	2.337866380778 -0.034982283926i
50	2.337901597983 -0.034997045700i
55	2.337867143229 -0.034981336325i
60	2.337950853642 -0.035017117849i

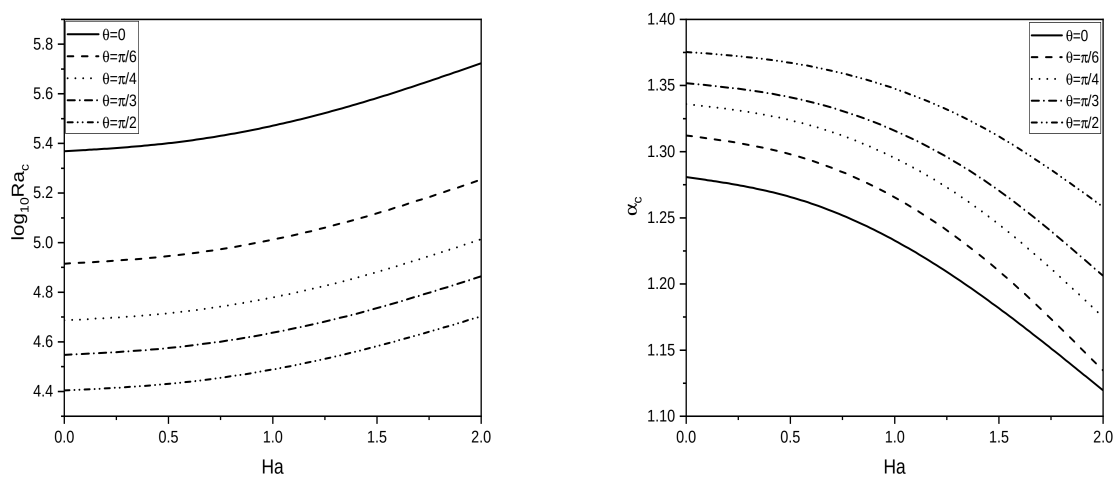

Figure 4.1: "Variation of critical Rayleigh number (Ra_c) and critical wavenumber (α_c) with Ha for different values of θ with Da=0.1, Rs=200, Ln=40, $Sr = 0.3$ and $D_f = 0.04$."

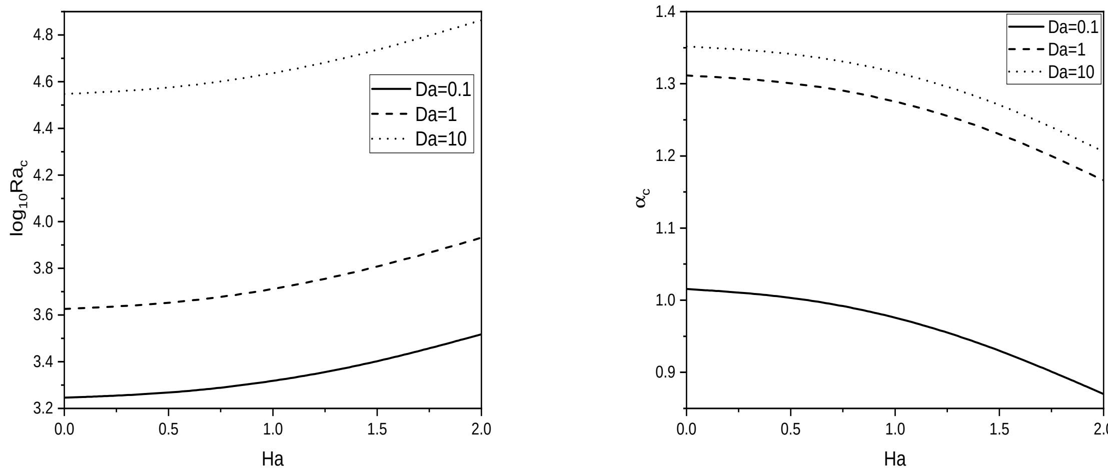

Figure 4.2: "Variation of critical Rayleigh number (Ra_c) and critical wavenumber (α_c) with Ha for different values of Da with $\theta = \pi/3$, $Rs = 200, Ln = 40, Sr = 0.3$ and $D_f = 0.04$."

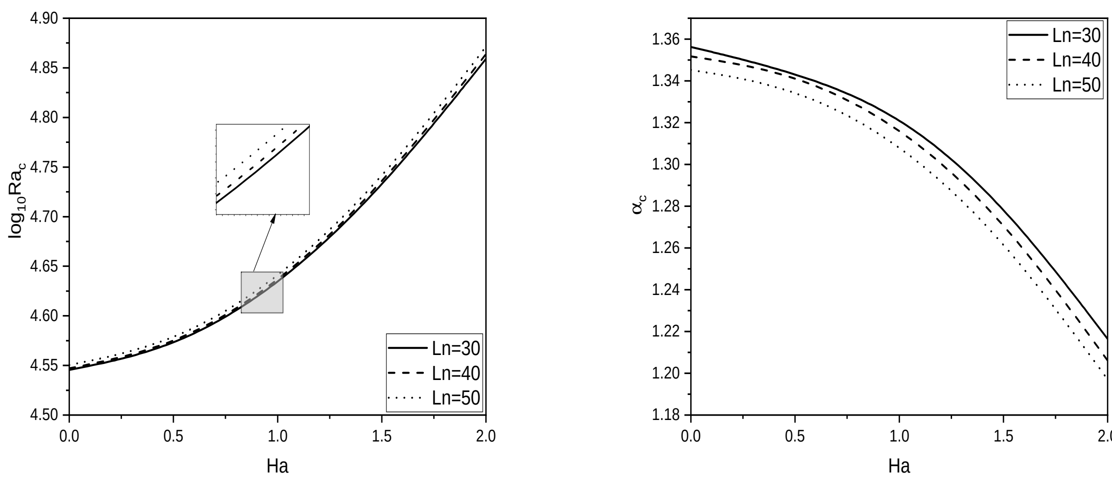

Figure 4.3: "Variation of critical Rayleigh number (Ra_c) and critical wavenumber (α_c) with Ha for different values of Ln with $\theta = \pi/3$, Rs=200, Da=0.1, $Sr = 0.3$ and $D_f = 0.04$."

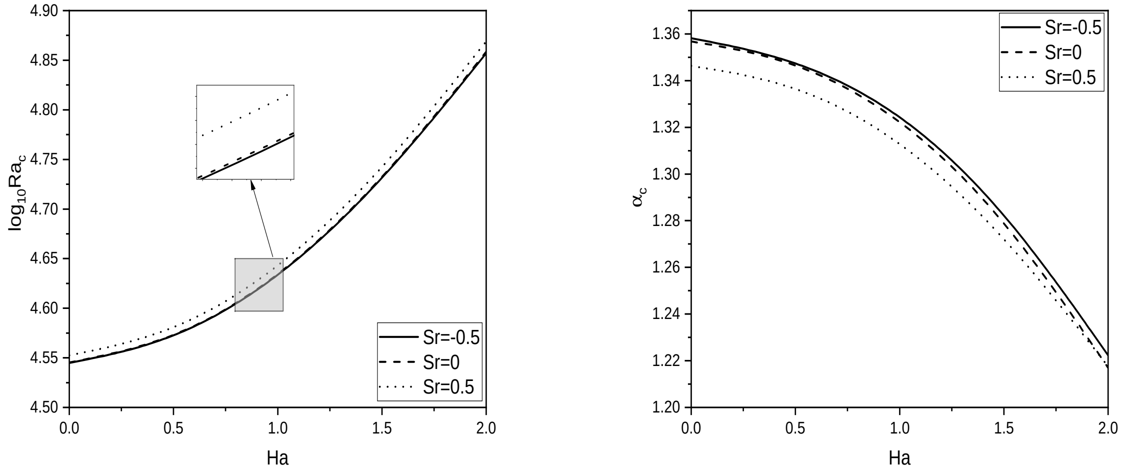

Figure 4.4: "Variation of critical Rayleigh number (Ra_c) and critical wavenumber (α_c) with Ha for different values of Sr with $\theta = \pi/3$, Ln=40, Da=0.1, $Rs = 200$ and $D_f = 0.04$."

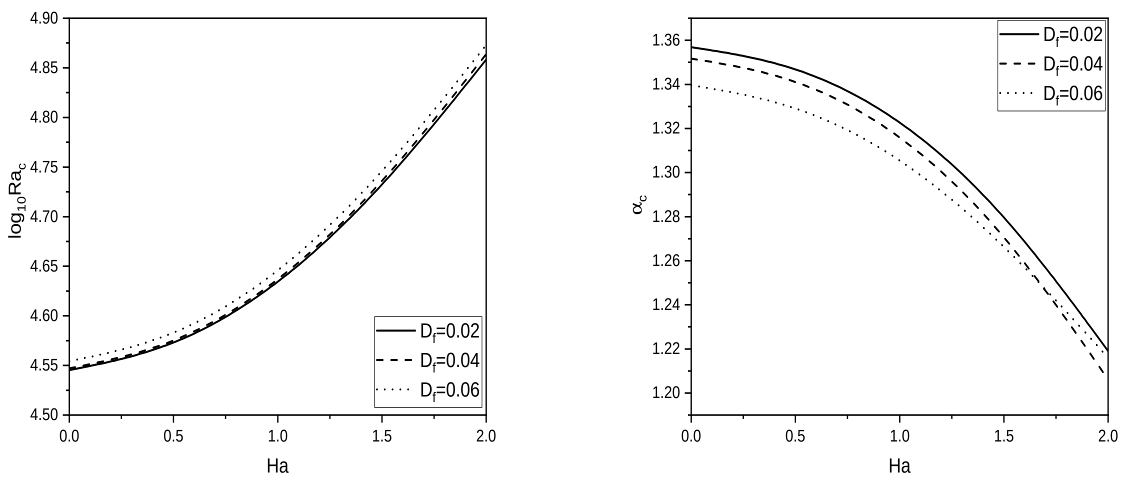

Figure 4.5: "Variation of critical Rayleigh number (Ra_c) and critical wavenumber (α_c) with Ha for different values of D_f with $\theta = \pi/3$, Ln=40, Da=0.1, $Rs = 200$ and $Sr = 0.3$."

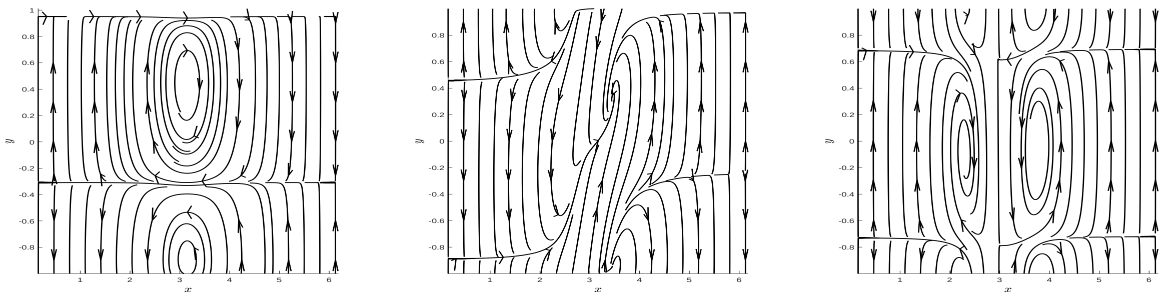

(a) "$\theta = 0$" (b) "$\theta = \pi/4$" (c) "$\theta = \pi/2$"

Figure 4.6: "The disturbance of streamlines for different values of θ."

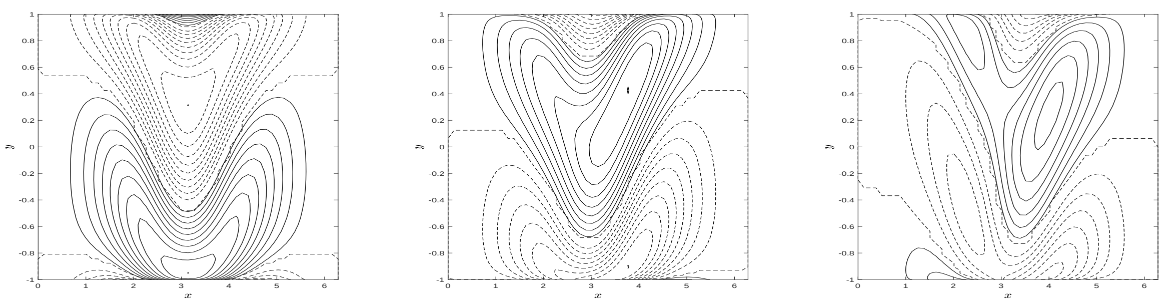

(a) "$\theta = 0$" (b) "$\theta = \pi/4$" (c) "$\theta = \pi/2$"

Figure 4.7: "The disturbance of isotherms for different values of θ."

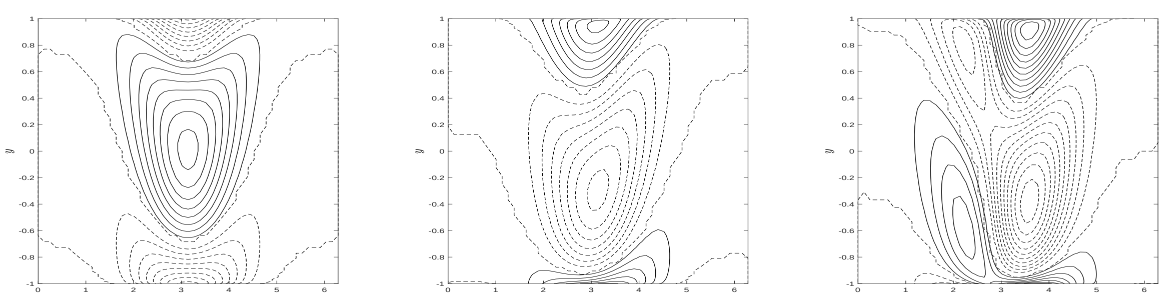

(a) "$\theta = 0$" (b) "$\theta = \pi/4$" (c) "$\theta = \pi/2$"

Figure 4.8: "The disturbance of isosolutes for different values of θ."

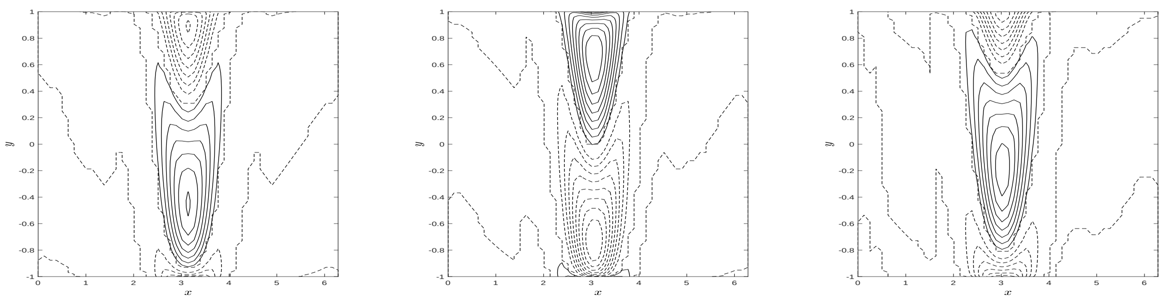

(a) “$\theta = 0$” (b) “$\theta = \pi/4$” (c) “$\theta = \pi/2$”

Figure 4.9: “The disturbance of isonanoconcentrations for different values of θ.”

4.6 Conclusions

The Brinkman-extended Darcy model is employed to examine the linear stability of double-diffusive convection in an inclined channel filled with a porous medium saturated with nanofluid under the impact of a transverse magnetic field. The critical Rayleigh number (Ra_c) and critical wavenumber (α_c) are computed and graphically presented for various values of θ, Da, Sr, Ln, and D_f versus Ha.

- A rise in the magnetic parameter increases the critical Rayleigh number. As a result, the Hartmann number (Ha) stabilizes the flow field.
- The flow in an inclined channel is stabilized by the thermo-solutal Lewis number (Ln), the Soret parameter (Sr), and the Dufour parameter (D_f). As a result, a rise in these factors delays the onset of convection.

Chapter 5

The stability of the nanofluid flow in an inclined porous channel with variable viscosity [1]

5.1 Introduction

The variable viscosity of fluids is an essential consideration in engineering and scientific contexts, as it influences the behavior of fluid flow in various domains. Fluid viscosity is a factor that effects product quality and processing conditions in sectors such as food, chemical processing, and polymer manufacturing, where it is influenced by temperature, pressure, and composition [109]. Umavathi *et al.* [38] investigated the linear and non-linear stability analysis of convection in a Maxwell nanofluid-saturated porous medium with double diffusing layers. In a Rayleigh-Bénard situation with rotation, recently Aanam *et al.* [39] theoretically investigated the dynamics of a ferrofluid with temperature and viscosity that are dependent on the magnetic field.

The literature review reveals that the stability properties of a nanofluid in an inclined channel with variable viscosity have not been reported in the literature. As a result, the current research examines the impact of variable viscosity in a nanofluid flow for an inclined channel (with inclination θ) filled with a porous medium.

[1] Published in "***Numerical Heat Transfer; Part A: Applications***" pp:1-14, DOI: https://doi.org/10.1080/10407782.2023.2252176

5.2 Mathematical Formulation

Consider an unsteady, incompressible nanofluid flow in an inclined channel of width 2L and inclination θ, with impermeable and completely thermally conducting walls. Let $Oxyz$ be the Cartesian coordinate system with x-axis in the flow direction and y-axis perpendicular to the flow direction, as depicted in Fig. 2.1. It is assumed that the porous medium is isotropic and homogenous. The walls $y = -L$ and $y = L$ are maintained at fixed temperatures T_1 and T_2, with nanoparticle volume fractions fixed at ϕ_2 and ϕ_1, respectively.

Also, we have assumed that the viscosity is an exponential function of temperature according to the Nahme law Sukanek *et al.* [110]

$$\mu(T) = \mu_l e^{-kT}$$

here, k is variable viscosity parameter, μ_l is viscosity at refrence temperature T_l.

Considering the Brownian motion and thermophoresis effects in the nanofluid, Darcy-Brinkman model for porous medium, and linear Oberbeck-Boussinesq approximation, the equations governing the flow are [50, 111]:

$$\nabla \cdot \vec{V} = 0 \tag{5.1}$$

$$\begin{aligned} \frac{\rho_f}{\epsilon}\left(\frac{\partial \vec{V}}{\partial t} + \frac{1}{\epsilon}(\vec{V}\cdot\nabla)\vec{V}\right) &= -\nabla p + \left[\mu\Delta\vec{V} + \nabla\mu\cdot\left(\nabla\vec{V} + \nabla\vec{V}^T\right)\right] - \frac{\mu}{K}\vec{V} \\ &\quad - \left[(1-\phi)\rho_f\ (1-\beta_T(T-T_1)) + \phi\rho_p\right]\mathbf{g}(\sin(\theta)\hat{e_{\mathrm{x}}} + \cos(\theta)\hat{e_{\mathrm{y}}}) \end{aligned} \tag{5.2}$$

$$(\rho C)_m\frac{\partial T}{\partial t} + (\rho C)_f\vec{V}\cdot\nabla T = k_m\nabla^2 T + \epsilon(\rho C)_p\left(+\frac{D_T}{T_1}\nabla T\cdot\nabla T + D_B\nabla\phi\cdot\nabla T\right) \tag{5.3}$$

$$\frac{\partial \phi}{\partial t} + \frac{1}{\epsilon}\vec{V}\cdot\nabla\phi = D_B\nabla^2\phi + \frac{D_T}{T_1}\nabla^2 T \tag{5.4}$$

The boundary conditions are:

$$\begin{aligned} \text{At} \quad y = -L: &\quad \vec{V} = 0, \quad T = T_1, \quad \phi = \phi_2 \\ \text{at} \quad y = L: &\quad \vec{V} = 0, \quad T = T_2, \quad \phi = \phi_1 \end{aligned} \tag{5.5}$$

According to Nikushchenko and Pavlovsky [111] here, $\Delta\vec{V} = -\nabla\times\nabla\times\vec{V}$.

The non-dimensional form of the Eqs. (5.1) -(5.4) (on using Eq. (2.6) in Eqs. (5.1) -(5.4) and removing asterisk) are:

$$\nabla \cdot \vec{V} = 0 \tag{5.6}$$

$$\begin{aligned}\frac{1}{\text{va}}\left(\frac{\partial \vec{V}}{\partial t} + \frac{1}{\epsilon}(\vec{V}\cdot\nabla)\vec{V}\right) = -\nabla p + Da\left[\mu\Delta\vec{V} + \nabla\mu\cdot\left(\nabla\vec{V} + \nabla\vec{V}^T\right)\right] - \mu\vec{V} \\ +\{RaT - Rn\phi - Rm\}(\sin(\theta)\hat{e_{\text{x}}} + \cos(\theta)\hat{e_{\text{y}}})\end{aligned} \tag{5.7}$$

$$\frac{\partial T}{\partial t} + \vec{V}.\nabla T = \nabla^2 T + \frac{N_A N_B}{Le}\nabla T\cdot\nabla T + \frac{N_B}{Le}\nabla\phi\cdot\nabla T \tag{5.8}$$

$$\frac{\partial \phi}{\partial t} + \frac{1}{\epsilon}\left(\vec{V}\cdot\nabla\phi\right) = \frac{1}{Le}\nabla^2\phi + \frac{N_A}{Le}\nabla^2 T \tag{5.9}$$

The corresponding boundary conditions become:

$$\begin{aligned}\text{At} \quad y = -L: \quad \vec{V} = 0, \quad T = 0, \quad \phi = 1 \\ \text{at} \quad y = L: \quad \vec{V} = 0, \quad T = 1, \quad \phi = 0\end{aligned} \tag{5.10}$$

5.3 Basic solution

The flow is supposed to be steady, parallel, continuous, unidirectional (x-direction), and completely developed in the basic stage. Eqs. (5.6)-(5.9) can be reduced to a system of ordinary differential equations using these three conditions:

$$Da\left\{\frac{\partial}{\partial y}\left(\mu(T_0)\frac{\partial U_b}{\partial y}\right)\right\} - \mu(T_0)U_b = \frac{dp_0}{dx} - (RaT_0 - Rn\phi_0 - Rm)\sin(\theta) \tag{5.11}$$

$$\frac{dp_0}{dy} = (RaT_0 - Rn\phi_0 - Rm)\cos(\theta) \tag{5.12}$$

$$\frac{dp_0}{dz} = 0 \tag{5.13}$$

$$\frac{d^2T_0}{dy^2} + \frac{N_B}{Le}\frac{d\phi_0}{dy}\frac{dT_0}{dy} + \frac{N_A N_B}{Le}\left(\frac{dT_0}{dy}\right)^2 = 0 \tag{5.14}$$

$$\frac{d^2\Phi_0}{dy^2} + N_A\frac{d^2T_0}{dy^2} = 0 \tag{5.15}$$

The following are the associated boundary conditions:

$$\begin{aligned} \text{At} \quad y = -1: \quad & U_b = 0, \quad T_0 = 0, \quad \phi_0 = 1 \\ \text{at} \quad y = 1: \quad & U_b = 0, \quad T_0 = 1, \quad \phi_0 = 0 \end{aligned} \tag{5.16}$$

Proceeding as in Chapter-2, and taking the approximation $\mu(T_0) = e^{-kT_0}$ [106], we get basic solution as:

$$T_0 = \frac{1+y}{2} \qquad \textit{and} \qquad \phi_0 = \frac{1-y}{2} \tag{5.17}$$

$$\begin{aligned} U_b = \frac{1}{8} e^{\frac{k}{4}(y+1)} \Big\{ & \operatorname{csch}(m) \operatorname{sech}(m) \Big(\sinh(m(1-y))(4\sigma - (Dak-2)(Ra+Rn))\sin(\theta) \\ & + e^{k/2} \sinh(m(1+y))(4\sigma - (Dak+2)(Ra+Rn))\sin(\theta) + \sin(\theta) e^{\frac{k}{4}(y+1)} \\ & \sinh(2m)(Ra+Rn)(Dak+2y) \Big) - 8\sigma e^{\frac{k}{4}(y+1)} \Big\} \end{aligned} \tag{5.18}$$

where:

$$\begin{aligned} \sigma = \Big\{ & \sinh^2(m) \Big\{ 2e^{k/2} \sin(\theta)(Ra+Rn)\big(4Dak^3 m \operatorname{csch}^2(m) + \sinh\left(\frac{k}{2}\right) \\ & \big(\coth(m)\big(16m^2\big(Dak^2-4\big) + k^2\big(Dak^2+4\big) - 8k^2 m \coth(m)\big) \\ & -8k^2 m\big) + \cosh\left(\frac{k}{2}\right)\big(2k\coth(m)\big(-2Dak^2 m\coth(m) + k^2 \\ & +16m^2\big) - 4Dak^3 m\big)\big) + 4k^4\coth(m) - 64k^2m^2\coth(m)\Big\}\Big\} \Big/ \\ & \Big\{ 2k\big(\big(e^k-1\big)\big(k^2+16m^2\big)\sinh(2m) + 16e^{k/2}km - 8\big(e^k+1\big)km\cosh(2m)\big)\Big\} \end{aligned}$$

and

$$m = \frac{\sqrt{k^2 + \frac{16}{Da}}}{4}$$

5.4 Linear stability analysis

As in Chapter - 2, by imposing infinitesimal disturbances (δ) on the basic state solutions, ignoring δ^2 and higher order terms, using the usual normal mode form [50] to express infinitesimal disturbances of corresponding field variables, and removing pressure terms from

the resulting equations, the linearized stability equations are obtained as:

$$
\begin{aligned}
&Da\Big[\mu_0\frac{d^4\hat{v}}{dy^4}+2\frac{d\mu_0}{dy}\frac{d^3\hat{v}}{dy^3}-\frac{d^2\hat{v}}{dy^2}\Big(2\mu_0(\alpha^2+\beta^2)-\frac{d^2\mu_0}{dy^2}\Big)-4(\alpha^2+\beta^2)\frac{d\hat{v}}{dy}\frac{d\mu_0}{dy}\\
&+(\alpha^2+\beta^2)\Big(\mu_0(\alpha^2+\beta^2)+\frac{d^2\mu_0}{dy^2}\Big)\hat{v}\Big]-\frac{i\alpha}{\mathrm{va}}\Big(\frac{U_b}{\epsilon}-c\Big)\Big[\frac{d^2\hat{v}}{dy^2}-(\alpha^2+\beta^2)\hat{v}\Big]\\
&+\frac{i\alpha}{\epsilon\mathrm{va}}\frac{d^2U_b}{dy^2}\hat{v}-\mu_0\Big[\frac{d^2\hat{v}}{dy^2}-(\alpha^2+\beta^2)\hat{v}\Big]-\frac{d\mu_0}{dy}\frac{d\hat{v}}{dy}-Dae^{-kT_0}k\Big[\frac{dU_b}{dy}\frac{d^2\hat{T}}{dy^2}\\
&+\Big(2\frac{d^2U_b}{dy^2}-k\frac{du_b}{dy}\Big)\frac{d\hat{T}}{dy}+\Big(\frac{d^3U_b}{dy^3}-k\frac{d^2U_b}{dy^2}+\frac{dU_b}{dy}\Big(\frac{k^2}{4}-i\alpha(\alpha^2+\beta^2)\Big)\Big)\hat{T}\Big]\\
&+ke^{-kT_0}\frac{dU_b}{dy}\hat{T}+ke^{-kT_0}\frac{d\hat{T}}{dy}U_b-U_b\frac{k^2}{2}e^{-kT_0}\hat{T}-Ra\frac{d\hat{T}}{dy}i\alpha\sin(\theta)\\
&-Ra(\alpha^2+\beta^2)\cos(\theta)\hat{T}+Rn\frac{d\hat{\phi}}{dy}i\alpha\sin(\theta)-Rn(\alpha^2+\beta^2)\cos(\theta)\hat{\phi}=0
\end{aligned}
\tag{5.19}
$$

$$
\begin{aligned}
&\frac{1}{\mathrm{va}}(-i\alpha c)\hat{\eta}+\frac{1}{\epsilon\mathrm{va}}\Big[\beta\hat{v}\frac{dU_b}{dy}+U_b\hat{\eta}i\alpha\Big]-Da\Big[\mu_0\frac{d^2\hat{\eta}}{dy^2}+\frac{d\mu_0}{dy}\frac{d\hat{\eta}}{dy}-\mu_0(\alpha^2+\beta^2)\hat{\eta}\Big]\\
&+Dake^{-kT_0}\beta\Big[\frac{dU_b}{dy}\frac{d\hat{T}}{dy}-\frac{k}{2}\hat{T}+\frac{d^2U_b}{dy^2}\hat{T}\Big]+\mu_0\hat{\eta}-\beta U_bke^{-kT_0}\hat{T}\\
&-\beta Ra\hat{T}sin(\theta)+\beta Rn\hat{\phi}sin(\theta)=0
\end{aligned}
\tag{5.20}
$$

$$
\begin{aligned}
&\hat{v}\frac{dT_0}{dy}+i\alpha(U_b-c)\hat{T}-\left[\frac{d^2\hat{T}}{dy^2}-(\alpha^2+\beta^2)\hat{T}\right]-\frac{N_B}{Le}\left[\frac{d\phi_0}{dy}+2N_A\frac{dT_0}{dy}\right]\frac{d\hat{T}}{dy}\\
&-\frac{N_B}{Le}\frac{dT_0}{dy}\frac{d\hat{\phi}}{dy}=0
\end{aligned}
\tag{5.21}
$$

$$
\frac{1}{\epsilon}\frac{d\phi_0}{dy}\hat{v}+i\alpha\left(\frac{U_b}{\epsilon}-c\right)\hat{\phi}-\frac{1}{Le}\left[\frac{d^2\hat{\phi}}{dy^2}-(\alpha^2+\beta^2)\hat{\phi}\right]-\frac{N_A}{Le}\Big[\frac{d^2\hat{T}}{dy^2}-(\alpha^2+\beta^2)\hat{T}\Big]=0 \tag{5.22}
$$

According to Srivastava *et al.* [112] $\hat{\mu}(T_0)=\frac{d\mu_0}{dT_0}\hat{T}$ represents the perturbation viscosity, and k is variable viscosity parameter.

5.5 Results and discussion

The set of Eqs. (5.19) - (5.22) expresses a generalized eigenvalue problem with perturbed eigenvalues in terms of wave speed. The spectral technique [107] is employed to find the solution to this eigenvalue problem.

To examine the validity of the method, the eigenvalue problem code is executed in MATLAB with a different grid point count (N), and the resulting least consistent eigenvalues are given in Table 5.1 for a set of other parameters chosen at random. For $N \geq 50$, the least consistent eigenvalue meets a convergence threshold of 10^{-7}. When $N \geq 50$, the results do not change. A similar trend may be noticed for different parameter values. As a consequence, $N = 50$ is used in the numerical calculation.

The present analysis's outcomes are compared to those of a vertical channel filled with a nanofluid-saturated porous medium. The critical Rayleigh number Ra_c and critical wavenumber α_c for the vertical channel are calculated from the current analysis when $Da = 10$, k=0, $Pr = 7$, $Ra = 100$, $Rn = 15$, $\epsilon = 0.6$, $N_A = 8$, $N_B = 0.2$, and $\theta = \pi/2$, which is consistent with the results of Srinivasacharya and Barman [50] as shown in Table 5.2.

The impact of variable viscosity on nanofluid flow stability in an inclined porous channel is investigated in this paper. The influence of inclination angle (θ), variable viscosity parameter (k), porosity parameter (ϵ), and Prandtl number (Pr) on critical Rayleigh number (Ra_c) and critical wavenumber (α_c) is depicted in Figs. 5.1-5.4. On the horizontal axis, the logarithm of the Darcy number is used to show all of the instability boundaries.

The plots for the variation of critical Rayleigh number (Ra_c) and critical wavenumber (α_c) for the inclination angle (θ) are shown in Fig. 5.1. As θ changes from horizontal to vertical, the logarithm of the critical Rayleigh number ($log_{10}Ra_c$) decreases. This demonstrates that θ destabilizes the flow. This is because when the channel is inclined, the gravitational force acting on the fluid causes a component of the force to act in the direction of the flow. This can lead to the development of instabilities in the nanofluid flow. It is worth noting that the rising Darcy number (Da) rises Ra_c indicating a stabilizing impact of permeability. Also, the flow is constant until $Da = 1$, and then there is a rapid spike in Ra_c as Da increases. The fluctuation of Ra_c is slow and smooth for small values of the Darcy number ($Da < 1$). When ($Da > 1$), there is a quick increase in Ra_c. The flow resistance decreases as permeability increases, and flow in the porous medium improves, indicating that viscous forces play a role in the momentum equation. When the inclination angle is fixed, it is seen that α_c increases as Da increases. Also, as θ shifts from horizontal to vertical, the critical wavenumber enhances.

Fig. 5.2 shows the variation in critical Rayleigh number (Ra_c) and critical wavenumber (α_c) for the variable viscosity parameter (k). Ra_c drops as we increase k from -0.5 to 0.5. However, as we raise Da, Ra_c increases slowly until $Da = 1$, and then there is a rapid spike in Ra_c as Da increases. However, as we increase k from -0.5 to 0.5, α_c is decreased. And when we increase Da, α_c increases until Da=1, then it becomes constant. Hence, k destabilizes the flow because variable viscosity affects the distribution and migration of nanoparticles, leading to the accumulation or segregation of nanoparticles in certain regions, disrupting flow patterns. The significant contrast in viscosity between nanoparticles and the base fluid introduces non-uniform shear stress distribution, causing flow instability.

Fig. 5.3 presents the boundaries of the instability region depending on the porosity parameter (ϵ) and the permeability parameter (Da). It is seen from Fig. 5.3 that increasing the porosity parameter tends to increase the critical Rayleigh number(Ra_c). This is because porosity is a ratio of void volume over total volume. In a porous medium, this is a measurement of the empty spaces. When the porosity rises, the volume of voids rises as well. Hence, porosity stabilizes the flow. Also, it is noted that there is a little variation in α_c when the value of the porosity parameter increases, but there is an increase in α_c as the value of Da grows.

The influence of the Prandtl number (Pr) on the boundaries of instability is seen in Fig. 5.4. The critical Rayleigh number rises as momentum diffusivity increases in terms of Pr. As a result, the Prandtl number has a stabilizing effect on the system. There is substantial flow resistance with small Darcy numbers in the porous medium. This flow resistance decreases as the permeability increases and the porous medium's flow increases, indicating the importance of the momentum equation of viscous forces. Moreover, when permeability increases, the wavenumber also increases. Also, when Pr rises, the wavenumber rises slowly.

Figs. 5.5-5.7 show streamlines, isotherms, and isonanoconcentrations for various θ values when with fixed values of other parameters. $Da = 1$, Pr=7, ϵ=0.6, Rn=15, Ra=100, Le=500, $N_A = 8$, $N_B = 0.2$, and k=0.5. Streamlines in a clockwise direction correlate to negative contours, whereas those in an anti-clockwise direction correspond to positive contours. When the channel is vertical, i.e., $\theta = \pi/2$, Fig. 5.5 shows the development of two vertical cell structures known as Rayleigh-Bernard convection cells. A counter-clockwise vortex forms close to the upper wall, while a clockwise vortex forms near the lower wall. The cells then stretch or elongate in the vertical direction as the inclination angle decreases, eventually forming a horizontal cell structure when the inclination angle reaches $\theta = 0$ i.e., when the channel becomes horizontal. Therefore, streamlines reorient the pattern from a horizontal structure to a vertical structure as the channel inclination changes from vertical to horizontal. Solid lines represent positive contours in the case of isotherms, isosolutes, and isonanoconcentrations contour, whereas dashed lines represent negative contours. A similar pattern is observed in the cases of isotherms and isonanoconcentrations.

Table 5.1: "Convergence of the least stable eigenvalue for $Da = 10$, k=0.5, $Pr = 7$, $Ra = 100$,$Rn = 15$, $\epsilon = 0.6$, $N_A = 8$, $N_B = 0.2$, $Le = 500$, α= 1, and $\beta = 0$."

N	**Least stable eigenvalue**
40	2.782696889086 -0.072169454812i
45	2.782696869479 -0.072169365646i
50	2.782697982103 -0.072165179703i
55	2.782697061391 -0.072156113180i
60	2.782694217221 -0.072164172382i

Table 5.2: "Critical values of α_c and Ra_c for different values of Le and β at $Da = 10$, $k = 0$, $Pr = 7$, $Rn = 15$, $\epsilon = 0.6$, $N_A = 8$, $N_B = 0.02$, and $\theta = \pi/2$"

			Present Results		**Srinivasacharya and Barman [50]**	
Da	β	Le	α_c	Ra_c	α_c	Ra_c
0.1	0	100	0.964500755	1418.197639	0.9645	1418.198
	0	300	0.963249683	1428.58010	0.9632	1428.580
	0	500	0.963040499	1430.804799	0.9631	1430.805
	0.5	500	0.901980216	1649.284165	0.9020	1649.284
	1	500	0.727248243	2915.056289	0.7273	2915.056
1	0	100	1.343032132	3030.342688	1.3430	3030.343
	0	300	1.342459409	3035.799127	1.3425	3035.799
	0	500	1.342402116	3037.208995	1.3424	3037.209
	0.5	500	1.295094713	3263.853616	1.2951	3263.854
	1	500	1.142297567	4203.373754	1.1423	4203.374
10	0	100	1.382342585	25247.08315	1.3824	25247.08
	0	300	1.382274144	25252.11631	1.3823	25252.12
	0	500	1.382280638	25253.49436	1.3819	25253.44
	0.5	500	1.33625209	27021.49202	1.3361	27021.49
	1	500	1.189422721	34195.04124	1.1894	34195.04

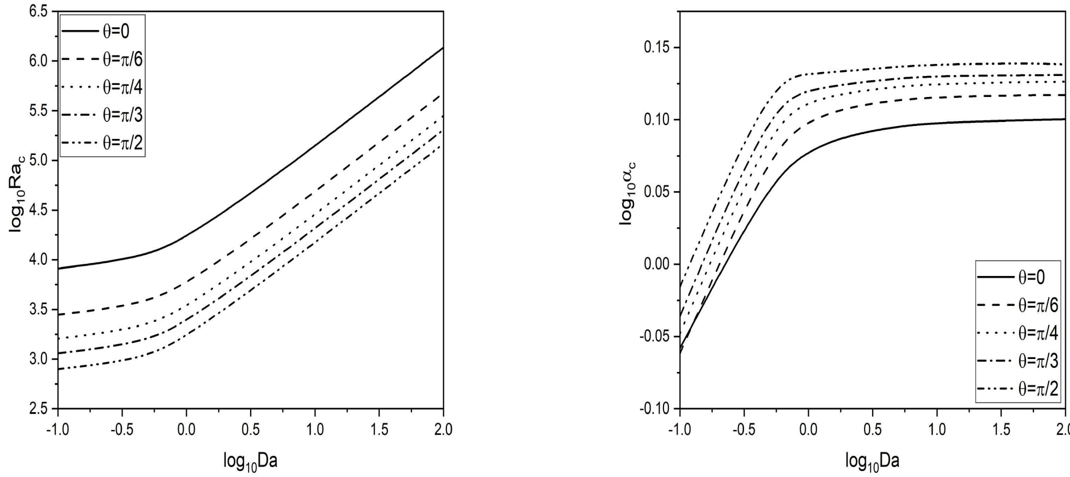

Figure 5.1: "For $k = 0.5, Le = 500$, ϵ=0.6, $Rn = 15, Pr = 7$, $N_A = 8$, and $N_B = 0.2$ instability boundaries for ($log_{10}Da$, $log_{10}Ra_c$)-plane and ($log_{10}Da$, $log_{10}\alpha_c$)-plane for various values of θ"

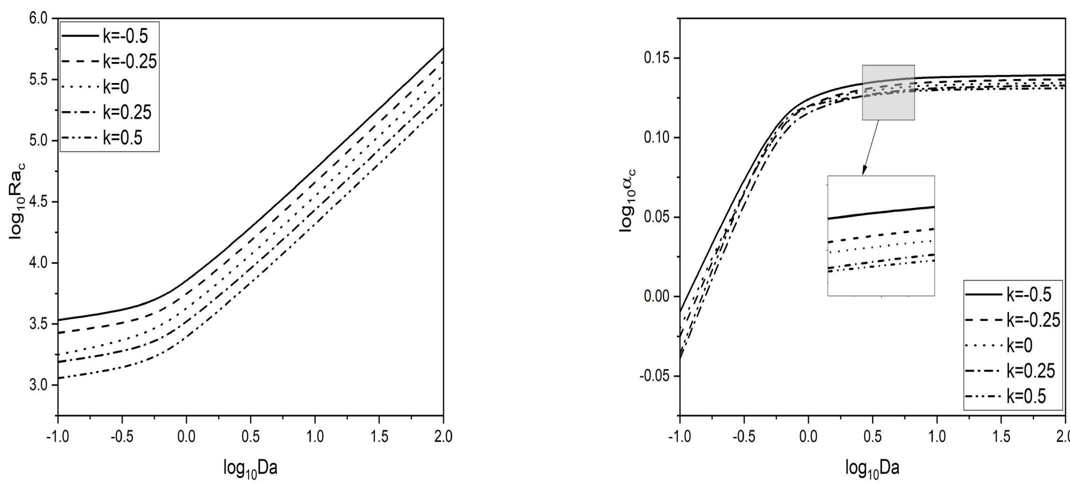

Figure 5.2: "For $\theta = \pi/3$, $Le = 500$, ϵ=0.6, $Rn = 15, Pr = 7$, $N_A = 8$, and $N_B = 0.2$ instability boundaries for ($log_{10}Da$, $log_{10}Ra_c$)-plane and ($log_{10}Da$, $log_{10}\alpha_c$)-plane for various values of k."

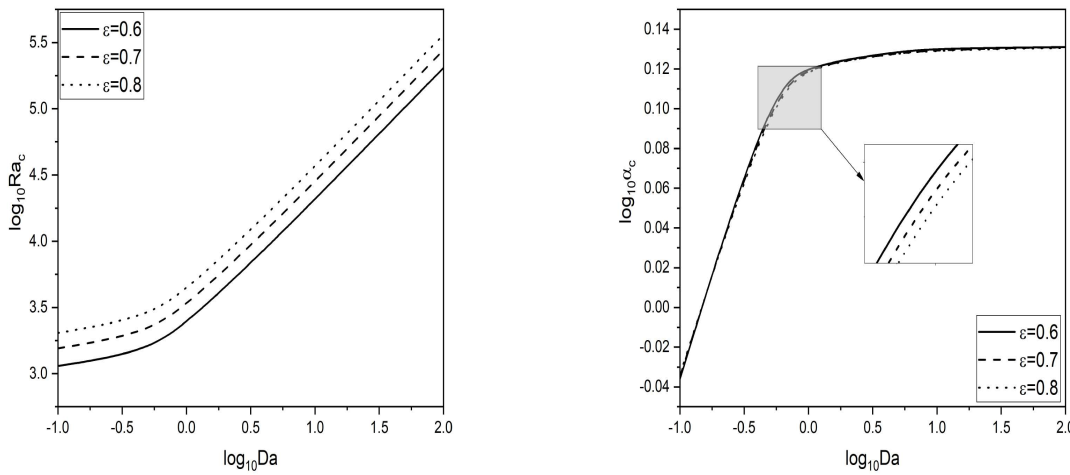

Figure 5.3: "For $\theta = \pi/3,\ k = 0.5, Le = 500, Rn = 15, Pr = 7,\ N_A = 8$, and $N_B = 0.2$ instability boundaries for ($log_{10}Da$, $log_{10}Ra_c$)-plane and ($log_{10}Da$, $log_{10}\alpha_c$)-plane for various values of ϵ."

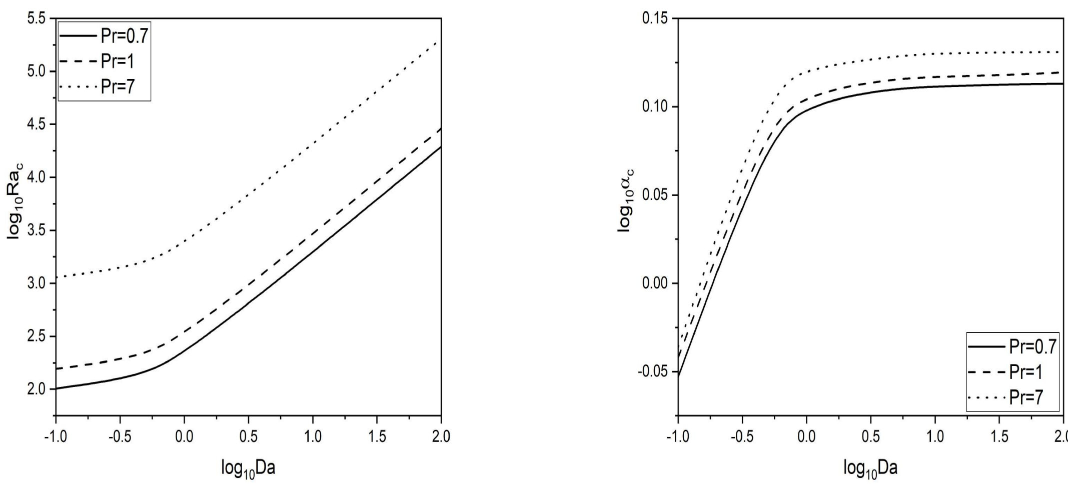

Figure 5.4: "For $\theta = \pi/3,\ k = 0.5,\ \epsilon$=0.6, $Rn = 15, Le = 500,\ N_A = 8$, and $N_B = 0.2$ instability boundaries for ($log_{10}Da$, $log_{10}Ra_c$)-plane and ($log_{10}Da$, $log_{10}\alpha_c$)-plane for various values of Pr."

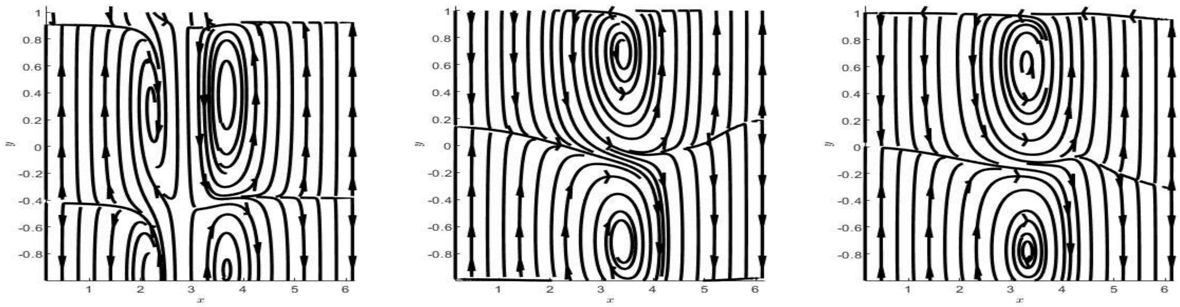

(a) "$\theta = 0$" (b) "$\theta = \pi/4$" (c) "$\theta = \pi/2$"

Figure 5.5: "The disturbance of streamlines for different values of θ."

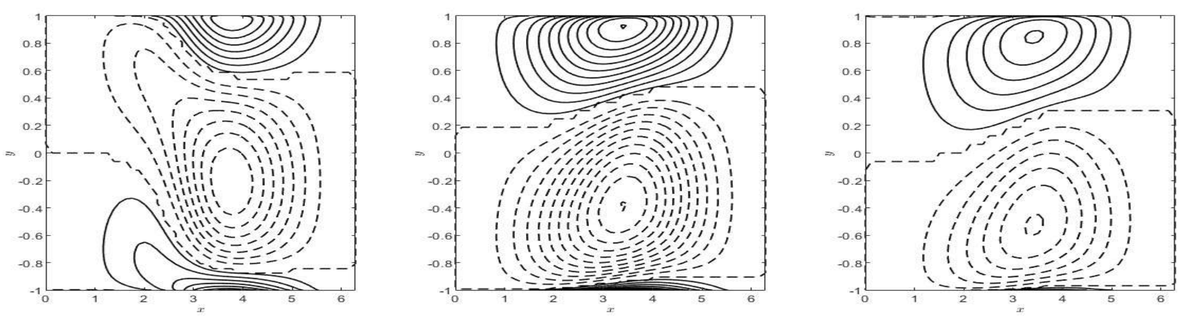

(a) "$\theta = 0$" (b) "$\theta = \pi/4$" (c) "$\theta = \pi/2$"

Figure 5.6: "The disturbance of isotherms for different values of θ."

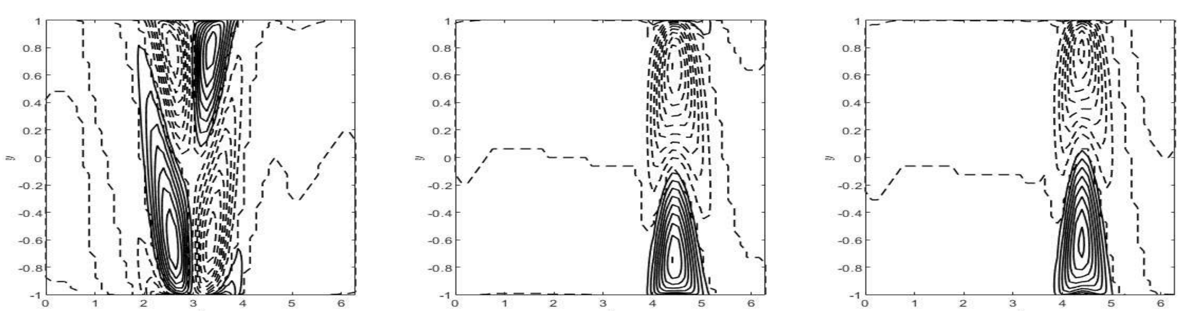

(a) "$\theta = 0$" (b) "$\theta = \pi/4$" (c) "$\theta = \pi/2$"

Figure 5.7: "The disturbance of isonanoconcentrations for different values of θ."

5.6 Conclusions

The Brinkman-extended Darcy model is employed to examine the linear stability of variable viscosity in an inclined channel with a porous medium saturated with nanofluid. The critical Rayleigh number (Ra_c) and critical wavenumber (α_c) are computed and graphically presented for various values of θ, k, Pr, and ϵ versus Da.

- The variable viscosity parameter destabilizes the flow as it affects the distribution and migration of nanoparticles, leading to the accumulation or segregation of nanoparticles in certain regions, disrupting flow patterns.
- The flow in an inclined channel is stabilized by the Prandtl number (Pr), and porosity parameter (ϵ). As a result, a rise in these factors delays the onset of convection.

Chapter 6

Influence of variable viscosity and local thermal non-equilibrium on nanofluid flow stability in an inclined porous channel [1]

6.1 Introduction

In this chapter, we examine the impact of LTNE with variable viscosity on convection stability in nanofluid flow for an inclined channel (with inclination θ) filled with a porous medium. The application of the present study may include the design of heat exchangers for improved thermal efficiency, enhanced cooling systems in various industries, optimizing enhanced oil recovery techniques, aiding in environmental engineering for wastewater treatment and contaminant transport, benefiting microfluidics for medical diagnostics and lab-on-a-chip systems, and contributing to geothermal energy extraction, aerospace, and aviation cooling systems.

[1] Published in "***Proceedings of the Institution of Mechanical Engineers, Part E: Journal of Process Mechanical Engineering***" pp:1-15, DOI: 10.1177/09544089241234406

6.2 Mathematical Formulation

Consider an unsteady, incompressible flow of a nanofluid in an inclined channel with a width of $2L$ and inclination θ, with impermeable and completely thermally conducting walls. Also, we have assumed that viscosity varies exponentially with temperature. according to the Nahme law Sukanek *et al.* [110]

$$\mu(T) = \mu_l e^{-kT}$$

where μ_l is the viscosity at the reference temperature T_l.

Fig. 2.1 depicts a a diagrammatic depiction of the problem. Assume that the angle of inclination with the horizontal line is θ. The LTNE state is assumed to exist between the fluid, particle, and solid-matrix phases. The three temperature models are taken into account. As a result, three heat transfer equations, one for each of the three phases, are considered. Except for the density changes in the buoyancy force term, the thermophysical characteristics of the fluid are considered to be constant. Assume that the porous medium is homogenous and isotropic. The temperatures of the left and right walls are T_1 and T_2 ($T_1 > T_2$), and nanoparticle volume fractions are ϕ_2 and ϕ_1, respectively.
Using the above assumptions, employing the Oberbeck- Boussinesq approximation and Darcy-Brinkman model, the governing equations that describe the flow can be expressed as follows [113, 50]:
Conservation of mass:

$$\nabla \cdot \vec{V} = 0 \tag{6.1}$$

Conservation of momentum:

$$\frac{\rho_f}{\epsilon}\frac{\partial \vec{V}}{\partial t} + \frac{\rho_f}{\epsilon^2}(\vec{V}\cdot\nabla)\vec{V} = -\nabla p + \left[\mu\Delta\vec{V} + \nabla\mu\cdot\left(\nabla\vec{V}^T + \nabla\vec{V}\right)\right] - \frac{\mu}{K}\vec{V} - \big[\phi\rho_p + (1-\phi)\rho_f (1 - \beta_T(T_f - T_1))\big]\mathbf{g}(\sin(\theta)\hat{e_{\mathrm{x}}} + \cos(\theta)\hat{e_{\mathrm{y}}}) \tag{6.2}$$

Conservation of energy:

$$\epsilon(\rho C)_f(1-\phi_1)\left(\frac{\partial T_f}{\partial t} + \frac{1}{\epsilon}\vec{V}\cdot\nabla T_f\right) = k_f\epsilon(1-\phi_1)\nabla^2 T_f + \epsilon(1-\phi_1)(\rho C)_p\big(D_B\nabla\phi\cdot\nabla T_f + \frac{D_T}{T_1}\nabla T_f\cdot\nabla T_f\big) - h_{fp}(T_f - T_p) - h_{fs}(T_f - T_s) \tag{6.3}$$

$$\epsilon(\rho C)_p\left(\frac{\partial T_p}{\partial t}+\frac{1}{\epsilon}\vec{V}\cdot\nabla T_p\right)\phi_1=\epsilon\phi_1 k_p\nabla^2 T_p+h_{fp}(T_f-T_p) \tag{6.4}$$

$$(1-\epsilon)(\rho C)_s\frac{\partial T_s}{\partial t}=(1-\epsilon)k_s\nabla^2 T_s+h_{fs}(T_f-T_s) \tag{6.5}$$

Conservation of nanoparticle:

$$\frac{\partial\phi}{\partial t}+\frac{1}{\epsilon}\vec{V}\cdot\nabla\phi=D_B\nabla^2\phi+\frac{D_T}{T_1}\nabla^2 T \tag{6.6}$$

The following are the conditions on the boundaries of the channel:

$$\begin{aligned}\text{At}\quad y=-L:&\quad \vec{V}=0,\quad T_f=T_1,\quad T_p=T_1, T_s=T_1,\quad \phi=\phi_2\\ \text{and}\quad\text{at}\quad y=L:&\quad \vec{V}=0,\quad T_f=T_2,\quad T_p=T_2, T_s=T_2,\quad \phi=\phi_1\end{aligned} \tag{6.7}$$

The non-dimensional form of the Eqs. (6.1) -(6.6) (on substituting (2.6) in (6.1) -(6.6) and removing asterisk) are:

$$\nabla\cdot\vec{V}=0 \tag{6.8}$$

$$\begin{aligned}\frac{1}{\text{va}}\frac{\partial\vec{V}}{\partial t}+\frac{1}{\text{va}\epsilon}(\vec{V}\cdot\nabla)\vec{V}=-\nabla p+Da\big[\mu\Delta\vec{V}+\nabla\mu\cdot\left(\nabla\vec{V}^T+\nabla\vec{V}\right)\big]-\mu\vec{V}+\{RaT_f\\ -Rn\phi-Rm\}(\sin(\theta)\hat{e_{\text{x}}}+\cos(\theta)\hat{e_{\text{y}}})\end{aligned} \tag{6.9}$$

$$\begin{aligned}\frac{\partial T_f}{\partial t}+\frac{1}{\epsilon}\left(\vec{V}.\nabla T_f\right)=\nabla^2 T_f+\frac{N_B}{Le}\nabla\phi\cdot\nabla T_f+\frac{N_A N_B}{Le}\nabla T_f\cdot\nabla T_f-N_{HP}(T_f-T_p)\\ -N_{HS}(T_f-T_s)\end{aligned} \tag{6.10}$$

$$\frac{\partial T_p}{\partial t}+\frac{1}{\epsilon}\left(\vec{V}\cdot\nabla T_p\right)=\epsilon_p\nabla^2 T_p+\gamma_p N_{HP}(T_f-T_p) \tag{6.11}$$

$$\frac{\partial T_s}{\partial t}=\epsilon_s\nabla^2 T_s+\gamma_s N_{HS}(T_f-T_s) \tag{6.12}$$

$$\frac{\partial\phi}{\partial t}+\frac{1}{\epsilon}\left(\vec{V}\cdot\nabla\phi\right)=\frac{1}{Le}\nabla^2\phi+\frac{N_A}{Le}\nabla^2 T_f \tag{6.13}$$

The corrosponding boundary conditions became:

$$\begin{aligned}\text{At}\quad y=-1:&\quad \vec{V}=0,\quad T_f=1,\quad T_p=1,\quad T_s=1,\quad \phi=0\\ \text{and}\quad\text{at}\quad y=1:&\quad \vec{V}=0,\quad T_f=0,\quad T_p=0,\quad T_s=0,\quad \phi=1\end{aligned} \tag{6.14}$$

6.3 Basic solution

The flow is supposed to be steady, parallel, continuous, unidirectional (x-direction), and completely developed in the basic stage. Eqs. (6.8)-(6.13) can be reduced to a system of ordinary differential equations using these three conditions:

$$Da\left\{\frac{\partial}{\partial y}\left(\mu(T_0)\frac{\partial U_b}{\partial y}\right)\right\} - \mu(T_0)U_b = \frac{dp_0}{dx} - (RaT_{f0} - Rn\phi_0 - Rm)\sin(\theta) \tag{6.15}$$

$$\frac{dp_0}{dy} = (RaT_{f0} - Rn\phi_0 - Rm)\cos(\theta) \tag{6.16}$$

$$\frac{dp_0}{dz} = 0 \tag{6.17}$$

$$\frac{d^2T_{f0}}{dy^2} + \frac{N_B}{Le}\frac{d\phi_0}{dy}\frac{dT_{f0}}{dy} + \frac{N_AN_B}{Le}\left(\frac{dT_{f0}}{dy}\right)^2 + N_{HP}(T_{p0} - T_{s0}) + N_{HS}(T_{s0} - T_{f0}) = 0 \tag{6.18}$$

$$\epsilon_p\frac{d^2T_{p0}}{dy^2} + \gamma_pN_{HP}(T_{f0} - T_{p0}) = 0 \tag{6.19}$$

$$\epsilon_s\frac{d^2T_{s0}}{dy^2} + \gamma_sN_{HS}(T_{f0} - T_{s0}) = 0 \tag{6.20}$$

$$\frac{d^2\Phi_0}{dy^2} + N_A\frac{d^2T_{f0}}{dy^2} = 0 \tag{6.21}$$

The following are the associated boundary conditions:

$$\begin{aligned} \text{At} \quad y = -1: \quad & U_b = 0, \quad T_{f0} = 0, \quad T_{p0} = 0, \quad T_{s0} = 0, \quad \phi_0 = 1 \\ \text{and} \quad \text{at} \quad y = 1: \quad & U_b = 0, \quad T_{f0} = 1, \quad T_{p0} = 1, \quad T_{s0} = 1, \quad \phi_0 = 0 \end{aligned} \tag{6.22}$$

Proceeding as in Chapter-2, and taking the approximation $\mu(T_0) = e^{-kT_0}$ [106], we get basic solution as:

$$T_{f0} = T_{p0} = T_{s0} = \frac{1+y}{2} \quad \text{and} \quad \phi_0 = \frac{1-y}{2} \tag{6.23}$$

$$\begin{aligned} U_b = \frac{1}{8}e^{\frac{k}{4}(y+1)}\Big\{&\text{csch}(m)\text{sech}(m)\Big(\sinh(m(1-y))(4\sigma - (Dak-2)(Ra+Rn))\sin(\theta) \\ &+e^{k/2}\sinh(m(1+y))(4\sigma - (Dak+2)(Ra+Rn))\sin(\theta) + \sin(\theta)e^{\frac{k}{4}(y+1)} \\ &\sinh(2m)(Ra+Rn)(Dak+2y)\Big) - 8\sigma e^{\frac{k}{4}(y+1)}\Big\} \end{aligned} \tag{6.24}$$

where:

$$\sigma = \Big\{ \sinh^2(m)\big\{2e^{k/2}\sin(\theta)(Ra+Rn)\big(4Dak^3 m\,\mathrm{csch}^2(m) + \sinh\big(\frac{k}{2}\big)\big(\coth(m)$$
$$\big(16m^2\big(Dak^2-4\big) + k^2\big(Dak^2+4\big) - 8k^2 m\coth(m)\big) - 8k^2 m\big)$$
$$+\cosh\big(\frac{k}{2}\big)\big(2k\coth(m)\big(-2Dak^2 m\coth(m) + k^2 + 16m^2\big) - 4Dak^3 m\big)\big)$$
$$+4k^4\coth(m) - 64k^2m^2\coth(m)\big\}\Big\} \Big/ \Big\{2k\big(\big(e^k-1\big)$$
$$\big(k^2+16m^2\big)\sinh(2m) + 16e^{k/2}km - 8\big(e^k+1\big)km\cosh(2m)\big)\Big\}$$

and

$$m = \frac{\sqrt{k^2 + \frac{16}{Da}}}{4}$$

6.4 Linear stability analysis

As in Chapter - 2, by imposing infinitesimal disturbances (δ) on the basic state solutions, ignoring δ^2 and higher order terms, using the usual normal mode form [50] to express infinitesimal disturbances of corresponding field variables, and removing pressure terms from the resulting equations, the linearized stability equations are obtained as:

$$\begin{aligned} &Da\Big[\mu_0\frac{d^4\hat{v}}{dy^4} + 2\frac{d\mu_0}{dy}\frac{d^3\hat{v}}{dy^3} - \frac{d^2\hat{v}}{dy^2}\Big(2\mu_0(\alpha^2+\beta^2) - \frac{d^2\mu_0}{dy^2}\Big) - 4(\alpha^2+\beta^2)\frac{d\hat{v}}{dy}\frac{d\mu_0}{dy} + (\alpha^2+\beta^2) \\ &\Big(\mu_0(\alpha^2+\beta^2) + \frac{d^2\mu_0}{dy^2}\Big)\hat{v}\Big] - \frac{i\alpha}{\mathrm{va}}\Big(\frac{U_b}{\epsilon} - c\Big)\Big[\frac{d^2\hat{v}}{dy^2} - (\alpha^2+\beta^2)\hat{v}\Big] + \frac{i\alpha}{\epsilon\mathrm{va}}\frac{d^2U_b}{dy^2}\hat{v} - \mu_0\Big[\frac{d^2\hat{v}}{dy^2} \\ &-(\alpha^2+\beta^2)\hat{v}\Big] - \frac{d\mu_0}{dy}\frac{d\hat{v}}{dy} - Ra\frac{d\hat{T}_f}{dy}i\alpha\sin(\theta) - Ra(\alpha^2+\beta^2)\cos(\theta)\hat{T}_f + Rn\frac{d\hat{\phi}}{dy}i\alpha\sin(\theta) \\ &-Rn(\alpha^2+\beta^2)\cos(\theta)\hat{\phi} = 0 \end{aligned} \tag{6.25}$$

$$\begin{aligned} &\frac{1}{\mathrm{v}a}(-i\alpha c)\hat{\eta} + \frac{1}{\epsilon\mathrm{va}}\Big[\beta\hat{v}\frac{dU_b}{dy} + U_b\hat{\eta}i\alpha\Big] - Da\Big[\mu_0\frac{d^2\hat{\eta}}{dy^2} + \frac{d\mu_0}{dy}\frac{d\hat{\eta}}{dy} - \mu_0(\alpha^2+\beta^2)\hat{\eta}\Big] \\ &+\mu_0\hat{\eta} - \beta Ra\hat{T}_f sin(\theta) + \beta Rn\hat{\phi} sin(\theta) = 0 \end{aligned} \tag{6.26}$$

$$\frac{1}{\epsilon}\frac{dT_{f0}}{dy}\hat{v}+i\alpha\Big(\frac{U_b}{\epsilon}-c\Big)\hat{T}_f-\left[\frac{d^2\hat{T}_f}{dy^2}-(\alpha^2+\beta^2)\hat{T}_f\right]-\frac{N_B}{Le}\Big[\frac{d\phi_0}{dy}+2N_A\frac{dT_{f0}}{dy}\Big]\frac{d\hat{T}_f}{dy}$$
$$-\frac{N_B}{Le}\frac{dT_{f0}}{dy}\frac{d\hat{\phi}}{dy}-N_{HP}(\hat{T}_p-\hat{T}_f)-N_{HS}(\hat{T}_s-\hat{T}_f)=0 \quad (6.27)$$

$$\frac{1}{\epsilon}\frac{dT_{p0}}{dy}\hat{v}+i\alpha\Big(\frac{U_b}{\epsilon}-c\Big)\hat{T}_p-\epsilon_p\left[\frac{d^2\hat{T}_p}{dy^2}-(\alpha^2+\beta^2)\hat{T}_p\right]-\gamma_pN_{HP}(\hat{T}_f-\hat{T}_p)=0 \quad (6.28)$$

$$i\alpha c\hat{T}_s+\epsilon_s\left[\frac{d^2\hat{T}_s}{dy^2}-(\alpha^2+\beta^2)\hat{T}_s\right]+\gamma_sN_{HS}(\hat{T}_f-\hat{T}_s)=0 \quad (6.29)$$

$$\frac{1}{\epsilon}\frac{d\phi_0}{dy}\hat{v}+i\alpha\left(\frac{U_b}{\epsilon}-c\right)\hat{\phi}-\frac{1}{Le}\left[\frac{d^2\hat{\phi}}{dy^2}-(\alpha^2+\beta^2)\hat{\phi}\right]-\frac{N_A}{Le}\Big[\frac{d^2\hat{T}_f}{dy^2}-(\alpha^2+\beta^2)\hat{T}_f\Big]=0 \quad (6.30)$$

6.5 Results and discussion

The set of Eqs. (6.25) - (6.30) expresses a generalised eigenvalue problem with perturbed eigenvalues in terms of wave speed. The spectral technique [107] is employed to find the solution to this eigenvalue problem.

To examine the validity of the method, the eigenvalue problem code is executed in MATLAB with a different grid point count (N), and the resulting least consistent eigenvalues are given in Table 6.1 for a set of other parameters chosen at random. For $N \geq 50$, the least consistent eigenvalue meets a convergence threshold of 10^{-7}. When $N \geq 50$, the results do not change. A similar trend may be noticed for different parameter values. As a consequence, $N = 50$ is used in the numerical calculation.

To validate the exactness of the method, our code was verified by comparing it with published results in a vertical channel filled with a nanofluid-saturated porous medium. The critical Rayleigh number (Ra_c) and critical wavenumber (α_c) for the vertical channel were calculated from the current analysis when $Pr = 7$, $Rn = 15$, $Rm = 0$, $\epsilon = 0.6$,$N_A = 8$, $N_B = 0.02$, $N_{HP} = 0$, $N_{HS} = 0$, ϵ_p=0, $\epsilon_s = 0$, γ_p=0, γ_s=0, $k = 0$ and $\theta = \pi/2$, which is consistent with the results of Srinivasacharya and Barman [50].

The impact of local thermal non-equilibrium on nanofluid flow stability with variable viscosity in an inclined porous channel is investigated in this paper. The flow is controlled by seventeen variables, which are as follows: Da, Pr, Ra, Rn, ϵ, N_A, N_B and Le (related to the state of LTE), inclination angle (θ), variable viscosity parameter (k), interphase heat transfer parameters N_{HS} and N_{HP}, modified thermal capacity ratios γ_p and γ_s, and modified thermal diffusivity ratios ϵ_p and ϵ_s. Because there are more parameters, the analysis is simplified to focus solely on the effect of LTNE parameters. As a result, for the rest of the discussion, the LTE parameters will be set to $Pr = 7$, $Da = 1$, $Rn = 5$, $k = 0.5$, $N_A = 8$, $N_B = 0.2$, $\epsilon = 0.6$, and $Le = 500$.

From the present analysis, we can get the special cases for horizontal channel $\theta = 0$, vertical channel $\theta = 0$ and constant viscosity $k = 0$. The critical values of Ra_c and α_c for these special cases are calculated and given below. The results of present study are compared with the benchmark results obtained by Srinivasacharya and Barman [50].

Case - I (Horizontal Channel): The Critical values of for the case of horizontal channel is calculated as $Ra_c = 17356$ and $\alpha_c = 1.2204$.

Case - II (Vertical Channel): The Critical values of for the case of vertical channel is calculated as $Ra_c = 1808.5$ and $\alpha_c = 1.3559$.

Case - III(Constant Viscosity): The Critical values of for the case of constant viscosity is calculated as $Ra_c = 4240.4$ and $\alpha_c = 1.3165$.

6.5.1 Effect of the interphase heat transfer parameter

For different LTNE parameters, the change of critical Rayleigh number (Ra_c) and critical wavenumber (α_c) are computed as functions of Nield numbers N_{HP} and N_{HS} and presented in Fig. 6.1 and Fig. 6.2. According to Fig. 6.1(a), as N_{HP} increases, the critical Rayleigh number (Ra_c) increases, whereas as N_{HS} increases, Ra_c decreases. Fig. 6.2(a) also depicts a similar trend for variation of Ra_c with inter-phase heat transfer parameters. As a result, for all values of N_{HP} stabilizes the flow whereas for all values of N_{HS} destabilizes it. An enhancement in the values of N_{HP} or N_{HS} enhances the heat-release from fluid to solid and fluid to the nanoparticle or vice versa, respectively. Furthermore, all three phases have almost similar temperatures and act as a single phase, resulting in a local thermal equilibrium state. This is because N_{HP} and N_{HS} becomes large, the temperature differences are inversely proportional to inter-phase heat transfer parameters. In case of critical wavenumber when N_{HP} rises, α_c increase, and when N_{HS} increase, α_c first drops upto certain values of N_{HS} then rapidly rises in the intermediate values as shown in Fig. 6.1(b). This could be due to fluid/particle dominance of heat transfer of fluid/solid-matrix. Furthermore, as shown in Fig. 6.2(b), when N_{HS} rises, α_c falls, and when N_{HP} rises, α_c rises.

6.5.2 Effect on the angle of inclination:

The plots for the variation of critical Rayleigh number (Ra_c) and critical wavenumber (α_c) as a function of Nield numbers N_{HP} and N_{HS} for the inclination angle (θ) are displayed in Fig. 6.3 and Fig. 6.4. The Fig. 6.3(a) shows that Ra_c decreases as θ changes from horizontal to vertical, whereas Ra_c does not change as N_{HP} increases. However, in the case of N_{HS}, Ra_c decreases as N_{HS} and θ both increase, as shown in Fig. 6.4(a). As a result, changing θ from horizontal to vertical destabilises the flow. In the case of critical wavenumber, as θ and N_{HP} increase, so does α_c, as shown in Fig. 6.3(b). Also, as θ moves from horizontal to vertical, α_c rises, and as N_{HS} increases, α_c falls until certain values of N_{HS} and then rises, as shown in Fig. 6.4(b). This could be due to fluid/particle heat transfer dominating fluid/solid matrix heat transfer.

6.5.3 Effect on the variable viscosity parameter:

Fig. 6.5 and Fig. 6.6 shows the variation of critical Rayleigh number (Ra_c) and critical wavenumber (α_c) as a function of Nield numbers N_{HP} and N_{HS} for variable viscosity parameter (k). We observed that as k increases from -0.5 to 0.5, Ra_c decreases and as we increase N_{HP} there is no variation in Ra_c, as displayed in Fig 6.5(a). And we see in the Fig. 6.6(a), as k increases, Ra_c decreases and as we increase N_{HS}, Ra_c drops from high values when N_{HS} is small to its minimum LTNE value. Hence, k destabilizes the flow. However, there is no uniform pattern for α_c as we increase k for N_{HP} and N_{HS} both as shown in Figs. 6.5(b) and 6.6(b). But as we increase N_{HP}, critical wavenumber (α_c) first increases then it became constant as displayed in Fig. 6.5(b). And with increase of N_{HS}, the value of critical wavenumber (α_c) decreases from high values when N_{HS} is small to its minimum LTNE value for intermediate N_{HS}, then bounces back to higher values for large N_{HS} as shown in Fig. 6.6(b). This might occur as a result of fluid/particle heat transfer dominating that of fluid/solid matrix.

6.5.4 Effect on the modified thermal capacity ratios:

Figs. 6.7- 6.10 shows the behaviour (Ra_c) and (α_c) with inter-phase heat transfer parameters N_{HP} and N_{HS} for different values of modified thermal capacity ratios γ_p and γ_s by fixing the other parameters values. As shown in Fig. 6.7(a), Ra_c gradually decreases as γ_p increases from 0.04 to 0.08, and Ra_c grows uniformly as N_{HP} increases. Whereas for N_{HS}, as shown in 6.8(a), Ra_c remains constant as γ_p increases, Ra_c decreases as N_{HS} increases. As a result, γ_p stabilizes the flow for all N_{HP} values while destabilizing it for all N_{HS} values. Furthermore, as γ_p rises, α_c falls slightly, but as N_{HP} rises, α_c rises, as shown in Fig. 6.7 (b). Also, as γ_p rises, α_c rises until a certain value of N_{HS} and then decreases, whereas as N_{HS} rises, α_c first falls for the intermediate values of N_{HS} before rising, as shown in Fig 6.8(b). This could happen as a result of fluid/particle heat transfer dominating fluid/solid matrix heat transfer.

As shown in Fig. 6.9(a), Ra_c rises as γ_s rises from 0.01 to 0.03; additionally, Ra_c rises uniformly as N_{HP} rises. In contrast, as shown in Fig. 6.10(a), Ra_c decreases as N_{HS} increases, but increases when γ_s decreases. As a result, γ_s stabilises the flow for all values of N_{HP} and N_{HS}. Furthermore, as γ_s and N_{HP} increase, so does α_c, as shown in Fig. 6.9(b). Also, as γ_s rises, α_c decreases, whereas as N_{HS} rises, α_c first falls in the intermediate values of N_{HS} before rising, as shown in 6.10(b).

6.5.5 Effect on the modified thermal diffusivity ratios:

Figs. 6.11 - 6.14 shows the variation of critical Rayleigh number (Ra_c) and critical wave number (α_c) with inter-phase heat transfer parameters N_{HP} and N_{HS} for different values of the modified thermal diffusivity ratios ϵ_p and ϵ_s by fixing the other parameters values. As displayed in Fig. 6.11(a), Ra_c decreases as ϵ_p rises from 0.7 to 0.9, and Ra_c increases uniformly as N_{HP} increase. In contrast, as shown in Fig. 6.12(a), Ra_c falls as N_{HS} increase, whereas Ra_c does not change as ϵ_p grows. As a result, for all values of N_{HP} and N_{HS}, ϵ_p destabilizes the flow. As illustrated in Fig. 6.11(b), as ϵ_p increases, α_c does not change, but as N_{HP} increases, α_c increases. Moreover, when N_{HS} rises, α_c first falls in the intermediate values of N_{HS} before rising, as shown in Fig. 6.12(b), whereas ϵ_p rises, α_c effects is nearly negligible. This could happen as a result of fluid/particle heat transfer taking precedence over fluid/solid matrix heat transfer.

As seen in Fig. 6.13(a), Ra_c does not change as ϵ_s rises from 0.1 to 0.3; additionally, Ra_c increases as N_{HP} rises. In contrast, as displayed in Fig. 6.14(a), Ra_c decreases as N_{HS} raises, but Ra_c remains unchanged as ϵ_s rises. As a result, ϵ_s destabilizes the flow for all values of N_{HP} and N_{HS} both. Additionally, as seen in Fig. 6.13(b), as ϵ_s and N_{HP} increases, α_c rises. Although N_{HS} rises, α_c first falls in the intermediate values of N_{HS} before rising, as seen in Fig. 6.14(b), but with N_{HS}, as ϵ_s rises, α_c decreases.

Table 6.1: "Least stable eigenvalue for different number of grid points with $Da = 0.5$, $Pr = 7$, $Ra = 10$, $Rn = 5$, $\epsilon = 0.6$, $N_A = 8$, $N_B = 0.02$, $Le = 100$, N_{HS}=200, N_{HP}=100, γ_p=0.08, γ_s=0.03, $\epsilon_p = 0.7$, $\epsilon_s = 0.2$, α= 1 and $\beta = 0$."

N	**Least stable eigenvalue**
40	3.435961960923 -0.224658384193i
45	3.435961961672 -0.224658362881i
50	3.435962593339 -0.224658392292i
55	3.435962132333 -0.224658589822i
60	3.435961982799 -0.224658381611i

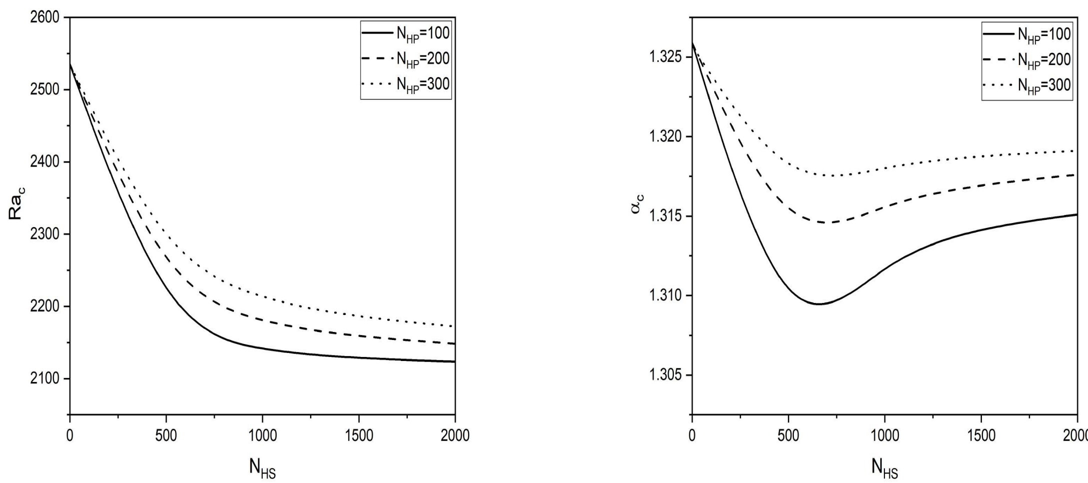

(a) (b)

Figure 6.1: "Variation of (a) critical Rayleigh number (Ra_c) and (b) critical wavenumber (α_c) with N_{HS} for different values of N_{HP} with $\gamma_p = 0.04$, $\gamma_s = 0.01$, $\epsilon_p = 0.7$, $\epsilon_s = 0.2$ and $\theta = \pi/3$."

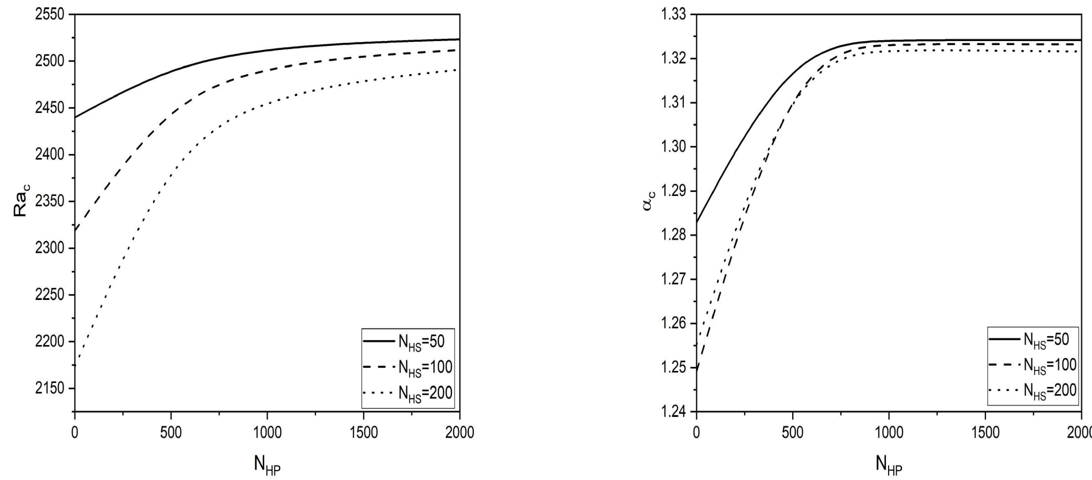

(a) (b)

Figure 6.2: "Variation of (a) critical Rayleigh number (Ra_c) and (b) critical wavenumber (α_c) with N_{HP} for different values of N_{HS} with $\gamma_p = 0.04$, $\gamma_s = 0.01$, $\epsilon_p = 0.7$, $\epsilon_s = 0.2$ and $\theta = \pi/3$. "

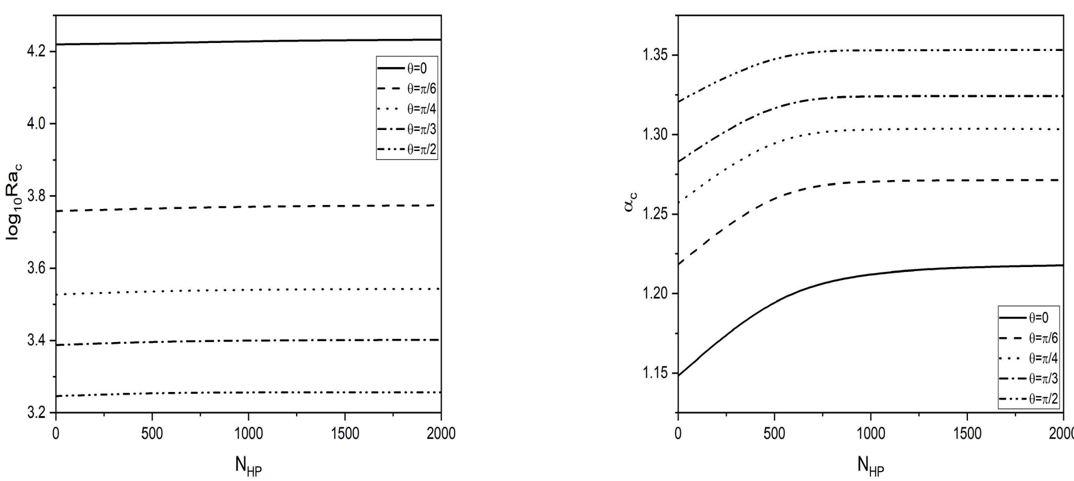

(a) (b)

Figure 6.3: "Variation of (a) critical Rayleigh number (Ra_c) and (b) critical wavenumber (α_c) with N_{HP} for different values of θ with N_{HS}=50, $\gamma_p = 0.04$, $\gamma_s = 0.01$, $\epsilon_p = 0.7$ and $\epsilon_s = 0.2$."

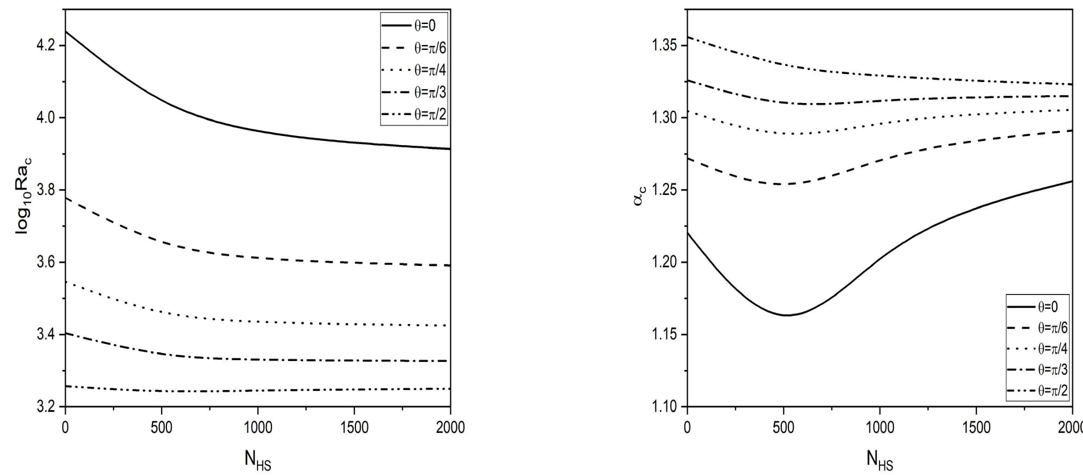

(a) (b)

Figure 6.4: "Variation of (a) critical Rayleigh number (Ra_c) and (b) critical wavenumber (α_c) with N_{HS} for different values of θ with N_{HP}=100, $\gamma_p = 0.04$, $\gamma_s = 0.01$, $\epsilon_p = 0.7$ and $\epsilon_s = 0.2$."

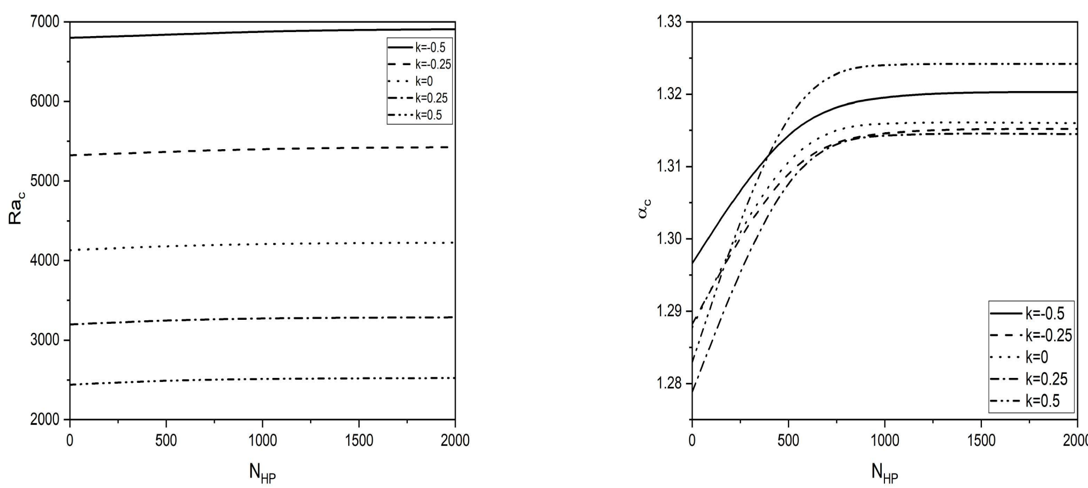

(a) (b)

Figure 6.5: "Variation of (a) critical Rayleigh number (Ra_c) and (b) critical wavenumber (α_c) with N_{HP} for different values of k with N_{HS}=50, $\gamma_p = 0.04$, $\gamma_s = 0.01$, $\epsilon_p = 0.7$ and $\epsilon_s = 0.2$."

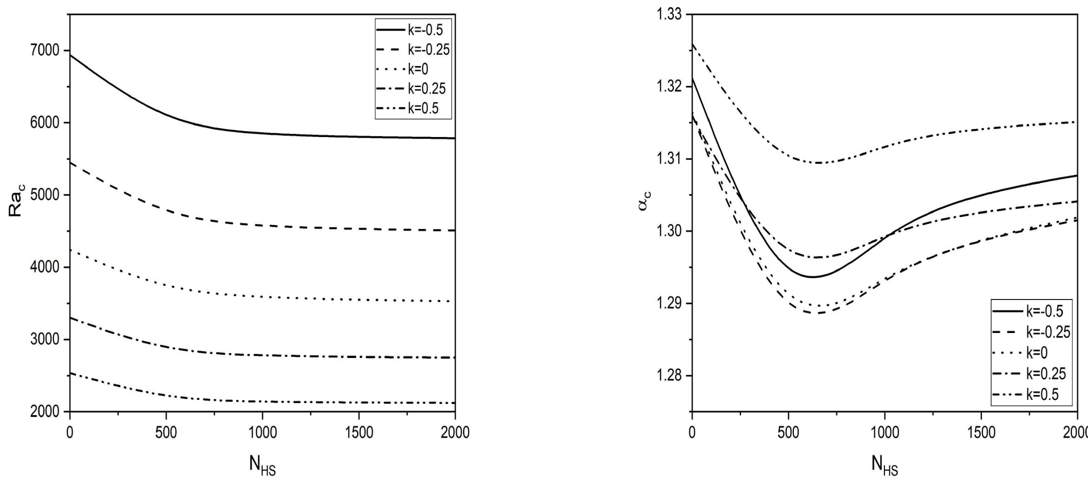

(a) (b)

Figure 6.6: "Variation of (a) critical Rayleigh number (Ra_c) and (b) critical wavenumber (α_c) with N_{HS} for different values of k with N_{HP}=100, $\gamma_p = 0.04$, $\gamma_s = 0.01$, $\epsilon_p = 0.7$ and $\epsilon_s = 0.2$."

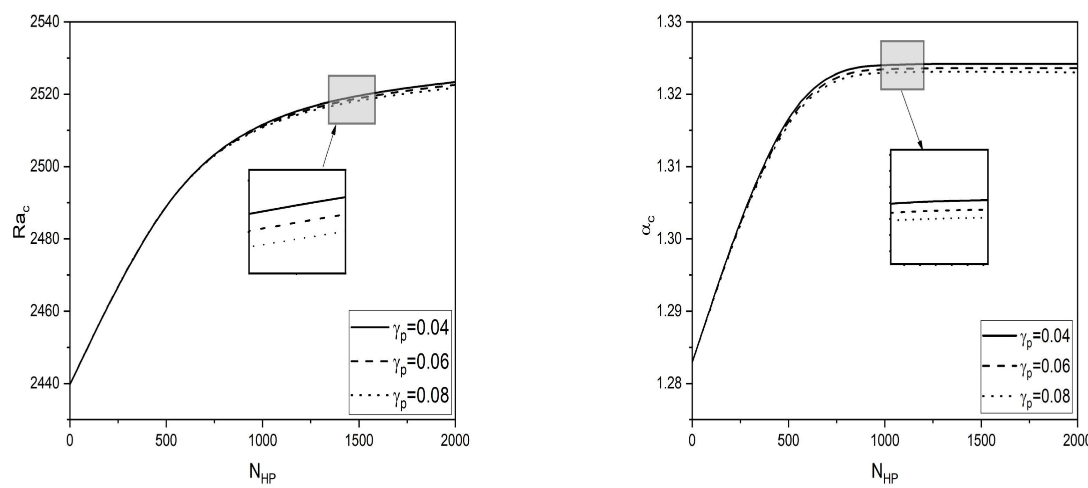

(a) (b)

Figure 6.7: "Variation of(a) critical Rayleigh number (Ra_c) and (b) critical wavenumber (α_c) with N_{HP} for different values of γ_p with N_{HS}=50, $\theta = \pi/3$, $\gamma_s = 0.01$, $\epsilon_p = 0.7$ and $\epsilon_s = 0.2$."

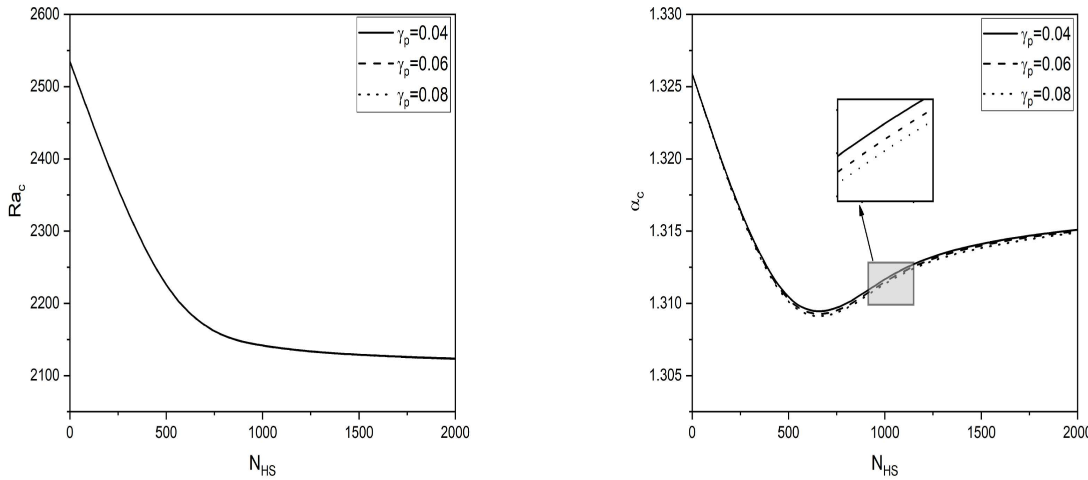

(a) (b)

Figure 6.8: "Variation of (a) critical Rayleigh number (Ra_c) and (b) critical wavenumber (α_c) with N_{HS} for different values of γ_p with N_{HP}=100, $\theta = \pi/3$, $\gamma_s = 0.01$, $\epsilon_p = 0.7$ and $\epsilon_s = 0.2$."

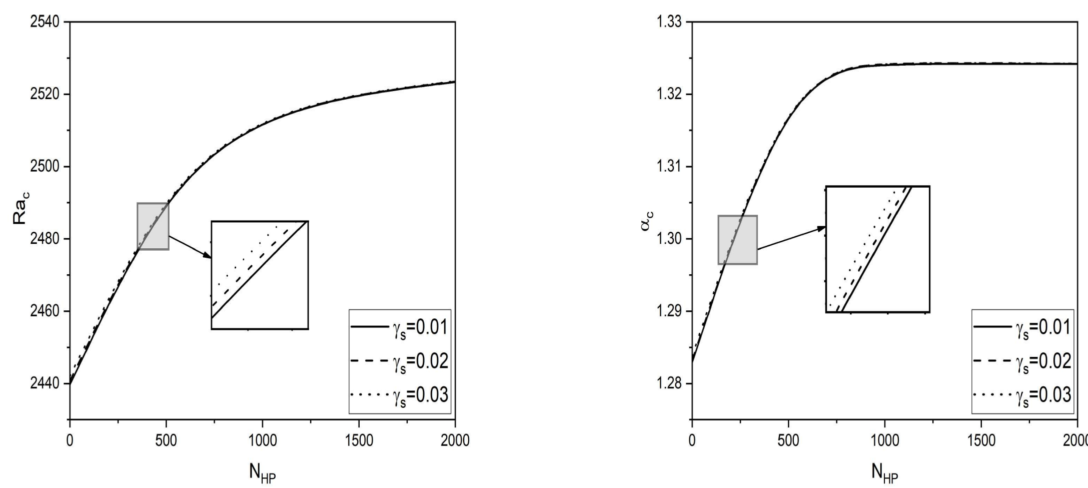

(a) (b)

Figure 6.9: "Variation of (a) critical Rayleigh number (Ra_c) and (b) critical wavenumber (α_c) with N_{HP} for different values of γ_s with N_{HS}=50, $\theta = \pi/3$, $\gamma_p = 0.04$ $\epsilon_p = 0.7$ and $\epsilon_s = 0.2$."

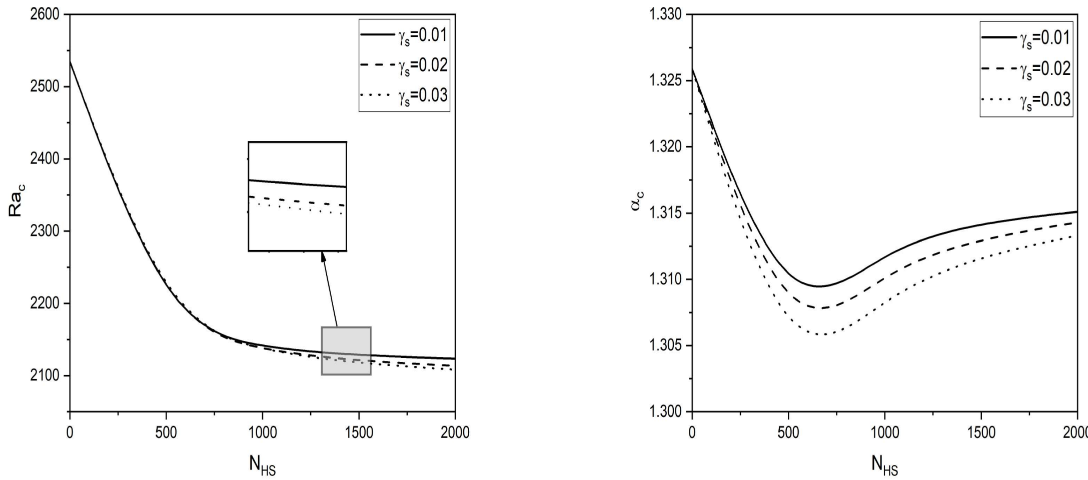

(a) (b)

Figure 6.10: "Variation of (a) critical Rayleigh number (Ra_c) and (b) critical wavenumber (α_c) with N_{HS} for different values of γ_s with N_{HP}=100, $\theta = \pi/3$, $\gamma_p = 0.04$ $\epsilon_p = 0.7$ and $\epsilon_s = 0.2$."

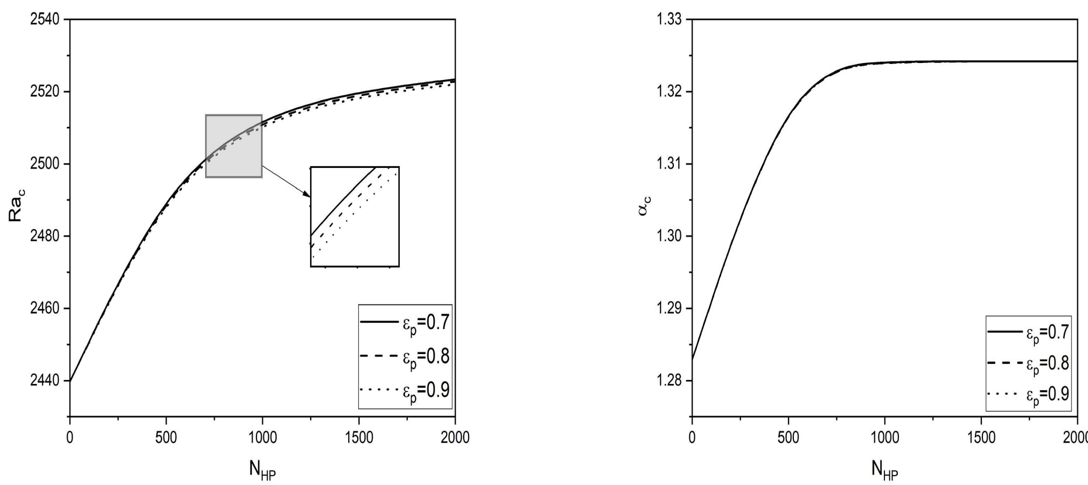

(a) (b)

Figure 6.11: "Variation of (a) critical Rayleigh number (Ra_c) and (b) critical wavenumber (α_c) with N_{HP} for different values of ϵ_p with N_{HS}=50, $\theta = \pi/3$, $\gamma_s = 0.01$, $\gamma_p = 0.04$ and $\epsilon_s = 0.2$."

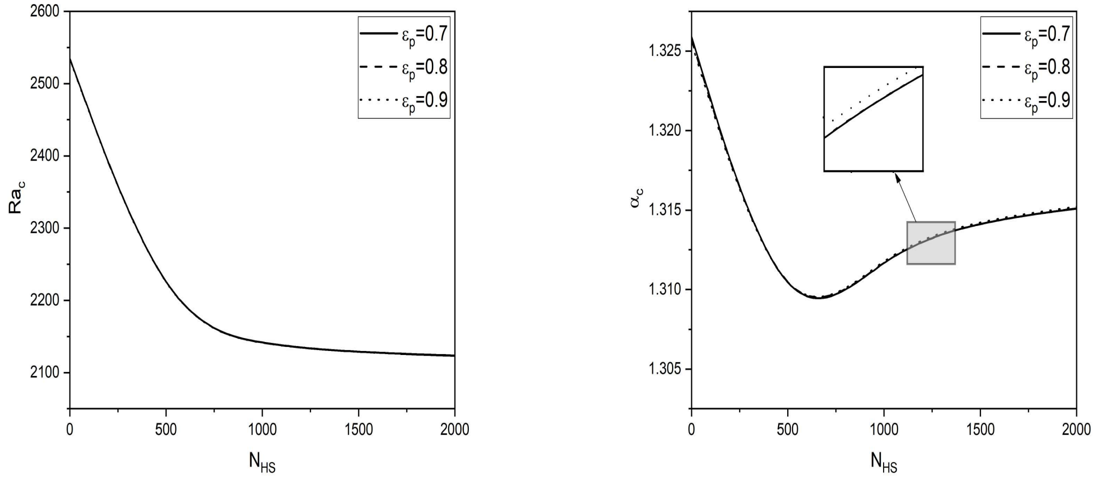

(a) (b)

Figure 6.12: "Variation of (a) critical Rayleigh number (Ra_c) and (b) critical wavenumber (α_c) with N_{HS} for different values of ϵ_p with N_{HP}=100, $\theta = \pi/3$, $\gamma_s = 0.01$, $\gamma_p = 0.04$ and $\epsilon_s = 0.2$."

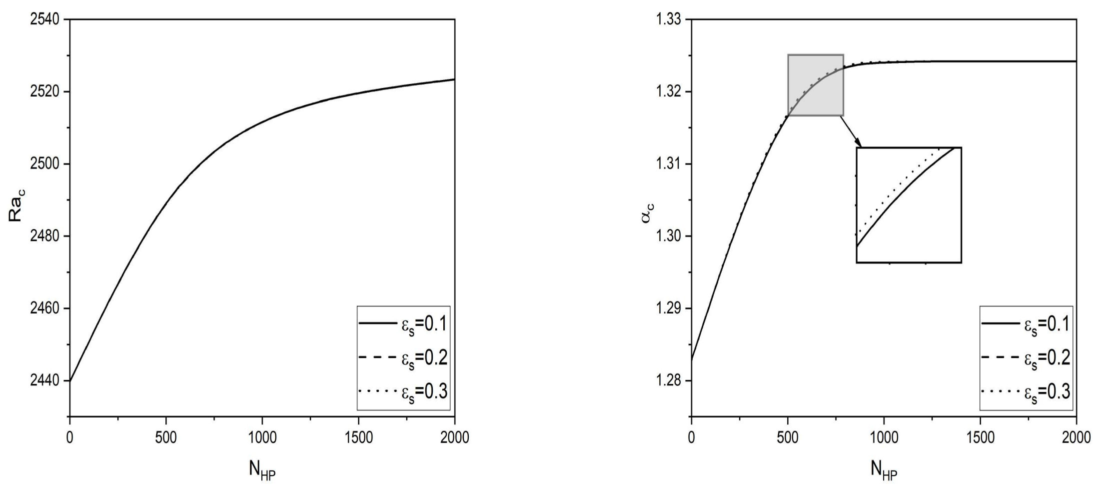

(a) (b)

Figure 6.13: "Variation of (a) critical Rayleigh number (Ra_c) and (b) critical wavenumber (α_c) with N_{HP} for different values of ϵ_s with N_{HS}=50, $\theta = \pi/3$, $\gamma_p = 0.04$ $\gamma_s = 0.01$, and $\epsilon_p = 0.7$."

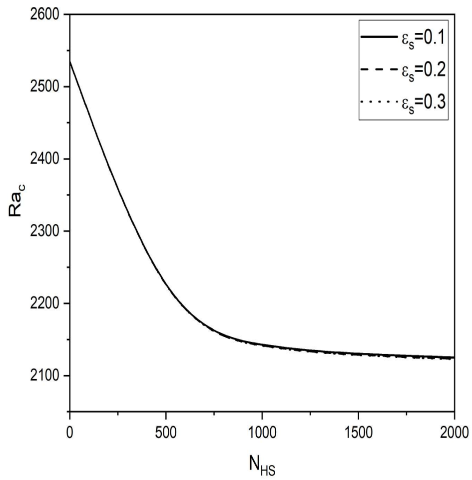

(a)

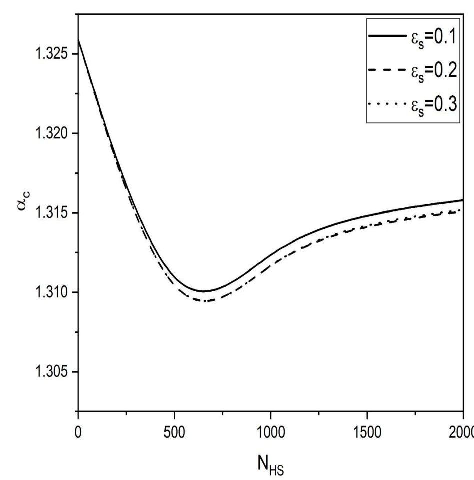

(b)

Figure 6.14: "Variation of (a) critical Rayleigh number (Ra_c) and (b) critical wavenumber (α_c) with N_{HS} for different values of ϵ_s with N_{HP}=100, $\theta = \pi/3$, $\gamma_p = 0.04$ $\gamma_s = 0.01$, and $\epsilon_p = 0.7$."

6.6 Conclusions

The effect of local thermal non-equilibrium (LTNE) on nanofluid flow onset convection in an inclined porous-medium channel with variable viscosity is studied. For the energy equation, Darcy-Brinkman model was used for porous medium, and the three medium temperature treatments have been used. The influence of LTNE parameters on the critical Rayleigh number and critical wavenumber is the only focus of this research with inclination $\theta = \pi/3$. For different values of the LTNE parameters, the results are graphically shown.

- When the destabilizing and stabilizing characteristics of N_{HP} and N_{HS} converge to zero and beyond sufficiently large values, the system acts as if it were in an LTE state.
- When N_{HP} increases, critical Rayleigh number (Ra_c) increases, and as N_{HS} increases, Ra_c falls. As a result, for all values of N_{HP} stabilizes the flow whereas for all values of N_{HS} destabilizes the flow field.
- When we raise N_{HP}, there is no change in critical Rayleigh number (Ra_c) for all values of inclination angle (θ), and variable viscosity parameter (k).
- γ_s stabilizes the flow for all values of N_{HP}.
- For all values of N_{HS}, γ_p, γ_s and ϵ_p and ϵ_s destabilize the flow.
- When we raise N_{HS}, critical wavenumber first decreases up to specific values of N_{HS} before quickly increasing in the intermediate levels. This is may be happen due to the domination of heat transfer of fluid/solid-matrix by fluid/particle.

Chapter 7

Influence of variable viscosity and double diffusion on the convective stability of a nanofluid flow in an inclined porous channel [1]

7.1 Introduction

The combined influence of variable viscosity and double diffusion has seral applications in science and engineering. Several researchers have considered the effects of variable viscosity and double diffusion seperately on the stability of the flow in a porous channel. After reviewing the relevant literature, it has been found that the stability analysis of a nanofluid in an inclined porous channel with double diffusive convection and changing viscosity has not been reported. This chapter investigates the simultaneous effects of variable viscosity and double diffusion on the convective stability of nanofluid flow in a porous inclined channel (at an angle of inclination θ).

[1]Published in "***Applied Mathematics and Mechanics (English Edition)*** 45(3), pp:563-580, DOI: https://doi.org/10.1007/s10483-024-3096-6"

7.2 Mathematical Formulation

Consider an unsteady, incompressible flow of a nanofluid in an inclined channel with a width of $2L$ and inclination θ, with impermeable and completely thermally conducting walls. Also, we have assumed that viscosity varies exponentially with temperature [110].

$$\mu(T) = \mu_l e^{-kT}$$

where μ_l is the viscosity at the reference temperature T_l.
Fig. 2.1 represent a schematic illustration of the problem. The porous medium is assumed to be homogenous and isotropic. The temperatures of the left and right walls are T_1 and T_2, respectively, nanoparticle volume fractions are ϕ_2 and ϕ_1, respectively. and the solute concentrations are C_1 and C_2 respectively.

Using the above assumptions and the Oberbeck-Boussinesq approximation, the following set of equations describes the flow [113, 50]:

$$\nabla \cdot \vec{V} = 0 \tag{7.1}$$

$$\begin{aligned} \frac{\rho_f}{\epsilon}\frac{\partial \vec{V}}{\partial t} + \frac{\rho_f}{\epsilon^2}(\vec{V}\cdot\nabla)\vec{V} = -\nabla p + \left[\nabla\mu\cdot\left(\nabla\vec{V} + \nabla\vec{V}^T\right) + \mu\Delta\vec{V}\right] - \frac{\mu}{K}\vec{V} \\ - \left\{(1 - \beta_T(T - T_1) \,-\, \beta_C(C - C_1))\,(1-\phi)\rho_f + \phi\rho_p\right\}\mathbf{g}(\sin(\theta)\hat{e_{\mathrm{x}}} + \cos(\theta)\hat{e_{\mathrm{y}}}) \end{aligned} \tag{7.2}$$

$$\begin{aligned} \frac{\partial T}{\partial t} + \vec{V}\cdot\nabla T = \alpha_m \nabla^2 T + \frac{\epsilon(\rho C)_p}{(\rho C)_f}\Big(\frac{D_T}{T_1}\nabla T\cdot\nabla T + D_B\nabla\phi\cdot\nabla T\Big) \\ + D_{TC}\nabla^2 C \end{aligned} \tag{7.3}$$

$$\frac{\partial \phi}{\partial t} + \frac{1}{\epsilon}\vec{V}\cdot\nabla\phi = \frac{D_T}{T_1}\nabla^2 T + D_B\nabla^2\phi \tag{7.4}$$

$$\frac{\partial C}{\partial t} + \frac{1}{\epsilon}\vec{V}\cdot\nabla C = D_S\nabla^2 C + D_{CT}\nabla^2 T \tag{7.5}$$

The non-dimensional form of the Eqs. (7.1) -(7.5) (on using Eq. (2.6) in Eqs. (7.1) -(7.5) and removing asterisk) are:

$$\nabla \cdot \vec{V} = 0 \tag{7.6}$$

$$\frac{1}{\mathrm{va}}\frac{\partial \vec{V}}{\partial t} + \frac{1}{\mathrm{va}\epsilon}(\vec{V}\cdot\nabla)\vec{V} = -\nabla p + Da\left[\nabla\mu\cdot\left(\nabla\vec{V} + \nabla\vec{V}^{T}\right) + \mu\Delta\vec{V}\right] - \mu\vec{V} + \left[RaT + \frac{Rs}{Ln}C - Rm - Rn\phi\right](\sin(\theta)\hat{e_{\mathrm{x}}} + \cos(\theta)\hat{e_{\mathrm{y}}}) \tag{7.7}$$

$$\frac{\partial T}{\partial t} + \vec{V}\cdot\nabla T = \nabla^2 T + \frac{1}{Le}\left(N_B\nabla\phi\cdot\nabla T + N_A N_B\nabla T\cdot\nabla T\right) + D_f\nabla^2 C \tag{7.8}$$

$$\frac{\partial \phi}{\partial t} + \frac{1}{\epsilon}\left(\vec{V}\cdot\nabla\phi\right) = \frac{N_A}{Le}\nabla^2 T + \frac{1}{Le}\nabla^2\phi \tag{7.9}$$

$$\frac{\partial C}{\partial t} + \frac{1}{\epsilon}\left(\vec{V}\cdot\nabla C\right) = \frac{1}{Ln}\nabla^2 C + Sr\nabla^2 T \tag{7.10}$$

The boundary conditions are:

$$\begin{aligned} y = -1: \quad \vec{V} = 0, \quad T = 0, \quad C = 0, \quad \phi = 1 \\ y = 1: \quad \vec{V} = 0, \quad T = 1, \quad C = 1, \quad \phi = 0 \end{aligned} \tag{7.11}$$

7.3 Basic solution

In the basic stage, the flow is regarded as continuous, one-directional (in the x-direction), and completely developed. Eqs. (7.6)-(7.10) may be reduced into set of ordinary differential equations by applying these conditions:

$$Da\left\{\frac{\partial}{\partial y}\left(\mu_0\frac{\partial U_b}{\partial y}\right)\right\} - \mu_0 U_b = \frac{dp_0}{dx} - \left(RaT_0 + \frac{Rs}{Ln}C_0 - Rn\phi_0 - Rm\right)\sin(\theta) \tag{7.12}$$

$$\frac{dp_0}{dy} = \left(RaT_0 + \frac{Rs}{Ln}C_0 - Rn\phi_0 - Rm\right)\cos(\theta) \tag{7.13}$$

$$\frac{dp_0}{dz} = 0 \tag{7.14}$$

$$\frac{d^2T_0}{dy^2} + \frac{N_B}{Le}\frac{d\phi_0}{dy}\frac{dT_0}{dy} + \frac{N_A N_B}{Le}\left(\frac{dT_0}{dy}\right)^2 + D_f\frac{d^2C_0}{dy^2} = 0 \tag{7.15}$$

$$\frac{d^2\phi_0}{dy^2} + N_A\frac{d^2T_0}{dy^2} = 0 \tag{7.16}$$

$$\frac{1}{Ln}\frac{d^2C_0}{dy^2} + Sr\frac{d^2T_0}{dy^2} = 0 \tag{7.17}$$

The boundary conditions are:

$$\begin{aligned} y = -1: &\quad U_b = 0, \quad T_0 = 0, \quad C_0 = 0, \quad \phi_0 = 1 \\ y = 1: &\quad U_b = 0, \quad T_0 = 1, \quad C_0 = 1, \quad \phi_0 = 0 \end{aligned} \tag{7.18}$$

Proceeding as in Chapter-2, and taking the approximation $\mu(T_0) = e^{-kT_0}$ [106], we get basic solution as:

$$T_0 = \frac{1+y}{2}, \quad \phi_0 = \frac{1-y}{2}, \quad \text{and} \quad C_0 = \frac{1+y}{2}. \tag{7.19}$$

$$\begin{aligned} U_b = \frac{1}{8}e^{(y+1)\frac{k}{4}}\Big\{&\text{sech}(m)\text{csch}(m)\Big(\sinh((1-y)m)\big(4\sigma + (2-Dak)\big(Ra + \frac{Rs}{Ln} + Rn\big)\big) \\ &\sin(\theta) + e^{k/2}\sinh((1+y)m)(4\sigma - (2+Dak)\big(Ra + \frac{Rs}{Ln} + Rn\big))\sin(\theta) \\ &+ \sin(\theta)e^{\frac{k}{4}(y+1)}\sinh(2m)\big(Ra + \frac{Rs}{Ln} + Rn\big)(Dak + 2y)\Big) - 8\sigma e^{\frac{k}{4}(y+1)}\Big\} \end{aligned} \tag{7.20}$$

where:

$$\begin{aligned} \sigma = \Bigg\{ &\sinh^2(m)\Big\{2e^{k/2}\sin(\theta)\Big(Ra + \frac{Rs}{Ln} + Rn\Big)\Big(4Dak^3m\text{csch}^2(m) + \sinh\left(\frac{k}{2}\right) \\ &\Big(\coth(m)\Big(16m^2\Big(Dak^2 - 4\Big) + k^2\Big(Dak^2 + 4\Big) - 8k^2m\coth(m)\Big) - 8k^2m\Big) \\ &+ \cosh\left(\frac{k}{2}\right)\Big(2k\coth(m)\Big(-2Dak^2m\coth(m) + k^2 + 16m^2\Big) \\ &-4Dak^3m\Big)\Big) + 4k^4\coth(m) - 64k^2m^2\coth(m)\Big\}\Bigg\} \Bigg/ \\ &\Big\{2k\Big(\big(e^k - 1\big)\big(k^2 + 16m^2\big)\sinh(2m) + 16e^{k/2}km - 8\big(e^k + 1\big)km\cosh(2m)\Big)\Big\} \end{aligned}$$

and

$$m = \frac{\sqrt{k^2 + \frac{16}{Da}}}{4}$$

7.4 Linear stability analysis

As in Chapter - 2, by imposing infinitesimal disturbances (δ) on the basic state solutions, ignoring δ^2 and higher order terms, using the usual normal mode form [50] to express infinitesimal disturbances of corresponding field variables, and removing pressure terms from the resulting equations, the linearized stability equations are obtained as:

$$
\begin{aligned}
Da\Big[\mu_0\frac{d^4\hat{v}}{dy^4}+2\frac{d\mu_0}{dy}\frac{d^3\hat{v}}{dy^3}-\frac{d^2\hat{v}}{dy^2}\Big(2\mu_0(\alpha^2+\beta^2)-\frac{d^2\mu_0}{dy^2}\Big)-4(\alpha^2+\beta^2)\frac{d\hat{v}}{dy}\frac{d\mu_0}{dy}+(\alpha^2+\beta^2)\\
\Big(\mu_0(\alpha^2+\beta^2)+\frac{d^2\mu_0}{dy^2}\Big)\hat{v}\Big]-\frac{i\alpha}{\mathrm{va}}\Big(\frac{U_b}{\epsilon}-c\Big)\Big[\frac{d^2\hat{v}}{dy^2}-(\alpha^2+\beta^2)\hat{v}\Big]+\frac{i\alpha}{\epsilon\mathrm{va}}\frac{d^2U_b}{dy^2}\hat{v}\\
-\mu_0\Big[\frac{d^2\hat{v}}{dy^2}-(\alpha^2+\beta^2)\hat{v}\Big]-\frac{d\mu_0}{dy}\frac{d\hat{v}}{dy}-Dae^{-kT_0}k\Big[\frac{dU_b}{dy}\frac{d^2\hat{T}}{dy^2}+\Big(2\frac{d^2U_b}{dy^2}-k\frac{dU_b}{dy}\Big)\frac{d\hat{T}}{dy}\\
+\Big(\frac{d^3U_b}{dy^3}-k\frac{d^2U_b}{dy^2}+\frac{dU_b}{dy}\Big(\frac{k^2}{4}-i\alpha(\alpha^2+\beta^2)\Big)\Big)\hat{T}\Big]+ke^{-kT_0}\frac{dU_b}{dy}\hat{T}+ke^{-kT_0}\frac{d\hat{T}}{dy}U_b\\
-U_b\frac{k^2}{2}e^{-kT_0}\hat{T}-i\alpha Ra\frac{d\hat{T}}{dy}\sin(\theta)-(\alpha^2+\beta^2)Ra\cos(\theta)\hat{T}-i\alpha\frac{Rs}{Ln}\frac{d\hat{C}}{dy}\sin(\theta)\\
-(\alpha^2+\beta^2)\frac{Rs}{Ln}\cos(\theta)\hat{C}+i\alpha Rn\frac{d\hat{\phi}}{dy}\sin(\theta)-(\alpha^2+\beta^2)Rn\cos(\theta)\hat{\phi}=0
\end{aligned}
\tag{7.21}
$$

$$
\begin{aligned}
(-i\alpha c)\frac{1}{\mathrm{va}}\hat{\eta}+\frac{1}{\epsilon\mathrm{va}}\Big[\beta\hat{v}\frac{dU_b}{dy}+U_b\hat{\eta}i\alpha\Big]-Da\Big[\mu_0\frac{d^2\hat{\eta}}{dy^2}+\frac{d\mu_0}{dy}\frac{d\hat{\eta}}{dy}-\mu_0(\alpha^2+\beta^2)\hat{\eta}\Big]+Dake^{-kT_0}\beta\\
\Big[\frac{dU_b}{dy}\frac{d\hat{T}}{dy}-\frac{k}{2}\hat{T}+\frac{d^2U_b}{dy^2}\hat{T}\Big]+\mu_0\hat{\eta}-\beta U_bke^{-kT_0}\hat{T}-\beta Ra\hat{T}sin(\theta)\\
-\beta\frac{Rs}{Ln}\hat{C}sin(\theta)+\beta Rn\hat{\phi}sin(\theta)=0
\end{aligned}
\tag{7.22}
$$

$$
\begin{aligned}
\hat{v}\frac{dT_0}{dy}+i\alpha(U_b-c)\hat{T}-\left[\frac{d^2\hat{T}}{dy^2}-(\alpha^2+\beta^2)\hat{T}\right]-\frac{N_B}{Le}\left[\frac{d\phi_0}{dy}+2N_A\frac{dT_0}{dy}\right]\frac{d\hat{T}}{dy}-\frac{N_B}{Le}\frac{dT_0}{dy}\frac{d\hat{\phi}}{dy}\\
-D_f\left[\frac{d^2\hat{C}}{dy^2}-(\alpha^2+\beta^2)\hat{C}\right]=0
\end{aligned}
\tag{7.23}
$$

$$
\frac{1}{\epsilon}\frac{d\phi_0}{dy}\hat{v}+i\alpha\left(\frac{U_b}{\epsilon}-c\right)\hat{\phi}-\frac{1}{Le}\left[\frac{d^2\hat{\phi}}{dy^2}-(\alpha^2+\beta^2)\hat{\phi}\right]-\frac{N_A}{Le}\Big[\frac{d^2\hat{T}}{dy^2}-(\alpha^2+\beta^2)\hat{T}\Big]=0 \tag{7.24}
$$

$$\frac{1}{\epsilon}\frac{dC_0}{dy}\hat{v} + i\alpha\left(\frac{U_b}{\epsilon} - c\right)\hat{C} - \frac{1}{Ln}\left[\frac{d^2\hat{C}}{dy^2} - (\alpha^2+\beta^2)\hat{C}\right] - Sr\left[\frac{d^2\hat{T}}{dy^2} - (\alpha^2+\beta^2)\hat{T}\right] = 0 \quad (7.25)$$

According to Srivastava *et al.* [112] $\hat{\mu}(T_0) = \frac{d\mu_0}{dT_0}\hat{T}$ represents the perturbation viscosity.

7.5 Results and discussion

A generalized eigenvalue problem with c as the complex eigenvalue is transformed by the set of governing equations (7.21)-(7.25). Chebyshev spectral collocation was used to find a solution to the problem in MATLAB, as described by Canuto *et al.* [107]. The investigation of the convergent behavior of the Chebyshev spectral method was carried out by varying the number of collocation points (N), and the most unstable eigenvalues were determined. These eigenvalues are enumerated in Table 7.1 for data selected at random for various parameters. The eigenvalue with the most instability was accurate to six decimal places when $N \geq 50$. It held for greater values of N. Furthermore, a comparable pattern has been observed for other flow governing values for parameters. Consequently, $N = 50$ was used to execute the numerical analysis.

To validate the accuracy of the procedure, our code was compared to results published on nanofluid-saturated porous medium is contained in a vertical channel. The current analysis determined the critical Rayleigh number and critical wavenumber for vertical channel when $Pr = 7$, $Rn = 15$, $Ln = 100$, $\epsilon = 0.6$,$N_A = 8$, $N_B = 0.02$, $Sr = 0$, $D_f = 0$, $k = 0$ and $\theta = \pi/2$, which is in accordance with the findings of Srinivasacharya and Barman [50].

In this paper, we investigate the effects of double-diffusive convection with variable viscosity on the flow stability of nanofluids in a porous inclined channel. The influences of the inclination angle (θ), Darcy number (Da), thermo-solutal Lewis number (Ln), Dufour number (D_f), and Soret number (Sr) on the critical Rayleigh number (Ra_c) and critical wavenumber (α_c) is shown in Figs. 7.1-7.5. All instability boundaries were depicted on the horizontal axis using the variable viscosity parameter.

Fig. 7.1 depicts the graphs illustrating the critical Rayleigh number and the critical wavenumber vary with variations in variable viscosity parameter (k) for various inclination angles (θ). As θ shifts from horizontal to vertical, the logarithm of the critical Rayleigh number ($log_{10}Ra_c$) decreases. This shows that θ destabilises the flow. This is due to the fact that the gravitational force operating on the fluid when the channel is inclined induces a proportional force to act in the flow direction. This can result in the formation of nanofluid flow instabilities. Ra_c falls as k rises. However, As θ oriented vertically, critical wavenumber increases, and as the variable viscosity parameter enhances, α_c first decreases and then rises.

For the permeability parameter (Darcy number), the variation in the critical Rayleigh number and critical wavenumber as a function of variable viscosity parameter is displayed in Fig. 7.2. Ra_c rises as the Da increases, indicating that permeability stabilises the system. It is figured that the porous layer has lower fluid permeability at lower Darcy numbers. This results in a pronounced high resistance as the fluid flows through the porous medium. Hence, the flow activity of the porous region was hindered. It is worth noting that raising k decreases Ra_c. Consequently, the influence of k stabilizes the system. α_c first drops and then rises as k rises for fixed Darcy numbers. However, as the permeability increased, the critical wavenumber increased, and the rate of growth was slower when Da increased from 1 to 10 than when Da increases from 0.1 to 1.

For varying values of the thermo-solutal Lewis number (Ln), Fig. 7.3 shows the variation in critical Rayleigh number and critical wavenumber versus the variable viscosity parameter. With a rise in the values of Ln, the Ra_c increased slightly. As a result, Ln stabilizes the flow at high values of Ln. This is because, in an inclined channel, the buoyancy forces due to the density gradient and gravitational forces due to the inclination act in different directions. The thermo-solutal Lewis number affects the relative strength of these forces and thus influences the stability of the flow. When the thermo-solutal Lewis number is high, the thermal diffusivity is much larger than the solute diffusivity. This means that temperature gradients have a stronger effect on flow than solute gradients. As a result, the buoyancy forces owing to the density gradient dominate the gravitational forces due to the inclination, and the flow becomes more stable. However, as the k increased, Ra_c gradually decreased from a high to a low value. As Ln grows α_c drops, and as k grows (α_c) first drops until k=0.5 and then increases.

Fig. 7.4 represents the influence of the Soret number (Sr) on the critical Rayleigh number and critical wavenumber. As the value of Sr rises, so does the value of Ra_c. However, the rate of growth is extremely slow. Hence flow of nanofluid through an inclined channel, the flow field is stabilised by the high values of Soret number. This happens because when the Soret parameter is high, the more diffusive component will move towards the hot region, while the less diffusive component will move towards the cold region. This creates a stabilizing effect, as the less diffusive component will accumulate at the bottom of the channel and the more diffusive component will accumulate at the top. As a result, the concentration and temperature fields become more uniform, and the flow becomes more stable. And as the variable viscosity parameter increases, Ra_c drops. This is because the Soret effect raises the solute's density gradient, which causes a convective instability at constant temperature. As Sr increases, α_c drops, and the critical wavenumber first decreases until k=0.5, then increases.

The critical Rayleigh number and critical wavenumber patterns against the k for different values of the Dufour parameter (D_f) are shown in Fig. 7.5. The Dufour parameter is a measure of the strength of the thermal diffusion effect. As shown in Fig. 7.5, Ra_c increases with the Dufour parameter value at large values. It is concluded that the system is stabilized for large values using the Dufour parameter (D_f). This is due to when the Dufour parameter is large, the more thermally diffusive component will move towards the hot region, where as the less thermally diffusive component will move towards the cold region. This leads to a concentration gradient that is contrary to the temperature gradient created by gravity. Consequently, the concentration and temperature fields become more uniform, and the flow becomes more stable. With an increase in k, Ra_c decreased. In addition, as the Dufour parameter is increased, the α_c decreases. When the k is increased, α_c first decreases for small values of k and then increases.

Noting that clockwise-oriented streamlines correspond to positive contours and counter-clockwise -oriented streamlines correspond to negative contours is essential when analyzing flow patterns. When the channel is horizontal, as indicated by $\theta = 0$ in Fig. 7.6, we observe the formation of two Rayleigh-Bénard convection cells, which are vertical cell structures. Near the upper wall, there is a counterclockwise vortex formation, and near the lower wall, there is a clockwise vortex formation. These cells then extend vertically as the angle of inclination increases, eventually transforming into structure of horizontal cells when channel becomes completely vertical. In conclusion, as channel's inclination varies from horizontal to vertical, the streamlines reconfigure the flow pattern from a vertical structure to a horizontal structure. On the isotherms, positive contour are denoted by solid lines and negative contour are indicated by dashed lines. This pattern holds true for isotherms, isosolutes, and isoconcentrations alike.

Table 7.1: "Convergence of the least stable eigenvalue for $Da = 1$, k=0.5, $Pr = 0.1$, $Rn = 10$, Rs=200, $\epsilon = 0.2$, $N_A = 8$, $N_B = 0.02$, $Le = 500$, Ln=40, $Sr = 0.3$, D_f=0.04, $\theta = \pi/3$, and $\beta = 0$."

N	Ra_c	α_c
40	10.312514413924	0.857299560606
45	10.312541497271	0.857252942876
50	10.312536312725	0.857285309558
55	10.312534712527	0.857291388872
60	10.312533214115	0.857485534098

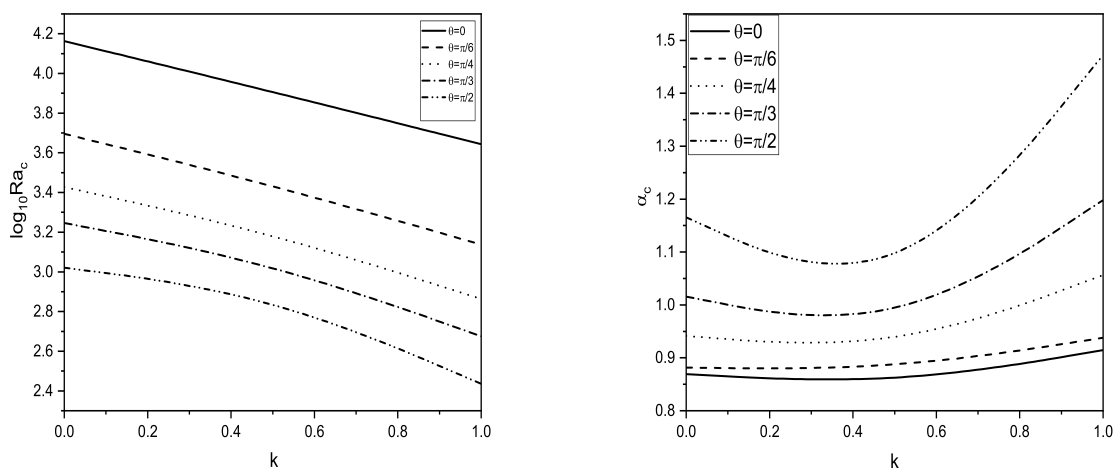

Figure 7.1: "Variation of critical Rayleigh number (Ra_c) and critical wavenumber (α_c) with k for different values of θ with Da=0.1, Rs=200, Ln=40, Sr=0.3 and $D_f = 0.04$."

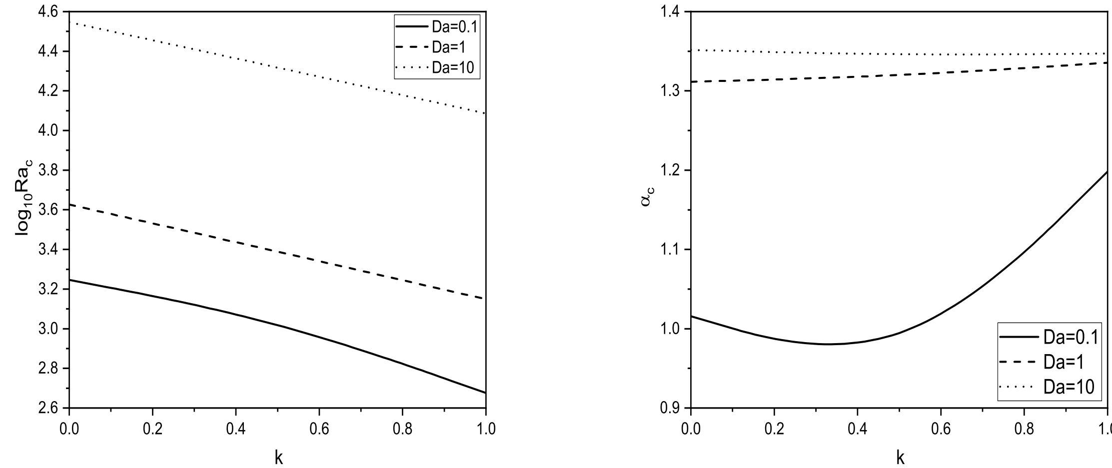

Figure 7.2: "Variation of critical Rayleigh number (Ra_c) and critical wavenumber (α_c) with k for different values of Da with $\theta = \pi/3$, Rs=200, Ln=40, Sr=0.3 and $D_f = 0.04$."

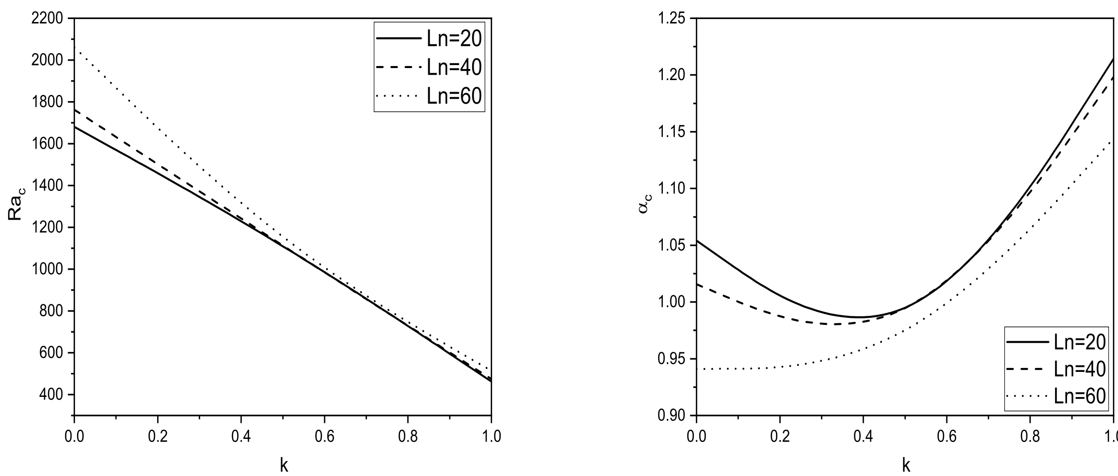

Figure 7.3: "Variation of critical Rayleigh number (Ra_c) and critical wavenumber (α_c) with k for different values of Ln with $\theta = \pi/3$, Rs=200,Da=0.1, $Sr = 0.3$ and $D_f = 0.04$."

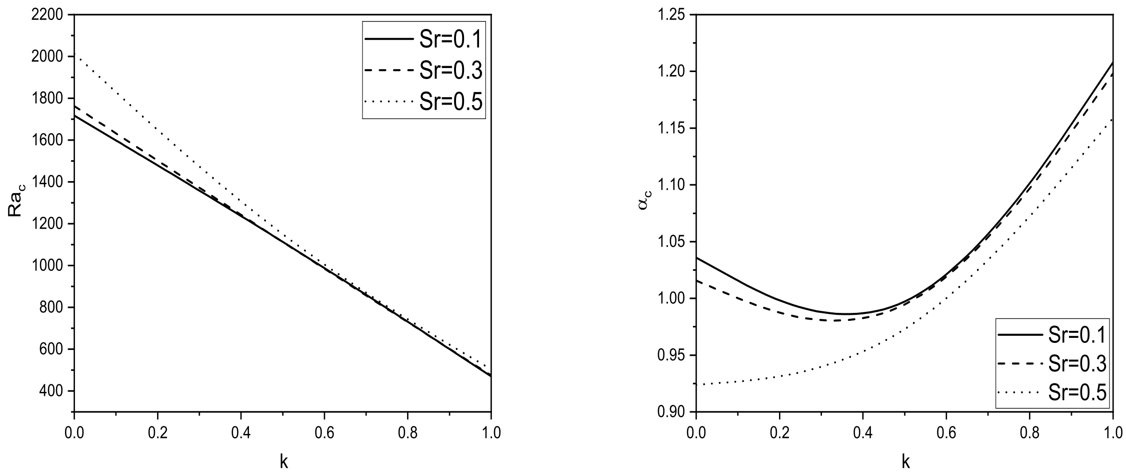

Figure 7.4: "Variation of critical Rayleigh number (Ra_c) and critical wavenumber (α_c) with k for different values of Sr with $\theta = \pi/3$, Ln=40, Da=0.1, $Rs = 200$ and $D_f = 0.04$."

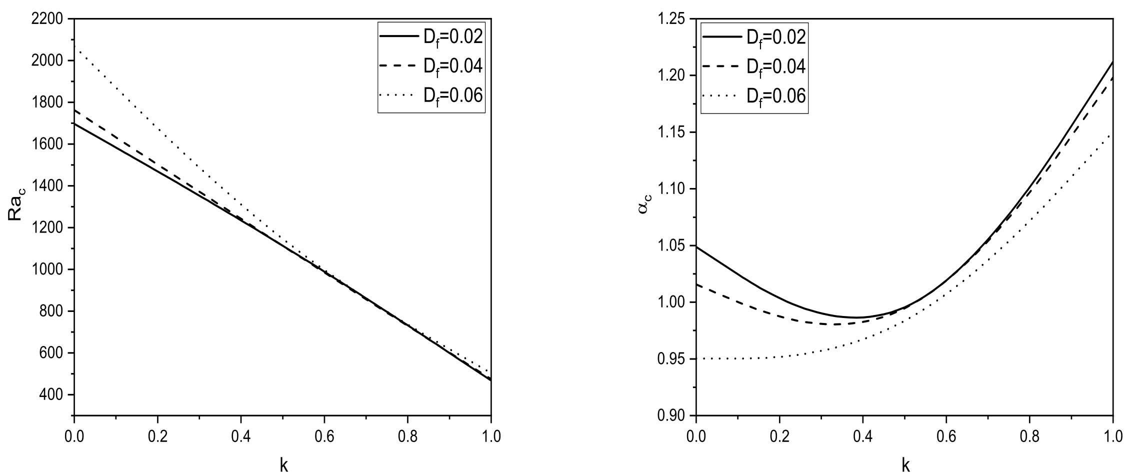

Figure 7.5: "Variation of critical Rayleigh number (Ra_c) and critical wavenumber (α_c) with k for different values of D_f with $\theta = \pi/3$, Ln=40, Da=0.1, $Rs = 200$ and $Sr = 0.3$. "

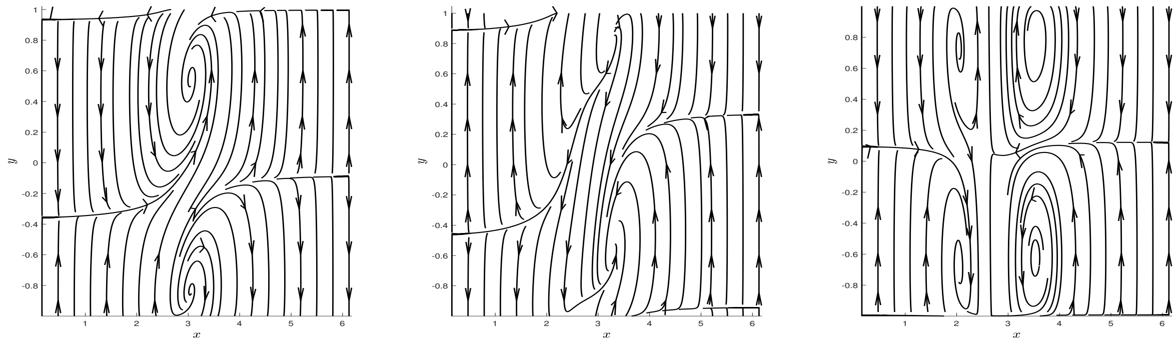

(a) “$\theta = 0$” (b) “$\theta = \pi/4$” (c) “$\theta = \pi/2$”

Figure 7.6: “The disturbance of streamlines for different values of θ.”

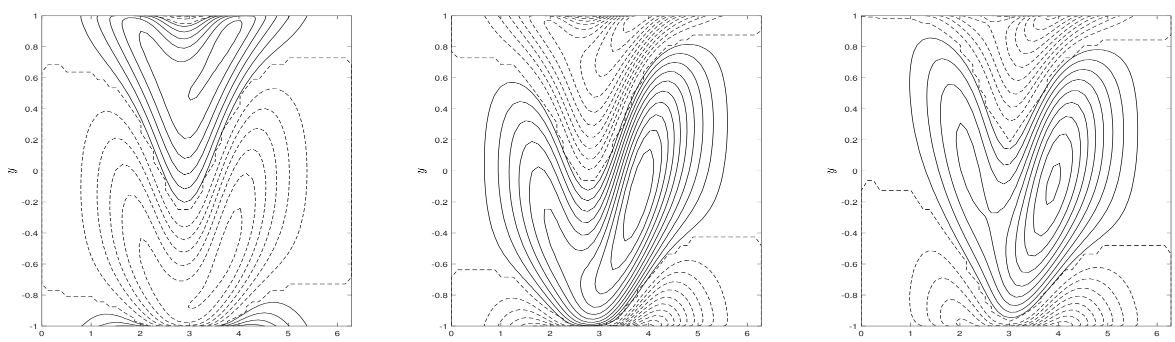

(a) “$\theta = 0$” (b) “$\theta = \pi/4$” (c) “$\theta = \pi/2$”

Figure 7.7: “The disturbance of isotherms for different values of θ.”

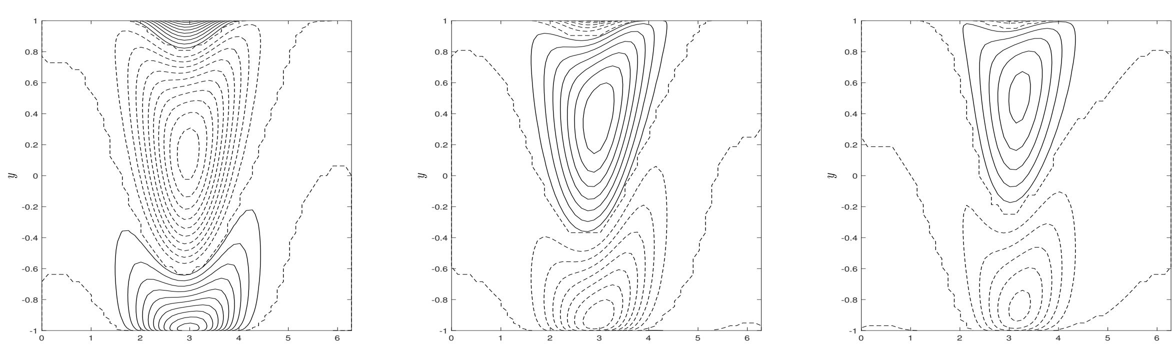

(a) “$\theta = 0$” (b) “$\theta = \pi/4$” (c) “$\theta = \pi/2$”

Figure 7.8: “The disturbance of isosolutes for different values of θ.”

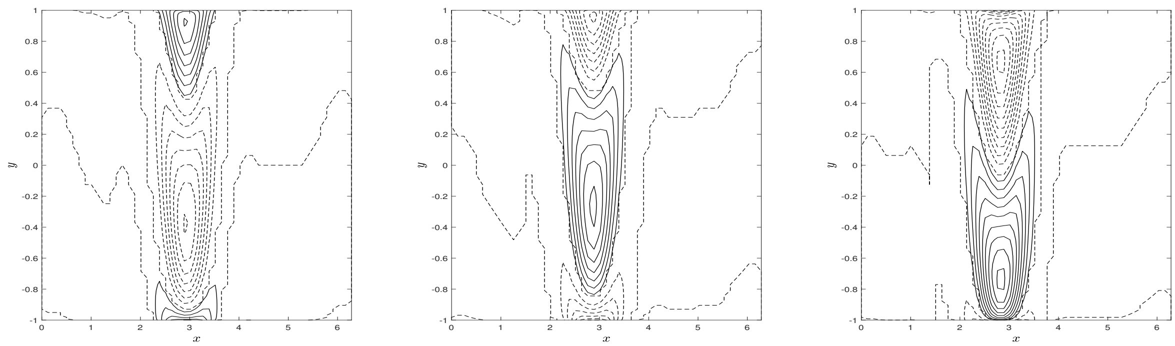

(a) “$\theta = 0$” (b) “$\theta = \pi/4$” (c) “$\theta = \pi/2$”

Figure 7.9: “The disturbance of isonanoconcentrations for different values of θ.”

7.6 Conclusions

The linear stability of nanofluid flow in a porous inclined channel while accounting for the effect of double-diffusive convection with variable viscosity is examined. The critical Rayleigh number and critical wavenumber for different parameters such as θ, Da, Sr, Ln, and D_f are computed and graphically shown with respect to k.

- A rise in the value of the variable viscosity parameter (k) emphasizes the stability of the fluid, as a result, the k stabilizes the flow field.
- permeability (Da), thermo-solutal Lewis number (Ln), Soret parameter (Sr) and Dufour parameter (D_f) help to stabilize flow within an inclined channel. As a result, an increase in these variables acts as a stumbling block to the onset of convection.

Part III

STABILITY OF CASSON FLUID FLOW IN AN INCLINED POROUS CHANNEL

Chapter 8

The heat source/sink effect on the stability of the Casson fluid flow in an inclined porous channel [1]

8.1 Introduction

In 1959, Casson [12] introduced Casson fluid, a non-Newtonian fluid characterized by shear-thinning and yield stress. This fluid is utilized in numerous industries, including food processing, cosmetics, and paint. It is utilized in medicine to simulate the behavior of biological fluids, particularly blood flow [14]. Mahanta *et al.* [67] investigated the effects of slip velocity on the MHD Casson flow at the point of stagnation using stability analysis across the stretching surface. Recently, in a rigid parallel channel with a homogeneous magnetic field, Kundenatti and Misbah [69] investigated the temporal stability of linear two-dimensional perturbations of plane Poiseuille flow of Casson fluid.

In industrial processes such as food and polymer processing, heat sources have a substantial effect on the Casson fluid dynamics by influencing temperature, velocity, and shear stress. Goud *et al.* [81] examined the implication of heat source on the motion of a Casson fluid through a fluctuating vertically permeable plate. Awais *et al.* [82] analysed the implications magnetic field on the flow of Casson fluid in a porous medium caused by a shrinking surface subjected to heat absorption/germination.

[1] Communicated in "***Fluid Dynamics***"

The stability properties of Casson fluid in an inclined porous channel with heat source or sink have not been explored, according to the literature review. Consequently, this Chapter investigates the effect of heat source or sink on convection stability in a Casson fluid flow in an inclined channel filled with a porous medium (at an angle of inclination θ).

8.2 Mathematical Formulation

Consider an unsteady, incompressible flow of a Casson fluid in a tilted channel with a width of $2L$ with two impermeable, completely thermally conducting walls and an inclination of θ. A schematic illustration of the problem is shown in Fig. 8.1. The presumption is the porous medium is homogenous and isotropic. Temperatures on both the lower and upper walls are maintained at T_1 and T_2, respectively. The presence of a heat source/sink is taken into account.

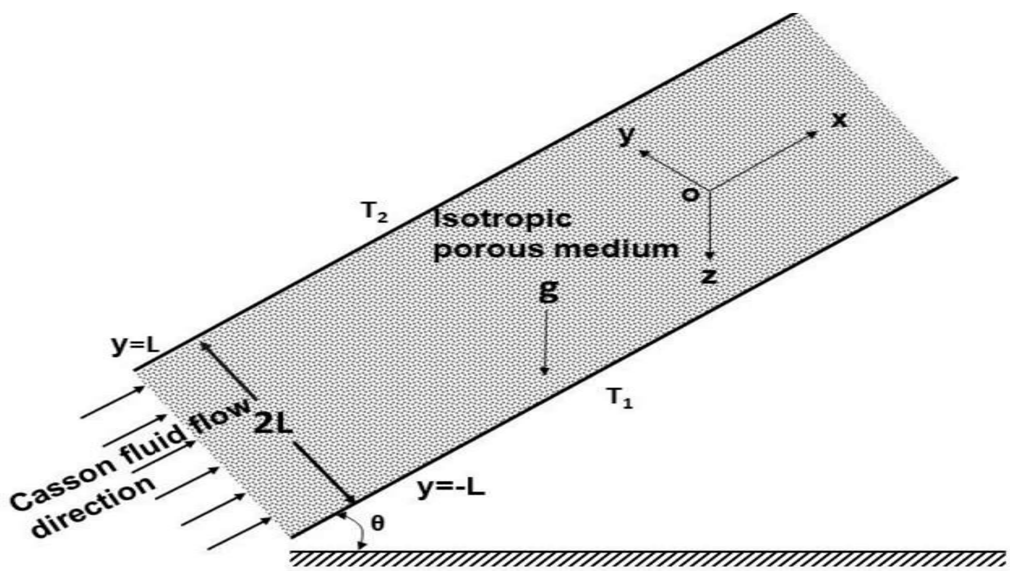

Figure 8.1: “Schematic representation of the problem.”

The dynamical equations for a Casson fluid with an isotropic rheology are as follows:

$$\tau_{ij} = \begin{cases} 2\Big(\mu_b + \frac{p_y}{\sqrt{2\pi}}\Big)e_{ij}, & \pi < \pi_c \\ 2\Big(\mu_b + \frac{p_y}{\sqrt{2\pi}}\Big)e_{ij}, & \pi > \pi_c \end{cases}$$

where μ_b is the dynamic plastic viscosity and π is square of deformation rate ($=e_{ab}e_{ab}$). Using the above assumptions and the Oberbeck-Boussinesq approximation, the following set of equations describes the flow [113, 50]:

$$\nabla \cdot \vec{V} = 0 \tag{8.1}$$

$$\frac{\rho}{\epsilon}\frac{\partial \vec{V}}{\partial t} + \frac{\rho}{\epsilon^2}(\vec{V}\cdot\nabla)\vec{V} = -\nabla p - \frac{\mu}{K}\vec{V} + \Big(1+\frac{1}{\gamma}\Big)\tilde{\mu}\nabla^2\vec{V} + \rho\mathbf{g}\beta_T(T-T_1)(\sin(\theta)\hat{e_{\text{x}}} + \cos(\theta)\hat{e_{\text{y}}}) \tag{8.2}$$

$$(\rho C)_p\left(\frac{\partial T}{\partial t} + \vec{V}\cdot\nabla T\right) = k\nabla^2 T + Q_0(T-T_1) \tag{8.3}$$

The conditions on the walls of the channel are:

$$y=-L: \quad \vec{V}=0, \quad T=T_1, \qquad y=L: \quad \vec{V}=0, \quad T=T_2 \tag{8.4}$$

where, γ is Casson parameter, and Q_0 is heat source/sink.
The non-dimensional form of the Eqs. (8.1) -(8.3) (on substituting (2.6) in (8.1) -(8.3) and removing asterisk) are:

$$\nabla \cdot \vec{V} = 0 \tag{8.5}$$

$$\frac{1}{\text{v}a}\frac{\partial \vec{V}}{\partial t} + \frac{1}{\epsilon \text{v}a}(\vec{V}\cdot\nabla)\vec{V} = -\nabla p - \vec{V} + \Lambda Da\Big(1+\frac{1}{\gamma}\Big)(\nabla^2\vec{V}) + RaT(\sin(\theta)\hat{e_{\text{x}}} + \cos(\theta)\hat{e_{\text{y}}}) \tag{8.6}$$

$$\frac{\partial T}{\partial t} + \vec{V}\cdot\nabla T = \nabla^2 T + QT \tag{8.7}$$

The boundary conditions are:

$$y=-1: \quad \vec{V}=0, \quad T=0, \qquad y=1: \quad \vec{V}=0, \quad T=1. \tag{8.8}$$

where Q is the heat source/sink parameter ($=\frac{Q_0 L^2}{k}$).

8.3 Basic solution

In the basic stage, the flow is regarded as continuous, one-directional (in the x-direction), and completely developed. Eqs. (8.5)-(8.7) may be reduced into set of ordinary differential equations by applying these conditions:

$$\Lambda Da\Big(1+\frac{1}{\gamma}\Big)\frac{d^2U_b}{dy^2}-U_b=\frac{\partial p_0}{\partial x}-RaT_0\sin(\theta) \tag{8.9}$$

$$\frac{\partial p_0}{\partial y}=RaT_0\cos(\theta) \tag{8.10}$$

$$\frac{\partial p_0}{dz}=0 \tag{8.11}$$

$$\frac{d^2T_0}{dy^2}+QT_0=0 \tag{8.12}$$

The boundary conditions are:

$$y=-1:\quad U_b=0,\quad T_0=0,\qquad y=1:\quad U_b=0,\quad T_0=1 \tag{8.13}$$

Proceeding as in Chapter-2, we get basic solution as:

$$T_0=\frac{1}{2}\Bigg(\frac{\cos(\sqrt{Q}y)}{\cos(\sqrt{Q})}+\frac{\sin(\sqrt{Q}y)}{\sin(\sqrt{Q})}\Bigg) \tag{8.14}$$

$$\begin{aligned}U_b=\sigma\left[\frac{\cosh(my)}{\cosh(m)}-1\right]+\Big(\frac{m^2}{Q+m^2}\Big)\frac{Ra}{2}\Bigg[\frac{\cosh(my)}{\cosh(m)}+\frac{\sinh(my)}{\sinh(m)}-\frac{\cos(\sqrt{Q}y)}{\cos(\sqrt{Q})}\\-\frac{\sin(\sqrt{Q}y)}{\sin(\sqrt{Q})}\Bigg]\sin(\theta)\end{aligned} \tag{8.15}$$

where:

$$\sigma=\frac{m\cosh(m)}{\sinh(m)-m\cosh(m)}\left[1+\Big(\frac{m^2}{Q+m^2}\Big)\times\frac{Ra}{2}\Bigg(\frac{\sinh(m)}{m\cosh(m)}-\frac{\sin(\sqrt{Q})}{\sqrt{Q}\cos(\sqrt{Q})}\Bigg)\right]\sin(\theta)$$

And

$$m=\frac{1}{\sqrt{\Lambda Da\Big(1+\frac{1}{\gamma}\Big)}}$$

8.4 Linear stability analysis

As in Chapter - 2, by imposing infinitesimal disturbances (δ) on the basic state solutions, ignoring δ^2 and higher order terms, using the usual normal mode form [50] to express infinitesimal disturbances of corresponding field variables, and removing pressure terms from the resulting equations, the linearized stability equations are obtained as:

$$\begin{aligned} \Lambda Da\Big(1+\frac{1}{\gamma}\Big)\left[\frac{d^4\hat{v}}{dy^4}-2\frac{d^2\hat{v}}{dy^2}(\alpha^2+\beta^2)+(\alpha^2+\beta^2)^2\hat{v}\right]-\frac{i\alpha}{\text{va}}\left(\frac{U_b}{\epsilon}-c\right)\left[\frac{d^2\hat{v}}{dy^2}\right. \\ \left.-(\alpha^2+\beta^2)\hat{v}\right]+\frac{i\alpha}{\epsilon\text{va}}\frac{d^2U_b}{dy^2}\hat{v}-\left[\frac{d^2\hat{v}}{dy^2}-(\alpha^2+\beta^2)\hat{v}\right]-i\alpha Ra\frac{d\hat{T}}{dy}\sin(\theta) \\ -(\alpha^2+\beta^2)Ra\cos(\theta)\hat{T}=0 \end{aligned} \tag{8.16}$$

$$\begin{aligned} (-i\alpha c)\frac{1}{\text{va}}\hat{\eta}+\frac{1}{\epsilon va}\left[\beta\hat{v}\frac{dU_b}{dy}+U_b\hat{\eta}i\alpha\right]-\Lambda Da\Big(1+\frac{1}{\gamma}\Big)\left[\frac{d^2\hat{\eta}}{dy^2}-(\alpha^2+\beta^2)\hat{\eta}\right]+\hat{\eta} \\ -\beta Ra\hat{T}\sin(\theta)=0 \end{aligned} \tag{8.17}$$

$$\frac{dT_0}{dy}\hat{v}+i\alpha\left(U_b-c\right)\hat{T}-Q\hat{T}-\left[\frac{d^2\hat{T}}{dy^2}-(\alpha^2+\beta^2)\hat{T}\right]=0 \tag{8.18}$$

8.5 Results and discussion

The equations from Eqs. (8.16) - (8.18) represent a generalized eigenvalue problem in which the eigenvalues are perturbed and expressed in terms of the wave speed. The spectral technique [107] is employed to find the solution to this eigenvalue problem.

In order to validate the accuracy of this method, we ran the MATLAB code for calculating eigenvalues with varying grid point numbers (N) and obtained least stable eigenvalues, which are presented in Table 8.1 for an arbitrary combination of parameters. When $N \geq 50$, the least stable eigenvalue reached convergence criterion of 10^{-7}, and these results remained constant despite varying parameter values. In our numerical calculations, we chose to use $N = 50$ as a result.

The results of $\theta = \pi/2$, $\gamma \to \infty$, $Pr = 7$, Q=0, and $N = 51$ in absence of Rn, Le, N_A, N_B, and ϕ_0 were obtained, which is in accordance with the findings of Srinivasacharya and Barman [50].

The influence of iinclination angle (θ), Casson parameter (γ), heat source/sink parameter (Q), Prandtl number (Pr) , and porosity parameter (ϵ) on the flow instability is studied in-depth in this paper. The remaining values of parameters are set as Ra = 100, Λ=1, α= 1 and $\beta = 0$.

Fig. 8.2 depicts the graphs illustrating critical Rayleigh number and critical wavenumber vary with variations in the Darcy number (Da) for various inclination angles (θ). When the angle θ varies from horizontal to vertical, critical Rayleigh number (Ra_c) demonstrates a decreasing trend. This phenomenon indicates that a change in the angle of inclination θ destabilizes the flow. This is due to the fact that gravitational force operating on the fluid when the channel is inclined induces a proportional force to act in the flow direction. This additional force component can contribute to the formation of instabilities in the Casson fluid flow. However, there is no change in α_c for an increase in Da, and only a small change for $\theta = 0$.

Fig. 8.3 depicts the fluctuation of the Ra_c and α_c for various values of the Casson parameter (γ). We observed that while Da rises, Ra_c rises as well, but as γ increases, Ra_c decreases. Hence, γ destabilises the flow because it determines the yield stress of the fluid. If the Casson parameter is too low, the yield stress of the fluid may not be high enough to support the weight of the fluid in the inclined channel, which can lead to flow instability. On the other hand, if the Casson parameter is too high, the yield stress of the fluid may be too high, leading to laminar flow that is resistant to any instabilities. In the case of critical wavenumbers, however, there is no change in α_c as Da rises, but there is a slight change for γ=0.5. While γ increases, α_c decreases.

For different values of the heat source/sink parameter (Q), Fig. 8.4 displays the variation of Ra_c and α_c. We noticed that as Da increases, so does Ra_c. However, as Q increases, Ra_c falls significantly. Hence Q destabilizes the flow. This can occur when the temperature gradient in the fluid is such that the viscosity decreases with increasing temperature. In this situation, the fluid near the heat source or sink will have a lower viscosity and can flow more easily than the surrounding fluid, which can cause the flow to become unstable. However, as Da and Q both rise, α_c increases.

Fig. 8.5 depicts the fluctuation of Ra_c and α_c for Prandtl number (Pr). We found that Ra_c rises when Pr rises. It demonstrates Pr stabilizes the flow field by promoting a more uniform temperature and viscosity profile, reducing thermal gradients, and promoting the development of thermal boundary layers that can dampen out disturbances in the flow. Moreover, α_c does not change as Da grows, although it does slightly change for Pr=0.3. Also, as Pr rises, α_c falls.

Fig. 8.6 illustrates the boundaries of the instability region as a function of the permeability parameter (Da) and porosity parameter (ϵ). It is noted from Fig. 8.6 that, the critical Rayleigh number tends to rise as the porosity parameter is increased (Ra_c). This is due to porosity is proportion of the total amount of space occupied by voids throughout the volume, It constitutes the measurement of the voids in a porous material. Hence ϵ stabilizes the flow. The volume of voids increases as porosity increases. Observations indicate that α_c decreases as the porosity parameter value increases, whereas α_c increases as Da increases.

Fig. 8.7 and Fig. 8.8 shows streamlines, and isotherms, for various θ values when "Da=1, Q=2, $Pr = 0.3$, $Ra = 100$, $\epsilon = 0.6$, Λ=1, α= 1 and $\beta = 0$." Noting that clockwise-oriented streamlines correspond to positive contours and counterclockwise-oriented streamlines correspond to negative contours is essential when analyzing flow patterns. When the channel is horizontal, as indicated by $\theta = 0$ in Fig. 8.8, we observe the formation of two Rayleigh-Bénard convection cells, which are vertical cell structures. Near the upper wall, there is a counterclockwise vortex formation, and near the lower wall, there is a clockwise vortex formation. These cells then extend vertically as the angle of inclination increases, eventually transforming into structure of horizontal cells when channel becomes completely vertical. In conclusion, as channel's inclination varies from horizontal to vertical, the streamlines reconfigure the flow pattern from a vertical structure to a horizontal structure. On the isotherms, positive contour are denoted by solid lines and negative contour are indicated by dashed lines. This pattern holds true for isotherms alike.

Table 8.1: "Convergence analysis of the least stable eigenvalue for $Da = 10$, $Pr = 0.3$, Q=2, $\epsilon = 0.6$, γ=0.5, $\theta = \pi/3$, Λ=1, and $\beta = 0$."

N	Ra_c	α_c
40	4391.611472458690	1.388296360208
45	4391.611471169493	1.388296363276
50	4391.611473475915	1.388329869083
55	4391.611222675459	1.388296016235
60	4391.611516403603	1.388296246072

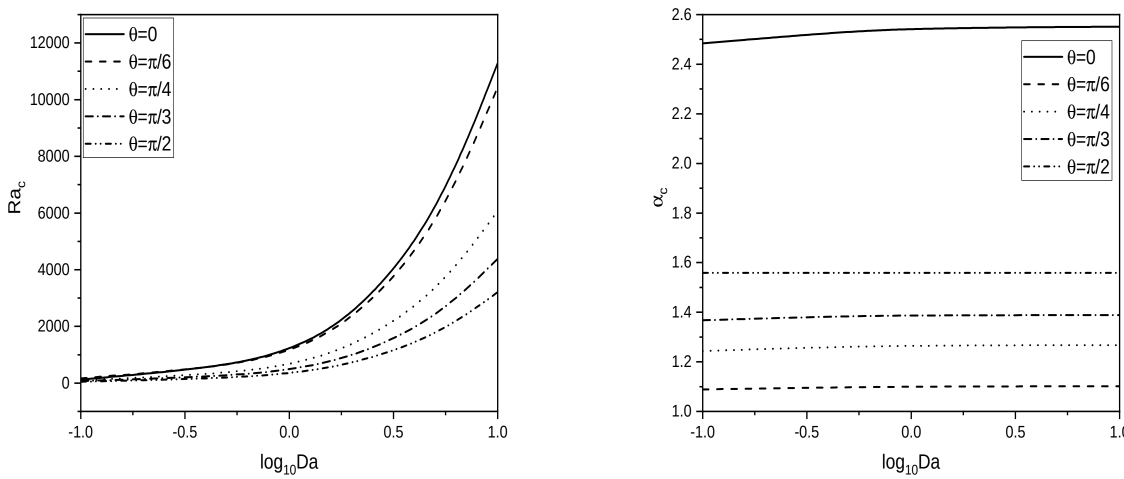

Figure 8.2: "Critical Rayleigh number (Ra_c) and critical wavenumber (α_c) variations with $log_{10}Da$ for different values of θ with Pr = 0.3, Q=2, ϵ = 0.6, γ=0.5, Λ=1, α= 1 and β = 0."

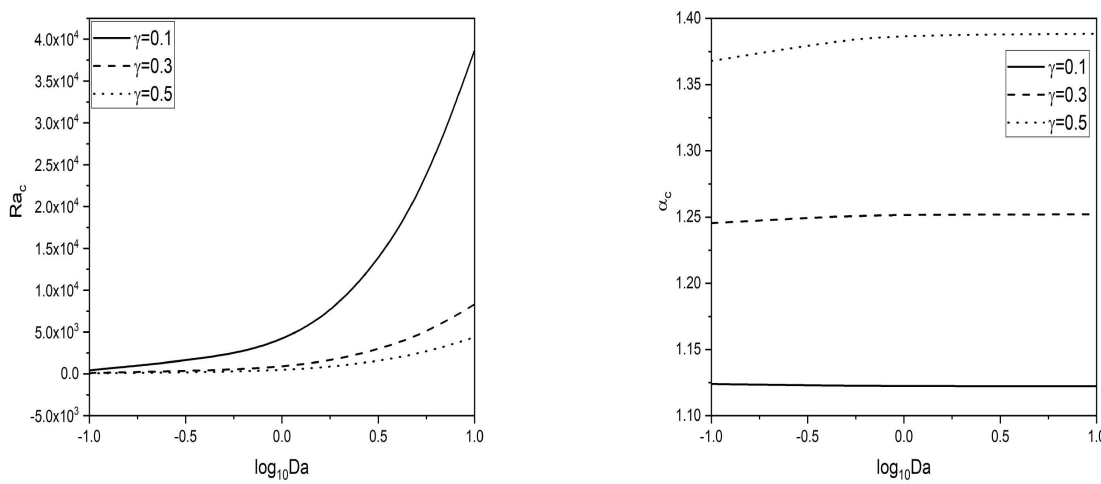

Figure 8.3: "Critical Rayleigh number (Ra_c) and critical wavenumber (α_c) variations with $log_{10}Da$ for different values of γ with Pr = 0.3, Q=2, ϵ = 0.6, θ=$\pi/3$, Λ=1, α= 1 and β = 0."

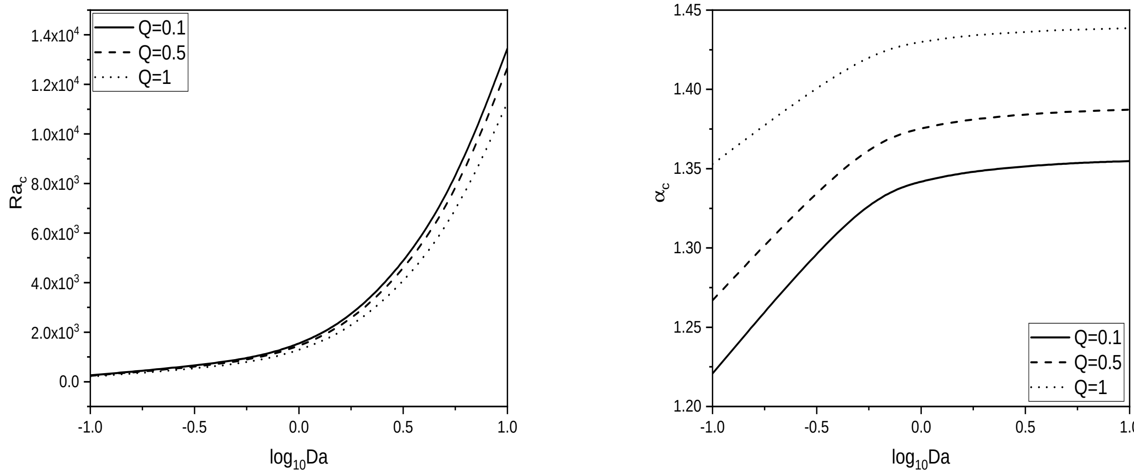

Figure 8.4: "Critical Rayleigh number (Ra_c) and critical wavenumber (α_c) variations with $log_{10}Da$ for different values of Q with Pr = 0.3, γ = 0.5, ϵ = 0.6, θ=$\pi/3$, Λ=1, α= 1 and β = 0."

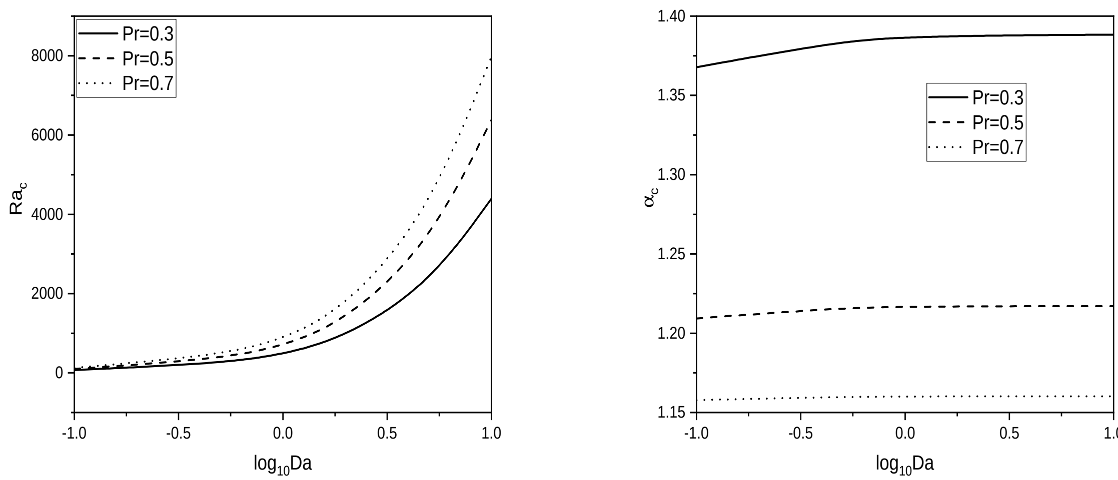

Figure 8.5: "Critical Rayleigh number (Ra_c) and critical wavenumber (α_c) variations with $log_{10}Da$ for different values of Pr with Q=2, ϵ = 0.6, γ = 0.5, θ=$\pi/3$, Λ=1, α= 1 and β = 0."

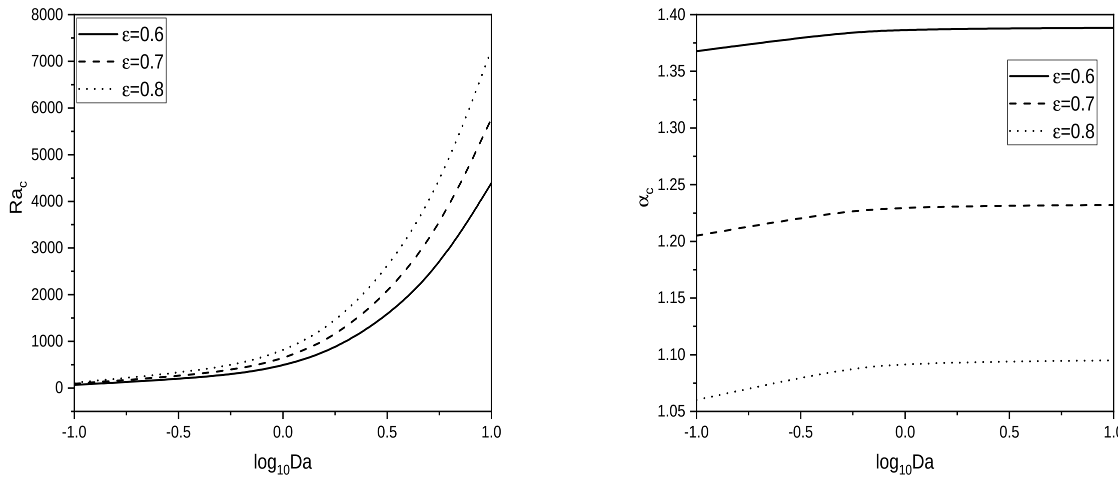

Figure 8.6: "Critical Rayleigh number (Ra_c) and critical wavenumber (α_c) variations with $log_{10}Da$ for different values of ϵ with Pr=0.3, Q=2, γ = 0.5, θ=$\pi/3$, Λ=1, α= 1 and β = 0."

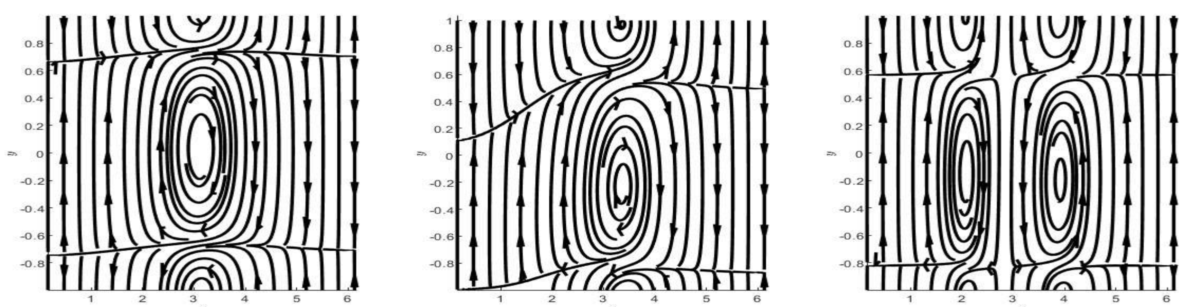

(a) "$\theta = 0$" (b) "$\theta = \pi/4$" (c) "$\theta = \pi/2$"

Figure 8.7: "The disturbance of streamlines for different values of θ."

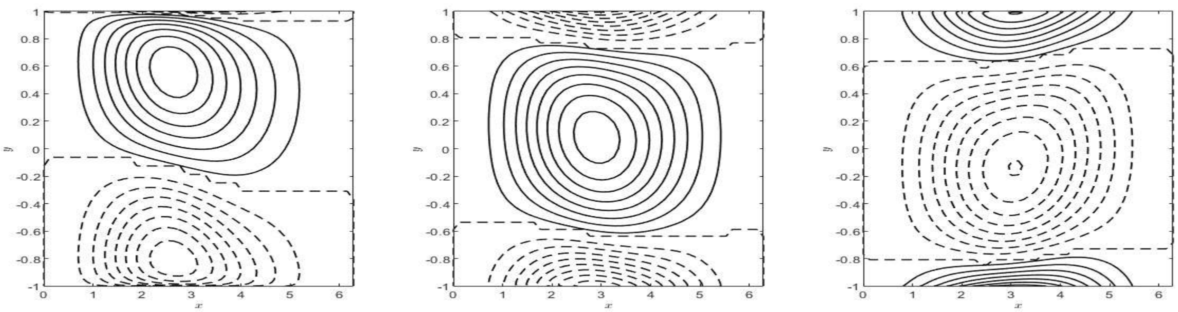

(a) "$\theta = 0$" (b) "$\theta = \pi/4$" (c) "$\theta = \pi/2$"

Figure 8.8: "The disturbance of isotherms for different values of θ."

8.6 Conclusions

The linear stability of Casson fluid flow in a porous inclined channel while accounting for the effect of heat source or sink is examined. The critical Rayleigh number and critical wavenumber for different parameters such as θ, ϵ, Pr, Q, and γ are computed and graphically shown with respect to Da.

- The channel's inclination (θ), heat source/sink parameter (Q) and Casson parameter (γ) destabilise the flow.
- The momentum equation is affected by viscous forces because flow resistance decreases with increasing permeability and improved flow in a porous media.
- Porosity (ϵ) and Prandtl number (Pr) help to stabilize flow within an inclined channel. As a result, an increase in these variables acts as a stumbling block to the onset of convection.
- When the channel is oriented vertically, the flow has the least stability.

Chapter 9

The impact of chemical reaction and radiation on the stability of the Casson fluid flow in an inclined porous channel [1]

9.1 Introduction

The behavior of Casson fluids is significantly impacted by radiation, which has biomedical and industrial implications. Linear stability analysis of thermally-radiated micropolar fluids in an MHD flow with convective boundary condition was investigated by Lund *et al.* [86]. Lund *et al.* [64] explored the stability of MHD stagnation point flow of Casson fluid over a contracting /expanding surface due to the influence of thermal radiation and viscous dissipation. Using the generalised Buongiorno's nanofluid model, Wakif *et al.* [87] examined effects of surface roughness and thermal radiation influence the thermo-magneto-hydrodynamic stability of nanofluids composed of alumina and copper oxide.

Chemical reactions influence the rheology, yield stress, and flow behavior of Casson fluids. Srivastava [90] investigated the electro-thermal convection stability of a binary fluid in a horizontal channel with chemical reaction. The effects of magnetic cross-field, thermal radiation, second order chemical reaction on the unsteady three dimensional flow of electrically conducting Cu–Al_2O_3/water hybrid nanofluid flow past a bidirectionally stretchable melting

[1] Communicated in "***Computational Mathematics and Mathematical Physics***"

surface was investigated by Suganya *et al.* [91].

The stability properties of Casson fluid in an inclined channel with radiation and chemical reactions have not been explored, according to the literature review. Consequently, this chapters investigates the effects of radiation and chemical reactions on convection stability in a Casson fluid flow in an inclined channel filled with a porous medium (at an angle of inclination θ).

9.2 Mathematical Formulation

Consider an unsteady, incompressible flow of a Casson fluid in a tilted channel with a width of $2L$ with two impermeable, completely thermally conducting walls and an inclination of θ. A schematic illustration of the problem is shown in Fig. 8.1. The porous medium is assumed to be homogenous and isotropic. The temperatures of the left and right walls are T_1 and T_2, respectively, and the concentrations are C_1 and C_2, respectively . The presence of a radiation and chemical reaction is taken into account.

By applying the Oberbeck-Boussinesq approximation and the aforementioned assumptions, the following set of equations describes the flow [113, 108]:

$$\nabla \cdot \vec{V} = 0 \tag{9.1}$$

$$\frac{\rho}{\epsilon}\frac{\partial \vec{V}}{\partial t} + \frac{\rho}{\epsilon^2}(\vec{V}\cdot\nabla)\vec{V} = -\nabla p + \left(1+\frac{1}{\gamma}\right)\tilde{\mu}\nabla^2\vec{V} - \frac{\mu}{K}\vec{V} + \rho\mathbf{g}\{\beta_T(T-T_1)+\beta_C(C-C_1)\} \tag{9.2}$$
$$(\sin(\theta)\hat{e_{\text{x}}} + \cos(\theta)\hat{e_{\text{y}}})$$

$$(\rho C)_p\left(\frac{\partial T}{\partial t} + \vec{V}\cdot\nabla T\right) = k\nabla^2 T - \nabla q_r \tag{9.3}$$

$$\frac{\partial C}{\partial t} + \vec{V}\cdot\nabla C = D\nabla^2 C - R^*(C-C_1) \tag{9.4}$$

The boundary conditions are:

$$\begin{aligned} &\text{At} \quad y=-L: \quad \vec{V}=0, \quad T=T_1, \quad C=C_1, \\ \text{and} \quad &\text{at} \quad y=L: \quad \vec{V}=0, \quad T=T_2, \quad C=C_2 \end{aligned} \tag{9.5}$$

where:

q_r is radiative heat flux, R^* is reaction rate of solute, D is mass diffusion coefficient.

The non-dimensional form of the Eqs. (9.1) -(9.4) (on substituting (2.6) in (9.1) -(9.4) and removing asterisk) are:

$$\nabla \cdot \vec{V} = 0 \tag{9.6}$$

$$\frac{1}{\text{v}a}\left(\frac{\partial \vec{V}}{\partial t} + \frac{1}{\epsilon}(\vec{V}\cdot\nabla)\vec{V}\right) = -\nabla p + \Lambda Da\Big(1+\frac{1}{\gamma}\Big)(\nabla^2\vec{V}) - \vec{V} + \{RaT + RsC\} \\ (\sin(\theta)\hat{e_{\text{x}}} + \cos(\theta)\hat{e_{\text{y}}}) \tag{9.7}$$

$$\frac{\partial T}{\partial t} + \vec{V}\cdot\nabla T = (1+R_d)\nabla^2 T \tag{9.8}$$

$$\frac{\partial C}{\partial t} + \frac{1}{\epsilon}\vec{V}\cdot\nabla C = \frac{Pr}{Sc}\nabla^2 C - R_c Pr C \tag{9.9}$$

The following are the boundary conditions:

$$\begin{aligned} y=-1: &\quad \vec{V}=0, \quad T=0, \quad C=0 \\ y=1: &\quad \vec{V}=0, \quad T=1, \quad C=1 \end{aligned} \tag{9.10}$$

where:
$R_d = \frac{-16\eta^2\sigma T^3}{3\beta_R}$ is radiation parameter, $Sc = \frac{\nu}{D}$ is Schmidt number, $R_c = \frac{R^* L^2}{\nu}$ is chemical reaction parameter.

9.3 Basic solution

In the basic stage, the flow is regarded as continuous, one-directional (in the x-direction), and completely developed. Eqs. (9.6)-(9.9) may be reduced into set of ordinary differential equations by applying these conditions:

$$\Lambda Da\Big(1+\frac{1}{\gamma}\Big)\frac{d^2U_b}{dy^2} - U_b = \frac{\partial p_0}{\partial x} - \{RaT_0 + RsC_0\}\sin(\theta) \tag{9.11}$$

$$\frac{\partial p_0}{\partial y} = \{RaT_0 + R_sC_0\}\cos(\theta) \tag{9.12}$$

$$\frac{\partial p_0}{dz} = 0 \tag{9.13}$$

$$(1+R_d)\frac{d^2T_0}{dy^2} = 0 \tag{9.14}$$

$$\frac{Pr}{Sc}\frac{d^2T_0}{dy^2} - R_cPrC_0 = 0 \tag{9.15}$$

The boundary conditions are:

$$\begin{aligned} y = -1: &\quad U_b = 0, \quad T_0 = 0, \quad C_0 = 0 \\ y = 1: &\quad U_b = 0, \quad T_0 = 1, \quad C_0 = 1 \end{aligned} \tag{9.16}$$

Proceeding as in Chapter-2, we get basic solution as:

$$T_0 = \frac{1+y}{2} \quad \text{and} \quad C_0 = \frac{1}{2}\left[\frac{\cosh(\sqrt{R_cSc})y}{\cosh(\sqrt{R_cSc})} + \frac{\sinh(\sqrt{R_cSc})y}{\sinh(\sqrt{R_cSc})}\right] \tag{9.17}$$

$$\begin{aligned} U_b = \sigma\left[\frac{\cosh(my)}{\cosh(m)} - 1\right] + \frac{1}{2}\left(\frac{m^2}{R_cSc - m^2}\right)Rs\Bigg[\frac{\cosh(my)}{\cosh(m)} + \frac{\sinh(my)}{\sinh(m)} \\ -\frac{\cosh(\sqrt{R_cSc}y)}{\cosh(\sqrt{R_cSc})} - \frac{\sinh(\sqrt{R_cSc}y)}{\sinh(\sqrt{R_cSc})}\Bigg]\sin(\theta) + \frac{Ra}{2}\left(y - \frac{\sinh(my)}{\sinh(m)}\right)\sin(\theta) \end{aligned} \tag{9.18}$$

where:

$$\sigma = \frac{m\cosh(m)}{\sinh(m) - m\cosh(m)}\left[1 - \frac{1}{2}\left(\frac{m^2}{R_cSc - m^2}\right)Rs\left(\frac{\sinh(m)}{m\cosh(m)} - \frac{\sinh(\sqrt{R_cSc})}{\sqrt{R_cSc}\cosh(\sqrt{R_cSc})}\right)\right]\sin(\theta)$$

And

$$m = \frac{1}{\sqrt{\Lambda Da\left(1 + \frac{1}{\gamma}\right)}}$$

9.4 Linear stability analysis

As in Chapter - 2, by imposing infinitesimal disturbances (δ) on the basic state solutions, ignoring δ^2 and higher order terms, using the usual normal mode form [50] to express infinitesimal disturbances of corresponding field variables, and removing pressure terms from

the resulting equations, the linearized stability equations are obtained as:

$$\begin{aligned}\Lambda Da\Big(1+\frac{1}{\gamma}\Big)\left[\frac{d^4\hat{v}}{dy^4}-2\frac{d^2\hat{v}}{dy^2}(\alpha^2+\beta^2)+(\alpha^2+\beta^2)^2\hat{v}\right]-\frac{i\alpha}{\mathrm{va}}\left(\frac{U_b}{\epsilon}-c\right)\left[\frac{d^2\hat{v}}{dy^2}\right.\\ \left.-(\alpha^2+\beta^2)\hat{v}\right]+\frac{i\alpha}{\epsilon\mathrm{va}}\frac{d^2U_b}{dy^2}\hat{v}-\left[\frac{d^2\hat{v}}{dy^2}-(\alpha^2+\beta^2)\hat{v}\right]-i\alpha Ra\frac{d\hat{T}}{dy}\sin(\theta)\\ -(\alpha^2+\beta^2)Ra\cos(\theta)\hat{T}-i\alpha Rs\frac{d\hat{C}}{dy}\sin(\theta)-(\alpha^2+\beta^2)Rs\cos(\theta)\hat{C}=0\end{aligned} \tag{9.19}$$

$$\begin{aligned}(-i\alpha c)\frac{1}{\mathrm{va}}\hat{\eta}+\frac{1}{\epsilon va}\left[\beta\frac{dU_b}{dy}\hat{v}+U_b\hat{\eta}i\alpha\right]-\Lambda Da\Big(1+\frac{1}{\gamma}\Big)\left[\frac{d^2\hat{\eta}}{dy^2}-(\alpha^2+\beta^2)\hat{\eta}\right]+\hat{\eta}\\ -\beta Ra\hat{T}\sin(\theta)-\beta Rs\hat{C}\sin(\theta)=0\end{aligned} \tag{9.20}$$

$$\frac{dT_0}{dy}\hat{v}+i\alpha\left(U_b-c\right)\hat{T}-(1+R_d)\left[\frac{d^2\hat{T}}{dy^2}-(\alpha^2+\beta^2)\hat{T}\right]=0 \tag{9.21}$$

$$\frac{1}{\epsilon}\frac{dC_0}{dy}\hat{v}+i\alpha\left(\frac{U_b}{\epsilon}-c\right)\hat{T}-\frac{Pr}{Sc}\left[\frac{d^2\hat{T}}{dy^2}-(\alpha^2+\beta^2)\hat{T}\right]+R_cPr\hat{C}=0 \tag{9.22}$$

9.5 Results and discussion

The equations from Eqs. (9.19) - (9.22) represent a generalized eigenvalue problem in which the eigenvalues are perturbed and expressed in terms of the wave speed. The spectral technique [107] is employed to find the solution to this eigenvalue problem.

In order to validate the accuracy of this method, we ran the MATLAB code for calculating eigenvalues with varying grid point numbers (N) and obtained least stable eigenvalues, which are presented in Table 9.1 for an arbitrary combination of parameters. When $N \geq 50$, the least stable eigenvalue reached convergence criterion of 10^{-7}, and these results remained constant despite varying parameter values. In our numerical calculations, we chose to use $N = 50$ as a result.

The results of $\theta = \pi/2$, $\gamma \to \infty$, $R_d = 0$, $Pr = 1$, $Sc = 1$, $N = 51$, and $R_c = 0$ in absence of Rn, Ha, Ln, N_A, N_B, D_f, ϕ_0, and Sr were obtained, which is in accordance with the findings of Srinivasacharya and Barman [108].

In this paper, we investigate the effect of radiation and chemical reactions on the stability of a Casson fluid flow in an inclined porous channel. The influence of the governing parameters inclination angle (θ), Darcy number (Da), Radiation parameter (R_d), chemical reaction parameter (R_c), Prandtl number (Pr) , and porosity parameter (ϵ) on the flow instability is studied.

Fig. 9.1 depicts the graphs illustrating the critical Rayleigh number (Ra_c) and the critical wavenumber (α_c) vary with variations in the Casson parameter (γ) for various inclination angles (θ). When θ oriented vertically, critical Rayleigh number (Ra_c) demonstrates a decreasing trend. This phenomenon indicates that a change in the angle of inclination θ destabilizes the flow. This behavior can be explained by the fact that, in inclined channels, the gravitational force operating on fluid includes a component parallel to the flow direction. This additional force component can contribute to the formation of instabilities in the Casson fluid flow. However, Ra_c drops as the Casson parameter (γ) increases, indicating destabilizing impact of Casson parameter. In the case of α_c, there is no change in α_c for an increase in γ, However, α_c increases when θ oriented vertically.

Fig. 9.2 depicts the fluctuation of the critical Rayleigh number and critical wavenumber for permeability parameter (Darcy number). As Da increases, Ra_c also increases, indicating the stabilizing influence on stability. This is because when the Darcy number is high, the viscous forces dominate over the inertial forces, resulting in a highly viscous flow. This can stabilize the flow and reduce the flow instabilities. Ra_c, however, falls as γ increases. In case of critical wavenumber (α_c), as we increase Da, α_c rises. The variation of α_c is slow when the Darcy number is greater than 1, but there is a rapid rise in α_c when Da is less than 1. As we increase γ, α_c decreases.

The critical Rayleigh numberand critical wavenumber for radiation parameter (R_d) are shown fluctuating in Fig. 9.3. It is noticed that there is a slight drop in Ra_c as R_d increases. It demonstrates that R_d had a destabilizing effect on the flow field because it introduces additional heat sources that can disrupt the flow pattern. Specifically, when the radiation parameter is high, the fluid absorbs radiation from the channel walls, causing it to heat up and become less viscous. This reduced viscosity may lead to formation of disturbances in the flow. Also, as we increase γ, Ra_c decreases. On the other hand, in the case of α_c, α_c grows as R_d increases. However, α_c falls as γ rises.

The critical Rayleigh number and critical wavenumber for chemical reaction parameter (R_c) are shown fluctuating in Fig. 9.4. We noticed that Ra_c stays the same while R_c goes from 0.1 to 25. It demonstrates the flow field's destabilising effect. Because chemical reactions can alter the composition of the fluid and change its rheological properties, such as viscosity and yield stress. These changes can affect the onset of flow, the development of shear layers, and the formation of instabilities in the flow. Ra_c, however, falls as γ rises. similar trend we have noticed in case of critical wavenumber (α_c).

Fig. 9.5 depicts the fluctuation of the critical Rayleigh number and critical wavenumber for Prandtl number (Pr). We found that Ra_c rises when Pr rises. It demonstrates Pr stabilizes the flow field by promoting a more uniform temperature and viscosity profile, reducing thermal gradients, and promoting the development of thermal boundary layers that can dampen out disturbances in the flow. Ra_c, however, falls as γ rises. As Pr rises, α_c lowers in the case of α_c. α_c, however, decreases then rises as γ grows.

Fig. 9.6 shows the boundaries of the region of instability as a function of the Casson parameter (γ) and the porosity parameter (ϵ). Observing Fig. 9.6, it is evident that the critical Rayleigh number tends to increase as the porosity parameter increases, because porosity introducing additional sources of dissipation, promoting a more uniform flow behavior, and enhancing convective heat transfer. The parameter ϵ therefore has a stabilizing influence on the flow. Notably, as the porosity parameter and γ values increase, the critical wavenumber (α_c) decreases.

Figs. 9.7 - 9.9 shows streamlines, isotherms, and isoconcentrations for various θ values when Da=1, Sc=0.6, Ra=10, Rs=5, ϵ=0.2, R_d=1.5, R_c=2, Pr = 25, Λ=1, γ=0.5, α= 1 and $\beta = 0$. Noting that clockwise-oriented streamlines correspond to positive contours and counterclockwise-oriented streamlines correspond to negative contours is essential when analyzing flow patterns. When the channel is horizontal, as indicated by $\theta = 0$ in Fig. 9.7, we observe the formation of two Rayleigh-Bénard convection cells, which are vertical cell structures. Near the upper wall, there is a counterclockwise vortex formation, and near the lower wall, there is a clockwise vortex formation. These cells then extend vertically as the angle of inclination increases, eventually transforming into structure of horizontal cells when channel becomes completely vertical. In conclusion, as channel's inclination varies from horizontal to vertical, the streamlines reconfigure the flow pattern from a vertical structure to a horizontal structure. On the isotherms, positive contour are denoted by solid lines and negative contour are indicated by dashed lines. This pattern holds true for isotherms and isoconcentrations alike.

Table 9.1: "Convergence of the least stable eigenvalue for $\theta = \pi/3$, $Da = 10$, $Pr = 7$, Rm=5, $\epsilon = 0.2$, R_d=1.5, Sc=10, R_c=2, γ=0.5, Λ=1, and $\beta = 0$."

N	Ra_c	α_c
40	26237.025775946910	0.973721784095
45	26237.025773685612	0.973788511858
50	26237.025775874259	0.973721550480
55	26237.025771606088	0.973721949615
60	26237.025771425291	0.973786567943

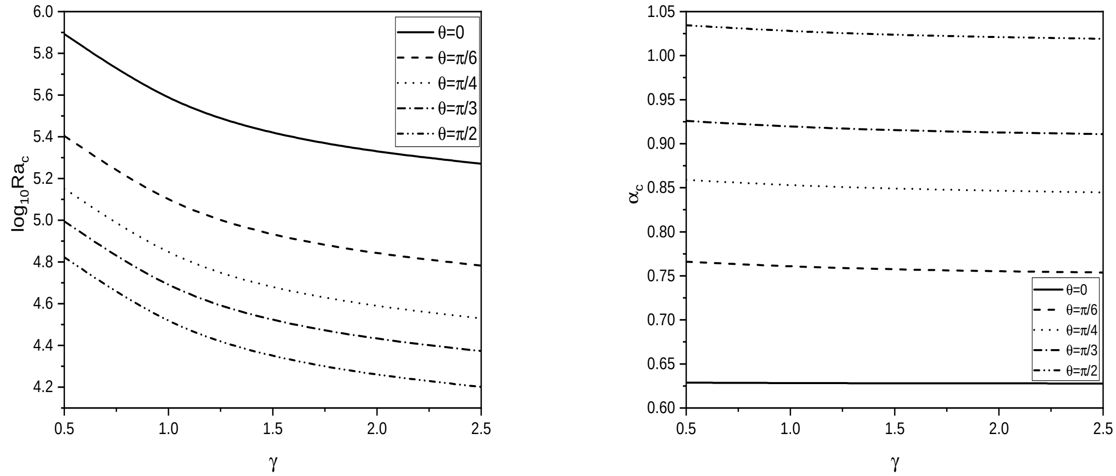

Figure 9.1: "Variation of critical Rayleigh number (Ra_c) and critical wavenumber (α_c) with γ for different values of θ with Da=1, Sc=0.6, Rs=5, R_d=1.5, R_c=2, $Pr = 25$, $\epsilon = 0.6$, Λ=1, and $\beta = 0$."

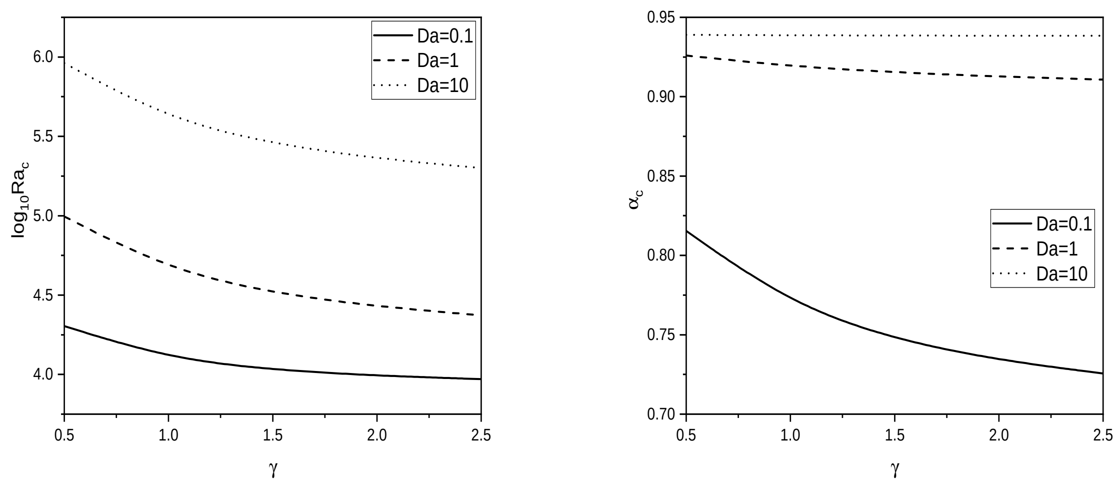

Figure 9.2: "Variation of critical Rayleigh number (Ra_c) and critical wavenumber (α_c) with γ for different values of Da with θ=$\pi/3$, Sc=0.6, Rs=5, R_d=1.5, R_c=2, $Pr = 25$, $\epsilon = 0.6$, Λ=1, and $\beta = 0$."

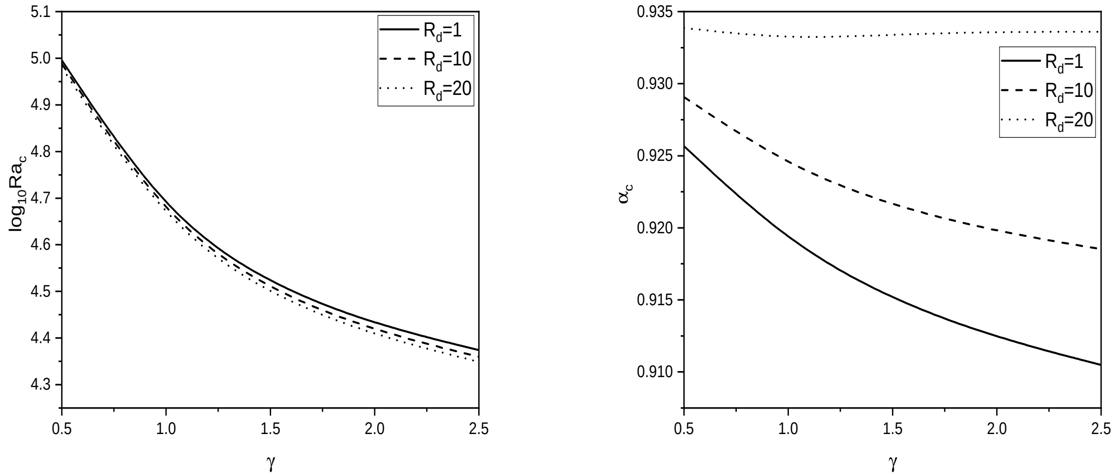

Figure 9.3: "Variation of critical Rayleigh number (Ra_c) and critical wavenumber (α_c) with γ for different values of R_d with θ=$\pi/3$, Da=1, Sc=0.6, Rs=5, R_c=2, Pr = 25, ϵ = 0.6, Λ=1, and β = 0."

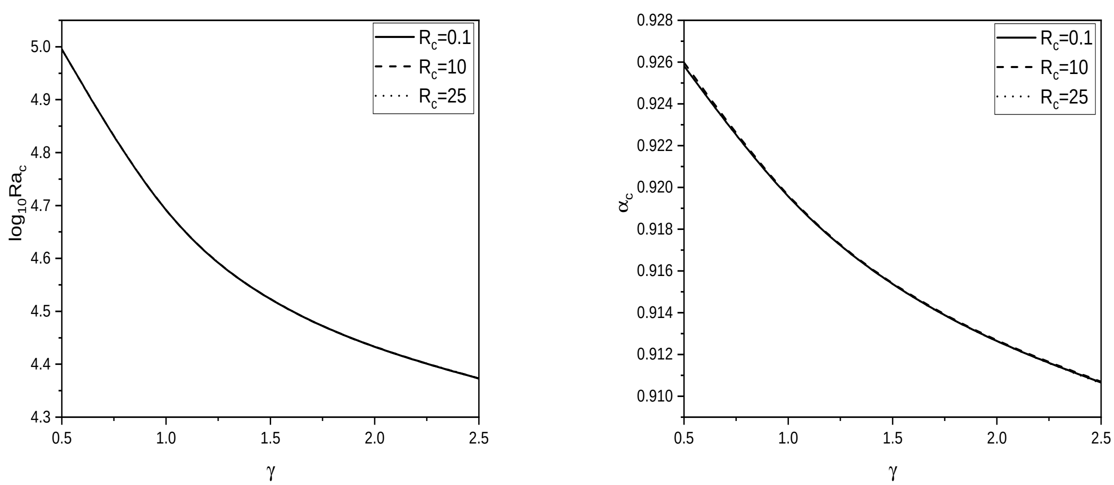

Figure 9.4: "Variation of critical Rayleigh number (Ra_c) and critical wavenumber (α_c) with γ for different values of R_c with θ=$\pi/3$, Da=1, Sc=0.6, Rs=5, R_d=1.5, Pr = 25, ϵ = 0.6, Λ=1, and β = 0."

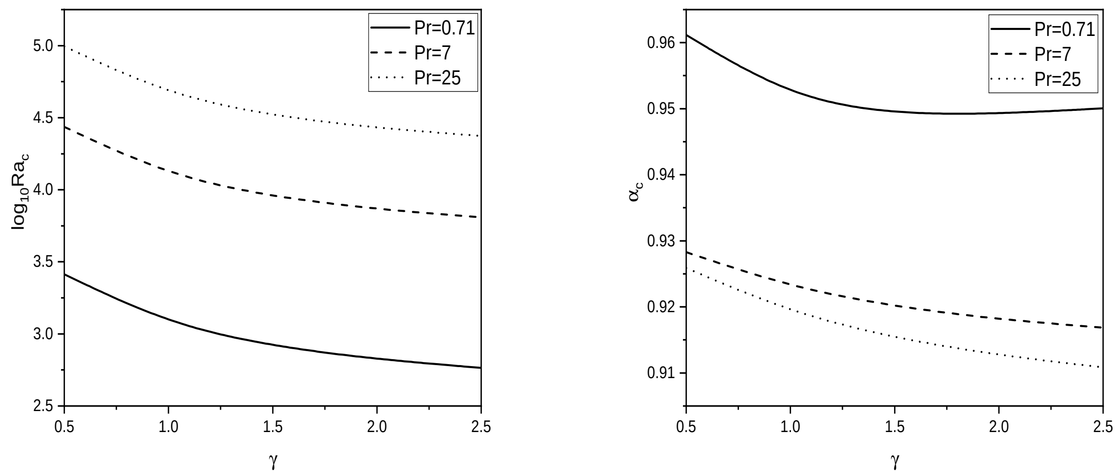

Figure 9.5: "Variation of critical Rayleigh number (Ra_c) and critical wavenumber (α_c) with γ for different values of Pr with θ=$\pi/3$, Da=1, Sc=0.6, Rs=5, R_d=1.5, R_c=2, $\epsilon = 0.6$, Λ=1, and $\beta = 0$."

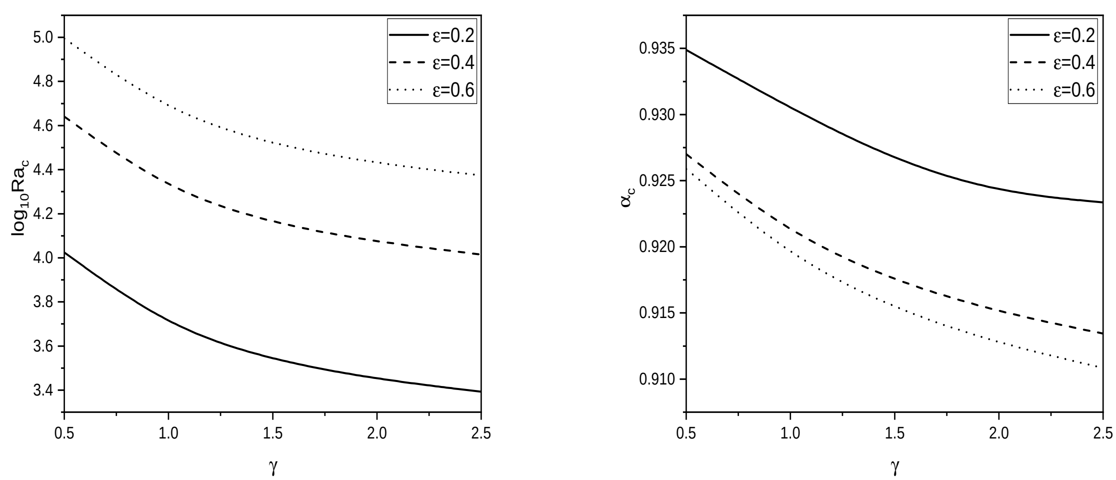

Figure 9.6: "Variation of critical Rayleigh number (Ra_c) and critical wavenumber (α_c) with γ for different values of ϵ with θ=$\pi/3$, Da=1, Sc=0.6, Rs=5, R_d=1.5, R_c=2, $Pr = 25$, Λ=1, and $\beta = 0$."

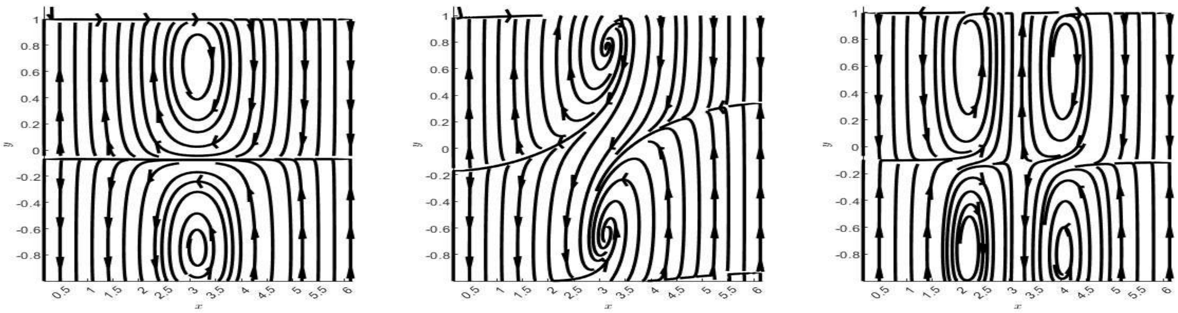

(a) “$\theta = 0$” (b) “$\theta = \pi/4$” (c) “$\theta = \pi/2$”

Figure 9.7: “The disturbance of streamlines for different values of θ.”

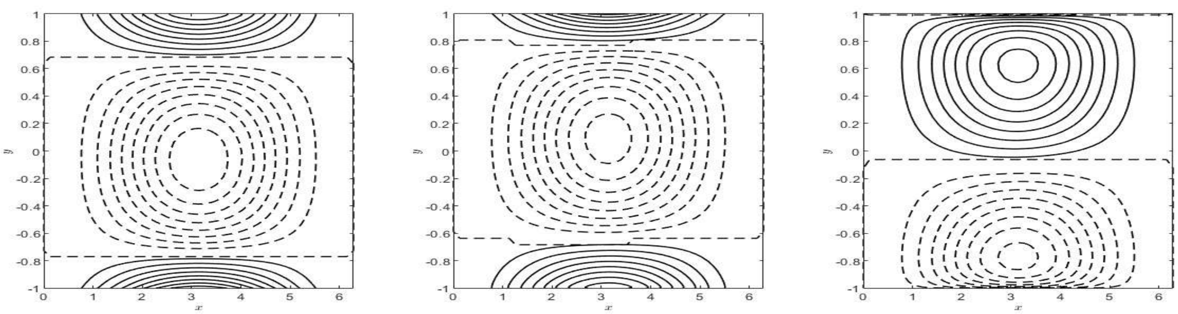

(a) “$\theta = 0$” (b) “$\theta = \pi/4$” (c) “$\theta = \pi/2$”

Figure 9.8: “The disturbance of isotherms for different values of θ.”

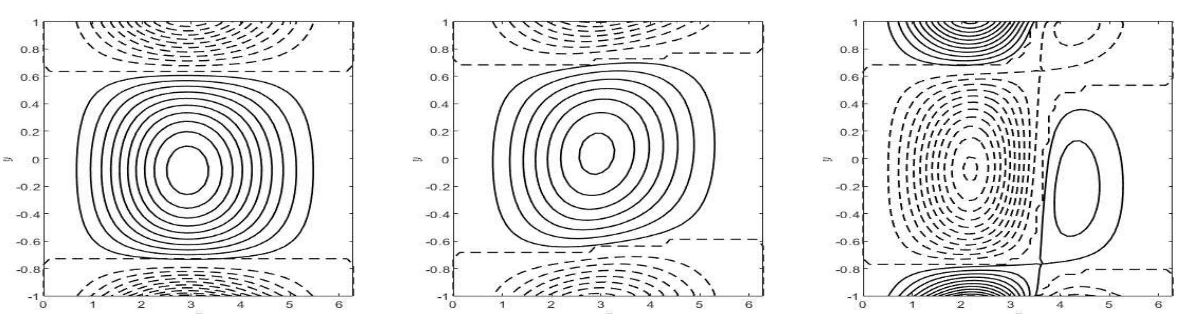

(a) “$\theta = 0$” (b) “$\theta = \pi/4$” (c) “$\theta = \pi/2$”

Figure 9.9: “The disturbance of isoconcentrations for different values of θ.”

9.6 Conclusions

The linear stability of Casson fluid flow in a porous inclined channel while accounting for the effects of radiation and chemical reactions is examined. The critical Rayleigh number and critical wavenumber for different parameters such as θ, Da, R_d, R_c, ϵ, and Pr are computed and graphically shown with respect to γ.

- The channel's inclination (θ), radiation parameter (R_d) and chemical reaction parameter (R_c) and Casson parameter (γ) destabilizes the flow.
- Porosity (ϵ) and Prandtl number (Pr) help to stabilize flow within an inclined channel. As a result, an increase in these variables acts as a stumbling block to the onset of convection.

Chapter 10

The variable viscosity effect on the stability of the Casson fluid flow in an inclined Porous channel [1]

10.1 Introduction

The stability properties of Casson fluid in an inclined porous channel with variable viscosity has yet to be studied, according to the literature review. Consequently, this chapter investigates the effect of variable viscosity on convection stability in a Casson fluid flow in an inclined channel filled with a porous medium (at an angle of inclination θ).

10.2 Mathematical Formulation

Consider an incompressible, unsteady flow of a Casson fluid in tilted channel with a width of $2L$ with two impermeable, completely thermally conducting walls and an inclination of θ. We've assumed that viscosity obeys the Nahme rule Sukanek *et al.* [110], which means that viscosity is modeled as an exponential function of temperature:

$$\mu(T) = \mu_l e^{-kT}$$

[1]Communicated in "***Reviews in Mathematical Physics***"

Fig. 8.1 depicts a schematic illustration of the problem. The porous medium is assumed to be homogenous and isotropic. The temperatures of the left and right walls are T_1 and T_2, respectively.

Using the above assumptions and the Oberbeck-Boussinesq approximation, the following set of equations describes the flow [113, 50]:

$$\nabla \cdot \vec{V} = 0 \tag{10.1}$$

$$\begin{aligned} \frac{\rho}{\epsilon}\frac{\partial \vec{V}}{\partial t} + \frac{\rho}{\epsilon^2}(\vec{V}\cdot\nabla)\vec{V} = -\nabla p + \left(1+\frac{1}{\gamma}\right)\left[\nabla\mu\cdot\left(\nabla\vec{V}^T + \nabla\vec{V}\right) + \mu\Delta\vec{V}\right] - \frac{\mu}{K}\vec{V} \\ +\rho\mathbf{g}\beta_T(T-T_1)(\sin(\theta)\hat{e_{\mathrm{x}}} + \cos(\theta)\hat{e_{\mathrm{y}}}) \end{aligned} \tag{10.2}$$

$$\frac{\partial T}{\partial t} + \vec{V}\cdot\nabla T = \alpha_m \nabla^2 T \tag{10.3}$$

The boundary conditions are:

$$y=-L: \quad \vec{V}=0, \quad T=T_1, \qquad\qquad y=L: \quad \vec{V}=0, \quad T=T_2 \tag{10.4}$$

According to Nikushchenko and Pavlovsky [111] here, $\Delta\vec{V} = -\nabla\times\nabla\times\vec{V}$.
The non-dimensional form of the Eqs. (10.1)-(10.3) (on substituting (2.6) in (10.1) -(10.3) and removing asterisk) are:

$$\nabla \cdot \vec{V} = 0 \tag{10.5}$$

$$\begin{aligned} \frac{1}{\mathrm{v}a}\frac{\partial \vec{V}}{\partial t} + \frac{1}{\epsilon \mathrm{v}a}(\vec{V}\cdot\nabla)\vec{V} = -\nabla p + Da\left(1+\frac{1}{\gamma}\right)\left[\nabla\mu\cdot\left(\nabla\vec{V}^T + \nabla\vec{V}\right) + \mu\Delta\vec{V}\right] - \mu\vec{V} \\ +RaT(\sin(\theta)\hat{e_{\mathrm{x}}} + \cos(\theta)\hat{e_{\mathrm{y}}}) \end{aligned} \tag{10.6}$$

$$\frac{\partial T}{\partial t} + \vec{V}\cdot\nabla T = \nabla^2 T \tag{10.7}$$

The following are the boundary conditions:

$$y=-1: \quad \vec{V}=0, \quad T=0, \qquad\qquad y=1: \quad \vec{V}=0, \quad T=1 \tag{10.8}$$

10.3 Basic solution

In the basic stage, the flow is regarded as continuous, one-directional (in the x-direction), and completely developed. Eqs. (10.5)-(10.7) may be reduced into set of ordinary differential equations by applying these conditions:

$$Da\Big(1+\frac{1}{\gamma}\Big)\left\{\frac{\partial}{\partial y}\left(\mu_0\frac{\partial U_b}{\partial y}\right)\right\}-\mu_0 U_b=\frac{\partial p_0}{\partial x}-RaT_0\sin(\theta) \tag{10.9}$$

$$\frac{\partial p_0}{\partial y}=RaT_0\cos(\theta) \tag{10.10}$$

$$\frac{\partial p_0}{dz}=0 \tag{10.11}$$

$$\frac{d^2T_0}{dy^2}=0 \tag{10.12}$$

The boundary conditions are:

$$y=-1: \quad U_b=0, \quad T_0=0, \qquad\qquad y=1: \quad U_b=0, \quad T_0=1 \tag{10.13}$$

Proceeding as in Chapter-2, and taking the approximation $\mu(T_0)=e^{-kT_0}$ according to Wall and Wilson [106], we get basic solution as:

$$T_0=\frac{1+y}{2} \tag{10.14}$$

$$\begin{aligned}U_b=\frac{1}{8}e^{\frac{1}{4}k(y+1)}\text{csch}(m)\text{sech}(m)\Big(-e^{\frac{1}{4}k(y+1)}\sinh(2m)\Big(4\sigma-Ra\sin(\theta)\Big(Da\Big(1+\frac{1}{\gamma}\Big)k\\ +2y\Big)\Big)+\sinh(m(1-y))\Big(Ra\Big(2-Da\Big(1+\frac{1}{\gamma}\Big)k\Big)\sin(\theta)+4\sigma\Big)\\ +e^{k/2}\sinh(m(y+1))\Big(4\sigma-Ra\Big(Da\Big(1+\frac{1}{\gamma}\Big)k+2\Big)\sin(\theta)\Big)\Big)\end{aligned} \tag{10.15}$$

where:

$$\sigma = \Bigg\{ Ra\sin(\theta)\Big(16\Big(Da\Big(1+\frac{1}{\gamma}\Big)e^{k/2}k^3m - 8k^2m\Big(\Big(Da\Big(1+\frac{1}{\gamma}\Big)k + e^k\Big(\Big(Da\Big(1+\frac{1}{\gamma}\Big)k$$

$$+2\Big)-2\Big)\cosh(2m)+\sinh(2m)\Big(\Big(Da\Big(1+\frac{1}{\gamma}\Big)\Big(e^k-1\Big)k^4+4\Big(e^k-1\Big)k^2$$

$$\Big(4\Big(Da\Big(1+\frac{1}{\gamma}\Big)m^2+1\Big)+2\Big(e^k+1\Big)k^3+32\Big(e^k+1\Big)km^2$$

$$-64\Big(e^k-1\Big)m^2\Big)\Big)+4k^2\Big(k^2-16m^2\Big)\sinh(2m)\Bigg\} \Bigg/$$

$$\Bigg\{4k\Big(\Big(e^k-1\Big)\Big(k^2+16m^2\Big)\sinh(2m)+16e^{k/2}km-8\Big(e^k+1\Big)km\cosh(2m)\Big)\Bigg\}$$

and

$$m = \frac{\sqrt{k^2+16/Da\Big(1+\frac{1}{\gamma}\Big)}}{4}$$

10.4 Linear stability analysis

As in Chapter - 2, by imposing infinitesimal disturbances (δ) on the basic state solutions, ignoring δ^2 and higher order terms, using the usual normal mode form [50] to express infinitesimal disturbances of corresponding field variables, and removing pressure terms from the resulting equations, the linearized stability equations are obtained as:

$$\begin{aligned}
&Da\Big(1+\frac{1}{\gamma}\Big)\Big[\mu_0\frac{d^4\hat{v}}{dy^4}+2\frac{d\mu_0}{dy}\frac{d^3\hat{v}}{dy^3}-\frac{d^2\hat{v}}{dy^2}\Big(2\mu_0(\alpha^2+\beta^2)-\frac{d^2\mu_0}{dy^2}\Big)-4(\alpha^2+\beta^2)\frac{d\hat{v}}{dy}\frac{d\mu_0}{dy}\\
&\quad+(\alpha^2+\beta^2)\Big(\mu_0(\alpha^2+\beta^2)+\frac{d^2\mu_0}{dy^2}\Big)\hat{v}\Big]-\frac{i\alpha}{\text{va}}\Big(\frac{U_b}{\epsilon}-c\Big)\Big[\frac{d^2\hat{v}}{dy^2}-(\alpha^2+\beta^2)\hat{v}\Big]\\
&\quad+\frac{i\alpha}{\epsilon\text{va}}\frac{d^2U_b}{dy^2}\hat{v}-\mu_0\Big[\frac{d^2\hat{v}}{dy^2}-(\alpha^2+\beta^2)\hat{v}\Big]-\frac{d\mu_0}{dy}\frac{d\hat{v}}{dy}-Da\Big(1+\frac{1}{\gamma}\Big)e^{-kT_0}k\Big[\frac{dU_b}{dy}\frac{d^2\hat{T}}{dy^2}\\
&\quad+\Big(2\frac{d^2U_b}{dy^2}-k\frac{dU_b}{dy}\Big)\frac{d\hat{T}}{dy}+\Big(\frac{d^3U_b}{dy^3}-k\frac{d^2U_b}{dy^2}+\frac{dU_b}{dy}\Big(\frac{k^2}{4}-i\alpha(\alpha^2+\beta^2)\Big)\Big)\hat{T}\Big]\\
&\quad+ke^{-kT_0}\frac{dU_b}{dy}\hat{T}+ke^{-kT_0}\frac{d\hat{T}}{dy}U_b-U_b\frac{k^2}{2}e^{-kT_0}\hat{T}-Ra\frac{d\hat{T}}{dy}i\alpha\sin(\theta)\\
&\quad-Ra(\alpha^2+\beta^2)\cos(\theta)\hat{T}=0
\end{aligned} \tag{10.16}$$

$$
\frac{1}{\mathrm{va}}(-i\alpha c)\hat{\eta}+\frac{1}{\epsilon \mathrm{va}}\Big[\beta\hat{v}\frac{dU_b}{dy}+U_b\hat{\eta}i\alpha\Big]-Da\Big(1+\frac{1}{\gamma}\Big)\Big[\mu_0\frac{d^2\hat{\eta}}{dy^2}+\frac{d\mu_0}{dy}\frac{d\hat{\eta}}{dy}-\mu_0(\alpha^2+\beta^2)\hat{\eta}\Big]
$$
$$
+Da\Big(1+\frac{1}{\gamma}\Big)ke^{-kT_0}\beta\Big[\frac{dU_b}{dy}\frac{d\hat{T}}{dy}-\frac{k}{2}\hat{T}+\frac{d^2U_b}{dy^2}\hat{T}\Big]+\mu_0\hat{\eta}-\beta U_b ke^{-kT_0}\hat{T}-\beta Ra\hat{T}sin(\theta)=0 \quad (10.17)
$$

$$
\hat{v}\frac{dT_0}{dy}+i\alpha(U_b-c)\hat{T}-\left[\frac{d^2\hat{T}}{dy^2}-(\alpha^2+\beta^2)\hat{T}\right]=0 \quad (10.18)
$$

10.5 Results and discussion

The equations from Eqs. (10.16) - (10.18) represent a generalized eigenvalue problem in which the eigenvalues are perturbed and expressed in terms of the wave speed. The spectral technique [107] is employed to find the solution to this eigenvalue problem. In order to validate the accuracy of this method, we ran the MATLAB code for calculating eigenvalues with varying grid point numbers (N) and obtained least stable eigenvalues, which are presented in Table 10.1 for an arbitrary combination of parameters. When $N \geq 50$, the least stable eigenvalue reached convergence criterion of 10^{-7}, and these results remained constant despite varying parameter values. In our numerical calculations, we chose to use $N = 50$ as a result.

The present analysis's outcomes are compared with a vertically oriented channel containing nanofluid-saturated porous material. The results of $\theta = \pi/2$, $\gamma \to \infty$, Pr=7, $k = 0$ and $N = 51$ in absence of Rn, Rm, N_A, N_B, and ϕ_0 were obtained which is in accordance with the findings of Srinivasacharya and Barman [50].

In this paper, we investigate the effect of variable viscosity on the stability of a Casson fluid flow in a porous inclined channel. The influence of the governing parameters inclination angle (θ), Casson parameter (γ), variable viscosity parameter (k), Prandtl number (Pr) , and porosity parameter (ϵ) on the flow instability is studied. Fig. 10.1 depicts the graphs illustrating the critical Rayleigh number (Ra_c) and the critical wavenumber (α_c) vary with variations in the Darcy number (Da) for various inclination angles (θ). When the angle θ varies from horizontal to vertical, Ra_c demonstrates a decreasing trend. This phenomenon indicates that a change in the angle of inclination θ destabilizes the flow. This behavior can be explained by the fact that, in inclined channels, the gravitational force operating on fluid includes a component parallel to the flow direction. This additional force component can contribute to the formation of instabilities in the Casson fluid flow. In the case of critical wavenumber, α_c rises as both θ and Da are increases.

Fig. 10.2 depicts the fluctuation of the critical Rayleigh number and critical wavenumber for various values of the Casson parameter (γ). We observed that while Da rises, Ra_c rises as well, but as γ increases, Ra_c decreases. Hence, γ destabilizes the flow because it determines the yield stress of the fluid. If the Casson parameter is too low, the yield stress of the fluid may not be high enough to support the weight of the fluid in the inclined channel, which can lead to flow instability. On the other hand, if the Casson parameter is too high, the yield stress of the fluid may be too high, leading to laminar flow that is resistant to any instabilities. In the case of critical wavenumbers, however, α_c rises as Da rises, but as γ increases, α_c decreases.

For various values of the variable viscosity parameter (k), Fig. 10.3 displays the variation of the critical Rayleigh number and critical wavenumber. We observed that Ra_c drops when we increase k. This indicates k destabilizes the flow. This is because when the viscosity of the Casson fluid decreases with increasing shear rate, it can cause the flow to become unstable and exhibit turbulent behavior. As the fluid moves down the inclined channel, it is subjected to increasing shear rates due to the effects of gravity, which can cause the viscosity to decrease. This can lead to fluid instabilities. On the other hand, if the viscosity of the Casson fluid increases with increasing shear rate, it can cause the flow to become unstable and exhibit shear-thickening behavior. This can lead to the formation of highly viscous regions in the flow, which can cause a buildup of stress and the formation of flow instabilities. But as Da rises, Ra_c rises as well. In the case of a critical wavenumber, α_c decreases as k increases. However, as Da increases, α_c also increases.

Fig. 10.4 depicts the fluctuation of the critical Rayleigh number and critical wavenumber for Prandtl number (Pr). We found that Ra_c rises when Pr rises. It demonstrates Pr stabilizes the flow field by promoting a more uniform temperature and viscosity profile, reducing thermal gradients, and promoting the development of thermal boundary layers that can dampen out disturbances in the flow. Moreover, α_c increases as Da grows. Also, as Pr rises, α_c falls.

Fig. 10.5 illustrates the boundaries of the instability region as a function of the permeability parameter (Da) and porosity parameter (ϵ). It is noted from Fig. 10.5 that, the critical Rayleigh number tends to rise as the porosity parameter is increased. This is due to porosity is proportion of the total amount of space occupied by voids throughout the volume, It constitutes the measurement of the voids in a porous material. Hence ϵ stabilizes the flow. The volume of voids increases as porosity increases. Observations indicate that α_c increases as the porosity parameter value increases, whereas α_c increases as Da increases.

Fig. 10.6 and Fig. 10.7 shows streamlines, and isotherms, for various θ values when "Da = 1, Pr = 7, Ra = 100, ϵ = 0.6, k=0.5, γ=0.5, α= 1 and β = 0." Noting that clockwise-oriented streamlines correspond to positive contours and counterclockwise-oriented streamlines correspond to negative contours is essential when analyzing flow patterns. When the channel is horizontal, as indicated by $\theta = 0$ in Fig. 10.6, we observe the formation of two Rayleigh-Bénard convection cells, which are vertical cell structures. Near the upper wall, there is a counterclockwise vortex formation, and near the lower wall, there is a clockwise vortex formation. These cells then extend vertically as the angle of inclination increases, eventually transforming into structure of horizontal cells when channel becomes completely vertical. In conclusion, as channel's inclination varies from horizontal to vertical, the streamlines reconfigure the flow pattern from a vertical structure to a horizontal structure. Solid lines represent positive contours on isotherms, while dashed lines represent negative contours. This pattern holds true for isotherms alike.

Table 10.1: "Convergence of the least stable eigenvalue for $Da = 1$, $Pr = 0.1$, $\epsilon = 0.2$, γ=0.5, k=0.5, $\theta = \pi/3$, and $\beta = 0$."

N	Ra_c	α_c
40	58.159398894469	1.156800614916
45	58.159398955057	1.156800432682
50	58.159391266456	1.156800693182
55	58.159398145969	1.156801042609
60	58.159401437386	1.156799879977

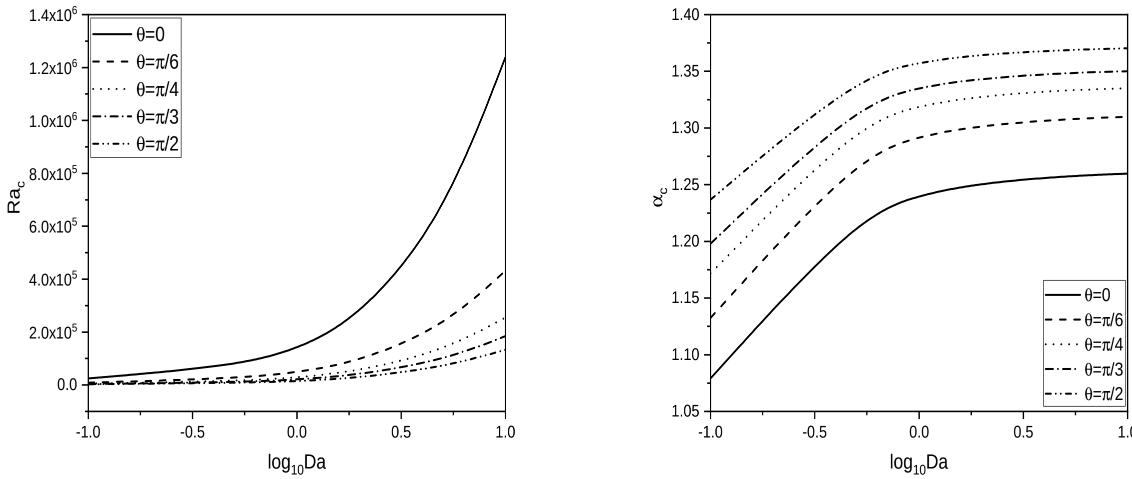

Figure 10.1: “Variation of critical Rayleigh number (Ra_c) and critical wavenumber (α_c) with $log_{10}Da$ for different values of θ with $Pr = 7$, $\epsilon = 0.6$, γ=0.5, k=0.5, and $\beta = 0$.”

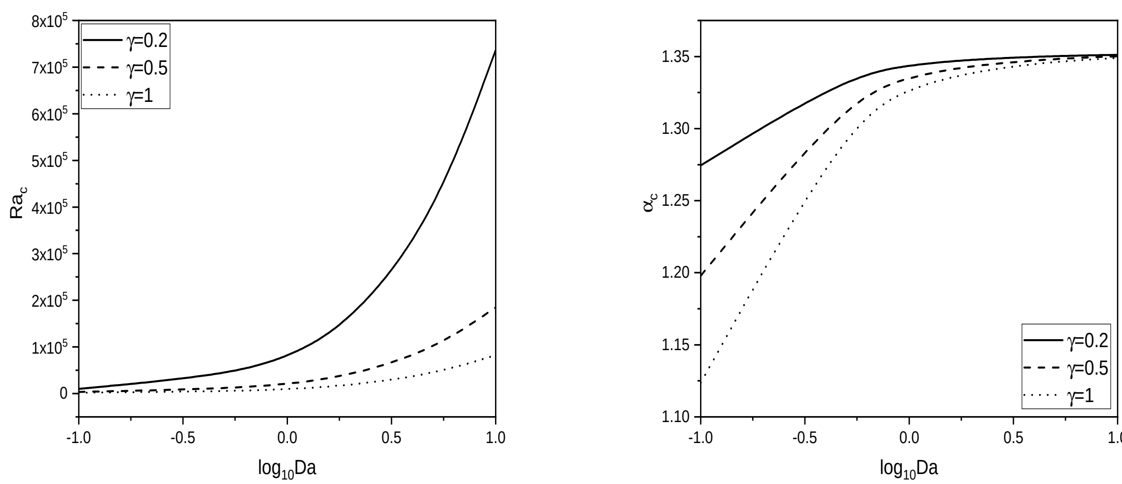

Figure 10.2: “Variation of critical Rayleigh number Ra_c and critical wavenumber α_c with $log_{10}Da$ for different values of γ with $Pr = 7$, $\epsilon = 0.6$, $\theta = \pi/3$, k=0.5, and $\beta = 0$.”

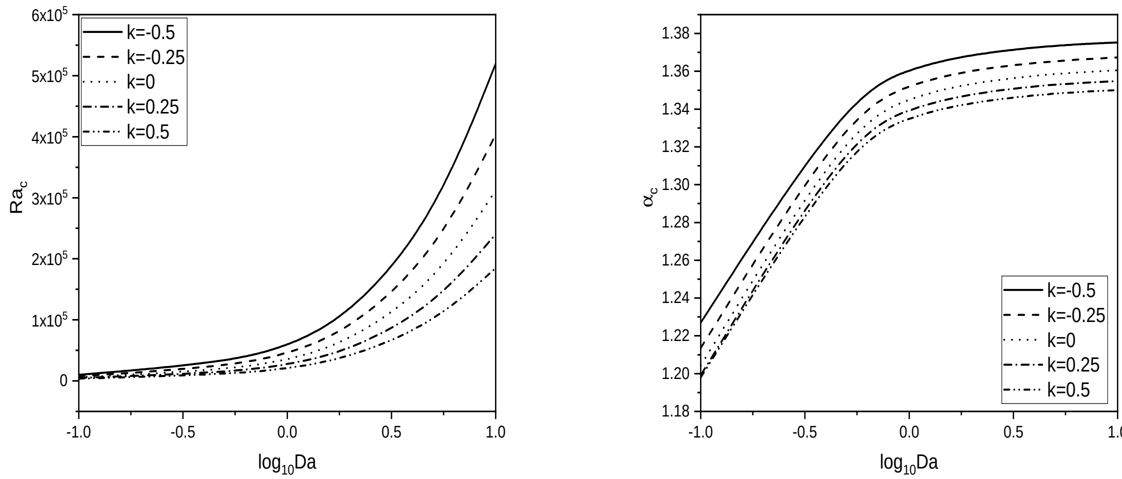

Figure 10.3: "Variation of critical Rayleigh number (Ra_c) and critical wavenumber (α_c) with $log_{10}Da$ for different values of k with $Pr = 7$, $\epsilon = 0.6$, $\theta = \pi/3$, γ=0.5, and $\beta = 0$."

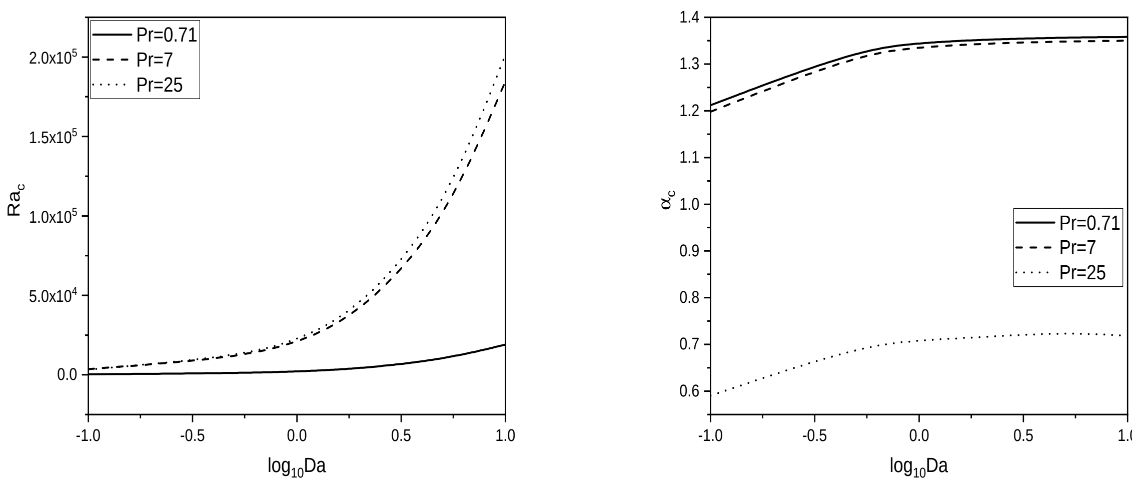

Figure 10.4: "Variation of critical Rayleigh number (Ra_c) and critical wavenumber (α_c) with $log_{10}Da$ for different values of Pr with $\epsilon = 0.6$, $\theta = \pi/3$, γ=0.5, k=0.5, and $\beta = 0$."

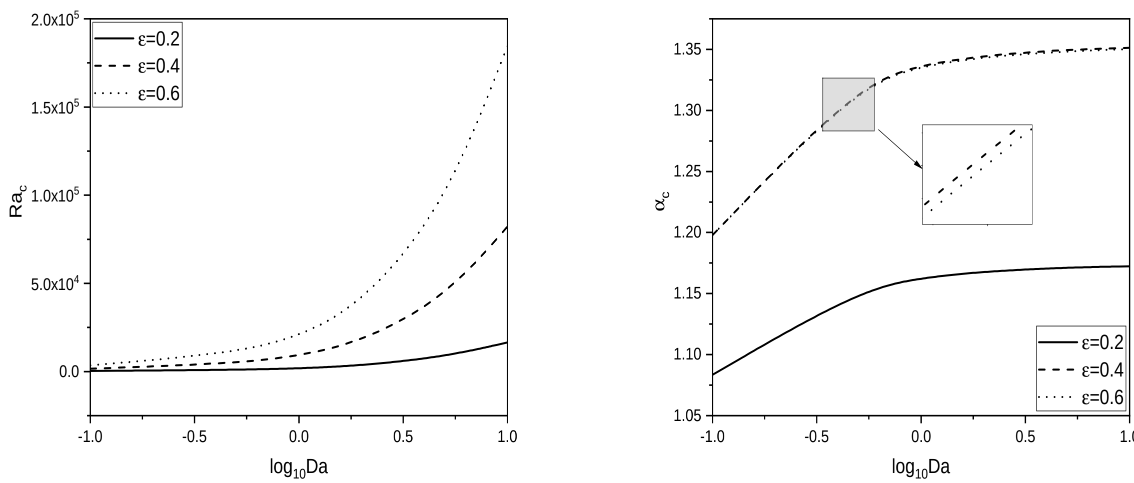

Figure 10.5: “Variation of critical Rayleigh number (Ra_c) and critical wavenumber (α_c) with $log_{10}Da$ for different values of ϵ with $Pr = 7$, $\theta = \pi/3$, γ=0.5, k=0.5, and $\beta = 0$.”

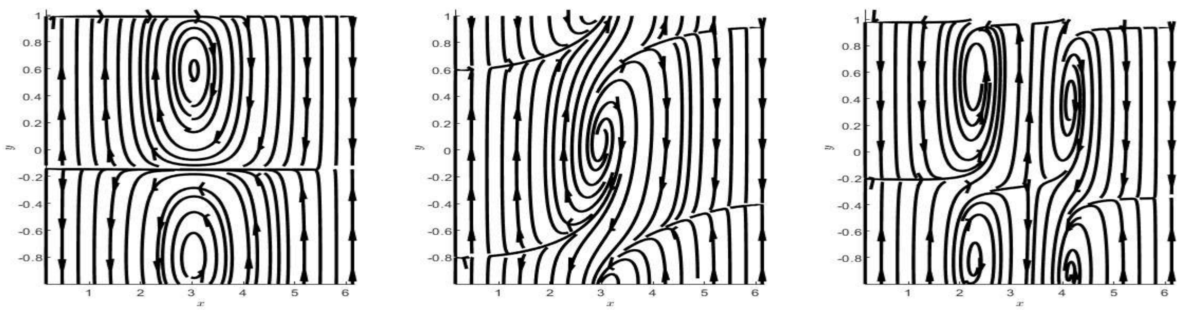

(a) "$\theta = 0$" (b) "$\theta = \pi/4$" (c) "$\theta = \pi/2$"

Figure 10.6: "The disturbance of streamlines for different values of θ."

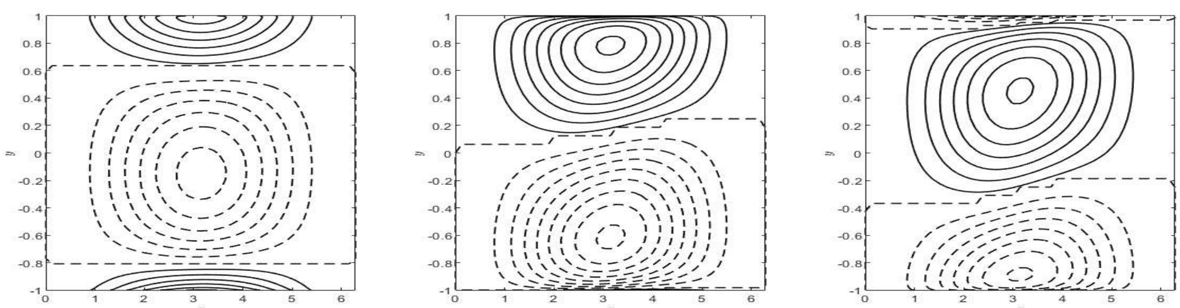

(a) "$\theta = 0$" (b) "$\theta = \pi/4$" (c) "$\theta = \pi/2$"

Figure 10.7: "The disturbance of isotherms for different values of θ."

10.6 Conclusions

The linear stability of Casson fluid flow in a porous inclined channel, taking into consideration the influence of variable viscosity, is examined. The critical Rayleigh number and critical wavenumber for different parameters such as θ, ϵ, Pr, k, and γ are computed and graphically shown with respect to Da.

- The channel's inclination (θ), the Casson parameter (γ), and the variable viscosity parameter (k) destabilizes the flow.
- Porosity (ϵ) and Prandtl number (Pr) help to stabilize flow within an inclined channel. As a result, an increase in these variables acts as a stumbling block to the onset of convection.
- When the channel is oriented vertically and k=0.5, the flow has the least stability.

Part IV

STABILITY OF DUSTY FLUID FLOW IN AN INCLINED POROUS CHANNEL

Chapter 11

The stability of two-phase dusty Casson fluid flow in an inclined porous channel [1]

11.1 Introduction

The interaction of a fluid with suspended solid particles in two-phase dusty fluid flow occurs in applications such as pneumatic transfer, fluidized bed reactors, and volcanic eruptions. This flow type takes into account both viscosity and yield stress. It has a wide range of applications in industries such as chemical processing, oil and gas, and biomedical fields [17]. The experimental properties of heat transmission and multi-phase flow in a long gravity-assisted heat pipe were discussed by Chen *et al.* [75]. Recently, Ali *et al.* [76] studied the effects of heat transfer and magnetic field on the magnetohydrodynamic two-phase free convective flow of dusty Casson fluid between parallel plates.

The stability properties of two-phase dusty Casson fluid in an inclined channel have not been explored, according to the literature review. Consequently, this chapter investigates the convection stability in two-phase dusty Casson fluid flow in an inclined channel filled with a porous medium (at an angle of inclination θ).

[1] Communicated in "***The ANZIAM Journal***"

11.2 Mathematical Formulation

Consider an unsteady, incompressible flow of two-phase dusty Casson fluid in a tilted channel with a width of $2L$ with two impermeable, completely thermally conducting walls and an inclination of θ. A schematic illustration of the problem is shown in Fig. 11.1. The porous medium is assumed to be homogenous and isotropic. Temperatures on both the lower and upper walls are kept at T_1 and T_2, respectively. Using the Oberbeck-Boussinesq approxima-

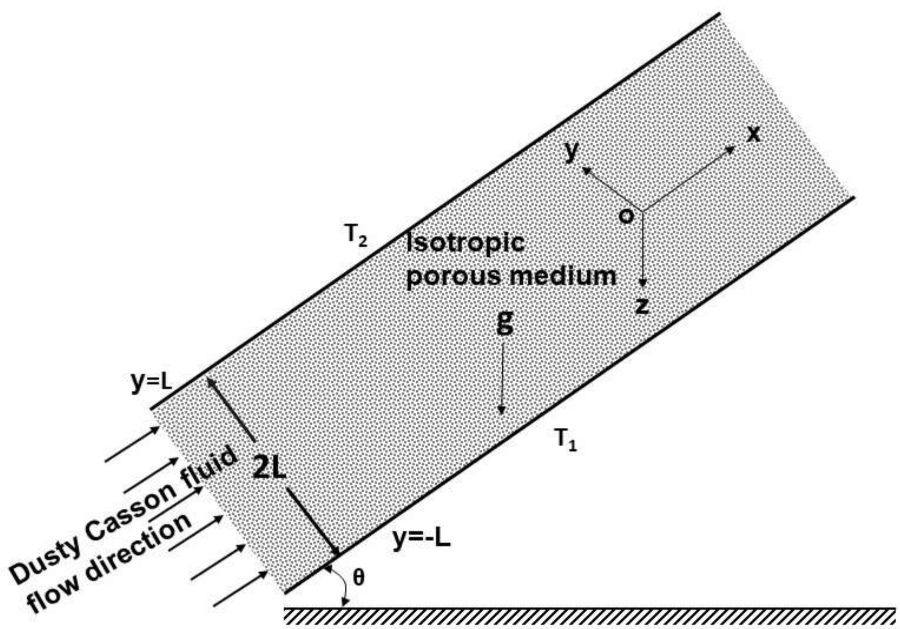

Figure 11.1: "Schematic representation of the problem."

tion, the following set of equations describes the flow [113, 50, 114]:

For the fluid phase:

$$\nabla \cdot \vec{V} = 0 \tag{11.1}$$

$$\begin{aligned} \frac{\rho}{\epsilon}\left(\frac{\partial \vec{V}}{\partial t} + \frac{1}{\epsilon}(\vec{V}\cdot\nabla)\vec{V}\right) = -\nabla p + \Big(1+\frac{1}{\gamma}\Big)\tilde{\mu}\nabla^2\vec{V} - \frac{\mu}{K}\vec{V} + \rho\mathbf{g}\beta_T(T-T_1) \\ (\sin(\theta)\hat{e_{\mathrm{x}}} + \cos(\theta)\hat{e_{\mathrm{y}}}) + \frac{\rho_p}{\tau_m}(\vec{V}_p - \vec{V}) \end{aligned} \tag{11.2}$$

$$\rho C_p \left(\frac{\partial T}{\partial t} + \vec{V} \cdot \nabla T \right) = k \nabla^2 T + \frac{\rho_p C_s}{\tau_T} (T_p - T) \tag{11.3}$$

For the particle phase:

$$\nabla \cdot \vec{V_p} = 0 \tag{11.4}$$

$$\frac{\rho_p}{\epsilon} \left(\frac{\partial \vec{V_p}}{\partial t} + \frac{1}{\epsilon} (\vec{V_p} \cdot \nabla) \vec{V_p} \right) = -\nabla p_p - \frac{\rho_p}{\tau_m} (\vec{V_p} - \vec{V}) \tag{11.5}$$

$$\rho_p C_s \left(\frac{\partial T_p}{\partial t} + \vec{V_p} \cdot \nabla T_p \right) = -\frac{\rho_p C_s}{\tau_T} (T_p - T) \tag{11.6}$$

The boundary conditions for the fluid phase:

$$y = -L: \quad \vec{V} = 0, \quad T = T_1, \qquad y = L: \quad \vec{V} = 0, \quad T = T_2 \tag{11.7}$$

The boundary conditions for the particle phase:

$$y = -L: \quad \vec{V_p} = 0, \quad T_p = T_1, \qquad y = L: \quad \vec{V_p} = 0, \quad T_p = T_2 \tag{11.8}$$

where $\vec{V} = (u, v, w)$ and $\vec{V_p}(u_p, v_p, w_p)$ represents Darcy velocity vector for fluid phase and particle phase, respectively. T and T_p are temperature for fluid phase and particle phase, p and p_p are pressure, and ρ and ρ_p denotes density. C_p and C_s denotes specific heat of fluid and particle phase at constant pressure, respectively. τ_m denotes Velocity relaxation time of the particles, τ_T denotes Thermal relaxation time of the particles.

The non-dimensional variables are:

$$x^*, y^*, z^* = \frac{x, y, z}{L}, \; (p^*, p_p^*) = \frac{k(p, p_p)}{\mu \alpha}, \; (\vec{V}^*, \vec{V}_p^*) = \frac{(\vec{V}, \vec{V_p})L}{\alpha}, \; t^* = \frac{\alpha t}{L^2}, \\ (T^*, T_p^*) = \frac{(T, T_p) - T_1}{T_2 - T_1}. \tag{11.9}$$

By substituting (11.9) in (11.1) -(11.6) and removing the asterisks, the equations (11.1) -(11.6) can be written as:

For the fluid phase:

$$\nabla \cdot \vec{V} = 0 \tag{11.10}$$

$$\frac{1}{\text{va}}\frac{\partial \vec{V}}{\partial t} + \frac{1}{\epsilon \text{va}}(\vec{V} \cdot \nabla)\vec{V} = -\nabla p + \Lambda Da\left(1 + \frac{1}{\gamma}\right)(\nabla^2 \vec{V}) - \vec{V} + RaT(\sin(\theta)\hat{e_{\text{x}}} + \cos(\theta)\hat{e_{\text{y}}}) + D_\rho \alpha_d Da(\vec{V_p} - \vec{V}) \tag{11.11}$$

$$\frac{\partial T}{\partial t} + \vec{V} \cdot \nabla T = \nabla^2 T + D_\rho \gamma_1 \alpha_T Pr(T_p - T) \tag{11.12}$$

For the particle phase:

$$\nabla \cdot \vec{V_p} = 0 \tag{11.13}$$

$$\frac{D_\rho}{\text{va}}\frac{\partial \vec{V_p}}{\partial t} + \frac{D_\rho}{\epsilon \text{va}}(\vec{V_p} \cdot \nabla)\vec{V_p} = -\nabla p_p - D_\rho \alpha_d Da(\vec{V_p} - \vec{V}) \tag{11.14}$$

$$\frac{\partial T_p}{\partial t} + \vec{V_p} \cdot \nabla T_p = -Pr\alpha_T(T_p - T) \tag{11.15}$$

The fluid phase's boundary conditions are as follows:

$$\vec{V} = 0, \quad T = 0, \quad at \quad y = -1, \quad and \quad \vec{V} = 0, \quad T = 1 \quad at \quad y = 1 \tag{11.16}$$

The particle phase's boundary conditions are as follows:

$$\vec{V_p} = 0, \quad T_p = 0, \quad at \quad y = -1, \quad and \quad \vec{V_p} = 0, \quad T_p = 1 \quad at \quad y = 1 \tag{11.17}$$

where, $D_\rho = \frac{\rho_p}{\rho}$ represents mass concentration parameter, $\alpha_d = \frac{L^2}{\tau_m \nu}$ represents Momentum dust particle, $\alpha_T = \frac{L^2}{\tau_T \nu}$ represents Thermal dust particle, $\gamma_1 = \frac{C_s}{C_p}$ denotes Specific heat ratio.

11.3 Basic solution

In the basic stage, the flow is regarded as continuous, one-directional (in the x-direction), and completely developed. Eqs. (11.10)-(11.15) may be reduced into set of ordinary differential equations by applying these conditions:

$$\Lambda Da\left(1 + \frac{1}{\gamma}\right)\frac{d^2 U_b}{dy^2} - U_b = \frac{\partial p_0}{\partial x} - RaT_0 \sin(\theta) - D_\rho \alpha_d Da(U_{pb} - U_b) \tag{11.18}$$

$$\frac{\partial p_0}{\partial y} = RaT_0 \cos(\theta) \tag{11.19}$$

$$\frac{\partial p_0}{dz} = 0 \tag{11.20}$$

$$\frac{d^2T_0}{dy^2} + D_\rho \gamma_1 \alpha_T Pr(T_{p0} - T_0) = 0 \tag{11.21}$$

$$\frac{\partial p_{p0}}{\partial x} + D_\rho \alpha_d Da(U_{pb} - U_b) = 0 \tag{11.22}$$

$$\frac{\partial p_{p0}}{\partial y} = 0 \tag{11.23}$$

$$\frac{\partial p_{p0}}{dz} = 0 \tag{11.24}$$

$$Pr\alpha_T(T_{p0} - T_0) = 0 \tag{11.25}$$

The boundary conditions are:

$$\begin{aligned} y = -1: \quad & U_b = 0, \quad U_{pb} = 0, \quad T_0 = 0, \quad T_{p0} = 0, \\ y = 1: \quad & U_b = 0, \quad U_{pb} = 0, \quad T_0 = 1 \quad T_{p0} = 1, \end{aligned} \tag{11.26}$$

where U_b, $p_0(x, y, z)$, and $T_0(y)$ is basic velocity in x-direction, basic pressure, and basic temperature in the fluid phase, and U_{pb}, $p_{p0}(x, y, z)$, and $T_{p0}(y)$ is basic velocity in x-direction, basic pressure, and basic temperature in the particle phase.
Proceeding as in Chapter-2, we get basic solution as:

$$T_0 = T_{p0} = \frac{1+y}{2} \tag{11.27}$$

$$U_b = (\sigma + \sigma_1)(\mathrm{sech}(m)\cosh(my) - 1) + \frac{1}{2}\mathrm{Ra}\sin(\theta)(y - \mathrm{csch}(m)\sinh(my)) \tag{11.28}$$

$$\begin{aligned} U_{pb} = -\frac{\sigma_1}{DaD_\rho \alpha_d} + (\sigma + \sigma_1)(\mathrm{sech}(m)\cosh(my) - 1) + \frac{1}{2}\mathrm{Ra}\sin(\theta) \\ (y - \mathrm{csch}(m)\sinh(my)) \end{aligned} \tag{11.29}$$

where:

$$\sigma = \frac{m}{\tanh(m) - m} - \sigma_1, \qquad \sigma_1 = 0 \quad \text{and} \quad m = \frac{1}{\sqrt{\Lambda Da\left(1 + \frac{1}{\gamma}\right)}}$$

11.4 Linear stability analysis

As in Chapter - 2, by imposing infinitesimal disturbances (δ) on the basic state solutions, ignoring δ^2 and higher order terms, using the usual normal mode form [50] to express infinitesimal disturbances of corresponding field variables, and removing pressure terms from the resulting equations, the linearized stability equations are obtained as:

$$\begin{aligned} \Lambda Da\Big(1+\frac{1}{\gamma}\Big)\left[\frac{d^4\hat{v}}{dy^4}-2\frac{d^2\hat{v}}{dy^2}(\alpha^2+\beta^2)+(\alpha^2+\beta^2)^2\hat{v}\right]-\frac{i\alpha}{\mathrm{va}}\left(\frac{U_b}{\epsilon}-c\right)\left[\frac{d^2\hat{v}}{dy^2}-(\alpha^2+\beta^2)\hat{v}\right]\\ +\frac{i\alpha}{\epsilon \mathrm{va}}\frac{d^2U_b}{dy^2}\hat{v}-\left[\frac{d^2\hat{v}}{dy^2}-(\alpha^2+\beta^2)\hat{v}\right]-Ra(\alpha^2+\beta^2)\cos(\theta)\hat{T}\\ -Ra\frac{d\hat{T}}{dy}i\alpha\sin(\theta)+DaD_\rho\alpha_d\Big[\frac{d^2\hat{v}_p}{dy^2}-(\alpha^2+\beta^2)\hat{v}_p\Big]-DaD_\rho\alpha_d\Big[\frac{d^2\hat{v}}{dy^2}-(\alpha^2+\beta^2)\hat{v}\Big]=0 \end{aligned} \tag{11.30}$$

$$\begin{aligned} -\frac{i\alpha D_\rho}{\mathrm{va}}\left(\frac{U_{pb}}{\epsilon}-c\right)\left[\frac{d^2\hat{v}_p}{dy^2}-(\alpha^2+\beta^2)\hat{v}_p\right]+\frac{i\alpha D_\rho}{\epsilon \mathrm{va}}\frac{d^2U_{pb}}{dy^2}\hat{v}-DaD_\rho\alpha_d\Big[\frac{d^2\hat{v}_p}{dy^2}\\ -(\alpha^2+\beta^2)\hat{v}_p\Big]+DaD_\rho\alpha_d\Big[\frac{d^2\hat{v}}{dy^2}-(\alpha^2+\beta^2)\hat{v}\Big]=0 \end{aligned} \tag{11.31}$$

$$\begin{aligned} \frac{1}{\mathrm{va}}(-i\alpha c)\hat{\eta}+\frac{1}{\epsilon va}\left[\beta\hat{v}\frac{dU_b}{dy}+U_b\hat{\eta}i\alpha\right]+\hat{\eta}-\Lambda Da\Big(1+\frac{1}{\gamma}\Big)\left[\frac{d^2\hat{\eta}}{dy^2}-(\alpha^2+\beta^2)\hat{\eta}\right]\\ -\beta Ra\hat{T}\sin(\theta)-DaD_\rho\alpha_d(\hat{\eta}_p-\hat{\eta})=0 \end{aligned} \tag{11.32}$$

$$\frac{D_\rho}{\mathrm{va}}(-i\alpha c)\hat{\eta}_p+\frac{D_\rho}{\epsilon va}\left[\beta\hat{v}_p\frac{dU_{pb}}{dy}+U_{pb}\hat{\eta}_p i\alpha\right]+DaD_\rho\alpha_d(\hat{\eta}_p-\hat{\eta})=0 \tag{11.33}$$

$$\frac{dT_0}{dy}\hat{v}+i\alpha\,(U_b-c)\,\hat{T}-\left[\frac{d^2\hat{T}}{dy^2}-(\alpha^2+\beta^2)\hat{T}\right]-D_\rho\alpha_T\gamma_1 Pr(\hat{T}_p-\hat{T})=0 \tag{11.34}$$

$$\frac{dT_{p0}}{dy}\hat{v}_p+i\alpha\,(U_{pb}-c)\,\hat{T}_p+Pr\alpha_T(\hat{T}_p-\hat{T})=0 \tag{11.35}$$

Where $\hat{\mathbf{u}}(y)=(\hat{u},\hat{v},\hat{w})$, $\hat{\mathbf{u}}_p(y)=(\hat{u}_p,\hat{v}_p,\hat{w}_p)$, $\hat{\eta}=\beta\hat{u}-\alpha\hat{w}$ and $\hat{\eta}_p=\beta\hat{u}_p-\alpha\hat{w}_p$.

11.5 Results and discussion

The equations from Eqs. (11.30) - (11.35) represent a generalized eigenvalue problem in which the eigenvalues are perturbed and expressed with respect to wave speed. The spectral technique [107] is employed to find solution to this eigenvalue problem.

Least stable eigenvalues, which are displayed in Table 11.1 for any given combination of parameters, were produced by executing the MATLAB code for computing eigenvalues with changing grid point numbers (N) to verify the method's accuracy. When $N \geq 50$, the least stable eigenvalue reached convergence criterion of 10^{-7}, and these results remained constant despite varying parameter values. In our numerical calculations, we chose to use $N = 50$ as a result.

The present analysis's outcomes are compared with a vertically oriented channel containing nanofluid-saturated porous material. The results of $\gamma \to \infty$, Pr=7, $\theta = \pi/2$, $\vec{V}_p$=0, T_p=0, p_p=0, α_T=0, α_d=0, D_ρ=0, in absence of N_B, N_A, ϕ, Le and Rm, were obtained which is in accordance with the findings of Srinivasacharya and Barman [50].

The Critical values of α_c and Ra_c for dusty Casson fluid and dusty fluid are presented in Table 11.2 for different values of inclindation angle θ and Darcy number Da at $Pr = 7$, $\epsilon = 0.3$, γ_1=0.1, D_ρ=10, α_T=1.2, α_d=1.2, Λ=1, and $\beta = 0$. The presence of dust particle in Casson fluid increases the critical Rayleigh number.

The convective stability in a two-phase dusty Casson fluid flow in a porous inclined channel is studied in this paper. The impact of inclination angle (θ), mass concentration parameter (D_ρ), momentum dust parameter (α_d), thermal dust parameter (α_T), Prandtl number (Pr) , and porosity parameter (ϵ) on the flow instability is studied in-depth in this paper. The problem demonstrates two distinct flow problems under the following conditions:

1. $\gamma \to \infty$ represents the Newtonian dusty fluid flow problem,

2. Non-Newtonian, dusty Casson fluid flow problem with a finite value for γ.

In Figs. 11.2-11.7, we observe a similar flow instability pattern for both phases. However, dusty fluids are always located below dusty Casson fluids.

Fig. 11.2 depicts the graphs illustrating the critical Rayleigh number (Ra_c) and the critical wavenumber (α_c) versus Darcy number (Da) for various inclination angles (θ). It is notable that Ra_c declines for both phases as θ oriented vertically indicates that flow is destabilized. This happens because when a channel is tilted, gravity acts perpendicular to the flow direction, causing density gradients to form within the flow. These density gradients can cause particles to descend to the bottom of the flow, while lighter fluid rises to the surface. In contrast, as the Darcy number (Da) increases, so does Ra_c, indicating that permeability has a stabilizing effect. In addition, once Da reaches 1, Ra_c increases rapidly as Da continues to ascend. For lower Darcy numbers ($Da < 1$), Ra_c displays slow and smooth fluctuations, highlighting that there is visible flow resistance within the porous medium. This resistance to flow reduces as permeability rises, resulting in enhanced flow within the porous medium and highlighting the importance of viscous forces in the momentum equation. In terms of the critical wavenumber (α_c), it increases as both Da and θ increases.

For distinct values of the mass concentration parameter (D_ρ), Fig. 11.3 displays the variation of Ra_c and α_c. We noticed that as Da increases, so does Ra_c. Also, as D_ρ increases, Ra_c increases. Hence, D_ρ stabilizes the flow. If the concentration of the dust particles is too high, they can settle out of the fluid and accumulate at the bottom of the channel. This can lead to a non-uniform distribution of dust particles, which can affect the fluid's rheological properties. On the other hand, if the concentration of the dust particles is too low, they may not significantly affect the fluid's flow properties. In this case, the fluid flow may still be unstable and turbulent due to the effects of gravity. However, as Da rises, α_c increases, but as D_ρ increases, α_c decreases.

The critical Rayleigh number and the critical wavenumber variations for different thermal dust parameter (α_T) values are shown in Fig.11.4. We've observed that as Da increases, so does Ra_c. However, there is no variation in Ra_c as α_T increases. Consequently, α_T does not significantly affect the stability of the two-phase dusty Casson fluid flow. This might occur because in the two-phase dusty Casson fluid flow, the thermal dust parameter mainly affects the thermal conductivity of the fluid by increasing it due to the presence of particles. However, this increase in thermal conductivity does not typically have a significant effect on flow stability. α_c increases as Da increases, whereas α_c does not alter as α_T increases.

Fig. 11.5 depicts the variations in Ra_c and α_c for distinct momentum dust parameter (α_d) values. We've observed that as Da and α_d both rise, so does Ra_c. This means that α_d stabilizes fluid flow. This could happen because the momentum dust parameter can also affect the rheological properties of the fluid, such as its viscosity and yield stress. The presence of solid particles can significantly alter the rheological properties of the fluid, leading to complex flow behavior. A higher momentum dust parameter can result in a higher viscosity and yield stress, which can stabilize the flow and prevent instabilities. Also, as Da increases, so does α_c, whereas as α_d increases, α_c decreases.

The impact of Prandtl number (Pr) on the instability boundaries is seen in Fig. 11.6. As momentum diffusivity increases, defined by the Prandtl number (Pr), so does the critical

Rayleigh number. As a consequence, It demonstrates Pr stabilizes the flow field by promoting a more uniform temperature and viscosity profile, reducing thermal gradients, and promoting the development of thermal boundary layers that can dampen out disturbances in the flow. Moreover, α_c increases as Da and Pr grows. Also, as Pr rises, α_c falls.

Fig. 11.7 depicts the boundaries of the instability region and how they vary as the permeability parameter (Da) and porosity parameter (ϵ) change. As shown in Fig. 11.7, the critical Rayleigh number (Ra_c) tends to increase as the porosity parameter increases. This trend occurs because porosity represents the proportion of a material's total volume that is occupied by vacancies, essentially measuring the voids within a porous material. Therefore, contributes to the stabilization of the flow. As porosity increases, so does the volume of spaces within the material. In addition, it can be observed that α_c, the critical wavenumber, increases as porosity parameter value and the value of Da increase.

Table 11.1: "Convergence of the least stable eigenvalue for $Da = 0.1$, $Pr = 1$, $\epsilon = 0.1$, γ=0.5, γ_1=0.1, D_ρ=10, α_T=1.2, α_d=1.2, $\theta = \pi/3$, Λ=1, and $\beta = 0$."

N	Ra_c	α_c
40	28.052287351685	1.152216157852
45	28.052576969270	1.152291455909
50	28.052499580168	1.152265881971
55	28.052886882916	1.152298501856
60	28.052510054723	1.152318752347

Table 11.2: "Critical values of α_c and Ra_c for different values of θ at $Pr = 7$, $\epsilon = 0.3$, γ_1=0.1, D_ρ=10, α_T=1.2, α_d=1.2, Λ=1, and $\beta = 0$."

		Dusty Casson fluid ($\gamma = 0.5$)		**Dusty fluid** ($\gamma \to \infty$)	
Da	θ	α_c	Ra_c	α_c	Ra_c
0.1	0	0.7015	8094.552	0.9765	4520.88
	$\pi/6$	1.1336	4423.292	0.9669	1775.746
	$\pi/4$	1.153	2649.027	0.9638	1104.42
	$\pi/3$	1.1687	1941.241	0.963	828.649
	$\pi/2$	1.1952	1424.023	0.9652	628.651
1	0	1.2542	66181.717	1.2474	10884.628
	$\pi/6$	1.27	24475.475	1.231	4358.982
	$\pi/4$	1.2859	14870.804	1.2315	2751.79
	$\pi/3$	1.2970	11017.496	1.2341	2091.649
	$\pi/2$	1.3140	8235.319	1.2406	1629.156
10	0	1.2686	618446.515	1.2809	90728.976
	$\pi/6$	1.2846	229414.251	1.2651	36625.694
	$\pi/4$	1.2997	139649.247	1.2652	23230.911
	$\pi/3$	1.3101	103600.359	1.2671	17717.842
	$\pi/2$	1.3259	77605.82	1.2723	13877.645

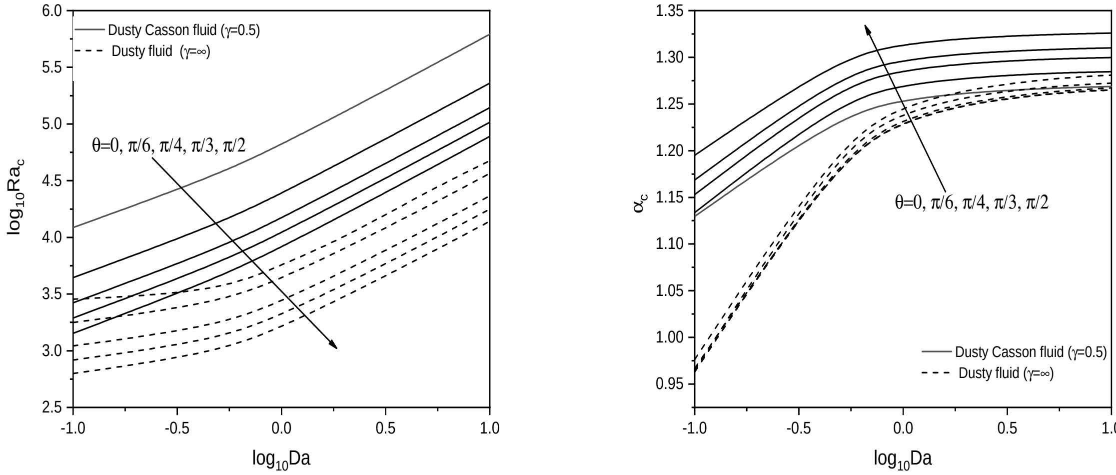

Figure 11.2: "Variation of critical Rayleigh number (Ra_c) and critical wavenumber (α_c) with $log_{10}Da$ for different values of θ with $Pr = 7$, $\epsilon = 0.3$, γ_1=0.1, D_ρ=10, α_T=1.2, α_d=1.2, Λ=1, and $\beta = 0$."

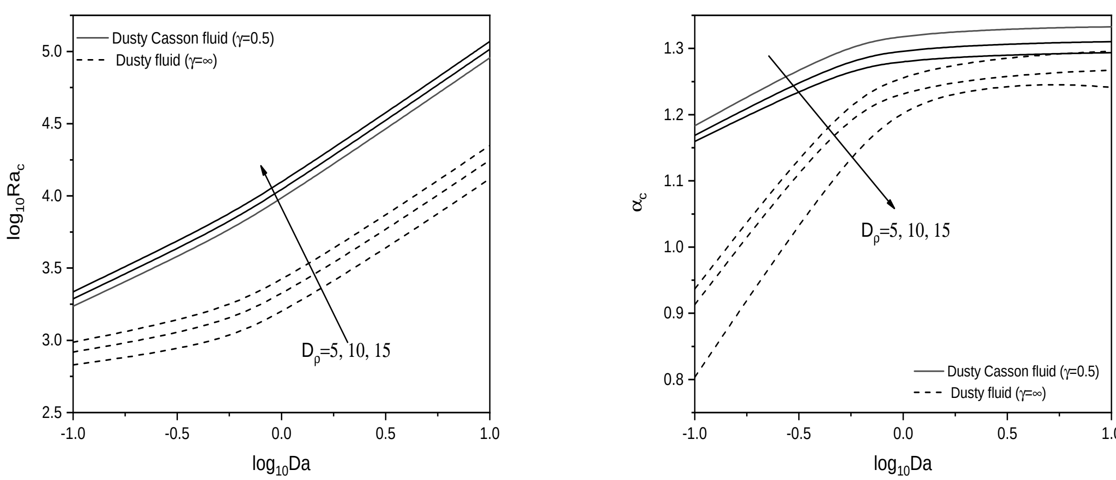

Figure 11.3: "Variation of critical Rayleigh number (Ra_c) and critical wavenumber (α_c) with $log_{10}Da$ for different values of D_ρ with $Pr = 7$, $\epsilon = 0.3$, γ_1=0.1, $\theta = \pi/3$, α_T=1.2, α_d=1.2, Λ=1, and $\beta = 0$."

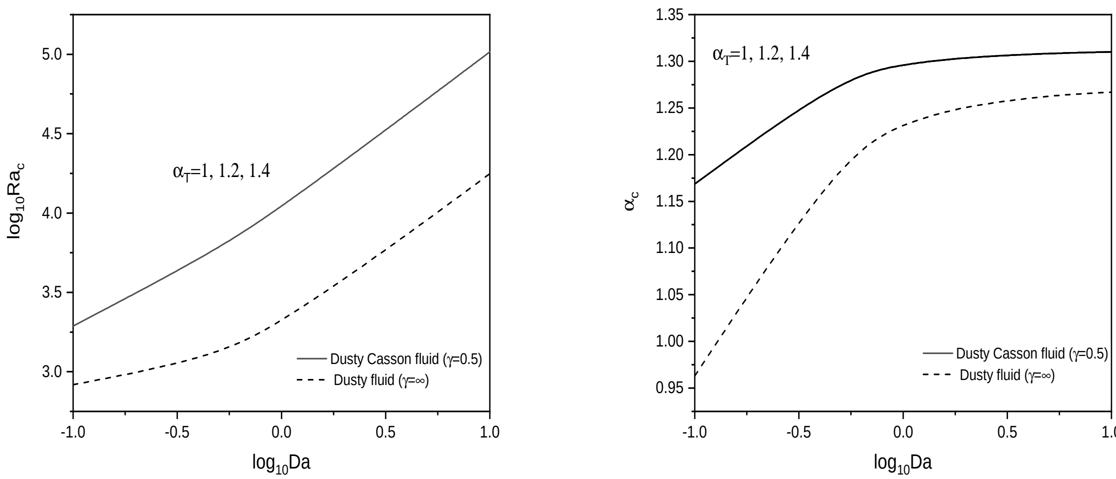

Figure 11.4: "Variation of critical Rayleigh number (Ra_c) and critical wavenumber (α_c) with $log_{10}Da$ for different values of α_T with $Pr = 7$, $\epsilon = 0.3$, γ_1=0.1, D_ρ=10, α_d=1.2, $\theta = \pi/3$, Λ=1, and $\beta = 0$."

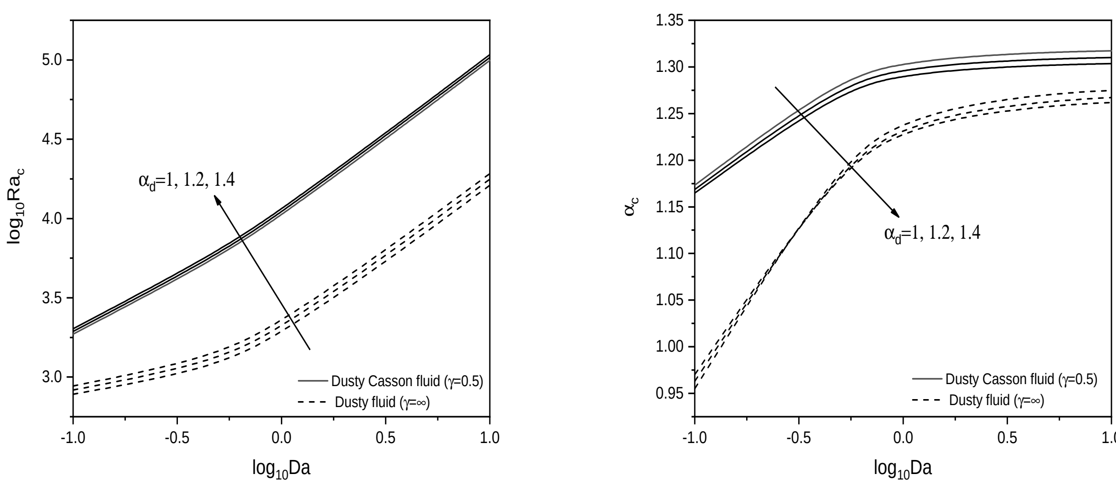

Figure 11.5: "Variation of critical Rayleigh number (Ra_c) and critical wavenumber (α_c) with $log_{10}Da$ for different values of α_d with $Pr = 7$, $\epsilon = 0.3$, γ_1=0.1, D_ρ=10, α_T=1.2, $\theta = \pi/3$, Λ=1, and $\beta = 0$."

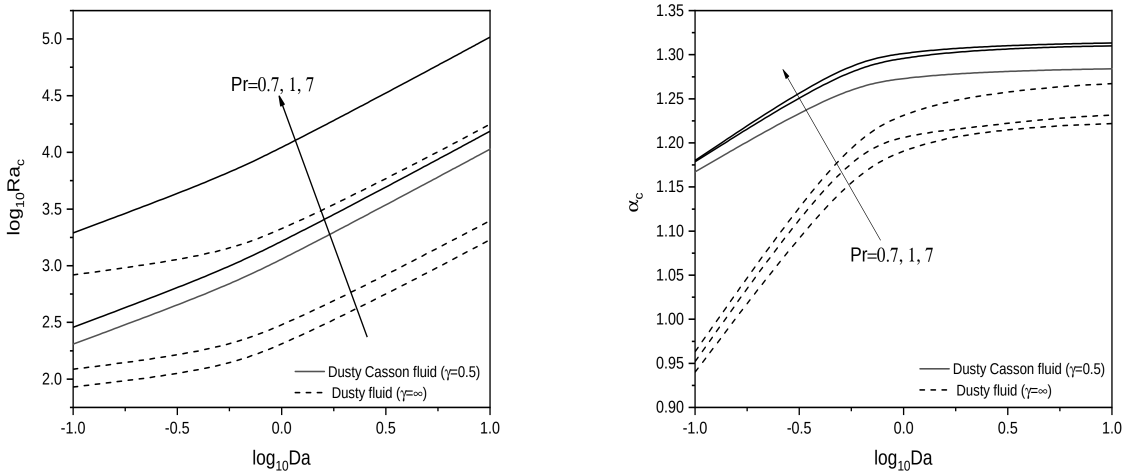

Figure 11.6: "Variation of critical Rayleigh number (Ra_c) and critical wavenumber (α_c) with $log_{10}Da$ for different values of Pr with $\epsilon = 0.3$, γ_1=0.1, D_ρ=10, α_T=1.2, α_d=1.2, $\theta = \pi/3$, Λ=1, and $\beta = 0$."

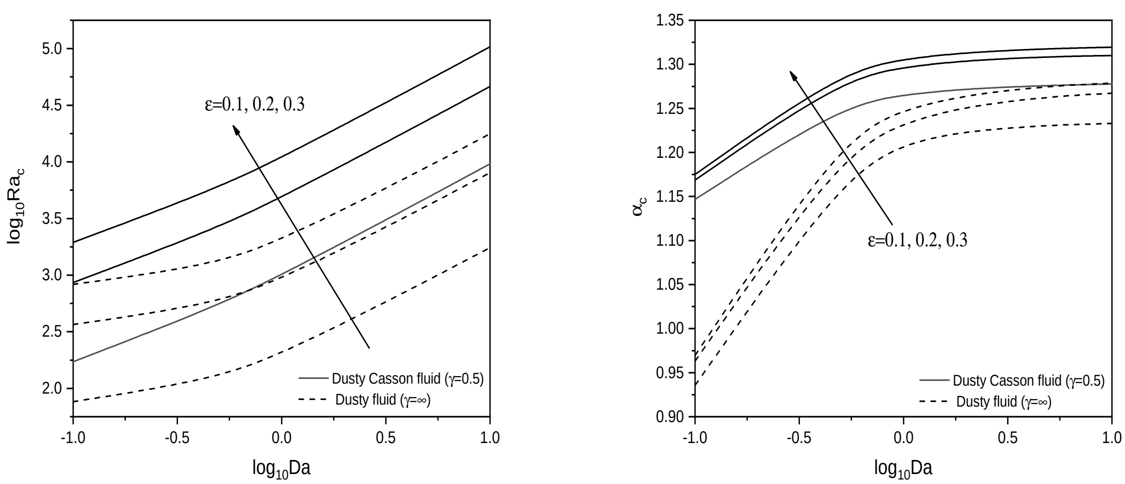

Figure 11.7: "Variation of critical Rayleigh number (Ra_c) and critical wavenumber (α_c) with $log_{10}Da$ for different values of ϵ with $Pr = 7$, γ_1=0.1, D_ρ=10, α_T=1.2, α_d=1.2, $\theta = \pi/3$, Λ=1, and $\beta = 0$."

11.6 Conclusions

The linear stability of two-phase dusty Casson fluid flow in a porous inclined channel is examined. The critical Rayleigh number and critical wavenumber for different parameters such as θ, D_ρ, α_T, α_d, Pr and ϵ are computed and graphically shown with respect to Da.

- The channel's inclination (θ) destabilizes the flow for both phases.
- The momentum equation is affected by viscous forces because flow resistance decreases with increasing permeability and improved flow in a porous media.
- Mass concentration parameter (D_ρ), momentum dust parameter (α_d), Prandtl number (Pr), and porosity parameter (ϵ) help to stabilize flow within an inclined channel. As a result, an increase in these variables acts as a stumbling block to the onset of convection.
- The flow stability was unaffected by the thermal dust parameter (α_T), as we raise α_T, Ra_c remains unchanged.
- When the channel is oriented vertically, the flow has the least stability.
- The neutral stability graphs for dusty phases are always situated below graphs for dusty Casson fluid.

Chapter 12

The effect of variable viscosity on the flow stability of two-phase dusty Casson fluid in a porous inclined channel [1]

12.1 Introduction

This chapter investigates the effect of variable viscosity convection stability in two-phase dusty Casson fluid flow in an inclined channel filled with a porous medium (at an angle of inclination θ).

12.2 Mathematical Formulation

Consider an unsteady, incompressible flow of a two-phase dusty Casson fluid in tilted channel with a width of $2L$ with two impermeable, completely thermally conducting walls and an inclination of θ. We've assumed that viscosity obeys the Nahme rule Sukanek *et al.* [110], which means that viscosity is modeled as an exponential function of temperature:

$$\mu(T) = \mu_l e^{-kT}$$

[1] Communicated in "***ZAMM - Journal of Applied Mathematics and Mechanics*** "

A schematic illustration of the problem is shown in Fig. 11.1. The porous medium is assumed to be homogenous and isotropic. Temperatures on both the upper and lower walls are kept at T_2 and T_1, respectively. Using the above assumptions and the Oberbeck-Boussinesq approximation, the following set of equations describes the flow [113, 50, 114]:
For the fluid phase:

$$\nabla \cdot \vec{V} = 0 \tag{12.1}$$

$$\begin{aligned}\frac{\rho}{\epsilon}\frac{\partial \vec{V}}{\partial t} + \frac{\rho}{\epsilon^2}(\vec{V}\cdot\nabla)\vec{V} = -\nabla p + \left(1+\frac{1}{\gamma}\right)\left[\nabla\mu\cdot\left(\nabla\vec{V}^T + \nabla\vec{V}\right) + \mu\Delta\vec{V}\right] - \frac{\mu}{K}\vec{V} \\ +\rho\mathbf{g}\beta_T(T-T_1)(\sin(\theta)\hat{e_{\mathrm{x}}} + \cos(\theta)\hat{e_{\mathrm{y}}}) + \frac{\rho_p}{\tau_m}(\vec{V}_p - \vec{V})\end{aligned} \tag{12.2}$$

$$\rho C_p\left(\frac{\partial T}{\partial t} + \vec{V}\cdot\nabla T\right) = k\nabla^2 T + \frac{\rho_p C_s}{\tau_T}(T_p - T) \tag{12.3}$$

For the particle phase:

$$\nabla \cdot \vec{V}_p = 0 \tag{12.4}$$

$$\frac{\rho_p}{\epsilon}\left(\frac{\partial \vec{V}_p}{\partial t} + \frac{1}{\epsilon}(\vec{V}_p\cdot\nabla)\vec{V}_p\right) = -\nabla p_p - \frac{\rho_p}{\tau_m}(\vec{V}_p - \vec{V}) \tag{12.5}$$

$$\rho_p C_s\left(\frac{\partial T_p}{\partial t} + \vec{V}_p\cdot\nabla T_p\right) = -\frac{\rho_p C_s}{\tau_T}(T_p - T) \tag{12.6}$$

The boundary conditions for the fluid phase:

$$y=-L: \quad \vec{V}=0, \quad T=T_1, \qquad y=L: \quad \vec{V}=0, \quad T=T_2 \tag{12.7}$$

The boundary conditions for the particle phase:

$$y=-L: \quad \vec{V}_p=0, \quad T_p=T_1, \qquad y=L: \quad \vec{V}_p=0, \quad T_p=T_2 \tag{12.8}$$

The non-dimensional form of the Eqs. (12.1) -(12.6) (on substituting (11.9) in (12.1) -(12.6) and removing asterisk) are: For the fluid phase:

$$\nabla \cdot \vec{V} = 0 \tag{12.9}$$

$$\begin{aligned}\frac{1}{\mathrm{v}a}\frac{\partial \vec{V}}{\partial t} + \frac{1}{\mathrm{v}a\epsilon}(\vec{V}\cdot\nabla)\vec{V} = -\nabla p + Da\left(1+\frac{1}{\gamma}\right)\left[\nabla\mu\cdot\left(\nabla\vec{V}^T + \nabla\vec{V}\right) + \mu\Delta\vec{V}\right] - \mu\vec{V} \\ +RaT(\sin(\theta)\hat{e_{\mathrm{x}}} + \cos(\theta)\hat{e_{\mathrm{y}}}) + D_\rho\alpha_d Da(\vec{V}_p - \vec{V})\end{aligned} \tag{12.10}$$

$$\frac{\partial T}{\partial t} + \vec{V} \cdot \nabla T = \nabla^2 T + D_\rho \gamma_1 \alpha_T Pr(T_p - T) \tag{12.11}$$

For the particle phase:

$$\nabla \cdot \vec{V_p} = 0 \tag{12.12}$$

$$\frac{D_\rho}{\text{v}a}\frac{\partial \vec{V_p}}{\partial t} + \frac{D_\rho}{\epsilon \text{v}a}(\vec{V_p} \cdot \nabla)\vec{V_p} = -\nabla p_p - D_\rho \alpha_d Da(\vec{V_p} - \vec{V}) \tag{12.13}$$

$$\frac{\partial T_p}{\partial t} + \vec{V_p} \cdot \nabla T_p = -Pr\alpha_T(T_p - T) \tag{12.14}$$

The fluid phase's boundary conditions are as follows:

$$\vec{V} = 0, \quad T = 0, \quad at \quad y = -1, \quad and \quad \vec{V} = 0, \quad T = 1 \quad at \quad y = 1 \tag{12.15}$$

The particle phase's boundary conditions are as follows:

$$\vec{V_p} = 0, \quad T_p = 0, \quad at \quad y = -1, \quad and \quad \vec{V_p} = 0, \quad T_p = 1 \quad at \quad y = 1 \tag{12.16}$$

12.3 Basic solution

In the basic stage, the flow is regarded as continuous, one-directional (in the x-direction), and completely developed. Eqs. (12.9)-(12.14) may be reduced into set of ordinary differential equations by applying these conditions:

$$Da\left(1 + \frac{1}{\gamma}\right)\left\{\frac{\partial}{\partial y}\left(\mu_b \frac{\partial U_b}{\partial y}\right)\right\} - \mu_0 U_b = \frac{\partial p_0}{\partial x} - RaT_0 \sin(\theta) - D_\rho \alpha_d Da(U_{p0} - U_b) \tag{12.17}$$

$$\frac{\partial p_0}{\partial y} = RaT_0 \cos(\theta) \tag{12.18}$$

$$\frac{\partial p_0}{dz} = 0 \tag{12.19}$$

$$\frac{d^2 T_0}{dy^2} + D_\rho \gamma_1 \alpha_T Pr(T_{p0} - T_0) = 0 \tag{12.20}$$

$$\frac{\partial p_{p0}}{\partial x} + D_\rho \alpha_d Da(U_{p0} - U_b) = 0 \tag{12.21}$$

$$\frac{\partial p_{p0}}{\partial y} = 0 \tag{12.22}$$

$$\frac{\partial p_{p0}}{dz} = 0 \tag{12.23}$$

$$Pr\alpha_T(T_{p0} - T_0) = 0 \tag{12.24}$$

The boundary conditions are:

$$\begin{aligned} y = -1: \quad & U_b = 0, \quad U_{pb} = 0, \quad T_0 = 0, \quad T_{p0} = 0, \\ y = 1: \quad & U_b = 0, \quad U_{pb} = 0, \quad T_0 = 1 \quad T_{p0} = 1, \end{aligned} \tag{12.25}$$

Proceeding as in Chapter-2, and taking the approximation $\mu(T_0) = e^{-kT_0}$ [106], we get basic solution as:

$$T_0 = T_{p0} = \frac{1+y}{2} \tag{12.26}$$

$$\begin{aligned} U_b = \frac{1}{8} e^{\frac{1}{4}k(y+1)} \Big(& \mathrm{sech}(m)\mathrm{csch}(m)\big((4(\sigma+\sigma_1)\sinh(m(1-y)) + \mathrm{Ra}(2-bk)\sin(\theta)) \\ & + e^{k/2}\sinh(m(y+1))(4(\sigma+\sigma_1) - \mathrm{Ra}(bk+2)\sin(\theta)) \\ & + e^{\frac{1}{4}k(y+1)}\mathrm{Ra}\sin(\theta)\sinh(2m)(bk+2y)\big) - 8(\sigma+\sigma_1)e^{\frac{1}{4}k(y+1)}\Big) \end{aligned} \tag{12.27}$$

$$U_{pb} = -\frac{\sigma_1}{DaD_\rho\alpha_d} + U_b \tag{12.28}$$

where:

$$\begin{aligned} \sigma = \Big\{ & 16e^{k/2}k^2m(bk\mathrm{Ra}\sin(\theta) - 4\sigma_1) + 8k^2m\cosh(2m)\big(4\left(e^k+1\right)\sigma_1 - \mathrm{Ra} \\ & \left(bk + e^k(bk+2) - 2\right)\sin(\theta)\big) + \sinh(2m)\big(\mathrm{Ra}\sin(\theta)\big(b\left(e^k-1\right)k^4 + 4\left(e^k-1\right)k^2 \\ & \left(4bm^2+1\right) + 2\left(e^k+1\right)k^3 + 32\left(e^k+1\right)km^2 - 64\left(e^k-1\right)m^2\big) + 4k\big(k^3 - \left(e^k-1\right) \\ & k^2\sigma_1 - 16\left(e^k-1\right)m^2\sigma_1 - 16km^2\big)\big)\Big\} \Big/ \\ & \Big\{4k\big(\left(e^k-1\right)\left(k^2+16m^2\right)\sinh(2m) + 16e^{k/2}km - 8\left(e^k+1\right)km\cosh(2m)\big)\Big\} \end{aligned}$$

$$\sigma_1 = 0, \qquad b = Da\Big(1 + \frac{1}{\gamma}\Big), \qquad \text{And} \qquad m = \frac{1}{\sqrt{b}}$$

12.4 Linear stability analysis

As in Chapter - 2, by imposing infinitesimal disturbances (δ) on the basic state solutions, ignoring δ^2 and higher order terms, using the usual normal mode form [50] to express infinitesimal disturbances of corresponding field variables, and removing pressure terms from

the resulting equations, the linearized stability equations are obtained as:

$$\begin{aligned}
& Da\Big(1+\frac{1}{\gamma}\Big)\Big[\mu_b\frac{d^4\hat{v}}{dy^4}+2\frac{d\mu_b}{dy}\frac{d^3\hat{v}}{dy^3}-\frac{d^2\hat{v}}{dy^2}\Big(2\mu_b(\alpha^2+\beta^2)-\frac{d^2\mu_b}{dy^2}\Big)-4(\alpha^2+\beta^2)\\
& \frac{d\hat{v}}{dy}\frac{d\mu_b}{dy}+(\alpha^2+\beta^2)\Big(\mu_b(\alpha^2+\beta^2)+\frac{d^2\mu_b}{dy^2}\Big)\hat{v}\Big]-\frac{i\alpha}{\text{va}}\Big(\frac{U_b}{\epsilon}-c\Big)\Big[\frac{d^2\hat{v}}{dy^2}-(\alpha^2+\beta^2)\hat{v}\Big]\\
& +\frac{i\alpha}{\epsilon\text{va}}\frac{d^2U_b}{dy^2}\hat{v}-\mu_b\Big[\frac{d^2\hat{v}}{dy^2}-(\alpha^2+\beta^2)\hat{v}\Big]-\frac{d\mu_b}{dy}\frac{d\hat{v}}{dy}-Da\Big(1+\frac{1}{\gamma}\Big)e^{-kT_0}k\Big[\frac{dU_b}{dy}\frac{d^2\hat{T}}{dy^2}\\
& +\Big(2\frac{d^2U_b}{dy^2}-k\frac{dU_b}{dy}\Big)\frac{d\hat{T}}{dy}+\Big(\frac{d^3U_b}{dy^3}-k\frac{d^2U_b}{dy^2}+\frac{dU_b}{dy}\Big(\frac{k^2}{4}-i\alpha(\alpha^2+\beta^2)\Big)\Big)\hat{T}\Big]\\
& +ke^{-kT_0}\frac{dU_b}{dy}\hat{T}+ke^{-kT_0}\frac{d\hat{T}}{dy}U_b-U_b\frac{k^2}{2}e^{-kT_0}\hat{T}+DaD_\rho\alpha_d\Big[\frac{d^2\hat{v}_p}{dy^2}-(\alpha^2+\beta^2)\hat{v}_p\Big]\\
& -DaD_\rho\alpha_d\Big[\frac{d^2\hat{v}}{dy^2}-(\alpha^2+\beta^2)\hat{v}\Big]-Ra\frac{d\hat{T}}{dy}i\alpha\sin(\theta)-Ra(\alpha^2+\beta^2)\cos(\theta)\hat{T}=0
\end{aligned}\tag{12.29}$$

$$\begin{aligned}
& -\frac{i\alpha D_\rho}{\text{va}}\left(\frac{U_{pb}}{\epsilon}-c\right)\left[\frac{d^2\hat{v}_p}{dy^2}-(\alpha^2+\beta^2)\hat{v}_p\right]+\frac{i\alpha D_\rho}{\epsilon\text{va}}\frac{d^2U_{pb}}{dy^2}\hat{v}_p-DaD_\rho\alpha_d\Big[\frac{d^2\hat{v}_p}{dy^2}\\
& -(\alpha^2+\beta^2)\hat{v}_p\Big]+DaD_\rho\alpha_d\Big[\frac{d^2\hat{v}}{dy^2}-(\alpha^2+\beta^2)\hat{v}\Big]=0
\end{aligned}\tag{12.30}$$

$$\begin{aligned}
& \frac{1}{\text{va}}(-i\alpha c)\hat{\eta}+\frac{1}{\epsilon\text{va}}\Big[\beta\hat{v}\frac{dU_b}{dy}+U_b\hat{\eta}i\alpha\Big]-Da\Big(1+\frac{1}{\gamma}\Big)\Big[\mu_b\frac{d^2\hat{\eta}}{dy^2}+\frac{d\mu_b}{dy}\frac{d\hat{\eta}}{dy}-\mu_b(\alpha^2+\beta^2)\hat{\eta}\Big]\\
& +Da\Big(1+\frac{1}{\gamma}\Big)ke^{-kT_0}\beta\Big[\frac{dU_b}{dy}\frac{d\hat{T}}{dy}-\frac{k}{2}\hat{T}+\frac{d^2U_b}{dy^2}\hat{T}\Big]+\mu_b\hat{\eta}-\beta U_bke^{-kT_0}\hat{T}-\beta Ra\hat{T}sin(\theta)\\
& -DaD_\rho\alpha_d(\hat{\eta}_p-\hat{\eta})=0
\end{aligned}\tag{12.31}$$

$$\frac{D_\rho}{\text{va}}(-i\alpha c)\hat{\eta}_p+\frac{D_\rho}{\epsilon va}\left[\beta\hat{v}_p\frac{dU_{pb}}{dy}+U_{pb}\hat{\eta}_pi\alpha\right]+DaD_\rho\alpha_d(\hat{\eta}_p-\hat{\eta})=0\tag{12.32}$$

$$\frac{dT_0}{dy}\hat{v}+i\alpha\left(U_b-c\right)\hat{T}-\left[\frac{d^2\hat{T}}{dy^2}-(\alpha^2+\beta^2)\hat{T}\right]-D_\rho\alpha_T\gamma_1Pr(\hat{T}_p-\hat{T})=0\tag{12.33}$$

$$\frac{dT_{p0}}{dy}\hat{v}_p+i\alpha\left(U_{pb}-c\right)\hat{T}_p+Pr\alpha_T(\hat{T}_p-\hat{T})=0\tag{12.34}$$

12.5 Results and discussion

The equations from Eqs. (12.29) - (12.34) represent a generalized eigenvalue problem in which the eigenvalues are perturbed and expressed in terms of the wave speed. The spectral technique [107] is employed to find the solution to this eigenvalue problem. In order to validate the accuracy of this method, we ran the MATLAB code for calculating eigenvalues with varying grid point numbers (N) and obtained least stable eigenvalues, which are presented in Table 12.1 for an arbitrary combination of parameters. When $N \geq 50$, the least stable eigenvalue reached convergence criterion of 10^{-7}, and these results remained constant despite varying parameter values. In our numerical calculations, we chose to use $N = 50$ as a result.

The present analysis's outcomes are compared with a vertically oriented channel containing nanofluid-saturated porous material. The results of $\gamma \to \infty$, Pr=7, $\theta = \pi/2$, k=0, $\vec{V_p}$=0, T_p=0, p_p=0, α_T=0, α_d=0, D_ρ=0, in absence of N_B, N_A, ϕ, Le and Rm, were obtained which is in accordance with the findings of Srinivasacharya and Barman [50].

This paper investigates, under two-phase conditions, the convective stability of a dusty Casson fluid flow in a porous inclined channel with changing viscosity. The influence of variable viscosity parameter (k), inclination angle (θ), mass concentration parameter (D_ρ), momentum dust parameter (α_d), thermal dust parameter (α_T), Prandtl number (Pr), and porosity parameter (ϵ) on the flow instability is studied in-depth in this paper. The problem demonstrates two distinct flow problems under the following conditions:

1. $\gamma \to \infty$ represents Newtonian dusty fluid flow problem,
2. Non-Newtonian dusty Casson fluid flow problem with a finite value for γ.

In Figs. 12.1-12.7, we observe a similar flow instability pattern for both phases. However, dusty fluids are always located below dusty Casson fluids.

Fig. 12.1 depicts the graphs illustrating the critical Rayleigh number (Ra_c) and the critical wavenumber (α_c) vary with variations in the Darcy number (Da) for various inclination angles (θ). As θ changes from horizontal to vertical, Ra_c decreases for both phases, demonstrating that destabilizes the fluid flow. This is due to when a channel is tilted, gravity acts perpendicular to the flow direction, causing density gradients to form within the flow. These density gradients can cause particles to descend to the bottom of the flow, while lighter fluid rises to the surface. In contrast, as the Darcy number (Da) increases, so does Ra_c, indicating that permeability has a stabilizing effect. In addition, once Da reaches 1, Ra_c increases rapidly as Da continues to ascend. For lower Darcy numbers ($Da < 1$), Ra_c displays slow and smooth fluctuations, highlighting that there is visible flow resistance within the porous medium. This resistance to flow falls as permeability rises, resulting in enhanced flow within the porous medium and highlighting the importance of viscous forces in the momentum equation. In terms of the critical wavenumber (α_c), it increases as both Da and θ increases.

For various values of the variable viscosity parameter (k), Fig. 12.2 displays the variation of the critical Rayleigh number and the critical wavenumber. We observed that Ra_c drops when we increase k. This indicates k destabilizes the fluid flow. Because of when the viscosity of the two-phase dusty Casson fluid decreases with increasing shear rate, it can cause the flow to become unstable and exhibit turbulent behavior. As the fluid moves down the inclined channel, it is subjected to increasing shear rates due to the effects of gravity, which can cause the viscosity to decrease. This can lead to fluid instabilities. On the other hand, if the viscosity of the two-phase dusty Casson fluid increases with increasing shear rate, it can cause the flow to become unstable and exhibit shear-thickening behavior. This can lead to the formation of highly viscous regions in the flow, which can cause a buildup of stress and the formation of flow instabilities. But as Da rises, Ra_c rises as well. In case of critical wavenumber, α_c decreases as k increases. However, as Da increases, α_c also increases.

For different values of the mass concentration parameter (D_ρ), Fig. 12.3 displays the variation of the critical Rayleigh number and the critical wavenumber. We noticed that as Da increases, so does Ra_c. Also, as D_ρ increases, Ra_c increases. Hence, D_ρ stabilizes the flow. If the concentration of the dust particles is too high, they can settle out of the fluid and accumulate at the bottom of the channel. This can lead to a non-uniform distribution of dust particles, which can affect the fluid's rheological properties. On the other hand, if the concentration of the dust particles is too low, they may not significantly affect the fluid's flow properties. In this case, the fluid flow may still be unstable and turbulent due to the effects of gravity. However, as Da rises, α_c increases, but as D_ρ increases, α_c decreases.

The critical Rayleigh number and the critical wavenumber variations for different thermal dust parameter (α_T) values are shown in Fig.12.4. We've observed that as Da increases, so does Ra_c. However, there is no variation in Ra_c as α_T increases. Consequently, α_T does not significantly affect the stability of the two-phase dusty Casson fluid flow. This might occur because in the two-phase dusty Casson fluid flow, the thermal dust parameter mainly affects the thermal conductivity of the fluid by increasing it due to the presence of particles. However, this increase in thermal conductivity does not typically have a significant effect on flow stability. α_c increases as Da increases, whereas α_c does not alter as α_T increases.

Fig. 12.5 depicts the variations in the critical Rayleigh number and critical wavenumber for distinct momentum dust parameter (α_d) values. We've observed that as Da and α_d both rise, so does Ra_c. This means that α_d stabilizes fluid flow. This could happen because the momentum dust parameter can also affect the rheological properties of the fluid, such as its viscosity and yield stress. The presence of solid particles can significantly alter the rheological properties of the fluid, leading to complex flow behavior. A higher momentum dust parameter can result in a higher viscosity and yield stress, which can stabilize the flow and prevent instabilities. Also, as Da increases, so does α_c, whereas as α_d increases, α_c decreases.

The impact of Prandtl number (Pr) on the instability boundaries is seen in Fig. 12.6. As momentum diffusivity increases, defined by the Prandtl number (Pr), so does the critical Rayleigh number. As a consequence, It demonstrates Pr stabilizes the flow field by promoting a more uniform temperature and viscosity profile, reducing thermal gradients, and promoting the development of thermal boundary layers that can dampen out disturbances in the flow. Moreover, α_c increases as Da and Pr grows. Also, as Pr rises, α_c falls.

Fig. 12.7 depicts the boundaries of the instability region and how they vary as the permeability parameter (Da) and porosity parameter (ϵ) change. As shown in Fig. 12.7, the critical Rayleigh number (Ra_c) tends to increase as the porosity parameter increases. This trend occurs because porosity represents the proportion of a material's total volume that is occupied by vacancies, essentially measuring the voids within a porous material. Therefore, contributes to the stabilization of the flow. As porosity increases, so does the volume of spaces within the material. In addition, it can be observed that α_c, the critical wavenumber, increases as porosity parameter value and the value of Da increase.

Table 12.1: "Convergence of the least stable eigenvalue for Da = 0.1, Pr = 0.1, ϵ = 0.1, γ=0.1, γ_1=0.1, D_ρ=10, α_T=1.2, α_d=1.2, $\theta = \pi/3$, k=0.5, and β = 0."

N	Ra_c	α_c
40	24.139683655331	1.112686406858
45	24.139879110283	1.112610790954
50	24.139208852480	1.112691392299
55	24.139401259160	1.112658138375
60	24.139908862954	1.112608748722

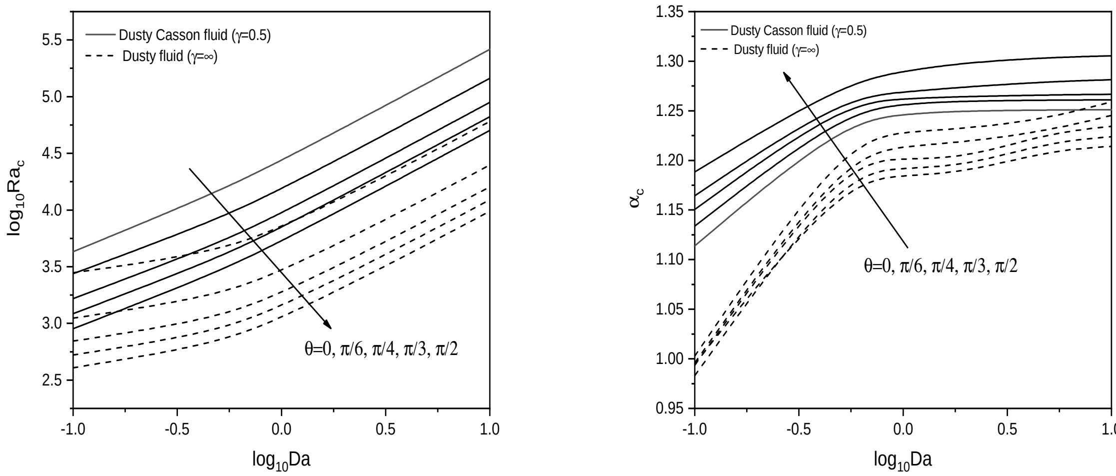

Figure 12.1: “Variation of critical Rayleigh number (Ra_c) and critical wavenumber (α_c) with $log_{10}Da$ for different values of θ with $Pr = 7$, k=0.5, $\epsilon = 0.3$, γ_1=0.1, D_ρ=10, α_T=1.2, α_d=1.2, Λ=1, and $\beta = 0$.”

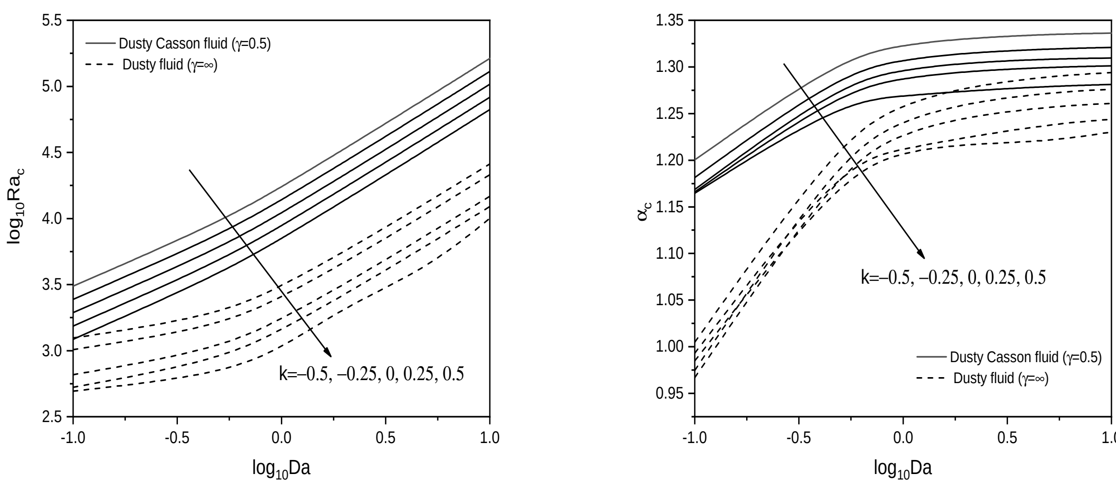

Figure 12.2: “Variation of critical Rayleigh number (Ra_c) and critical wavenumber (α_c) with $log_{10}Da$ for different values of k with $\theta = \pi/3$, $Pr = 7$, $\epsilon = 0.3$, γ_1=0.1, D_ρ=10, α_T=1.2, α_d=1.2, Λ=1, and $\beta = 0$.”

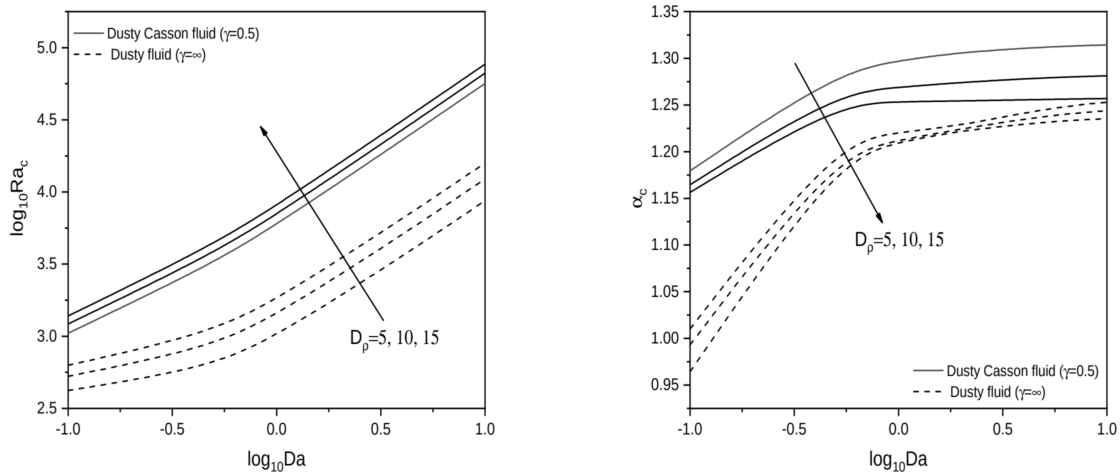

Figure 12.3: "Variation of critical Rayleigh number (Ra_c) and critical wavenumber (α_c) with $log_{10}Da$ for different values of D_ρ with $Pr = 7$, k=0.5, $\epsilon = 0.3$, γ_1=0.1, $\theta = \pi/3$, α_T=1.2, α_d=1.2, Λ=1, and $\beta = 0$."

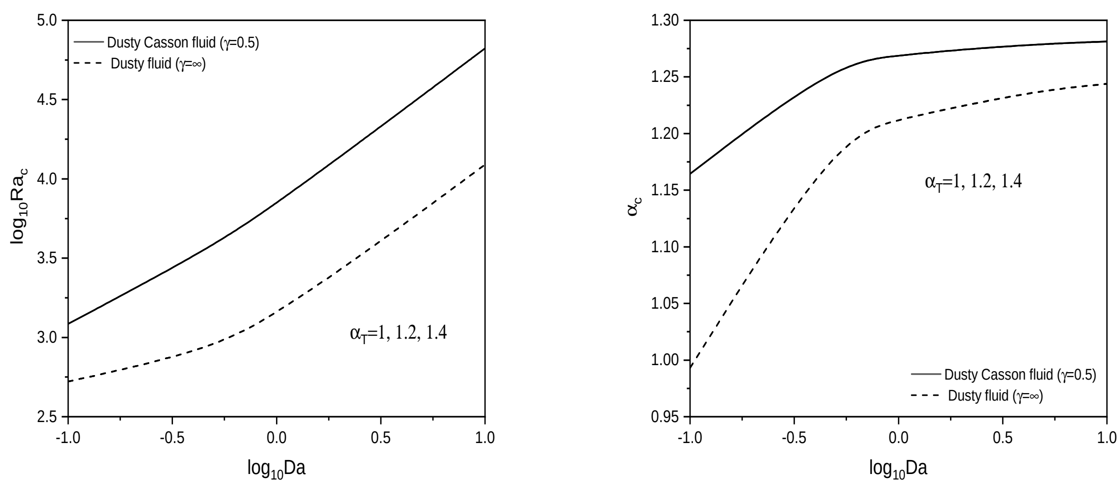

Figure 12.4: "Variation of critical Rayleigh number (Ra_c) and critical wavenumber (α_c) with $log_{10}Da$ for different values of α_T with $Pr = 7$, k=0.5, $\epsilon = 0.3$, γ_1=0.1, D_ρ=10, α_d=1.2, $\theta = \pi/3$, Λ=1, and $\beta = 0$."

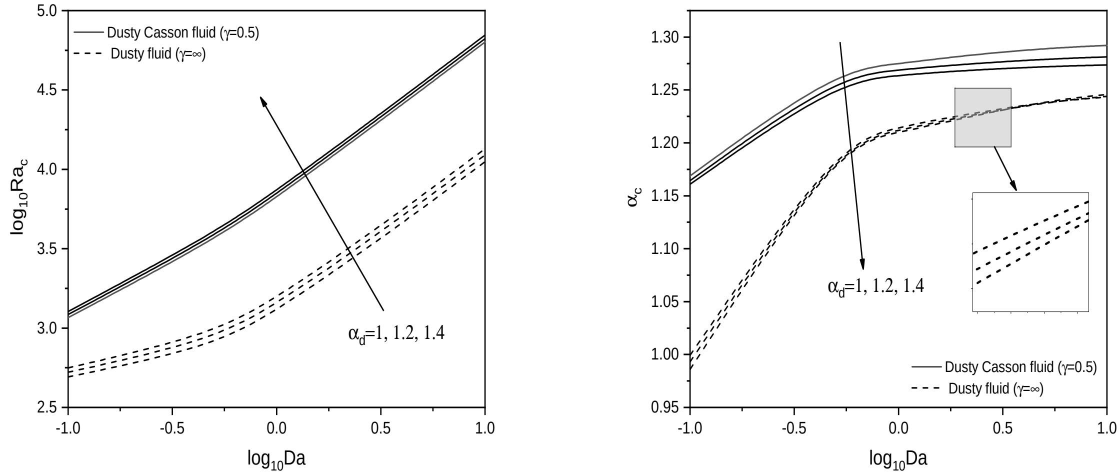

Figure 12.5: "Variation of critical Rayleigh number (Ra_c) and critical wavenumber (α_c) with $log_{10}Da$ for different values of α_d with $Pr = 7$, k=0.5, $\epsilon = 0.3$, γ_1=0.1, D_ρ=10, α_T=1.2, $\theta = \pi/3$, Λ=1, and $\beta = 0$."

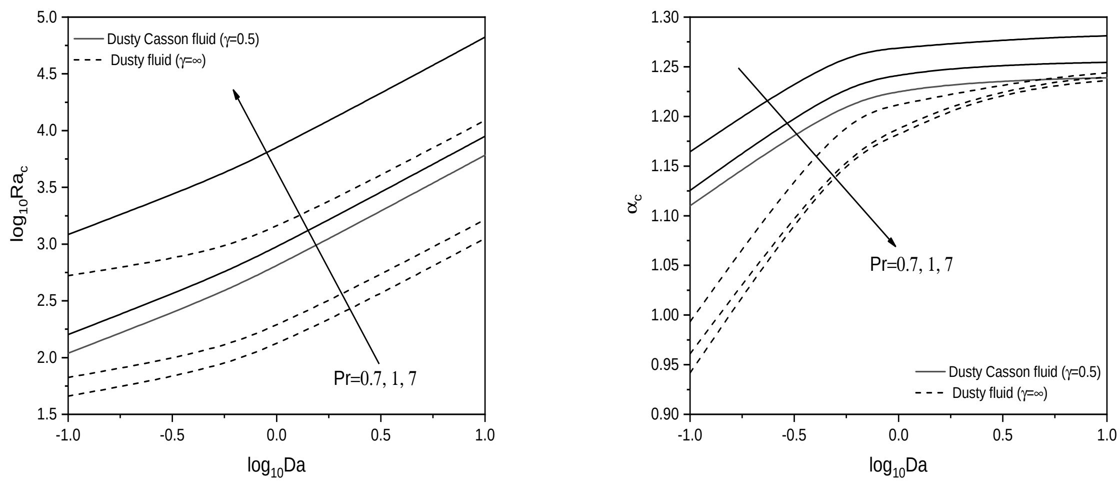

Figure 12.6: "Variation of critical Rayleigh number (Ra_c) and critical wavenumber (α_c) with $log_{10}Da$ for different values of Pr with $\epsilon = 0.3$, k=0.5, γ_1=0.1, D_ρ=10, α_T=1.2, α_d=1.2, $\theta = \pi/3$, Λ=1, and $\beta = 0$."

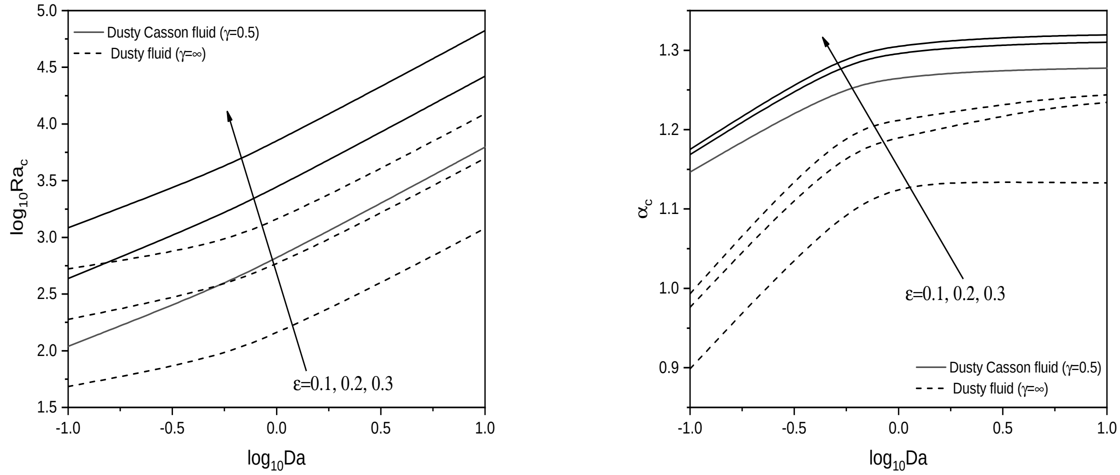

Figure 12.7: "Variation of critical Rayleigh number (Ra_c) and critical wavenumber (α_c) with $log_{10}Da$ for different values of ϵ with $Pr = 7$, k=0.5, γ_1=0.1, D_ρ=10, α_T=1.2, α_d=1.2, $\theta = \pi/3$, Λ=1, and $\beta = 0$."

12.6 Conclusions

The linear stability of two-phase dusty Casson fluid flow in a porous inclined channel while accounting for the effect of changing viscosity is examined. The critical Rayleigh number and critical wavenumber for different parameters such as θ, k, D_ρ, α_T, α_d, Pr and ϵ are computed and graphically shown with respect to Da.

- The variable viscosity parameter (k), and channel's inclination angle (θ) destabilizes the flow for both phases.
- Mass concentration parameter (D_ρ), momentum dust parameter (α_d), Prandtl number (Pr), and porosity parameter (ϵ) help to stabilize flow within an inclined channel. As a result, an increase in these variables acts as a stumbling block to the onset of convection.
- When the channel is oriented vertically, and k=0.5 the flow has the least stability.

Chapter 13

The effects of heat source/sink and radiation on the flow stability of two-phase dusty Casson fluid in a porous inclined channel [1]

13.1 Introduction

The stability properties of two-phase dusty Casson fluid in an inclined porous channel with heat source/sink and radiation effect has not been. Consequently, this chapter investigates the heat source/sink and radiation effect convection stability in two-phase dusty Casson fluid flow in an inclined porous channel (at an angle of inclination θ).

13.2 Mathematical Formulation

Consider an unsteady, incompressible flow of a two-phase dusty Casson fluid in tilted channel with a width of $2L$ with two impermeable, completely thermally conducting walls and an inclination of θ. A schematic illustration of the problem is shown in Fig. 11.1. The porous medium is assumed to be homogenous and isotropic. Temperatures on both the upper and lower walls are kept at T_2 and T_1, respectively. Using the above assumptions and

[1] Communicated in "***Transport in Porous Media***"

the Oberbeck-Boussinesq approximation, the following set of equations describes the flow [113, 50, 114]:
For the fluid phase:

$$\nabla \cdot \vec{V} = 0 \tag{13.1}$$

$$\begin{aligned}\frac{\rho}{\epsilon}\left(\frac{\partial \vec{V}}{\partial t} + \frac{1}{\epsilon}(\vec{V}\cdot\nabla)\vec{V}\right) = -\nabla p + \Big(1+\frac{1}{\gamma}\Big)\tilde{\mu}\nabla^2\vec{V} - \frac{\mu}{K}\vec{V} + \rho \mathbf{g}\beta_T(T-T_1)\\ (\sin(\theta)\hat{e_{\mathrm{x}}} + \cos(\theta)\hat{e_{\mathrm{y}}}) + \frac{\rho_p}{\tau_m}(\vec{V}_p - \vec{V})\end{aligned} \tag{13.2}$$

$$\rho C_p\left(\frac{\partial T}{\partial t} + \vec{V}\cdot\nabla T\right) = k\nabla^2 T + Q_0(T-T_1) - \nabla q_r + \frac{\rho_p C_s}{\tau_T}(T_p - T) \tag{13.3}$$

For the particle phase:

$$\nabla \cdot \vec{V_p} = 0 \tag{13.4}$$

$$\frac{\rho_p}{\epsilon}\left(\frac{\partial \vec{V_p}}{\partial t} + \frac{1}{\epsilon}(\vec{V_p}\cdot\nabla)\vec{V_p}\right) = -\nabla p_p - \frac{\rho_p}{\tau_m}(\vec{V_p} - \vec{V}) \tag{13.5}$$

$$\rho_p C_s\left(\frac{\partial T_p}{\partial t} + \vec{V_p}\cdot\nabla T_p\right) = -\frac{\rho_p C_s}{\tau_T}(T_p - T) \tag{13.6}$$

The boundary conditions for the fluid phase:

$$y=-L: \quad \vec{V}=0, \quad T=T_1, \quad y=L: \quad \vec{V}=0, \quad T=T_2 \tag{13.7}$$

The boundary conditions for the particle phase:

$$y=-L: \quad \vec{V_p}=0, \quad T_p=T_1, \quad y=L: \quad \vec{V_p}=0, \quad T_p=T_2 \tag{13.8}$$

where, Q_0 is dimensional heat source/sink, and $q_r = -16\eta^2\sigma T^3\nabla T/3\beta_R$ radiative heat flux. The non-dimensional form of the Eqs. (13.1) -(13.6) (on substituting (11.9) in (13.1) -(13.6) and removing asterisk) are: For the fluid phase:

$$\nabla \cdot \vec{V} = 0 \tag{13.9}$$

$$\begin{aligned}\frac{1}{\mathrm{va}}\frac{\partial \vec{V}}{\partial t} + \frac{1}{\epsilon \mathrm{va}}(\vec{V}\cdot\nabla)\vec{V} = -\nabla p + \Lambda Da\Big(1+\frac{1}{\gamma}\Big)(\nabla^2\vec{V}) - \vec{V} + RaT\\ (\sin(\theta)\hat{e_{\mathrm{x}}} + \cos(\theta)\hat{e_{\mathrm{y}}}) + D_\rho\alpha_d Da(\vec{V_p} - \vec{V})\end{aligned} \tag{13.10}$$

$$\frac{\partial T}{\partial t} + \vec{V} \cdot \nabla T = (1 + R_d)\nabla^2 T + QT + D_\rho \gamma_1 \alpha_T Pr(T_p - T) \tag{13.11}$$

For the particle phase:

$$\nabla \cdot \vec{V_p} = 0 \tag{13.12}$$

$$\frac{D_\rho}{\text{v}a}\frac{\partial \vec{V_p}}{\partial t} + \frac{D_\rho}{\epsilon \text{v}a}(\vec{V_p} \cdot \nabla)\vec{V_p} = -\nabla p_p - D_\rho \alpha_d Da(\vec{V_p} - \vec{V}) \tag{13.13}$$

$$\frac{\partial T_p}{\partial t} + \vec{V_p} \cdot \nabla T_p = -Pr\alpha_T(T_p - T) \tag{13.14}$$

The fluid phase's boundary conditions are as follows:

$$\vec{V} = 0, \quad T = 0, \quad at \quad y = -1, \quad and \quad \vec{V} = 0, \quad T = 1 \quad at \quad y = 1 \tag{13.15}$$

The particle phase's boundary conditions are as follows:

$$\vec{V_p} = 0, \quad T_p = 0, \quad at \quad y = -1, \quad and \quad \vec{V_p} = 0, \quad T_p = 1 \quad at \quad y = 1 \tag{13.16}$$

where R_d=$\frac{16\eta^2\sigma T^3}{3\beta_R}$ represents radiation parameter, and $Q = \frac{Q_0 L^2}{k}$ represents heat source/sink parameter.

13.3 Basic solution

In the basic stage, the flow is regarded as continuous, one-directional (in the x-direction), and completely developed. Eqs. (13.9)-(13.14) may be reduced into set of ordinary differential equations by applying these conditions:

$$\Lambda Da\Big(1 + \frac{1}{\gamma}\Big)\frac{d^2 U_b}{dy^2} - U_b = \frac{\partial p_0}{\partial x} - RaT_0 \sin(\theta) - D_\rho \alpha_d Da(U_{pb} - U_b) \tag{13.17}$$

$$\frac{\partial p_0}{\partial y} = RaT_0 \cos(\theta) \tag{13.18}$$

$$\frac{\partial p_0}{dz} = 0 \tag{13.19}$$

$$(1 + R_d)\frac{d^2 T_0}{dy^2} + QT_0 + D_\rho \gamma_1 \alpha_T Pr(T_{p0} - T_0) = 0 \tag{13.20}$$

$$\frac{\partial p_{p0}}{\partial x} + D_\rho \alpha_d Da(U_{pb} - U_b) = 0 \tag{13.21}$$

$$\frac{\partial p_{p0}}{\partial y} = 0 \tag{13.22}$$

$$\frac{\partial p_{p0}}{dz} = 0 \tag{13.23}$$

$$Pr\alpha_T (T_{p0} - T_0) = 0 \tag{13.24}$$

The boundary conditions are:

$$\begin{aligned} y = -1: \quad & U_b = 0, \quad U_{pb} = 0, \quad T_0 = 0, \quad T_{p0} = 0, \\ y = 1: \quad & U_b = 0, \quad U_{pb} = 0, \quad T_0 = 1 \quad T_{p0} = 1, \end{aligned} \tag{13.25}$$

Proceeding as in Chapter-2, we get basic solution as:

$$T_0 = T_{p0} = \frac{1}{2}\left(\frac{\cos(\sqrt{m}y)}{\cos(\sqrt{m})} + \frac{\sin(\sqrt{m}y)}{\sin(\sqrt{m})}\right) \tag{13.26}$$

$$\begin{aligned} U_b = \frac{1}{2\left(m + m_1^2\right)}\Big(&\operatorname{sech}(m_1)\cosh(m_1 y)\big(2(\sigma + \sigma_1)\big(m + m_1^2\big) - m_1^2 \mathrm{Ra}\sin(\theta)\big) \\ &-2(\sigma + \sigma_1)\left(m + m_1^2\right) + m_1^2 \mathrm{Ra}\sin(\theta)\big(2\csc\left(2\sqrt{m}\right)\sin\left(\sqrt{m}(y+1)\right) \\ &-\operatorname{csch}(m_1)\sinh(m_1 y)\big)\Big) \end{aligned} \tag{13.27}$$

$$\begin{aligned} U_{pb} = -\frac{\sigma_1}{DaD_\rho \alpha_d} + \frac{1}{2\left(m + m_1^2\right)}\Big(&\operatorname{sech}(m_1)\cosh(m_1 y)\big(2(\sigma + \sigma_1)\big(m + m_1^2\big) - m_1^2 \mathrm{Ra}\sin(\theta)\big) \\ &-2(\sigma + \sigma_1)\left(m + m_1^2\right) + m_1^2 \mathrm{Ra}\sin(\theta)\big(2\csc\left(2\sqrt{m}\right)\sin\left(\sqrt{m}(y+1)\right) \\ &-\operatorname{csch}(m_1)\sinh(m_1 y)\big)\Big) \end{aligned} \tag{13.28}$$

where:

$$\sigma = \frac{\tanh(m_1)\left(\frac{m_1 \mathrm{Ra}\sin(\theta)}{m + m_1^2} - \frac{2\sigma_1}{m_1}\right) - \frac{m_1^2 \mathrm{Ra}\tan\left(\sqrt{m}\right)\sin(\theta)}{\sqrt{m}\left(m + m_1^2\right)} + 2\sigma_1 + 2}{\frac{2\tanh(m_1)}{m_1} - 2},$$

$$\sigma_1 = 0, \quad m_1 = \frac{1}{\sqrt{\Lambda Da\left(1 + \frac{1}{\gamma}\right)}}, \quad \text{And,} \quad m = \frac{Q}{1 + R_d}$$

13.4 Linear stability analysis

As in Chapter - 2, by imposing infinitesimal disturbances (δ) on the basic state solutions, ignoring δ^2 and higher order terms, using the usual normal mode form [50] to express infinitesimal disturbances of corresponding field variables, and removing pressure terms from the resulting equations, the linearized stability equations are obtained as:

$$\Lambda Da\Big(1+\frac{1}{\gamma}\Big)\left[\frac{d^4\hat{v}}{dy^4}-2\frac{d^2\hat{v}}{dy^2}(\alpha^2+\beta^2)+(\alpha^2+\beta^2)^2\hat{v}\right]-\frac{i\alpha}{\mathrm{va}}\left(\frac{U_b}{\epsilon}-c\right)\left[\frac{d^2\hat{v}}{dy^2}-(\alpha^2+\beta^2)\hat{v}\right]$$
$$+\frac{i\alpha}{\epsilon\mathrm{va}}\frac{d^2U_b}{dy^2}\hat{v}-\left[\frac{d^2\hat{v}}{dy^2}-(\alpha^2+\beta^2)\hat{v}\right]-Rai\alpha\frac{d\hat{T}}{dy}\sin(\theta)-Ra(\alpha^2+\beta^2)\cos(\theta)\hat{T}$$
$$+DaD_\rho\alpha_d\Big[\frac{d^2\hat{v}_p}{dy^2}-(\alpha^2+\beta^2)\hat{v}_p\Big]-DaD_\rho\alpha_d\Big[\frac{d^2\hat{v}}{dy^2}-(\alpha^2+\beta^2)\hat{v}\Big]=0 \tag{13.29}$$

$$-\frac{i\alpha D_\rho}{\mathrm{va}}\left(\frac{U_{pb}}{\epsilon}-c\right)\left[\frac{d^2\hat{v}_p}{dy^2}-(\alpha^2+\beta^2)\hat{v}_p\right]+\frac{i\alpha D_\rho}{\epsilon\mathrm{va}}\frac{d^2U_{pb}}{dy^2}\hat{v}-DaD_\rho\alpha_d\Big[\frac{d^2\hat{v}_p}{dy^2}-(\alpha^2+\beta^2)\hat{v}_p\Big]$$
$$+DaD_\rho\alpha_d\Big[\frac{d^2\hat{v}}{dy^2}-(\alpha^2+\beta^2)\hat{v}\Big]=0 \tag{13.30}$$

$$\frac{1}{\mathrm{va}}(-i\alpha c)\hat{\eta}+\frac{1}{\epsilon va}\left[\beta\hat{v}\frac{dU_b}{dy}+U_b\hat{\eta}i\alpha\right]-\Lambda Da\Big(1+\frac{1}{\gamma}\Big)\left[\frac{d^2\hat{\eta}}{dy^2}-(\alpha^2+\beta^2)\hat{\eta}\right]+\hat{\eta}$$
$$-\beta Ra\hat{T}\sin(\theta)-DaD_\rho\alpha_d(\hat{\eta}_p-\hat{\eta})=0 \tag{13.31}$$

$$\frac{D_\rho}{\mathrm{va}}(-i\alpha c)\hat{\eta_p}+\frac{D_\rho}{\epsilon va}\left[\beta\hat{v}_p\frac{dU_{pb}}{dy}+U_{pb}\hat{\eta}_p i\alpha\right]+DaD_\rho\alpha_d(\hat{\eta}_p-\hat{\eta})=0 \tag{13.32}$$

$$\frac{dT_0}{dy}\hat{v}+i\alpha\left(U_b-c\right)\hat{T}-(1+R_d)\left[\frac{d^2\hat{T}}{dy^2}-(\alpha^2+\beta^2)\hat{T}\right]-Q\hat{T}-D_\rho\alpha_T\gamma_1 Pr(\hat{T}_p-\hat{T})=0 \tag{13.33}$$

$$\frac{dT_{p0}}{dy}\hat{v}_p+i\alpha\left(U_{pb}-c\right)\hat{T}_p+Pr\alpha_T(\hat{T}_p-\hat{T})=0 \tag{13.34}$$

13.5 Results and discussion

The equations from Eqs. (13.29) - (13.34) represent a generalized eigenvalue problem in which the eigenvalues are perturbed and expressed in terms of the wave speed. The spectral technique [107] is employed to find the solution to this eigenvalue problem. In order to validate the accuracy of this method, we ran the MATLAB code for calculating eigenvalues with varying grid point numbers (N) and obtained least stable eigenvalues, which are presented in Table 13.1 for an arbitrary combination of parameters. When $N \geq 50$, the least stable eigenvalue reached convergence criterion of 10^{-7}, and these results remained constant despite varying parameter values. In our numerical calculations, we chose to use $N = 50$ as a result.

The present analysis's outcomes are compared with a vertically oriented channel containing nanofluid-saturated porous material. The results of $\gamma \to \infty$, Pr=7, $\theta = \pi/2$, $\vec{V_p}$=0, T_p=0, p_p=0, α_T=0, α_d=0, D_ρ=0, Q=0, and R_d=0 in absence of N_B, N_A, ϕ, Le and Rm, were obtained which is in accordance with the findings of Srinivasacharya and Barman [50].

This paper investigates, under two-phase conditions, the convective stability of a dusty Casson fluid flow in a porous inclined channel with changing viscosity. The influence of heat source/sink parameter (Q), Radiation parameter (R_d), inclination angle (θ), mass concentration parameter (D_ρ), momentum dust parameter (α_d), thermal dust parameter (α_T), Prandtl number (Pr) , and porosity parameter (ϵ) on the flow instability is studied in-depth in this paper. The problem demonstrates two distinct flow problems under the following conditions:

1. $\gamma \to \infty$ represents the Newtonian dusty fluid flow problem,

2. Non-Newtonian, dusty Casson fluid flow problem with a finite value for γ.

In Figs. 13.1-13.8, we observe a similar flow instability pattern for both phases. However, dusty fluids are always located below dusty Casson fluids.

Fig. 13.1 depicts the graphs illustrating the critical Rayleigh number (Ra_c) and the critical wavenumber (α_c) vary with variations in the Darcy number (Da) for various inclination angles (θ). As θ changes from horizontal to vertical, Ra_c decreases for both phases, demonstrating that destabilizes the fluid flow. This is due to when a channel is tilted, gravity acts perpendicular to the flow direction, causing density gradients to form within the flow. These density gradients can cause particles to descend to the bottom of the flow, while lighter fluid rises to the surface. In contrast, as the Darcy number (Da) increases, so does Ra_c, indicating that permeability has a stabilizing effect. In addition, once Da reaches 1, Ra_c increases rapidly as Da continues to ascend. For lower Darcy numbers ($Da < 1$), Ra_c displays slow and smooth fluctuations, highlighting that there is visible flow resistance within the porous medium. This resistance to flow falls as permeability rises, resulting in enhanced flow within the porous medium and highlighting the importance of viscous forces in the momentum equation. In terms of the critical wavenumber, it increases as both Da and θ increases.

For different values of the mass concentration parameter (D_ρ), Fig. 13.2 displays the variation of the critical Rayleigh number and the critical wavenumber. We noticed that as Da increases, so does Ra_c. Also, as D_ρ increases, Ra_c increases. Hence, D_ρ stabilizes the flow. If the concentration of the dust particles is too high, they can settle out of the fluid and accumulate at the bottom of the channel. This can lead to a non-uniform distribution of dust particles, which can affect the fluid's rheological properties. On the other hand, if the concentration of the dust particles is too low, they may not significantly affect the fluid's flow properties. In this case, the fluid flow may still be unstable and turbulent due to the effects of gravity. However, as Da rises, α_c increases, but as D_ρ increases, α_c decreases.

For different values of the heat source/sink parameter (Q), Fig. 13.3 displays the variation of the critical Rayleigh number (Ra_c) and critical wavenumber (α_c). We noticed that as Da increases, so does Ra_c. However, as Q increases, Ra_c falls significantly. Hence Q destabilizes the flow due to the coupling between heat transfer and fluid flow. When a fluid is subjected to a heat source or sink, it causes temperature variations, which in turn affect the fluid's properties, such as density and viscosity. In the case of a two-phase dusty Casson fluid flow, the presence of particles further complicates the situation, as the particles can interact with the fluid and alter its properties. However, as Da and Q both rise, α_c increases.

The critical Rayleigh number and critical wavenumber for radiation parameter (R_d) are shown fluctuating in Fig. 13.4. We have noticed that there is a slight increase in Ra_c as R_d increases. It demonstrates that R_d had a stabilizing effect on the flow field. Because Radiation parameter can promote thermal equilibrium by balancing the energy transfer in the fluid. This can reduce the temperature gradients and promote a more uniform temperature distribution in the fluid. As a result, the fluid's properties, such as density and viscosity, become more stable and predictable, leading to a more stable flow. Additionally, the presence of particles in a two-phase dusty Casson fluid flow can also promote stability. The particles can act as a stabilizing mechanism by damping the fluid's motion and reducing turbulence. Also, as we increase Da, Ra_c increases. However, when R_d rises, α_c decreases. But as Da rises, α_c rises as well.

The critical Rayleigh number and critical wavenumber variations for different thermal dust parameter (α_T) values are shown in Fig.13.5. We've observed that as Da increases, so does Ra_c. However, there is no variation in Ra_c as α_T increases. Consequently, α_T does not significantly affect the stability of the two-phase dusty Casson fluid flow. This might occur because in the two-phase dusty Casson fluid flow, the thermal dust parameter mainly affects the thermal conductivity of the fluid by increasing it due to the presence of particles. However, this increase in thermal conductivity does not typically have a significant effect on the flow stability. α_c increases as Da increases, whereas α_c does not alter as α_T increases.

Fig. 13.6 depicts the variations in the critical Rayleigh number and critical wavenumber for different momentum dust parameter (α_d) values. We've observed that as Da and α_d both rise, so does Ra_c. This means that α_d stabilizes fluid flow. This could happen because the momentum dust parameter can also affect the rheological properties of the fluid, such as its viscosity and yield stress. The presence of solid particles can significantly alter the rheological properties of the fluid, leading to complex flow behavior. A higher momentum dust parameter can result in a higher viscosity and yield stress, which can stabilize the flow and prevent instabilities. Also, as Da increases, so does α_c, whereas as α_d increases, α_c decreases.

The impact of Prandtl number (Pr) on the instability boundaries is seen in Fig. 13.7. As momentum diffusivity increases, defined by the Prandtl number (Pr), so does the critical Rayleigh number. As a consequence, It demonstrates Pr stabilizes the flow field by promoting a more uniform temperature and viscosity profile, reducing thermal gradients, and promoting the development of thermal boundary layers that can dampen out disturbances in the flow. Moreover, α_c increases as Da and Pr grows. Also, as Pr rises, α_c falls.

Fig. 13.8 depicts the boundaries of the instability region and how they vary as the permeability parameter (Da) and porosity parameter (ϵ) change. As shown in Fig. 13.8, the critical Rayleigh number (Ra_c) tends to increase as the porosity parameter increases. This trend occurs because porosity represents the proportion of a material's total volume that is occupied by vacancies, essentially measuring the voids within a porous material. Therefore, contributes to the stabilization of the flow. As porosity increases, so does the volume of spaces within the material. In addition, it can be observed that α_c, the critical wavenumber, increases as porosity parameter value and the value of Da increase.

Table 13.1: "Convergence of the least stable eigenvalue for $Da = 0.1$, $Pr = 0.1$, $\epsilon = 0.1$, γ=0.1, γ_1=0.1, D_ρ=10, α_T=1.2, α_d=1.2, R_d=0.5, Q=0.3, $\theta = \pi/3$, Λ=1, and $\beta = 0$."

N	Ra_c	α_c
40	31.098136130712	1.221563612044
45	31.098160037968	1.221554606938
50	31.098167907749	1.221533438558
55	31.098184630907	1.221386254531
60	31.098144341013	1.221403510588

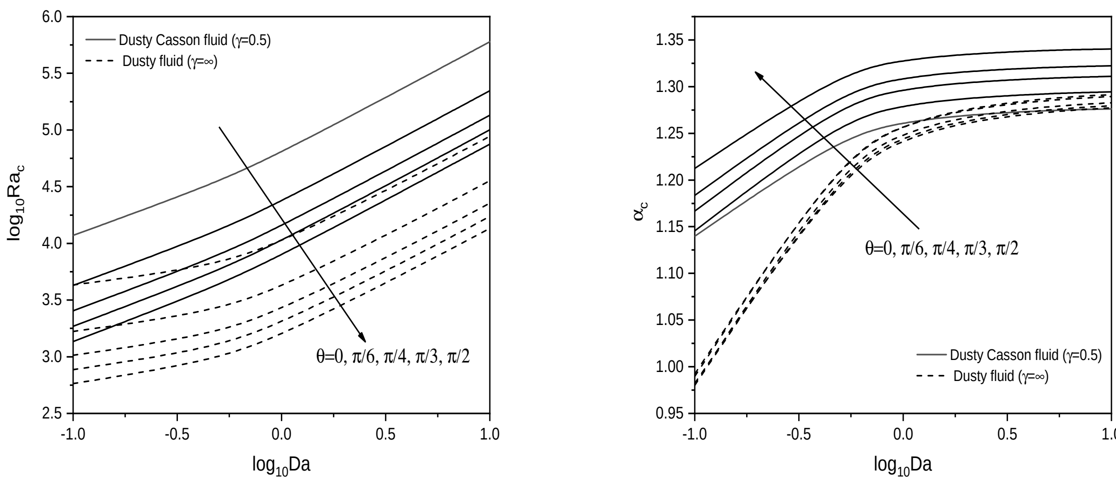

Figure 13.1: "Variation of critical Rayleigh number (Ra_c) and critical wavenumber (α_c) with $log_{10}Da$ for different values of θ with $Pr = 7$, $\epsilon = 0.3$, γ_1=0.1, D_ρ=10, α_T=1.2, α_d=1.2, R_d=0.5, Q=0.3, Λ=1, and $\beta = 0$."

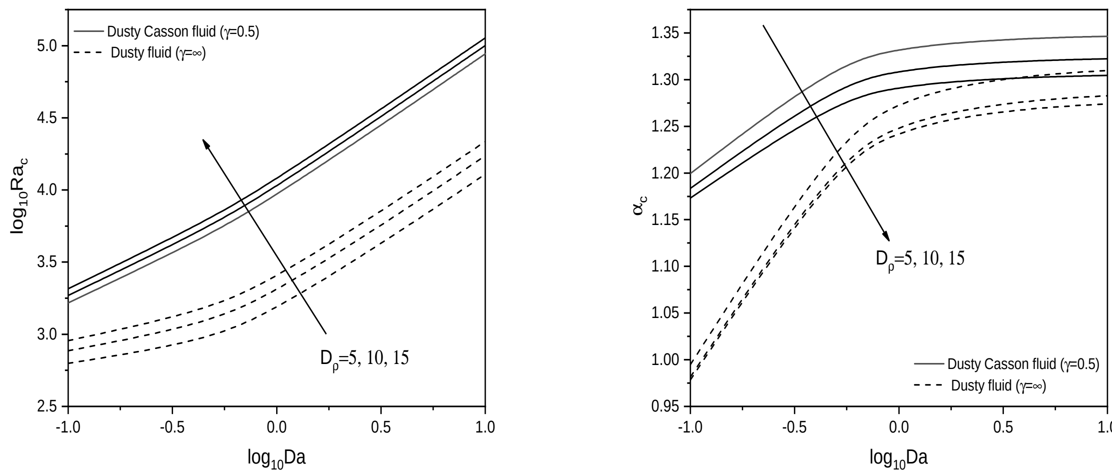

Figure 13.2: "Variation of critical Rayleigh number (Ra_c) and critical wavenumber (α_c) with $log_{10}Da$ for different values of D_ρ with $Pr = 7$, $\epsilon = 0.3$, γ_1=0.1, α_T=1.2, α_d=1.2, R_d=0.5, Q=0.3, $\theta = \pi/3$, Λ=1, and $\beta = 0$."

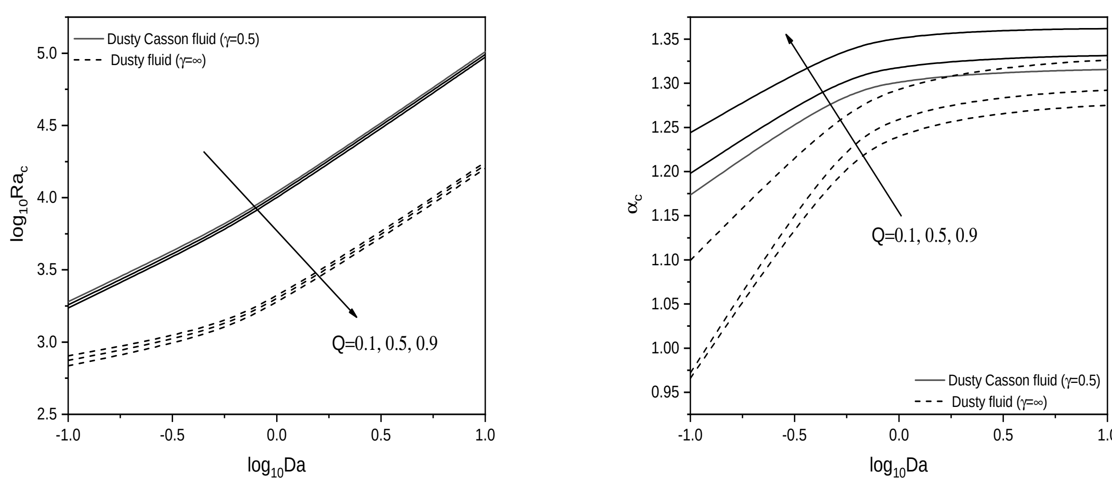

Figure 13.3: "Variation of critical Rayleigh number (Ra_c) and critical wavenumber (α_c) with $log_{10}Da$ for different values of Q with $Pr = 7$, $\epsilon = 0.3$, γ_1=0.1, D_ρ=10, α_T=1.2, α_d=1.2, R_d=0.5, $\theta = \pi/3$, Λ=1, and $\beta = 0$."

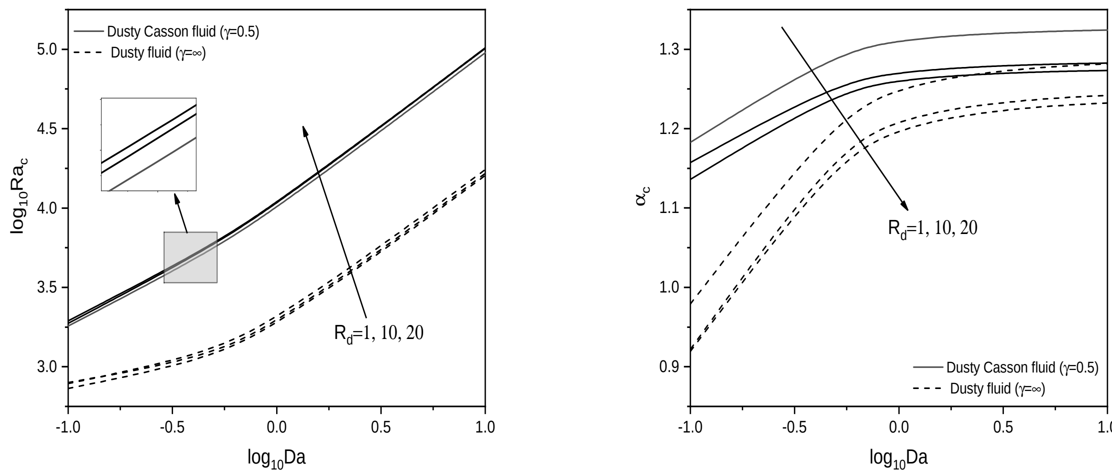

Figure 13.4: "Variation of critical Rayleigh number (Ra_c) and critical wavenumber (α_c) with $log_{10}Da$ for different values of R_d with $Pr = 7$, $\epsilon = 0.3$, γ_1=0.1, D_ρ=10, α_T=1.2, α_d=1.2, Q=0.3, $\theta = \pi/3$, Λ=1, and $\beta = 0$."

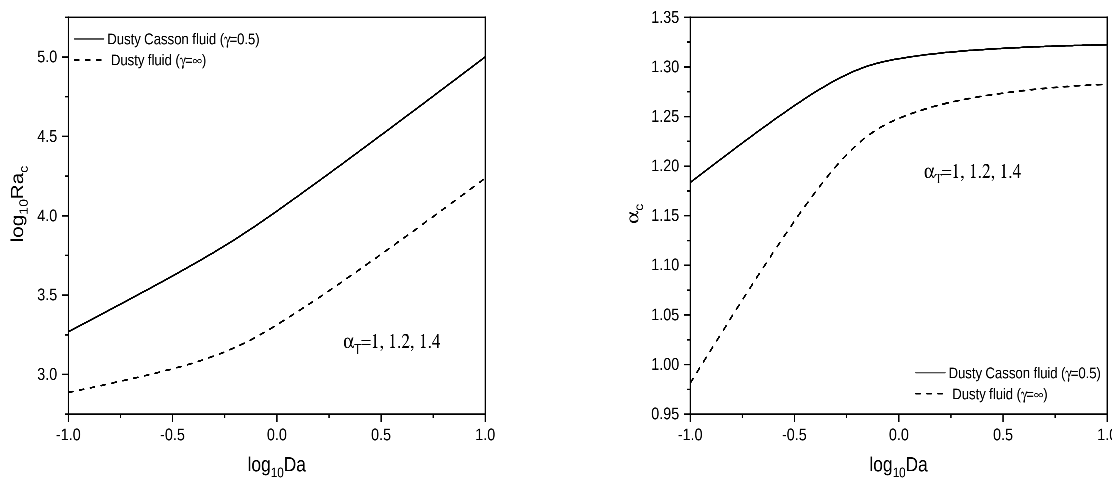

Figure 13.5: "Variation of critical Rayleigh number (Ra_c) and critical wavenumber (α_c) with $log_{10}Da$ for different values of α_T with $Pr = 7$, $\epsilon = 0.3$, γ_1=0.1, D_ρ=10, α_d=1.2, R_d=0.5, Q=0.3, $\theta = \pi/3$, Λ=1, and $\beta = 0$."

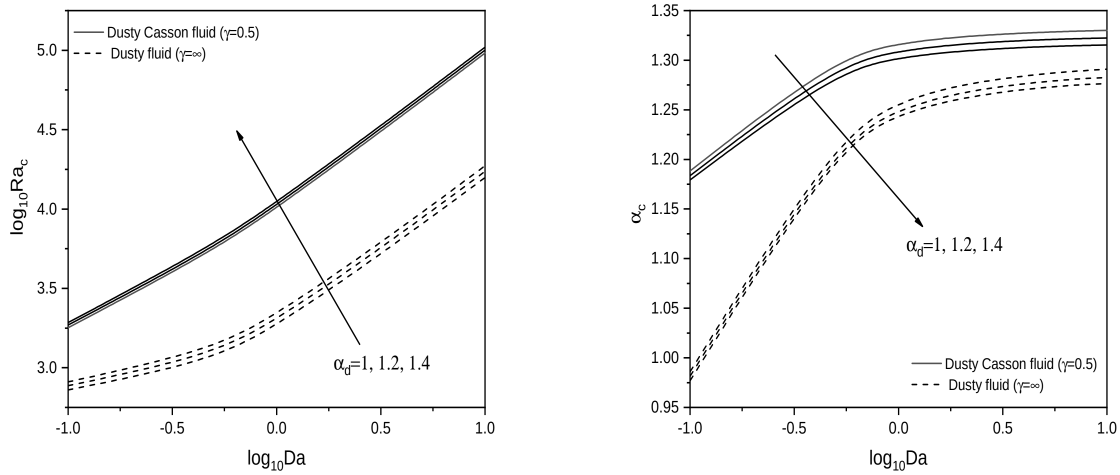

Figure 13.6: "Variation of critical Rayleigh number (Ra_c) and critical wavenumber (α_c) with $log_{10}Da$ for different values of α_d with $Pr = 7$, $\epsilon = 0.3$, γ_1=0.1, D_ρ=10, α_T=1.2, R_d=0.5, Q=0.3, $\theta = \pi/3$, Λ=1, and $\beta = 0$."

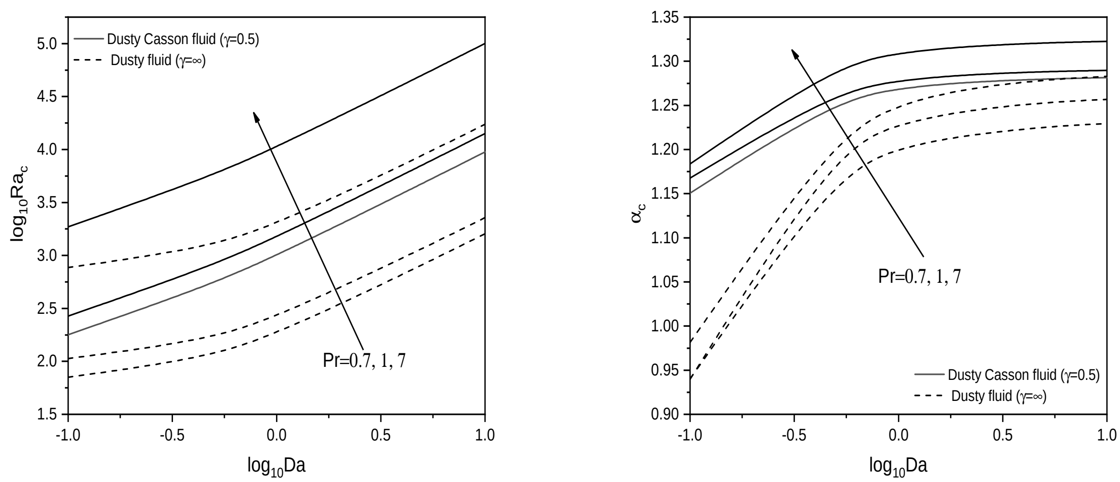

Figure 13.7: "Variation of critical Rayleigh number (Ra_c) and critical wavenumber (α_c) with $log_{10}Da$ for different values of Pr with $\epsilon = 0.3$, γ_1=0.1, D_ρ=10, α_T=1.2, α_d=1.2, R_d=0.5, Q=0.3, $\theta = \pi/3$, Λ=1, and $\beta = 0$."

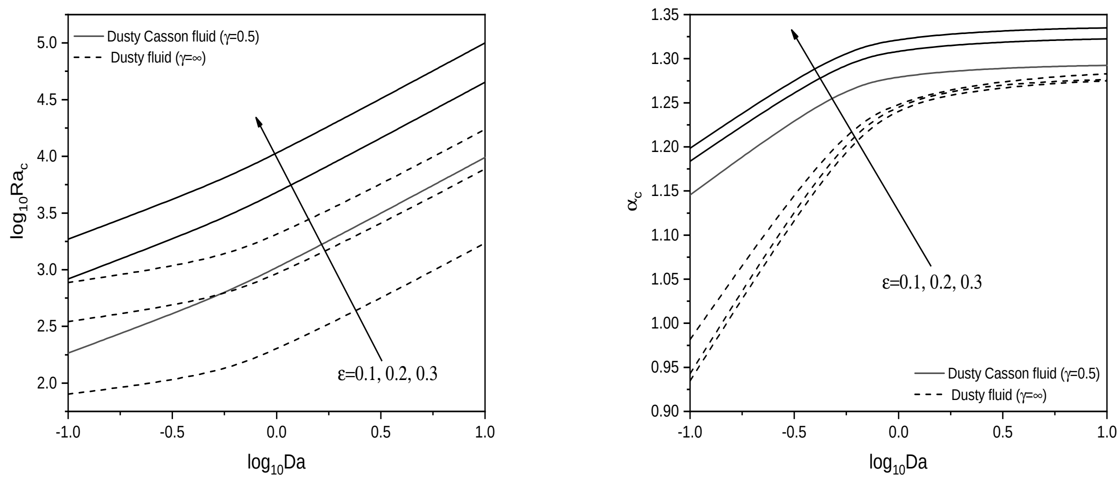

Figure 13.8: "Variation of critical Rayleigh number (Ra_c) and critical wavenumber (α_c) with $log_{10}Da$ for different values of ϵ with $Pr = 7$, γ_1=0.1, D_ρ=10, α_T=1.2, α_d=1.2, R_d=0.5, Q=0.3, $\theta = \pi/3$, Λ=1, and $\beta = 0$."

13.6 Conclusions

The linear stability of two-phase dusty Casson fluid flow in a porous inclined channel while accounting for the effects of heat source or sink and radiation is examined. The critical Rayleigh number and critical wavenumber for different parameters such as θ, γ, D_ρ, Q, R_d, α_T, α_d, Pr and ϵ are computed and graphically shown with respect to Da.

- The Casson parameter (γ), channel's inclination angle (θ), heat source/sink parameter (Q) and destabilizes the flow.
- Mass concentration parameter (D_ρ), radiation parameter (R_d), momentum dust parameter (α_d), Prandtl number (Pr), and porosity parameter (ϵ) help to stabilize flow within an inclined channel. As a result, an increase in these variables acts as a stumbling block to the onset of convection.

Part V

SUMMARY AND CONCLUSIONS

Chapter 14

Summary and Conclusions

Linear stability of convection in an inclined porous channel filled with nanofluid, Casson fluid, and dusty fluid has been investigated in this thesis. The study examines the impact of parameters such as double diffusion, magnetic field, interphase heat transfer parameter (LTNE), variable viscosity, heat source/sink, thermal radiation, and chemical reaction on the onset of convection.

The governing partial differential equations of the flow and their associated boundary conditions in the Chapters - 2 through Chapters - 13 are initially cast into dimensionless form using suitable transformations. Small perturbations are imposed on the basic velocity, temperature, nanoparticle volume fraction and pressure. The generalized eigenvalue problem for the perturbed state is obtained from a normal mode analysis. This eigenvalue problem is solved using the Chenyshev spectral collocation method in MATLAB. The effects of various geometrical and fluid parameters on the onset of convection is presented through graphs and discussed. The important observations made from this study are listed below:

- The disturbances are least stable for dusty, Casson, and nanofluid fluids for vertical inclination ($\theta = \pi/2$), and the variable viscosity parameter (k) is 0.5.
- An increase in Hartmann number (Ha), porosity parameter (ϵ), and Prandtl number (Pr) causes a delay in convection for $\theta = \pi/3$.
- The increasing thermo-solutal Lewis number (Ln), Soet number (Sr), Darcy number (Da), and Dufour number (D_f) for both variable and constant viscosity induce delays in convection.

- As N_{HP} increases, the critical Rayleigh number (Ra_c) rises, and as N_{HS} climbs, Ra_c falls. As a result, in both circumstances where the flow is regulated by constant and variable viscosity, for all values of N_{HP} stabilize the flow, but for all values N_{HS} destabilize the flow field. When we increase N_{HP}, however, there is no change in the critical Rayleigh number Ra_c on inclination from horizontal to vertical.

- For all values of N_{HP}, γ_p, γ_s, ϵ_p, and ϵ_s stabilize the flow with constant viscosity, while γ_s stabilizes the flow with variable viscosity field.

- For all values of N_{HS}, γ_p, and ϵ_p, destabilize the flow with constant viscosity, while γ_p, γ_s, ϵ_p, and ϵ_s destabilizes the flow with variable viscosity field.

- For a nanofluid flow, streamlines form Rayleigh-Bernard convection cells when the channel is vertical ($\theta = \pi/2$). As the inclination angle decreases, the cells expand vertically and create a horizontal cell structure at $\theta = 0$. Changing the channel inclination from vertical to horizontal reorients streamlines from horizontal to vertical.

- For a Casson fluid flow in an inclined channel, convection occurs sooner for increasing values of the heat source/sink parameter (Q), Casson parameter (γ), radiation parameter (R_d), and chemical reaction parameter (R_c).

- When the radiation parameter (R_d) of two-phase dusty fluids increases, convection is delayed; conversely, when the heat source/sink parameter (Q) increases, it occurs sooner. However, the increasing mass concentration parameter (D_ρ) and momentum dust parameter (α_d) result in delay in convection when two-phase dusty fluid flow is controlled by both constant and variable viscosity fields. However, there is no significant effect on the increased thermal dust parameter (α_T).

- For both constant and variable viscosity fields, the neutral stability graphs for dusty Casson fluid always situated below the neutral stability graphs for dusty phases.

The work presented in the thesis can be extended by studying the analysis in various non-Newtonian fluids like Micropolar fluids, Couple stress fluids, Power-law fluids and the geometry can be changed to pipe, through annulus and an inclined pipe. Further, this work can be extended to study the analysis on nonlinear stability.

Bibliography

[1] H. P. G. Darcy. *Les fontaines publiques de la ville de Dijon.* Victor Dalmont, Paris, 1856.

[2] H. C. Brinkman. A calculation of the viscous force exerted by a flowing fluid on a dense swarm of particles. *Applied Scientific Research*, 1(1):27–34, 1949.

[3] P. Forchheimer. Wasserbewegung durch boden. *Zeitschrift des Verines Deutscher Ingenieure*, 45:1782–1788, 1901.

[4] S US Choi and Jeffrey A Eastman. Enhancing thermal conductivity of fluids with nanoparticles. Technical report, Argonne National Lab.(ANL), Argonne, IL (United States), 1995.

[5] SM Sohel Murshed and CA Nieto De Castro. A critical review of traditional and emerging techniques and fluids for electronics cooling. *Renewable and Sustainable Energy Reviews*, 78:821–833, 2017.

[6] Mojtaba Bezaatpour and Hadi Rostamzadeh. Simultaneous energy storage enhancement and pressure drop reduction in flat plate solar collectors using rotary pipes with nanofluid. *Energy and Buildings*, 239:110855, 2021.

[7] Hongyun Zhang, Kongxiang Wang, Wei Yu, Lingling Wang, and Huaqing Xie. Ternary molten salt energy storage coupled with graphene oxide-tin nanofluids for direct absorption solar collector. *Energy and Buildings*, 253:111481, 2021.

[8] Laith Jaafer Habeeb and Hasan Shakir Majdi. Nanofluids and computational applications in medicine and biology. In *Applications of Nanobiotechnology.* IntechOpen, 2019.

[9] Mojgan Sheikhpour, Mohadeseh Arabi, Alibakhsh Kasaeian, Ali Rokn Rabei, and Zahra Taherian. Role of nanofluids in drug delivery and biomedical technology: Methods and applications. *Nanotechnology, Science and Applications*, pages 47–59, 2020.

[10] Raj Kamal Tiwari and Manab Kumar Das. Heat transfer augmentation in a two-sided lid-driven differentially heated square cavity utilizing nanofluids. *International Journal of heat and Mass transfer*, 50(9-10):2002–2018, 2007.

[11] J Buongiorno. Convective transport in nanofluids. 2006.

[12] N Casson. Flow equation for pigment-oil suspensions of the printing ink-type. *Rheology of disperse systems*, pages 84–104, 1959.

[13] James Freeman Steffe. *Rheological methods in food process engineering*. Freeman press, 1996.

[14] A-RA Khaled and Kambiz Vafai. The role of porous media in modeling flow and heat transfer in biological tissues. *International Journal of Heat and Mass Transfer*, 46(26):4989–5003, 2003.

[15] Yvette Baxter-Drayton and John F Brady. Brownian electrorheological fluids as a model for flocculated dispersions. *Journal of Rheology*, 40(6):1027–1056, 1996.

[16] QD Nguyen and DV Boger. Measuring the flow properties of yield stress fluids. *Annual Review of Fluid Mechanics*, 24(1):47–88, 1992.

[17] George Rudinger. *Fundamentals of gas particle flow*, volume 2. Elsevier, 2012.

[18] Donald A Nield, Adrian Bejan, et al. *Convection in porous media*, volume 3. Springer, 2006.

[19] KR Rajagopal, M Ruzicka, and AR Srinivasa. On the oberbeck-boussinesq approximation. *Mathematical Models and Methods in Applied Sciences*, 6(08):1157–1167, 1996.

[20] D. A. Nield and A. Bejan. *Convection in Porous Media*, volume 5th edn. Springer, New York, NY, 2017.

[21] CW Horton and FT Rogers Jr. Convection currents in a porous medium. *Journal of Applied Physics*, 16(6):367–370, 1945.

[22] Lapwood. Convection of a fluid in a porous medium. In *Mathematical Proceedings of the Cambridge Philosophical Society*, volume 44, pages 508–521. Cambridge University Press, 1948.

[23] Herbert E Huppert and J Stewart Turner. Double-diffusive convection. *Journal of Fluid Mechanics*, 106:299–329, 1981.

[24] Mahantesh S Swamy. Effect of cross-diffusion on the onset of double-diffusive reaction convection in a porous layer. *Journal of Porous Media*, 20(7), 2017.

[25] N Deepika. Linear and nonlinear stability of double-diffusive convection with the soret effect. *Transport in Porous Media*, 121(1):93–108, 2018.

[26] Cédric Beaume, Alain Bergeon, and Edgar Knobloch. Three-dimensional doubly diffusive convectons: instability and transition to complex dynamics. *Journal of Fluid Mechanics*, 840:74–105, 2018.

[27] Abbes Attia, Mahmoud Mamou, Smail Benissaad, and Nabil Ouazaa. Linear and nonlinear stability of soret-dufour lapwood convection near double codimension-2 points. *Heat Transfer—Asian Research*, 48(3):763–792, 2019.

[28] IS Shivakumara, KR Raghunatha, MN Savitha, and M Dhananjaya. Implication of cross-diffusion on the stability of double diffusive convection in an imposed magnetic field. *Zeitschrift für angewandte Mathematik und Physik*, 72(3):117, 2021.

[29] BM Shankar, SB Naveen, and IS Shivakumara. Stability of double-diffusive natural convection in a vertical porous layer. *Transport in Porous Media*, 141(1):87–105, 2022.

[30] Najat J Noon and SA Haddad. Stability analysis for rotating double-diffusive convection in the presence of variable gravity and reaction effects: Darcy model. *Special Topics & Reviews in Porous Media: An International Journal*, 13(4), 2022.

[31] Joginder Singh Dhiman, Prabhugouda M Patil, and Sumixal Sood. Modified stability analysis of double-diffusive convection in viscoelastic fluid layer saturating porous media. *Heat Transfer*, 52(2):1497–1528, 2023.

[32] Fangyou Yan, Wensi He, Qingzhu Jia, Qiang Wang, Shuqian Xia, and Peisheng Ma. Prediction of ionic liquids viscosity at variable temperatures and pressures. *Chemical Engineering Science*, 184:134–140, 2018.

[33] S Ijaz, Iqra Shahzadi, S Nadeem, and Anber Saleem. A clot model examination: with impulsion of nanoparticles under influence of variable viscosity and slip effects. *Communications in Theoretical Physics*, 68(5):667, 2017.

[34] David A Yuen, S Balachandar, and U Hansen. Modelling mantle convection: A significant challenge in geophysical fluid dynamics. *Geophysical and Astrophysical Convection*, pages 257–294, 2000.

[35] S Manjunatha and BJ Gireesha. Effects of variable viscosity and thermal conductivity on mhd flow and heat transfer of a dusty fluid. *Ain Shams Engineering Journal*, 7(1):505–515, 2016.

[36] Nisheet Goyal and Eckart Meiburg. Unstable density stratification of miscible fluids in a vertical hele-shaw cell: influence of variable viscosity on the linear stability. *Journal of Fluid Mechanics*, 516:211–238, 2004.

[37] Dhananjay Yadav, GS Agrawal, and Rama Bhargava. Onset of double-diffusive nanofluid convection in a layer of saturated porous medium with thermal conductivity and viscosity variation. *Journal of Porous Media*, 16(2), 2013.

[38] JC Umavathi, Dhananjay Yadav, and Monica B Mohite. Linear and nonlinear stability analyses of double-diffusive convection in a porous medium layer saturated in a maxwell nanofluid with variable viscosity and conductivity. *Elixir Mech Eng*, 79:30407–30426, 2015.

[39] Neha Aanam A, PG Siddheshwar, Smita S Nagouda, S Pranesh, et al. Effects of variable viscosity and rotation modulation on ferroconvection. *Journal of Thermal Analysis and Calorimetry*, 147(7):4667–4682, 2022.

[40] Xuan Zhang and Oleg Zikanov. Mixed convection in a horizontal duct with bottom heating and strong transverse magnetic field. *Journal of fluid mechanics*, 757:33–56, 2014.

[41] Agnieszka Hudoba and Sergei Molokov. Linear stability of buoyant convective flow in a vertical channel with internal heat sources and a transverse magnetic field. *Physics of Fluids*, 28(11):114103, 2016.

[42] Nidhi Singh, Manish K Khandelwal, and Peng Yu. Instability of mixed convection flow in a differentially heated channel under a transverse magnetic field with internal heating. *Physics of Fluids*, 33(9):094102, 2021.

[43] Christopher Camobreco, Alban Potherat, and Gregory Sheard. Linear stability analysis of pulsatile quasi-two-dimensional duct flows under a transverse magnetic field. 2020.

[44] A Kasaeian, R Daneshazarian, O Mahian, L Kolsi, A J Chamkha, S Wongwises, and I Pop. Nanofluid flow and heat transfer in porous media: A review of the latest developments. *International Journal of Heat and Mass Transfer*, 107:778–791, 2017.

[45] G C Rana and R Chand. Onset of thermal convection in a rotating nanofluid layer saturating a darcy-brinkman porous medium: a more realistic model. *Journal of Porous Media*, 18(6), 2015.

[46] J C Umavathi and J Prathap Kumar. Onset of convection in a porous medium layer saturated with an Oldroyd-B nanofluid. *ASME Journal of Heat Transfer*, 139(1):Article ID : 012401, 2016.

[47] I K Khalid, N F M Mokhtar, I Hashim, Z B Ibrahim, and S S A Gani. Effect of internal heat source on the onset of double-diffusive convection in a rotating nanofluid layer with feedback control strategy. *Advances in Mathematical Physics*, 2017:Article ID : 2789024, 2017.

[48] P Akbarzadeh and O Mahian. The onset of nanofluid natural convection inside a porous layer with rough boundaries. *Journal of Molecular Liquids*, 272:344–352, 2018.

[49] D Yadav. The density-driven nanofluid convection in an anisotropic porous medium layer with rotation and variable gravity field: A numerical investigation. *Journal of Applied and Computational Mechanics*, 6(3):699–712, 2020.

[50] D Srinivasacharya and D Barman. Linear stability of convection in a vertical channel filled with nanofluid saturated porous medium. *Heat Transfer*, 50(4):3220–3239, 2021.

[51] Ketchate C G N Kapen, P T, D Fokwa, and G Tchuen. Linear stability analysis of (cu-al2o3)/water hybrid nanofluid flow in porous media in presence of hydromagnetic, small suction and injection effects. *Alexandria Engineering Journal*, 60(1):1525–1536, 2021.

[52] C D N Ketchate, P T Kapen, D Fokwa, and G Tchuen. Stability analysis of mixed convection in a porous horizontal channel filled with a newtonian al_2o_3 / water nanofluid in presence of magnetic field and thermal radiation. *Chinese Journal of Physics*, 79:514–530, 2022.

[53] Gupta U Kaur, J and R P Sharma. Nonlinear stability analysis for the rheology of oldroyd-b nanofluids embedded by darcy–brinkman porous media using a two-phase model. *Proceedings of the Institution of Mechanical Engineers, Part E: Journal of Process Mechanical Engineering*, page 09544089221141600, 2022.

[54] N Banu and DAS Rees. Onset of darcy–benard convection using a thermal non-equilibrium model. *International Journal of Heat and Mass Transfer*, 45(11):2221–2228, 2002.

[55] DB Ingham and I Pop. *Transport phenomena in porous media III*, volume 3. Elsevier, 2005.

[56] B Straughan. *Convection with local thermal non-equilibrium and microfluidic effects*, volume 32. Springer, 2015.

[57] A Mahajan and M Sharma. Effects of local thermal nonequilibrium on the onset of convection in a magnetic nanofluid layer. *Heat Transfer Research*, 51(7):689–705, 2020.

[58] Puneet Rana, Vishal Gupta, and Lokendra Kumar. Ltne magneto-thermal stability analysis on rough surfaces utilizing hybrid nanoparticles and heat source with artificial neural network prediction. *Applied Nanoscience*, pages 1–20, 2021.

[59] C Siddabasappa and PG Siddheshwar. Linear and global stability analyses on the influences of thermal non-equilibrium and non-uniform gravity field on darcy–brinkman–bénard convection. *International Journal of Applied and Computational Mathematics*, 7(4):1–21, 2021.

[60] D. Srinivasacharya and B Dipak. Effect of local thermal non-equilibrium on the stability of the flow in a vertical channel filled with nanofluid saturated porous medium. *Journal of Heat Transfer*, 144:id 014501, 2022.

[61] NK Enagi, Krishna B Chavaraddi, Sridhar Kulkarni, and GK Ramesh. Effect of maximum density and internal heating on the stability of rotating fluid saturated porous layer using ltne model. *Heliyon*, 8(6):e09620, 2022.

[62] Rusya Iryanti Yahaya, Norihan Md Arifin, and Siti Suzilliana Putri Mohamed Isa. Stability analysis on magnetohydrodynamic flow of casson fluid over a shrinking sheet with homogeneous-heterogeneous reactions. *Entropy*, 20(9):652, 2018.

[63] M Hamid, M Usman, ZH Khan, R Ahmad, and W Wang. Dual solutions and stability analysis of flow and heat transfer of casson fluid over a stretching sheet. *Physics Letters A*, 383(20):2400–2408, 2019.

[64] Liaquat Ali Lund, Zurni Omar, Ilyas Khan, Dumitru Baleanu, and Kottakkaran Sooppy Nisar. Dual similarity solutions of mhd stagnation point flow of casson fluid with effect of thermal radiation and viscous dissipation: stability analysis. *Scientific reports*, 10(1):1–13, 2020.

[65] Shahanaz Parvin, Siti Suzilliana Putri Mohamed Isa, Norihan Md Arifin, and Fadzilah Md Ali. Dual numerical solutions on mixed convection casson fluid flow due to the

effect of the rate of extending and compressing sheet–stability analysis. *CFD Letters*, 12(8):76–84, 2020.

[66] Ubaidullah Yashkun, Fatinnabila Kamal, Khairy Zaimi, Nor Ashikin Abu Bakar, and Norshaza Atika Saidin. Stability analysis on stagnation-point flow and heat transfer towards a permeable stretching/shrinking sheet with heat source in a casson fluid. *CFD Letters*, 12(6):1–15, 2020.

[67] G Mahanta, S Shaw, MK Nayak, and JC Pati. Effects on mhd casson stagnation point flow with stability analysis over the stretching surface in the presence of slip velocity. *Int J Appl Eng Res*, 16:823–829, 2021.

[68] Debasish Dey, Rupjyoti Borah, and Ardhendu Sekhar Khound. Stability analysis on dual solutions of mhd casson fluid flow with thermal and chemical reaction over a permeable elongating sheet. *Heat Transfer*, 51(4):3401–3417, 2022.

[69] Ramesh B Kudenatti et al. The onset of instability in a hydromagnetic channel flow of casson fluid: the accurate solutions. *Applied Mathematics and Computation*, 436:127475, 2023.

[70] PG Saffman. On the stability of laminar flow of a dusty gas. *Journal of fluid mechanics*, 13(1):120–128, 1962.

[71] B Mahanthesh and BJ Gireesha. Thermal marangoni convection in two-phase flow of dusty casson fluid. *Results in physics*, 8:537–544, 2018.

[72] Farhad Ali, Muhammad Bilal, Nadeem Ahmad Sheikh, Ilyas Khan, and Kottakkaran Sooppy Nisar. Two-phase fluctuating flow of dusty viscoelastic fluid between non-conducting rigid plates with heat transfer. *IEEE Access*, 7:123299–123306, 2019.

[73] Farhad Ali, Muhammad Bilal, Madeha Gohar, Ilyas Khan, Nadeem Ahmad Sheikh, and Kottakkaran Sooppy Nisar. A report on fluctuating free convection flow of heat absorbing viscoelastic dusty fluid past in a horizontal channel with mhd effect. *Scientific Reports*, 10(1):1–15, 2020.

[74] Sk Reza-E-Rabbi, Sarder Firoz Ahmmed, SM Arifuzzaman, Tanmoy Sarkar, and Md Shakhaoath Khan. Computational modelling of multiphase fluid flow behaviour over a stretching sheet in the presence of nanoparticles. *Engineering Science and Technology, an International Journal*, 23(3):605–617, 2020.

[75] Juanwen Chen, Jiwen Cen, Wenbo Huang, and Fangming Jiang. Multiphase flow and heat transfer characteristics of an extra-long gravity-assisted heat pipe: an experimental study. *International journal of heat and mass transfer*, 164:120564, 2021.

[76] Gohar Ali, Farhad Ali, Arshad Khan, Abdul Hamid Ganie, and Ilyas Khan. A generalized magnetohydrodynamic two-phase free convection flow of dusty casson fluid between parallel plates. *Case Studies in Thermal Engineering*, 29:101657, 2022.

[77] IL Animasaun, EA Adebile, and AI Fagbade. Casson fluid flow with variable thermophysical property along exponentially stretching sheet with suction and exponentially decaying internal heat generation using the homotopy analysis method. *Journal of the Nigerian Mathematical Society*, 35(1):1–17, 2016.

[78] D Mythili and R Sivaraj. Influence of higher order chemical reaction and non-uniform heat source/sink on casson fluid flow over a vertical cone and flat plate. *Journal of Molecular Liquids*, 216:466–475, 2016.

[79] Oluwole Daniel Makinde and Lazarus Rundora. Unsteady mixed convection flow of a reactive casson fluid in a permeable wall channel filled with a porous medium. In *Defect and Diffusion Forum*, volume 377, pages 166–179. Trans Tech Publ, 2017.

[80] QM Zaigham Zia, Ikram Ullah, Met al Waqas, A Alsaedi, and T Hayat. Cross diffusion and exponential space dependent heat source impacts in radiated three-dimensional (3d) flow of casson fluid by heated surface. *Results in physics*, 8:1275–1282, 2018.

[81] B Shankar Goud, P Pramod Kumar, and Bala Siddulu Malga. Effect of heat source on an unsteady mhd free convection flow of casson fluid past a vertical oscillating plate in porous medium using finite element analysis. *Partial Differential Equations in Applied Mathematics*, 2:100015, 2020.

[82] Muhammad Awais, Muhammad Asif Zahoor Raja, Saeed Ehsan Awan, Muhammad Shoaib, and Hafiz Muhammad Ali. Heat and mass transfer phenomenon for the dynamics of casson fluid through porous medium over shrinking wall subject to lorentz force and heat source/sink. *Alexandria Engineering Journal*, 60(1):1355–1363, 2021.

[83] M Riaz Khan, Amnah S Al-Johani, Awatif MA Elsiddieg, Tareq Saeed, and A Mousa Abd Allah. The computational study of heat transfer and friction drag in an unsteady mhd radiated casson fluid flow across a stretching/shrinking surface. *International Communications in Heat and Mass Transfer*, 130:105832, 2022.

[84] Cedric Gervais Njingang Ketchate, Pascalin Tiam Kapen, Didier Fokwa, and Ghislain Tchuen. Stability analysis of non-newtonian blood flow conveying hybrid magnetic nanoparticles as target drug delivery in presence of inclined magnetic field and thermal radiation: Application to therapy of cancer. *Informatics in Medicine Unlocked*, 27:100800, 2021.

[85] Shahirah Abu Bakar, Norihan Md Arifin, Fadzilah Md Ali, Norfifah Bachok, Roslinda Nazar, and Ioan Pop. A stability analysis on mixed convection boundary layer flow along a permeable vertical cylinder in a porous medium filled with a nanofluid and thermal radiation. *Applied Sciences*, 8(4):483, 2018.

[86] Liaquat Ali Lund, Zurni Omar, Sumera Dero, and Ilyas Khan. Linear stability analysis of mhd flow of micropolar fluid with thermal radiation and convective boundary condition: Exact solution. *Heat Transfer—Asian Research*, 49(1):461–476, 2020.

[87] Abderrahim Wakif, Ali Chamkha, Thirupathi Thumma, IL Animasaun, and Rachid Sehaqui. Thermal radiation and surface roughness effects on the thermo-magneto-hydrodynamic stability of alumina–copper oxide hybrid nanofluids utilizing the generalized buongiorno's nanofluid model. *Journal of Thermal Analysis and Calorimetry*, 143(2):1201–1220, 2021.

[88] Caulfield M J, Qiao G G, and Solomon D H. Some aspects of the properties and degradation of polyacrylamides. *Chemical reviews*, 102(9):3067–3084, 2002.

[89] V Steinberg and H Brand. Convective instabilities of binary mixtures with fast chemical reaction in a porous medium. *The Journal of Chemical Physics*, 78(5):2655–2660, 1983.

[90] Atul K Srivastava. Stability analysis of electro-thermo convection of binary fluid with chemical reaction in a horizontal porous layer. *Alexandria Engineering Journal*, 55(4):3153–3171, 2016.

[91] Suganya S T, Muthtamilselvan M, and Abdalla B. Effects of radiation and chemical reaction on cu–al_2o_3 water hybrid flow past a melting surface in the existence of cross magnetic field. 2021.

[92] A Barletta and DAS Rees. Local thermal non-equilibrium analysis of the thermoconvective instability in an inclined porous layer. *International Journal of Heat and Mass Transfer*, 83:327–336, 2015.

[93] A Barletta and M Celli. Instability of combined forced and free flow in an inclined porous channel. *International Journal of Computational Methods*, 13(02):1640001, 2016.

[94] Anjanna Matta and Antony A Hill. Double-diffusive convection in an inclined porous layer with a concentration-based internal heat source. *Continuum Mechanics and Thermodynamics*, 30(1):165–173, 2018.

[95] M Celli and A Barletta. Onset of buoyancy driven convection in an inclined porous layer with an isobaric boundary. *International Journal of Heat and Mass Transfer*, 132:782–788, 2019.

[96] Baole Wen and Gregory P Chini. On moderate-rayleigh-number convection in an inclined porous layer. *Fluids*, 4(2):101, 2019.

[97] Anjanna Matta and Nagaraju Gajjela. The detailed study of thermal instability analysis in an inclined porous medium. In *AIP Conference Proceedings*, volume 2246, page 020079. AIP Publishing LLC, 2020.

[98] Kamalika Roy, R Ponalagusamy, and PVSN Murthy. The effects of double-diffusion and viscous dissipation on the oscillatory convection in a viscoelastic fluid saturated porous layer. *Physics of Fluids*, 32(9):094108, 2020.

[99] Gian C Rana and V Sharma. Effect of rotation on the onset of convection in rivlin-ericksen fluid heated from below in a brinkman porous medium. *International Journal of Fluid Mechanics Research*, 39(6), 2012.

[100] Gian C Rana, SK Kango, and Sanjeev Kumar. Effect of rotation on the onset of convection in walters's (model b') fluid heated from below in a darcy-brinkman porous medium. *Journal of Porous Media*, 15(12), 2012.

[101] GC Rana, R Chand, and Veena Sharma. Electrohydrodynamic instability of a rotating walters'(model b') fluid in a porous medium: Brinkman model. *Mechanics and Mechanical Engineering*, 23(1):138–143, 2019.

[102] Tzou. Thermal instability of nanofluids in natural convection. *International Journal of Heat and Mass Transfer*, 51(11-12):2967–2979, 2008.

[103] Mustafa Turkyilmazoglu. Single phase nanofluids in fluid mechanics and their hydrodynamic linear stability analysis. *Computer Methods and Programs in Biomedicine*, 187:105171, 2020.

[104] Nidhi Singh and Manish K Khandelwal. Linear stability perspective on mixed convection flow of nanofluids in a differentially heated vertical channel. *International Communications in Heat and Mass Transfer*, 134:105989, 2022.

[105] P Falsaperla and G Mulone. Thermal convection in an inclined porous layer with brinkman law. *Ricerche di Matematica*, 67(2):983–999, 2018.

[106] DP Wall and SK Wilson. The linear stability of channel flow of fluid with temperature-dependent viscosity. *Journal of Fluid Mechanics*, 323:107–132, 1996.

[107] C Canuto, M Yousuff Hussaini, A Quarteroni, A Thomas Jr, et al. *Spectral methods in fluid dynamics*. Springer Science & Business Media, 2012.

[108] Darbhasayanam Srinivasacharya and Dipak Barman. Influence of magnetic field on the stability of double diffusive nanofluid convection in a vertical porous channel. *Journal of Porous Media*, 25(9), 2022.

[109] Raghavendra Rohith Kasibhatla, Andreas König-Haagen, Fabian Rösler, and Dieter Brüggemann. Numerical modelling of melting and settling of an encapsulated pcm using variable viscosity. *Heat and Mass Transfer*, 53:1735–1744, 2017.

[110] Peter C Sukanek, Charles A Goldstein, and Robert L Laurence. The stability of plane couette flow with viscous heating. *Journal of Fluid Mechanics*, 57(4):651–670, 1973.

[111] Dmitry Nikushchenko and Valery Pavlovsky. Fluid motion equations in tensor form. *Advances on Tensor Analysis and Their Applications; Bulnes, F., Ed*, pages 49–72, 2020.

[112] Harshal Srivastava, Amaresh Dalal, Kirti Chandra Sahu, and Gautam Biswas. Temporal linear stability analysis of an entry flow in a channel with viscous heating. *International Journal of Heat and Mass Transfer*, 109:922–929, 2017.

[113] A Barletta and L Storesletten. Thermoconvective instabilities in an inclined porous channel heated from below. *International journal of heat and mass transfer*, 54(13-14):2724–2733, 2011.

[114] MA Seddeek, SN Odda, and MS Abdelmeguid. Numerical study for the effects of thermophoresis and variable thermal conductivity on heat and mass transfer over an accelerating surface with heat source. *Computational materials science*, 47(1):93–98, 2009.